universität wien

DISSERTATION / DOCTORAL THESIS

Titel der Dissertation / Title of the Doctoral Thesis

„Physical basis of thermal soot measurement methods“

verfasst von / submitted by

Mag. rer. nat. Theresa Haller

angestrebter akademischer Grad / in partial fulfillment of the requirements for the degree of

Doktorin der Naturwissenschaften (Dr. rer. nat.)

Wien, 2021 / Vienna, 2021

Studienkennzahl lt. Studienblatt / degree programm code as it appears on the student record sheet:	A 796 605 411
Dissertationsgebiet lt. Studienblatt / field of study as it appears on the student record sheet:	Physik
Betreut von / Supervisor:	Univ. Prof. Dr. Regina Hitzenberger

Jakob,

es wäre vollkommen absurd

- ja geradezu grotesk -

dir eine Dissertation zu widmen.

Also so:

Der Mensch kann zwar tun, was er will,
aber er kann nicht wollen, was er will.
(Arthur Schopenhauer)

Peace, kloaner Bruader.

(ahjo, und: Kreide)

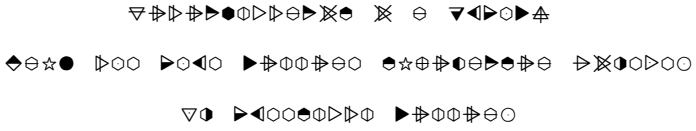

Für meine Oma

(die sich sehr gefreut hätte…)

Abstract

Carbonaceous aerosols contribute a large fraction (20-40% in PM2.5; Pöschl, 2005) to the atmospheric aerosol and have diverse impacts on climate and human health. This importance makes reliable measurement methods essential.

Thermal-optical measurement techniques are widely used to classify carbonaceous aerosols using their thermal stability: A filter sample is heated stepwise first in an inert atmosphere, then in an oxidizing atmosphere and the carbon evolving from the filter is monitored together with a transmission / reflection laser signal that tracks the darkening of the sample occurring during the heating in the inert atmosphere. Although results for total carbon (TC) are comparable for different thermal-optical measurement techniques, values for elemental carbon (EC) vary by up to 44% especially in the presence of brown carbon (BrC). Charring of organic material during the inert heating phase has been reported as a major confounder but at the start of this work no literature about structural changes occurring during thermal-optical analyses was available.

In this work combustion aerosol standard (CAST) soot as well as atmospheric aerosol samples (some of them washed with water) were heated in a thermal-optical instrument following the NIOSH870 (Birch and Cary, 1996) and the EUSAAR2 (Cavalli et al., 2010) protocols. Raman spectra of the unheated and heated samples were analyzed. For the CAST soot samples UV-Vis spectroscopy and transmission electron microscopy were also applied. For the atmospheric aerosol samples air mass back trajectories were calculated and major ions (Na^+, NH_4^+, Mg^{2+}, Ca^{2+}, K^+, Cl^-, NO_2^-, NO_3^-, SO_4^-) were analyzed. All samples were analyzed for black and brown carbon using the integrating sphere technique.

CAST soot samples with high amounts of BrC showed an increase of structural ordering at 870°C in He when the sample was heated following NIOSH870. For atmospheric aerosol samples the temperature level where structural changes occurred during EUSAAR2 varied for different samples while the structure of the washed atmospheric aerosol samples did not change.

It is remarkable that for most investigated samples, changes of the optical properties did not coincide with changes of structural ordering: Samples darkened continuously also at temperature levels, where no changes of structural ordering were visible. So the darkening of a sample during thermal-optical analysis is not necessarily caused by the building of graphitic-like structures.

Zusammenfassung

Kohlenstoffhaltige Aerosole tragen einen großen Teil (20-40% in PM2,5; Pöschl, 2005) zum atmosphärischen Aerosol bei und haben vielfältige Auswirkungen auf das Klima und die menschliche Gesundheit. Zuverlässige Messmethoden für diesen Teil des atmosphärischen Aerosols sind daher notwendig.

Zur Klassifizierung von kohlenstoffhaltigen Aerosolen werden häufig thermo-optische Messtechniken eingesetzt in denen die unterschiedliche thermische Stabilität der verschiedenen Kohlenstoff-fraktionen genutzt wird: Die Probe wird zunächst in einer inerten Atmosphäre, dann in einer oxidierenden Atmosphäre schrittweise aufgeheizt. Die Kohlenstoffmenge, die während des Heizens in die Gasphase übergeht wird gleichzeitig mit einem Transmissions-/Reflexionslasersignal, das die Schwärzung der während des Aufheizens in der inerten Atmosphäre verfolgt, gemessen. Obwohl die Ergebnisse für Gesamtkohlenstoff (TC) für verschiedene thermo-optische Messtechniken vergleichbar sind, variieren die Werte für den elementaren Kohlenstoff (EC) um bis zu 44%, insbesondere in Gegenwart von braunem Kohlenstoff (BrC). Das Verkohlen von organischem Material während der inerten Heizphase in Helium ist als eine der Hauptursachen für die Unterschiede bekannt. Dennoch war zu Beginn dieser Arbeit keine Literatur über Strukturänderungen während thermo-optischer Analysen verfügbar.

In dieser Arbeit wurden Verbrennungsaerosol-Standard (CAST) Ruße sowie atmosphärische Aerosolproben (einige davon mit Wasser gewaschen) in einem thermo-optischen Gerät nach dem NIOSH870- und dem EUSAAR2-Protokoll (Birch and Cary, 1996; Cavalli et al., 2010) erhitzt. Raman-Spektren der nicht aufgeheizten und aufgeheizten Proben wurden analysiert. Die CAST-Rußproben wurden zusätzlich mit UV-Vis Spektroskopie und Transmissionselektronenmikroskopie untersucht. Für die atmosphärischen Aerosolproben wurden Rückwärtstrajektorien der Luftmassen berechnet und die bedeutendsten Ionen (Na^+, NH_4^+, Mg^{2+}, Ca^{2+}, K^+, Cl^-, NO_2^-, NO_3^-, SO_4^-) analysiert. Alle Proben wurden unter Verwendung der Ulbrichtkugel-Methode auf schwarzen (BC) und braunen Kohlenstoff (BrC) analysiert.

CAST-Rußproben mit hohem BrC-Gehalt zeigten eine Zunahme der strukturellen Ordnung bei 870 °C in He, wenn die Probe nach dem NIOSH870-Protokoll erhitzt wurde. Bei atmosphärischen Aerosolproben variierte das Temperaturniveau, bei dem während EUSAAR2 strukturelle Veränderungen auftraten, für verschiedene Proben, während sich die Struktur der gewaschenen atmosphärischen Aerosolproben nicht änderte. Bemerkenswert ist, dass bei den meisten untersuchten Proben Änderungen der optischen Eigenschaften nicht mit Änderungen der Strukturordnung einhergingen: Die Schwärzung der Proben erfolgte kontinuierlich auch während Temperaturniveaus, bei denen keine Änderungen der strukturellen Ordnung sichtbar waren. Die Schwärzung einer Probe bei thermo-optischen Analysen wird also nicht zwangsläufig durch den Aufbau graphitähnlicher Strukturen verursacht.

Table of contents

Abstract i
Zusammenfassung ii
1. Introduction 1
1.1. Nomenclature 2
1.2. Atmospheric aerosol 3
1.3. Carbonaceous Aerosol 4
1.3.1. Climate and health effects 4
1.3.2. Sources 4
1.4. Thermal-optical measurement 5
2. Theoretical background soot 7
2.1. Formation process and structure of soot 7
2.2. Properties of CAST soot 8
3. Theoretical background of analysis of soot structure 9
3.1. Raman spectroscopy 9
3.1.1. Theoretical Background 9
3.1.2. Interpretation of Raman spectra of soot and related carbonaceous material 11
3.2. WAXD 14
4. Instrumentation 15
4.1. miniCAST generator 15
4.2. EC/OC analyzer (Sunset Instruments Inc.) 16
4.3 Confocal Raman microscope 18
4.4 Integrating Sphere 20
4.5 WAXD 21
5. Preparatory tests 22
5.1 WAXD 22
5.2 Raman 27
5.2.1 Quartz fiber background 27
5.2.2 Comparability of two parallel filter samples 29
5.2.3. Influence of different Baselines 29
6. Experimental 32
6.1 Sampling 32
6.1.1. Pretreatment and storage of filters 32

6.1.2. Sampling of CAST soot 32
6.1.3. Sampling of atmospheric aerosol 33
6.2. Measurement scheme 33
6.2.1. Sample preparation (heating and washing of the samples) 34
6.2.2. Measurement of Raman spectra and data processing 36
7. Overview Publication 1 38
Structural changes of CAST soot during a thermal–optical measurement protocol (T. Haller, C. Rentenberger, J. C. Meyer, L. Felgitsch, H. Grothe, and R. Hitzenberger, 2019) .....
8. Overview Publication 2 41
Investigation of structural changes of atmospheric aerosol samples during two thermal–optical measurement procedures (EUSAAR2, NIOSH870) (T. Haller, E. Sommer, T. Steinkogler, C. Rentenberger, A. Wonaschuetz, A. Kasper-Giebl, H. Grothe, and R. Hitzenberger, 2021).....
9. Additional results 43
9.1 Raman spectra of additional CAST-samples 43
9.2 Additional analyses of atmospheric aerosol samples 47
9.2.1 Comparison of EC/OC ratios and structural changes 47
9.2.2. Possible influence of sources and source regions on structural changes 48
10. Summary and overall conclusion 51
Literature 53
11. Publication 1 60
12. Publication 2 85
Appendix: Additional published material 110
Acknowledgements 123
Curriculum Vitae 124

1. Introduction

Carbonaceous aerosol is a large and important fraction of the atmospheric aerosol. It contributes 20-40% to PM2.5 (Pöschl, 2005; Yttri et al., 2007) and was found to have diverse impacts on climate and human health (e.g. Bond and Bergstrom, 2006; Highwood and Kinnersley, 2006). Especially the light absorbing fractions black carbon (BC) and brown carbon (BrC) have direct and indirect effects on the energy balance of the earth because of their capability to absorb solar radiation in the atmosphere and their potential to act as cloud condensation nuclei and ice nuclei. Because of this importance, reliable measurements of carbonaceous aerosols are necessary. However, carbonaceous aerosols can be highly complex mixtures of carbonaceous substances ranging from non-absorbing organic molecules to highly light absorbing graphitic-like material (Pöschl, 2005). Different measurement methods use these diverse physical and chemical properties to distinguish between often operationally defined fractions: while BC and BrC are classified optically, organic carbon (OC) and elemental carbon (EC) are classified thermochemically by using their different thermal stability. Although total carbon (TC) values can be measured reliably within 5-15%, results for EC and OC can be biased by up to 44% for measurements with different thermal-optical techniques especially in the presence of BrC (e.g. Reisinger et al., 2008; Cavalli et al., 2010; Yu et al., 2002; Cheng et al., 2012; Hitzenberger et al., 2006; Kim et al., 2015; Wonaschuetz et al., 2009; Zhang, Trzepla et al., 2021, Giannoni et al., 2016). In thermal-optical measurement techniques, a filter sample is heated stepwise, first in an inert atmosphere, then in an oxidizing atmosphere. As a first rough distinction, carbon evolving in the absence of oxygen at temperatures below 550-700°C is assigned to OC and carbon evolving at temperatures above ca. 600°C in the presence of oxygen is assigned to EC (Bond and Bergstrom, 2006; Chow et al., 2004; Andreae and Gelencsér, 2006). Pyrolysis of organic species during the inert phase is monitored with a laser signal transmitted through or reflected by the sample and EC and OC values are corrected for so called pyrolytic carbon (PC) after the measurement. However, this laser-correction is based on assumptions that are not fulfilled in all cases (see section 1.4.), so charring is still a major confounder in thermal-optical measurement techniques. Although different studies addressed the charring of OC during thermal-optical analyses on a thermal or optical level, at the beginning of this work no study was found that analyzed the actual structural changes occurring during thermal-optical analyses. Some studies addressed the influence of charring during thermal-optical analyses and investigated the influence of certain substances on charring, without analyzing the structure of the pyrolysis products (e.g. Wang et al., 2010; Yang and Yu 2002; Yu et al., 2002; Giannoni et al., 2016; Liu et al., 2019). Other authors investigated structural changes of soot during heating, but not in a thermal-optical instrument (e.g. Bladt et al., 2014; Ess et al., 2016; Ivleva et al., 2007). But to the best of my knowledge no study to date addressed structural changes during heating in a thermal-optical instrument following the gas atmospheres, heating rates and temperature levels of thermal-optical measurement protocols.

The aim of the present work was to fill this gap and to shed light on the changes of structural ordering of the carbonaceous material heated during thermal-optical measurement procedures. For this purpose combustion aerosol standard (CAST) soot samples as well as atmospheric aerosol

samples were heated in a thermal-optical instrument following the NIOSH870 and EUSAAR2 protocols. The unheated and heated samples were then analyzed with Raman spectroscopy.

1.1. Nomenclature

Different terms are used for the fractions of carbonaceous aerosols (BC, BrC, LAC, EC, OC, TC) which are operationally defined and commonly tied to the measurement methods. However, sometimes the terms “BC”, “EC” and “soot” are used interchangeably to describe the black, thermally refractory part of combustion products with graphitic-like internal structure. As suggested by Petzold et al. (2013) and Andreae and Gelencsér (2006) a careful definition of these terms is therefore important:

The term soot describes the product of incomplete combustion of biogenic or fossil fuels. Although the term sometimes is used only for the black, graphitic-like part of the combustion aerosol, in this work it is used for all particulate products of incomplete combustion which can also include organic carbon, brown carbon and inorganic substances.

The term black carbon (BC) refers to highly light-absorbing carbonaceous species which absorb light equally well over the whole visible wavelength range and appear therefore black (Bond and Bergstrom, 2006). In this work the term BC is used for results obtained with the integrating sphere method (see section 4.5). Since the integrating sphere is calibrated using a carbon black standard (Elftex 124, Cabot Corporation), BC can be seen as “Elftex equivalent” in this work. Brown carbon (BrC) is the part of light absorbing carbon (LAC) that absorbs visible light more weakly in the long-wavelength range than in the short-wavelength range and therefore appears brown. In this work, the term BrC is used for results obtained with the integrating sphere method and refers to the part of light absorbing carbon (LAC) with similar optical properties as the humic acic sodium salt (Acros Organics, no. 68131-04-4) used for calibration (see section 4.5). BrC can therefore be seen as “humic acid sodium salt equivalent” and refers to the total mass of BrC including other atoms. (The humic acid sodium salt used here contains 47% carbon by mass). The sum of BrC and BC is reported as LAC in this work.

From a chemical point of view, the term elemental carbon (EC) would describe a substance that consists only of carbon atoms such as pure graphite, carbon nanotubes, diamond, fullerenes etc. However, the term EC became established for the thermally refractory fraction of carbonaceous aerosols that does not evolve at temperatures below 550-700°C in the absence of oxygen and combusts at temperatures above 600°C in the presence of oxygen (Andreae and Gelencsér, 2006). The term organic carbon (OC) became established for the fraction of carbonaceous material that evolves at temperatures below 550-700°C in the absence of oxygen (Bond end Bergstrom, 2006; Chow et al., 2004). EC and OC are used in this work for values obtained with the thermal-optical measurement methods EUSAAR2 and NIOSH870, which include an optical correction for pyrolyzed carbon (PC) (see below in section 1.4).

The thermal stability of EC and the optical properties of BC can both be related to graphitic-like structures found in “mature” soot particles obtained under oxygen rich burning conditions and high temperatures (see section 2).

1.2. Atmospheric aerosol

This section is based on the IPCC fifth assessment report (IPCC, 2013) chapter 7 (clouds and aerosols) and the articles by Putaud et al. (2004) and Bond et al. (2013).

Atmospheric aerosols are complex mixtures of various organic and inorganic species deriving from natural as well as from anthropogenic sources. Particles can be emitted directly by a source as primary particles or can be formed from gaseous precursors, as secondary particles. Major constituents of atmospheric aerosols are organic carbon, black carbon, inorganic species (e.g. sulfates, nitrates, ammonium salts, sea salt), mineral dust and primary biological aerosol particles (e.g. pollen, fungal spores, plant debris) (IPCC, 2013). The composition of different aerosol types in atmospheric aerosols varies for different regions depending on the governing aerosol sources. Carbonaceous material contributes between 20% in alpine areas and 40% in urban areas to PM2.5 (Pöschl, 2005). In European urban and urban background sites, organic matter is a major component of PM2.5 and PM10, while BC contributes 5-10% to PM2.5 at all (urban, rural and natural) European sites (Putaud et al., 2004). Mineral dust is most abundant in urban South Asia and China where it contributes up to about 35% to PM10 (IPCC, 2013). In Europe mineral species can be major contributors to PM10 at kerbside sites (Putaud et al., 2004). Sulfates, deriving from marine and volcanic emissions or oxidation of sulfur containing gases from natural and anthropogenic sources, generally contribute 10-30% to particulate mass but less than 10% in rural Africa, South America and urban Oceania (IPCC, 2013). Nitrates and ammonium salts contribute 6% and 4% to particulate mass (IPCC, 2013). However, during cold periods in Europe, characterized by high pollution levels (PM10 >50 µg/m3), nitrates can be major contributors to PM10 and PM2.5 (Putaud et al., 2004). This can partially be explained by a higher stability of particulate ammonium nitrate (NH_4NO_3) at lower temperatures (Putaud et al., 2004). Sea salt constitutes the largest fraction of particulate mass with 50-70% in coastal remote sites located less than 50 km from a seashore (IPCC, 2013; Putaud et al., 2004).

About 70% or more of the particulate matter can be clearly attributed to one of the described major components. However, part of particulate matter generally remains unclassified because e.g. of the uncertainty in the estimation of organic matter (when the ratio of organic carbon to organic matter is unknown) or because of a possible presence of water (IPCC, 2013).

Atmospheric aerosols can be internal or external mixtures of different compounds where both mixing states can also coexist relatively soon after emission (Okada and Hitzenberger, 2001; Zhang et al., 2014; Ye et al., 2018; IPCC, 2013; Deboudt et al., 2010; Pratt and Prather, 2010; Bondy et al., 2018; Adachi et al., 2010; Adachi and Buseck, 2013; China et al., 2013; Cappa et al., 2012). Internally mixed particles can develop by condensation of gas-phase species on already existing particles or by collision of small aerosol particles and subsequent coagulation (IPCC, 2013), so externally mixed aerosols can become internally mixed when different aerosol types age together as it is reported e.g. for dust and biomass burning aerosol (Hand et al., 2010). In urban aerosol up to 90% of the particles are internally mixed with secondary organic species. Particles deriving from biomass combustion often are internal mixtures of OC, EC and inorganic species such as ammonium, nitrates and sulfates (IPCC, 2013).

1.3. Carbonaceous Aerosol

Carbonaceous aerosol species (apart from carbonates) span a rather continuous range from highly light absorbing compounds with graphitic-like structures (referred to as EC or BC depending on the measurement method) to non-absorbing organic molecules (Pöschl, 2005). Especially the organic fraction of carbonaceous aerosols is highly divers: Hundreds of different organic compounds have been detected but only 10-40% of these species identified on a molecular level (Pöschl, 2005). Depending on the (chemical, optical, structural etc.) properties of carbonaceous particles, they have different impacts on climate and health. However, the complexity of carbonaceous compounds makes reliable measurements challenging.

1.3.1. Climate and health effects

Carbonaceous aerosols are reported to have several effects on climate and human health. Traffic-related air pollution is correlated with severe health effects up to enhanced mortality (Pöschl et al., 2005; Mesquita et al., 2017). Ultrafine particulate matter (d < 100 nm) can enter into deep regions of the lung, penetrate the membranes of the respiratory tract and enter the blood stream and the interstitial fluid (Pöschl et al., 2005; Mesquita et al., 2017). A significant fraction of polycyclic aromatic hydrocarbons (PAHs) deriving from fossil fuel combustion or biomass burning was found to have potential toxicity (Mesquita et al., 2017; Fushimi et al., 2021).

The effects of carbonaceous aerosols on climate are divers and can lead to positive as well as negative radiative forcing. Generally direct, indirect and semi direct effects can be differentiated: Light absorbing carbon (LAC) absorbs solar radiation which increases atmospheric temperature leading to a (positive) direct effect on radiative forcing (Bond et al., 2013). A change of the atmospheric temperature structure caused by elevated layers of LAC influences – as a semi-direct effect – cloud formation, life time and distribution. Carbonaceous particles can act as cloud condensation nuclei and ice nuclei (Spracklen et al., 2011; Pierce et al., 2007; Prenni et al., 2012; Häusler et al., 2018; Ikhenazene et al., 2019) which influence cloud distribution and droplet or ice particle concentration in clouds, leading to an indirect effect on radiative forcing. Semi-direct and indirect effects generally can lead to positive or negative radiative forcing, so that the extent of the overall-effect is unclear (e.g. Bond et al., 2013; IPCC, 2013; Zhang, Wang et al., 2021; Liu and Matsui, 2021).

Light absorbing carbon together with other light absorbing species cause positive radiative forcing when they are deposited on snow or ice fields in the Arctic, reduce their reflectivity and lead to lowered surface albedo and increased ice melt, both of which exert positive forcing on the radiative balance (Bond et al., 2013; Kang et al., 2020; Tuccella et al., 2021).

1.3.2. Sources

Carbonaceous aerosols are produced by natural and anthropogenic sources. These sources can emit primary particles or gaseous species which can lead to the formation of secondary particles by chemical or photo-chemical reactions (IPCC, 2013; Pöschl, 2005). Natural sources of primary carbonaceous particles include emissions from wild fires and emissions by the biosphere (pollen, spores, bacteria, viruses, fragments of animals and plants). Burning forests and savannas are the largest sources of BC on a global scale (Bond et al., 2013). The main natural sources of aerosol precursor gases are the oceans (emission of e.g. dimethylsulphide) and the terrestrial biosphere

(emission of volatile organic compounds). From these precursors, secondary organic aerosol material (SOA) can be built by photo-chemical reactions, a process that is enhanced in the presence of nitrogen oxides and primary organic particles deriving e.g. from anthropogenic sources (IPCC, 2013).

Anthropogenic sources of carbonaceous aerosols include diesel engines, industry, and residential fuel combustion. On- and off-road diesel engines are responsible for about 70% of BC in Europe (Bond et al., 2013). Generally, all of these sources do not only emit primary particles alone but also aerosol precursor gases such as SO_2, NO_x, ammonia and volatile organic compounds (VOC) from which secondary aerosol species can be formed. In urban and near-city areas SOA contributes therefore a large fraction to organic aerosol mass (Zhang et al., 2005; IPCC, 2013; Volkamer et al., 2006) up to about 40% at northern midlatitudes (De Gouw and Jimenez, 2009).

Biomass combustion is one of the major sources of BrC in the atmospheric aerosol (e.g. Kirchstetter and Novakov, 2004; Hoffer et al., 2006; Laskin et al., 2015). BrC can be emitted directly from forest fires, biomass combustion or other low-temperature combustion processes in primary particles, or it can possibly be produced in atmospheric multiphase reactions by oxidation of volatile organic compounds emitted e.g. by biomass burning, vehicle exhaust or fossil fuel combustion (Laskin et al., 2015). Atmospheric humic-like substances (HULIS) can be formed e.g. via chemical reactions of biomass burning smoke in cloud droplets (IPCC, 2013; Laskin et al., 2015; Gelenscér et al., 2003). HULIS were found to have mostly polycyclic ring structures with hydrocarbon side chains and are important components of BrC (Laskin et al., 2015; Graber and Rudic, 2006; Andreae and Gelencsér, 2006). Nakayama et al. (2010) found that SOA produced by gas-phase oxidation of aromatic hydrocarbons absorbs solar radiation mostly in the UV wavelength range. However, SOA with similar properties as HULIS can be formed e.g. from alpha pinine and chatechol – the latter is reported to be abundant in emissions from biomass combustion (Ofner et al., 2010; Saleh et al., 2013).

1.4. Thermal-optical measurement

In thermal-optical measurements, carbonaceous aerosol species are separated into organic carbon (OC) and elemental carbon (EC). The idea behind the method is to use the differences in thermal stability of organic substances (referred to as OC) and substances with graphitic-like structures (referred to as EC). However the boundary between OC and EC is not sharp. Thermal, optical and structural properties transition continuously from non-absorbing organic carbon over light absorbing organic carbon (e.g. BrC) to black thermally refractory material with graphitic like structures (Pöschl, 2005).

In thermal-optical measurements, a filter sample is heated stepwise first in an inert atmosphere, then in an oxidizing atmosphere. (In the instrument used in this work the inert atmosphere is realized with He, the oxidizing atmosphere with a mixture of He and O_2 (for a description of the instrument see section 4.2). The temperature levels and durations differ for different measurement protocols and the maximum temperature of the inert heating phase ranges from 580°C (IMPROVE_A, Chow et al., 2004) to 870°C (NIOSH870, Panteliadis et al., 2015; Birch and Cary, 1996).OC is thought to evolve during the inert phase because of its low thermal stability while the more refractory EC should combust only in the subsequent oxidizing phase (for definitions of carbonaceous fractions see section 1.1). However, OC can pyrolyze during the inert

heating phase and the pyrolyzed material – often referred to as pyrolyzed carbon (PC) – can remain on the filter and evolves only at higher temperatures and/or in the presence of oxygen together with EC. The darkening of the filter is monitored with a transmission and/or reflectance laser signal in order to differentiate between EC and PC in the subsequent analysis: A split point is set where the laser signal reaches its initial value and the carbon that has evolved prior to this split point is assigned to OC and accordingly the carbon that has evolved after the split point is assigned to EC. The fraction of carbon that has left the filter in the oxidizing phase but before the split point is often referred to as PC.

This laser correction is based on the assumption that PC has the same optical properties as EC or that it burns off totally before EC does. However, both assumptions are not fulfilled (Subramanian et al., 2006; Han et al., 2007). Yang and Yu (2002) found that the light absorption coefficient of PC is not the same as for EC at the wavelength used in their thermal-optical instrument (680 nm) and that it is not even constant during the whole measurement procedure. This uncertainty in the estimation of PC leads to uncertainties in the EC/OC split.

Several studies were conducted to optimize the original temperature protocol (i.e. number of temperature levels, their height and durations and the maximum temperature level in the inert phase) described by Birch and Cary (1996) to minimize pyrolysis and to improve the uncertainties in the EC/OC split (e.g. Chow et al., 2004; Cavalli et al., 2010; Cheng et al., 2012; Bautista et al., 2015). Cavallli et al. (2012) developed a measurement protocol – EUSAAR2 – that reduces charring for ambient European aerosols and which subsequently was selected as European standard method for EC and OC measurements (Brown et al., 2017). Despite all refinements of the thermal-optical measurement procedures, pyrolysis is still a major confounder under certain circumstances: Atmospheric aerosols are complex mixtures of carbonaceous and non-carbonaceous substances (see section 1.2) and several inorganic constituents present in the sample can influence the charring behavior of the organic substances. Ammonium bisulfate, for example, enhances the charring of starch and cellulose by a factor 2-3 but the same substance reduces the charring of levoglucosan by about 15 % (Yu et al., 2002). Generally, water soluble organic carbons were found to be responsible for a large fraction (13-66%) of charring (Yu et al., 2002; Piazzalunga et al., 2011; Giannoni et al., 2016). Metal salts enhance the charring of diesel soot and atmospheric aerosol samples and reduce the oxidation temperature of EC (Wang et al., 2010; Bladt et al., 2014).

These complex and sometimes contradictory effects of different aerosol species make a simple prediction of the charring of real-world-aerosols challenging. Besides, there are very few studies investigating the charring behavior during thermal-optical analyses in terms of structural changes. Often the terms “charring” and “pyrolysis“ are used to describe the darkening of a sample and it is implicitly assumed that a more structured phase of carbon – such as graphene-layers or graphitic-like structures similar to the structures in EC – is formed. In this work, changes of structural ordering during heating in a thermal-optical instrument are investigated.

2. Theoretical background soot

2.1. Formation process and structure of soot

The formation of soot is a rather complex process that is still not fully understood (e.g. Wang 2011; Valencia et al., 2021). The variety of fuels and combustion conditions leads to a large number of possible pathways to the nucleation of nanoparticles that can only be simulated for the most "simple" conditions (e.g. combustion of pure hydrocarbons in premixed flames). For more complex fuels and combustion conditions, however, a prediction of the pathways which lead to nucleation and the formation of soot on an elementary level is not possible (Wang, 2011).

An overview of the processes that lead to soot formation – using the example of propane (C_3H_8) combustion – is given e.g. by Wang (2011): The initial step of the nucleation of carbonaceous nanoparticles is the dehydrogenation of the C_3H_8 molecules and the formation of acetylene (C_2H_2). Although this process is endothermic, the increase of the entropy (ΔS) due to dehydrogenation is larger than the increase of the enthalpy (ΔH), so the Gibbs free energy (ΔG = ΔH-TΔS, with T the temperature) decreases, which leads to a dominance of acetylene in the system. From acetylene benzene is created in an exothermic radical reaction and the Gibbs free energy is again reduced. Subsequently, molecular mass grows by formation of polycyclic aromatic hydrocarbons (PAH) from benzene rings. Since during this phase the Gibbs free energy is reduced slightly for each addition of an aromatic ring, the building of PAHs can be highly reversible (Wang, 2011). High temperatures – needed to ensure fast kinetics on the one hand – can lead to a fragmentation of already existing PAHs and limit therefore their growth on the other hand. For the nucleation process it is necessary, that PAHs survive this fragmentation, which is often the case for e.g. naphthalene, pyrene or coronene, consisting of two, three and six benzenoid rings, respectively (Wang , 2011). However, the exact pathways that lead to the formation of PAHs and subsequent nucleation are highly sensitive to the conditions (local chemistry and temperature, fuel structure and composition) in the flame, and cannot be predicted accurately from the current state of knowledge.

PAHs that survive this process are stacked into clusters with an extent of 1-2 nm where the binding between two PAHs is realized by covalent bonds or by aliphatic linkages (Wang, 2011; Chung and Violi, 2011; Heidenreich et al., 1968. After this nucleation process, these blocks of stacked PAHs coagulate and form aggregates while the single clusters still undergo surface reactions (Frenklach, 2002) so that the space between them is filled and the surface of an aggregate is smoothed to a spherical shape (Wang, 2011). Depending on the residence time and the conditions in the flame additional PAHs can condense on the surface of the spheres (Kholghy et al., 2016). These primary particles have sizes between 10 and 50 nm and are often described to have an onion-shell-like structure with concentrically arranged graphene-layers (e.g. Heidenreich et al., 1968; Bond et al., 2013; Uy et al., 2014; Pawlyta et al., 2016, Kholghy et al., 2016). The layers are roughly parallel but are not perfectly stacked like the single layers in graphite (Heidenreich et al., 1968) so the in-plane distances of the C-atoms are similar to those in graphite, but the distances between the layers are larger than in graphite (Houska and Warren, 1954).

In a next step the spherical primary particles coagulate and form agglomerates with fractal structures and sizes >100 nm (e.g. Michelsen et al., 2020; Bond et al., 2013). Low volatile and semi volatile

substances from the exhaust can condense on the surface of solid soot particles, and can form additional organic coatings (Török et al., 2018). In summary, the composition, morphology and internal structure of particles deriving from incomplete combustion depend on their residence time in the burning zone, the fuel composition, the conditions in the flame, the temperature and the temperature-gradient (Wang, 2011).

2.2. Properties of CAST soot

The combustion aerosol standard (CAST, Jing-CAST Technologies) instrument used in this study and described in section 4.1 produces soot particles in a propane and air co-flow diffusion flame with different fuel to air ratios. The structure and composition of CAST soot particles depends on the ratio of carbon to oxygen (C/O) in the burning chamber. A dividing line between fuel rich and fuel lean burning conditions can be defined at the stoichiometric C/O ratio of C/O_{stoic}=0.3 (Schnaiter et al. 2006) where theoretically all carbon would be oxidized (Moore et al. 2014) following the equation $C_3H_8+5O_2 \rightarrow 4H_2O+3CO_2$. Burning conditions with C/O > C/O_{stoic} are defined as fuel rich, and conditions with C/O < C/O_{stoic} as fuel lean (or oxygen rich).

Moore et al. (2014) investigated the properties of CAST soot under different burning conditions: The diameters of CAST soot particles range from <10 nm to about 130 nm and the largest particles are produced under C/O ratios slightly below C/O_{stoic}. Particle concentrations are higher for fuel rich conditions than for fuel lean conditions. Soot generated under fuel lean burning conditions was found to be similar to diesel soot consisting of agglomerates of spheres with graphitic like structures and is dominated by EC / BC (e.g. Kim et al, 2015; Mamakos et al, 2013). Fuel rich burning conditions, on the other hand, result in less structured particles with a large amount of organic carbon. However, not only the EC/OC ratio depends on C/O but also the composition of the organic part of the aerosol differs: Under fuel rich combustion conditions particle coatings containing larger amounts of PAHs and aromatic compounds are formed, while coatings containing larger amounts of oxygenated, aliphatic compounds are produced under fuel- lean conditions (Moore et al., 2014). Figure 1 summarizes the properties of soot produced under different C/O ratios.

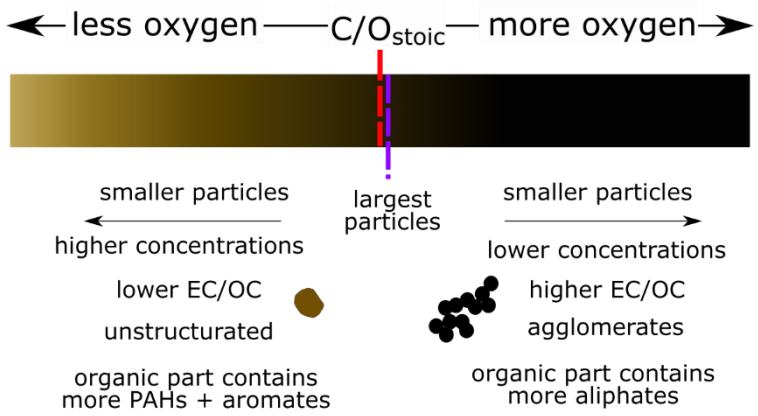

Figure 1: Overview of CAST aerosol properties depending on C/O ratios.

3. Theoretical background of analysis of soot structure

3.1. Raman spectroscopy

Raman spectroscopy can be used to analyze soot and related carbonaceous materials because of its sensitivity to different carbon-to-carbon bonding types. It gives information about e.g. crystallite structures of graphite as well as about molecular structures of non-ordered or amorphous carbonaceous materials. The following section is based on the books by Naumer and Heller (eds) (1997), Haarer and Spiess (eds) (1995) and Dieing et al. (eds) (2011).

3.1.1. Theoretical Background

Raman spectroscopy uses light scattered inelastically by a molecule. The frequencies of the scattered light are related to the energies of the eigen-oscillations or vibrational modes of the molecule and can be used to deduce details of the molecular structure.

When a molecule is illuminated with monochromatic light with frequency ν_0, oscillations of electrons and vibrations of the whole molecule are excited. The oscillating electrons on the one hand reemit an electromagnetic wave with the excitation frequency ν_0 – this process is known as Rayleigh scattering. Raman scattering, on the other hand, is caused by vibrations of the whole molecule (i.e. the relative motion of the atoms in the molecule). From a quantum-mechanical point of view, the incident photons with energy $E_0 = h\nu_0$(with h, the Planck constant) hit the molecule, transfer part of their energy and induce molecular vibrations with frequencies ν_i and energies $E_i = h\nu_i$. As a consequence, the inelastically scattered photon has the energy $E = E_0 - E_i = h(\nu_0 - \nu_i)$ when energy is transferred from the incident photon to the molecule (Stokes shift) or $E = E_0 + E_i = h(\nu_0 + \nu_i)$ when energy of an already excited molecule is transferred to the photon (anti-Stokes shift). The frequency corresponding to this energy is $\nu = \nu_0 \pm \nu_i$. Generally the spectrum of Raman shifts ν_i (or more often the spectrum of the corresponding wavelengths) is referred to as “Raman spectrum”.

In the classical explanation of Raman scattering, the molecule is seen as a coupled harmonic oscillator and the incoming and scattered light are described as electromagnetic waves. The electric field (Ɛ) of the incoming radiation oscillates with frequency ν_0 and maximum amplitude ε_0:

$$\varepsilon=\varepsilon_0 \cos 2\pi\nu_0 t \qquad (1)$$

This electric field forces the electrons and atomic nuclei to oscillate. The electrons follow the excitation frequency and oscillate with ν_0 because they are easily movable. As a consequence an oscillating dipole moment μ is induced, which is proportional to Ɛ and to the polarizability α of the molecule:

$$\mu = \alpha\varepsilon = \alpha\varepsilon_0 \cos 2\pi\nu_0 t \qquad (2)$$

The atomic nuclei are also forced to oscillate in the electric field. As a consequence the molecule orbitals are stretched and compressed and the average distances between electrons and nuclei change

continuously. In a stretched orbital the electrons are more weakly bound to the nucleus than in a compressed orbital which means that the polarizability α changes with the distance.

The oscillation of the atomic nucleus with frequency $\nu_i$and maximum deflection q_0 can be described by the distance q from the equilibrium position:

$$q = q_0 \cos(2\pi \nu_i t) \quad (3)$$

The polarizability $\alpha(q)$ can then be expanded around the equilibrium position as

$$\alpha(q) = \alpha_0 + \left(\frac{\delta\alpha}{\delta q}\right)_0 q + \cdots \quad (4)$$

With (1) and (2) and by breaking off the expansion after the second term, the dipole moment μ can be written as:

$$\mu = \alpha_0 E_0 \cos(2\pi\nu_0 t) + \left(\frac{\delta\alpha}{\delta q}\right)_0 q_0 \cos(2\pi\nu_i t)\, E_0 \cos(2\pi\nu_0 t) \quad (5)$$

Using the trigonometric conversion $\cos\beta cos\gamma = \cos(\beta-\gamma) + \cos(\beta+\gamma)$, μ can be split into three terms:

$$\mu = \alpha_0 E_0 \cos(2\pi\nu_0 t) + \left(\frac{\delta\alpha}{\delta q}\right)_0 q_0 E_0 [\cos(2\pi(\nu_0 - \nu_i)t) + \cos(2\pi(\nu_0 + \nu_i)t)] \quad (6)$$

The first term derives from the oscillation of the electrons and corresponds to the Rayleigh scattered light with frequency ν_0, the second term to the Stokes (ν_0-ν_i) and the third term to the anti-Stokes (ν_0+ν_i) Raman scattering. When the polarizability does not change in the equilibrium position, i.e. $\left(\frac{\delta\alpha}{\delta q}\right)_0 = 0$, the two Raman terms disappear. Depending on the geometry of the molecule, this can be the case for some vibrational modes, which means that these vibrations are Raman-inactive. Vibrational modes with changing polarizability, on the other hand, are Raman-active so scattered light with frequencies corresponding to the energies of these vibrations can be observed. Intensities of Raman scattered light are lower than those of Rayleigh scattered light by ca. two orders of magnitude (Naumer and Heller, 1997), so the observation of the Raman scattered spectrum is challenging. To address this, often only the Stokes shifted region of the spectrum is analyzed because of the typically higher intensities compared to the anti-Stokes shifted range. Since Raman scattering can be measured using different excitation wavelengths, only the Raman shift ν_i is relevant. Commonly Raman spectra are plotted depending on the Raman shift in terms of wavenumber 1/Δλ, where Δλ is the difference between the wavelength of the incoming beam ($\lambda_0 = c/\nu_0$, with c the speed of light) and the wavelength of the Raman scattered light ($\lambda = c/\nu$).

3.1.2. Interpretation of Raman spectra of soot and related carbonaceous material

Raman spectra of soot typically show two broad overlapping peaks at ≈1350 cm^{-1} (D-peak or defect peak) and at ≈1580 cm^{-1} (G-peak or graphite peak) which can be seen as a superposition of bands assigned to different vibrational modes in a graphitic lattice (Fig. 3) (e.g. Sadezky et al., 2005).

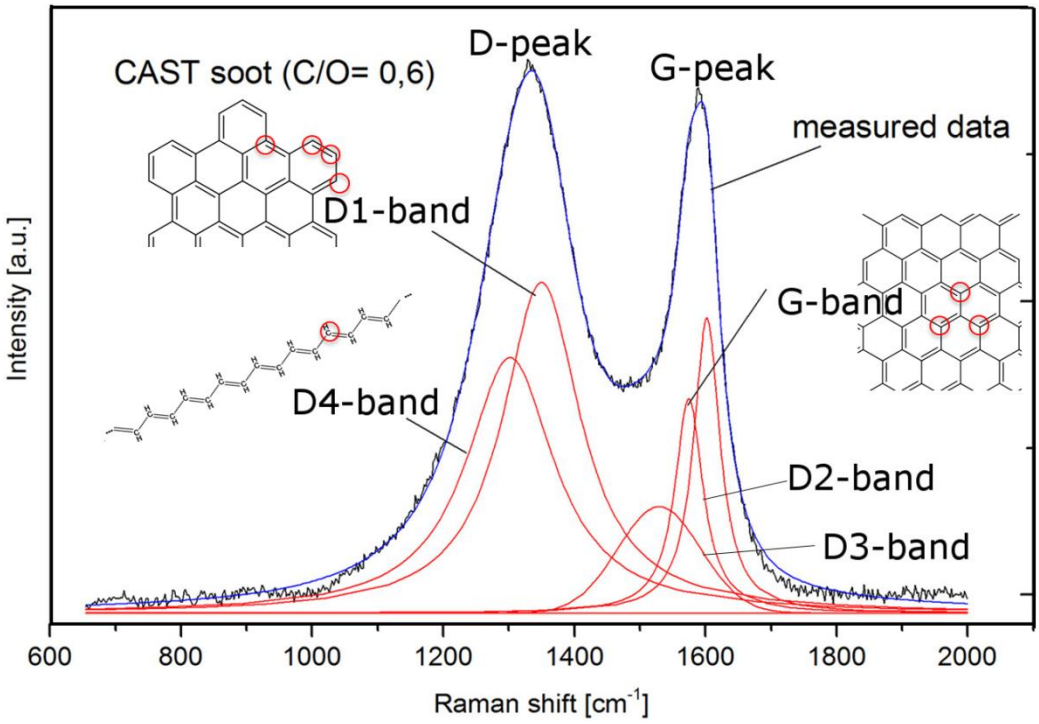

Figure 2: Raman spectrum obtained for a combustion aerosol standard (CAST) soot from propane combustion (C/O=0.6). The black solid line is the measured spectrum, the red lines are curves fitted according to Sadezky et al. (2005), and the blue line is the sum of the fitted curves.

The number and shapes of the curves used for fitting are widely discussed in the literature and several authors propose different combinations of Lorentzian and / or Gaussian fitting curves (Dippel et al., 1999; Jawhari et al., 1995; Sze et al., 2001; Cuesta et al., 1994). Sadezky et al. (2005) compared nine different fitting methods for eight types of industrial soot and found that a combination of four Lorentzian (G-, D1-, D2-, D4- bands) and one Gaussian (D3-band) curve (Fig. 2) fits their measured data best. The initial positions and the shapes they used for fitting are listed in Table 1. (Note the difference between “G-band”, which is used here for the fitting curve, and “G-peak”, which is used for the second peak in the Raman spectrum.) Each band corresponds to vibrational modes of carbon-to-carbon bonds in soot.

Band	Shape	Position [cm^{-1}]	Vibration mode
D1-band	Lorentzian	≈1360	Disordered graphitic lattice (A_{1g}-symmetry), graphene layer edges
D2-band	Lorentzian	≈1620	Disordered graphitic lattice (E_{2g}-symmetry), surface graphene layers
D3-band	Gaussian	≈1500	Amorphous carbon
D4-band	Lorentzian	≈1180	Disordered graphitic lattice (A_{1g}-symmetry), polyenes, ionic impurities
G-band	Lorentzian	≈1580	Ideal graphitic lattice (E_{2g}-symmetry)

Table 1: Band positions and shapes of Raman spectra of soot, as described by Sadezky et al. (2005).

Two typical vibrational modes of aromatic rings in a graphene layer are shown in Figure 3. The stretching mode (Fig. 3) has E_{2g} symmetry and is associated with the G-peak. In the breathing mode (Fig. 3), the symmetry is reduced to A_{1g} symmetry which is associated with the D-peak.

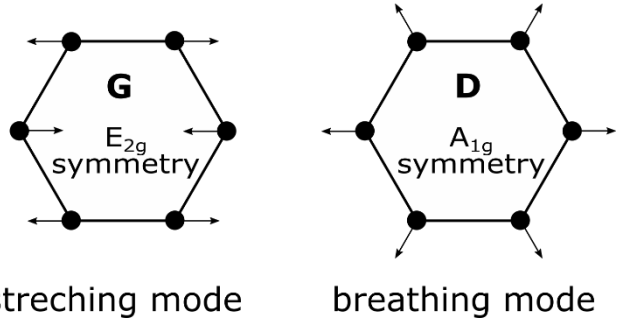

Figure 3: Two typical vibrational modes of aromatic rings in a graphene layer. The stretching mode with E_{2g} symmetry is generally possible in highly ordered graphite and is associated with the G-peak in the soot spectrum. The breathing mode with A_{1g} symmetry is only possible at graphene layer edges or defects and is associated with the D-peak.

In an ideal infinite graphitic lattice the carbon atoms cannot oscillate in the breathing mode, so only vibrations in the stretching mode are excited and lead to a sharp G-peak at about 1580 cm^{-1} (Sadezky et al. 2005). In disordered graphite, the G-peak broadens because of additional vibrations with E_{2g} symmetry at the surface of graphene layers (D2-band) (Sadezky et al. 2005). Next to lattice defects or at the edges of graphene layers also vibrations in the breathing mode can be excited (D1 and D4-bands) and the D-peak at about 1350 cm^{-1} appears. Additionally, polyenes contribute to the D4-band, and the presence of amorphous carbon (i.e. molecules with sp_2 and sp_3 bonded carbon atoms) leads to the D3-band between the two main peaks.

For disordered graphite Tuinstra and Koenig (1970) found that the ratio of the D-peak and G-peak intensities I(D)/I(G) varies inversely with the graphitic crystallite size L_a and a wavelength dependent factor $C_1(\lambda)$:

$$I(D)/I(G) = C_1(\lambda){L_a}^{-1} \quad (7)$$

However, for crystallite sizes < 2nm this relation is not valid. Ferrari and Robertson (2000) state for crystallite sizes < 2nm and amorphous carbon that I(D)/I(G) is proportional to the probability to find a sixfold aromatic ring in a cluster. They state that I(D)/I(G) is therefore proportional to the crystallite size area (L_a^2) with a wavelength dependent factor $C_2(\lambda)$:

$$I(D)/I(G) = C_2(\lambda){L_a}^2 \quad (8)$$

Relations (7) and (8) give a curve with an increasing branch for L_a< 2nm, a decreasing branch for L_a> 2nm and a peak in a broad transition regime at 2 nm (Fig. 4).

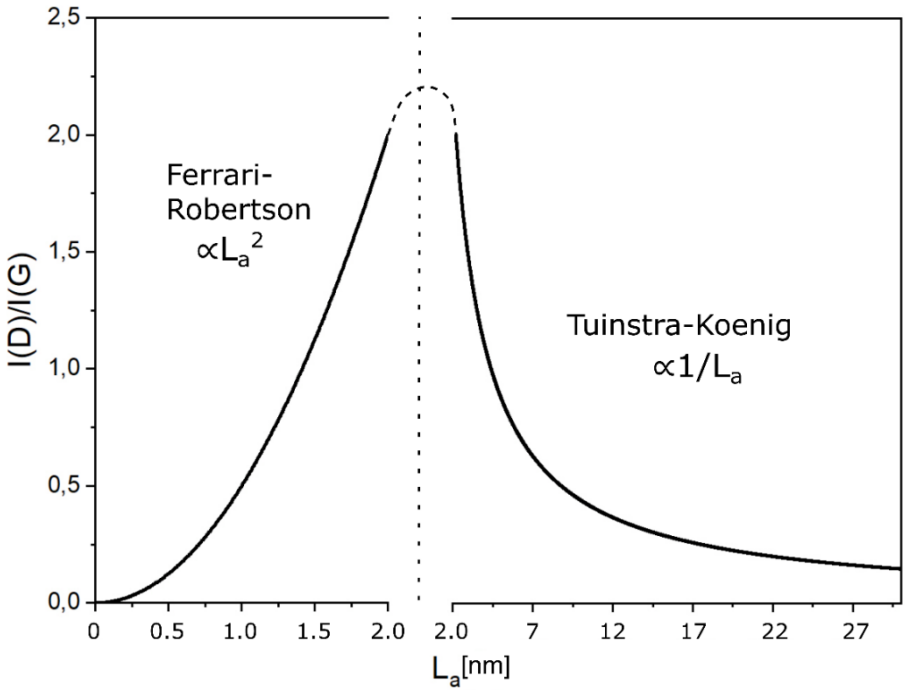

Figure 4: Variation of I(D)/I(G) with crystallite size L_a (using the functions given by Tuinstra and Koenig (1970) and Ferrari and Robertson (2000) with the constants given by Ferrari and Robertson (2000)). For L_a<2nm the curve follows a L_a^2 relation as proposed by Ferrari and Robertson (2000), for L_a>2nm the $1/L_a$ relation given by Tuinstra and Koenig (1970) is used. The broad transition regime between the increasing and decreasing branch is indicated by the gap in the x-axis.

Zickler et al. (2006) verified this relation experimentally. They compared Raman spectra of charcoal and different carbon fibers with crystallite sizes measured by X-ray diffraction (XRD). In contrast to Ferrari and Robertson (2000) and Tuinstra and Koenig (1970) they used the areas of the fitted D and G bands (A(D), A(G)) as well as the intensities (I(D), I(G)) and found that A(D)/A(G) and I(D)/I(G) increase with L_a for L_a<2nm and decrease for L_a>2nm. Generally it is not unambiguously clear in the literature whether peak heights, peak areas or full widths at half maximum (FWHM) should be used to calculate L_a (Zickler et al., 2006; Sadezky et al., 2005). Zickler et al. (2006) found that the equations predicted by Ferrari and Robertson (2000) and Tuinstra and Koenig (1970) are oversimplifications when exact crystallite sizes are calculated, but the qualitative trend is visible in their experimental data also when they compare peak intensities to the crystallite sizes. Therefore it seems valid to use the ratios of D- and G-peak intensities for qualitative comparisons of the structural ordering of different soots as it was done by several other authors (Commodo et al., 2016; Ess et al., 2016; Ivleva et al., 2007).

Care must be taken when relations (7) and (8) are used for the interpretation of Raman spectra of soot samples: values of L_a range up to 3nm for different soot types (Sadezky et al., 2005) so the actual L_a of an investigated substance is critical for the decision whether the increasing or decreasing branch of the relation should be used.

3.2. WAXD

This section is based on the books by Oeser (2019) and Demtröder (2010). X-ray diffraction is commonly used for structural analyses of materials with long- or short-range ordering. While small-angle X-ray scattering (SAXS) gives information about the morphology of particulate matter (e.g. size, shape, surface to volume ratio, pore size), wide-angle X-ray diffraction (WAXD) is used when information about structures in the sub-nanometer range is needed (e.g. crystallinity, lattice constants etc.).

When an X-ray beam with wave vector $\overrightarrow{k_0}$ and wavelength $\lambda = 2\pi/|\overrightarrow{k_0}|$ impinges on a solid object, under suited conditions the beam is elastically scattered by the electron shell of each atom in the material, so each atom is the origin of an elementary wave with wavelength λ. These waves interfere when the atoms are arranged in a crystal lattice with interlayer distance d, and an interference maximum can be observed at the angle θ (or scattering vector $\vec{q} = \vec{k} - \overrightarrow{k_0}$, with $\vec{k}$ the wave vector of the scattered beam, Fig. 5) when Bragg's law is fulfilled:

$$d = \lambda/2 \sin\theta = 2\pi/|\vec{q}| \qquad (9)$$

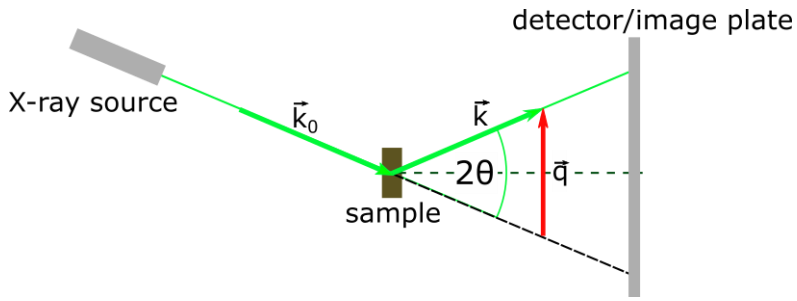

Figure 5: Schematic illustration of X-ray diffraction. An X-ray beam with wave vector $\overrightarrow{k_0}$ illuminates a sample with long- or short-range order and is scattered by $\vec{q}$ in the direction of $\vec{k} = \overrightarrow{k_0} + \vec{q}$. The angle between incoming and scattered beam is 2θ.

Depending on the orientation of the crystal, equation (9) holds for all interlayer distances, so the positions of the interference maxima correspond to the distances between the layers in the lattice. The relative peak intensities, on the other hand, give information about the arrangement of different atoms in the unit cell and the electron density distribution. For ideal crystals the interference maxima are sharp but they broaden for materials with short-range order or for small crystallite sizes, so the peak width is linked to the degree of structural ordering.

4. Instrumentation

4.1. miniCAST generator

In the miniCAST soot generator (type 5201C, Jing-CAST Technologies; sootgenerator.com) propane combusts with air in a co-flow diffusion flame. As visualized in Fig. 6 propane flows into the burning chamber where it is mixed with filtered air (in this work a HEPA filter was used). The air stream surrounds the fuel inlet and the two gases are mixed by diffusion in the burning chamber. Optionally nitrogen can be mixed into the fuel stream but this option was not used in this work. The coaxial inner tube has a diameter of 10 mm, the outer tube has a diameter of 30 mm to ensure a laminar flow of the gases (Moore et al., 2014). The combustion in a diffusion flame is comparable with combustion in the flame e.g. of a candle; the combustion speed is limited by the rate of diffusion, so the oxygen content inside the flame is insufficient for a complete combustion and as a consequence a relatively large amount of soot is produced (up to 10^8 particles/cm^3, mass output 20-550 mg/h; sootgenerator.com, last access 10.06.2021).

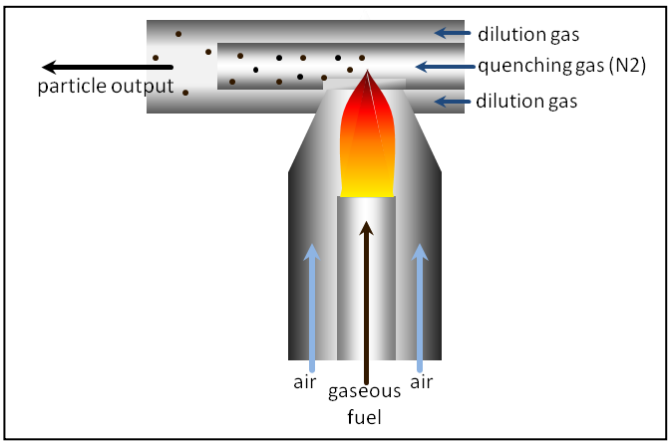

Figure 6: Principle of a miniCAST soot generator: Air and gaseous fuel (propane) are mixed in the burning chamber by diffusion. The flame is quenched with 7l/min N_2 and the particle stream is diluted with filtered air to prevent particle coagulation.

Directly after the burning zone the flame is quenched with nitrogen (constant flow of 7 l/min) in order to prevent further oxidation of the combustion products. The particle stream is then diluted with filtered air to prevent particle coagulation. The compositions and structure of the particles can be modified by changing the flow rates of air (Q_{air}) and fuel (Q_{fuel}) or by mixing N_2 into the fuel stream (the latter was not used in this work). The ratio of carbon to oxygen in the flame can be calculated as (Schnaiter et al., 2006):

$$C/O = 7.16 \frac{Q_{fuel}}{Q_{air}} \quad (1)$$

As described in section 2.3, particles with a wide range of chemical and physical properties – depending on the C/O ratio – can be produced in quantities that allow a relatively fast collection of adequate amounts of standard soots. In a long term study covering several months Moore et al. (2014) found that the miniCAST soot generator was stable over time within 10% in terms of particle diameter. The manufacturer states a repeatability of ±5% for particle size and number concentration (personal communication Jing, 11.05.2021).

4.2. EC/OC analyzer (Sunset Instruments Inc.)

In this study a dual optics EC/OC analyser (Sunset Instruments Inc.) was used for thermal optical analyses and as a means for the preparation of heated samples (sample preparation see section 6.2.1). The principle of the thermal-optical measurement in the EC/OC analyser is shown in Fig. 7.

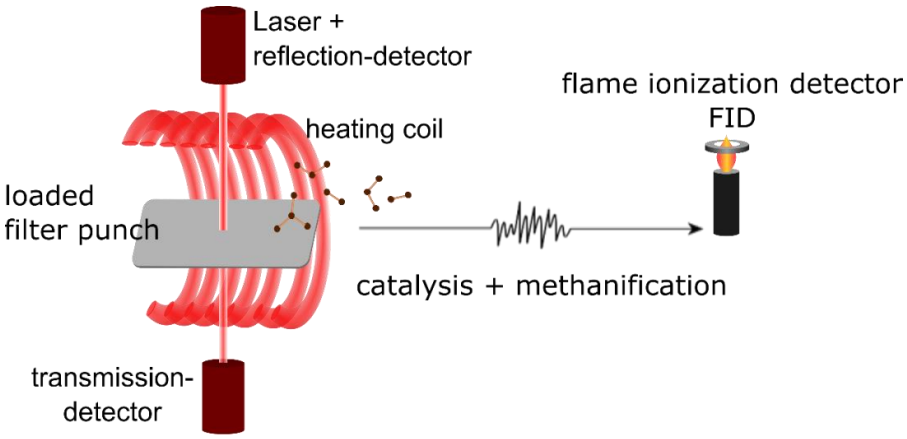

Figure 7: Principle of the thermal-optical analysis in an EC/OC analyzer (Sunset Instruments Inc): The sample is heated in the front oven (symbolized here by the heating coil) and sample material leaves the filter because of fragmentation, evaporation or oxidation. These gaseous products are transported to the MnO_2 oven, where they are oxidized to CO_2 which is then converted into methane by a heated nickel catalyst. Methane is then detected in a flame ionization detector (FID). The FID signal is therefore proportional to the amount of carbon leaving the filter.

The sample – normally a (1x1) cm or (1x1.5) cm punch of a loaded quartz fiber filter – is placed in the front oven on a quartz spoon. The front oven consists of a quartz tube (inner diameter ≈1.5 cm) wrapped with a heating coil. For monitoring the darkening of a sample during the inert heating phase, a He-Ne laser (635 nm) and a detector (for laser reflectance) are mounted above the sample, and a second detector (for laser transmission) is mounted below the sample. During a measurement cycle the laser signals reflected by and transmitted through the sample are recorded. A temperature sensor is placed approximately 2 cm behind the center of the sample. For an accurate temperature measurement, this sensor is calibrated approximately once a year using an external temperature sensor which is inserted into the oven and placed at the sample position. This calibration is important for reliable results: Pavlovic et al. (2014) found significant differences of up to 12% for OC and up to 7% for EC, for measurements before and after calibration.

For a rapid cooling of the sample after the inert phase and at the end of a measurement cycle, a blower is placed next to the oven.

During a measurement cycle, the sample is first heated in an inert (He) atmosphere, then in an oxidizing ($He+O_2$) atmosphere. In this work, the NIOSH870 (Birch and Cary, 1996) and EUSAAR2 (Cavalli et al., 2010) temperature protocols were used (Table 2). The heating rates, temperatures and duration times of the temperature steps, gas atmospheres and the power of the blower can be defined in parameter files and are then controlled by the measurement software (in this work OCEC835 and OCEC820 were used).

Carrier Gas	NIOSH870		EUSAAR2	
	duration [s]	temperature [°C]	duration [s]	temperature [°C]
He	80	310	120	200
He	60	475	150	300
He	60	615	180	450
He	90	870	180	650
He	45	550	30	-
He+O_2	45	550	120	500
He+O_2	45	625	120	550
He+O_2	45	700	70	700
He+O_2	45	775	80	850
He+O_2	120	850	-	-

Table 2: Duration times, temperatures and gas atmospheres for the NIOSH870 (Birch and Cary, 1996), EUSAAR2 (Cavalli et al., 2010) protocols.

Helium (quality 99.999%) as well as a helium and oxygen mixture (10% O_2 in He, quality of both gases 99.999%) are inserted through the front of the oven (flow rates between 7 and 9 cm^3/min), each together with a pure He stream of 48-52 cm^3/min so that the sample is surrounded by a constant (inert or oxidizing) gas flow of 55-61 cm^3/min during a measurement cycle. Because of the dilution with He, the oxygen content of the gas mixture during the oxidizing phase lies between 1.19% and 1.58%.

During the heating of the sample volatile and / or thermal refractory substances evaporate, decompose or oxidize and leave the filter. Subsequently these (carbon containing) compounds are transported to the heated (870°C) manganese dioxide (MnO_2) oven which is placed directly after the front oven. Here the vaporized or fragmented carbonaceous compounds are oxidized and quantitatively converted to CO_2. The CO_2 leaves the MnO_2 oven together with the He or He+O_2 stream, is then mixed with hydrogen and flows through a heated (500°C) nickel catalyst where it is converted to methane. The methane is then measured in a flame ionization detector (FID), so the signal of the FID is proportional to the amount of carbon that had left the filter earlier (the delay due to the gas transport is taken into account in the evaluation). However, the FID-signal depends on the exact gas flow rates so a calibration factor for the FID signal is obtained automatically by injecting a well-defined amount of methane (accomplished with a fixed volume loop of a methane-helium mixture with 5.0% CH_4 in He) into the front oven after each measurement run. The FID signal is then calibrated for each measurement separately by the software.

The FID signal and the transmission and reflectance laser signals are used to calculate EC, OC and TC in the analysis software (Calc415 and Calc359 – distributed by Sunset Instruments Inc.): A split point is set at the position where the (transmission or reflectance) laser signal reaches its initial value after the dark material produced in the inert phase has left the filter. The calibrated FID signal is integrated from zero to the position of the split point and the integral is reported as OC. The integral between the split point and the end of the measurement is reported as EC.

4.3 Confocal Raman microscope

This section is based on the book by Dieing et al. (2011) and the instrument manual of the Horiba Jobin Yvon LabRAM 800HR confocal Raman microscope used in this study (a schematic setup is shown in Fig. 8). In a Raman microscope a laser beam illuminates the sample through a microscope objective. This setup enables focussing the beam on a small selected area of the sample (e.g. a single particle) and to increase therefore the lateral resolution. The addition of a confocal hole in the light path allows to increase the resolution in the vertical axis by reducing the optical slice thickness.

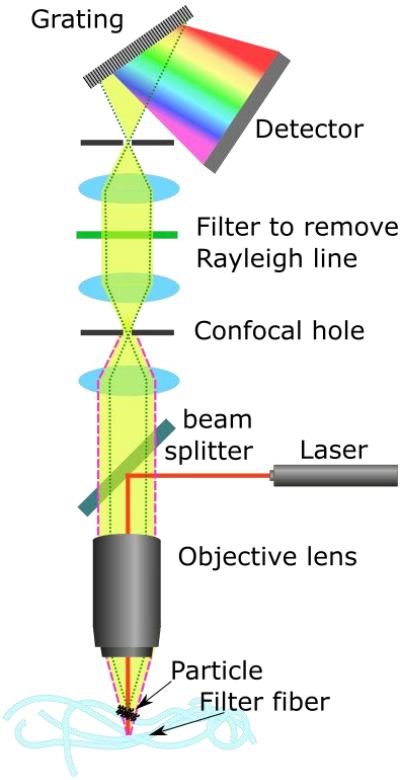

Figure 8: Schematic of a confocal Raman microscope. The scattered light passes an objective lens, is then focused on the confocal hole where only light rays coming from the focal plane of the objective pass (green dotted lines). Rays coming from below (red dashed lines) or above the focal plane are blocked. An edge or notch filter blocks the Rayleigh line. The scattered light is then diffracted by a grating and detected by e.g. a CCD or photo detector.

The instrument used in this work is equipped with a 632.8 nm HeNe-laser (maximum output <20 mW) and a 532 nm frequency-doubled NdYAG DPSS laser (Oxxius LMX-532, maximum output <52 mW). The laser beam is directed over a beam splitter to the objective lens and focused on the sample. In this work a long wide distance (LWD) 100x magnification objective (MPlanN, NA= 0.75, WD 0.21 mm, Olympus) and a 20x magnification objective (CF Plan, NA=0.35, WD 20.5 mm, Nikon) were used. The diameter of the laser spot equals the lateral resolution (2Δx) of the objective and depends on the refractive index of the medium between objective and sample (n ≈1 for air), the excitation wavelength λ and the numerical aperture ($NA = n \sin\theta$, with 2θ the opening angle) of the objective:

$$\Delta x = n * 0.61 \frac{\lambda}{NA} \quad (9)$$

In the case of a 20x objective with NA=0.35 and an excitation wavelength of ≈ 633 nm, the lateral resolution is ≈2 µm, for a 100x objective with NA=0.8 it goes down to ≈ 1 µm.

As described in section 3.1.1, molecular oscillations are stimulated by the laser and Rayleigh scattered light as well as Raman scattered light are emitted according to their specific characteristics and pass the objective lens. However, the laser beam reaches also regions above and below the focal plane, so light emerges not only from the focused object (dotted green line in Fig. 8), but also from the surrounding material (dashed red line in Fig. 8). Light from outside the focal plane can be blocked by a confocal hole with adjustable width: The light scattered by the sample is focused by the objective and an additional lens onto the confocal hole but only light from the focal plane passes the aperture, whereas light from below and above the focal plane is blocked. A small aperture of the confocal hole allows therefore obtaining a spectrum that originates mainly from the focused object (e.g. a single particle).

The minimum slice thickness in z-direction (dz) (i.e. the span around the focal plane from where light passes the confocal hole) depends on the refractive index n' of the sample, the excitation wavelength λ and the numerical aperture NA of the objective. Assuming a minimally opened confocal hole, the resulting slice thickness can be calculated by (e.g. Park et al., 2004):

$$dz \cong \frac{0.64\lambda}{n\prime - \sqrt{n\prime^2 - NA^2}} \qquad (10)$$

For the setup in this work dz is approximately 2 µm, using a refractive index for soot of n'=1.67 (e.g. Zhao et al., 2020), λ=532 nm and the numerical aperture of the 100x objective NA=0.75.

After the confocal hole the light beam does still contain the Rayleigh scattered light, which is then blocked by an edge or notch filter. Subsequently only Raman scattered light is focused through a lens and an entrance slit (width 400 µm is used here) on an optical grating (300 gr/mm is used here) where the spectrum is split up and detected with a CCD camera (Peltier cooled to -60°C). The spectral resolution depends on the grating constant, the size of the entrance slit and the focal length of the lens as well as on the resolution of the detector and is about 3-4 cm^{-1} in the used setup. Generally, the wavelength of the incident beam can be chosen arbitrarily since the Raman frequencies do not depend on the excitation wavelength. However, visible light is often used in Raman microscopy due to the easier technical realization: The intensity of Raman scattered light is proportional to λ^{-4}, so excitation with visible light gives spectra with higher intensities compared to the excitation with near-infrared light.

Depending on the substance, not only molecular vibrations are induced by the laser but also electrons themselves can be moved to a higher state of excitation. By relaxation to a lower energy level, fluorescence light can be emitted which might mask the less intensive Raman bands. A fluorescence background is therefore often visible in Raman spectra of soot. To some extent the fluorescence can be reduced by lowering the laser intensity, or by closing the confocal hole and blocking at least part of the interfering fluorescence from other regions. Nevertheless, a subtraction of the fluorescence background is needed before spectral analyses can be performed (see section 6.2.2).

4.4 Integrating Sphere

An extension of the Integrating Sphere technique (original method described by Heintzenberg, 1982; adapted by Hitzenberger et al., 1996) was used for BC and BrC measurements. The extension of the original method, which could detect only BC, is described by Wonaschuetz et al. (2009) and allows quantifying also BrC.

The integrating sphere (Labsphere, Inc) with a diameter of 15.24 cm is coated internally with a nearly ideally diffusively reflective (>99%) material (Spectraflect™). A 75 W halogen lamp with a stabilized current source (2.3 A), equipped with an opal glass plate as diffusor is mounted horizontally at the outside of the sphere. The light passes an interference filter (in this setup three changeable filters with wavelengths of 450, 550 and 650 nm and 25 nm half-width are used), a second diffusor (a Nuclepore™ filter with 0.2 µm pore size) and enters the sphere through a circular port. A silicon photodiode is mounted at the bottom of the sphere normal to the light source. A baffle, covered with Spectraflect™, shields the detector from any remaining direct light of the halogen lamp so that only light that had interacted (been scattered, transmitted, reflected) with the sample is measured. The signal of the photodiode is amplified with different levels of sensibility, which are necessary because of the strong wavelength dependence of the halogen spectrum.

A vial with the immersed sample is placed in the center of the sphere using a sample holder suspended from the lid which covers the sample port at the top of the sphere. Parts of the sample holder and the inside of the lid are manufactured from Teflon®, and the rest is covered with a white diffusively reflective paint.

A punch of a filter sample with a well-defined area (in this work circular filter punches with diameters between 5 and 10 mm were used) is inserted into a transparent PE vial together with 2 ml of acetone and 2 ml of a 20:80 mixture of isopropanol and ultrapure water. This mixture serves as a solvent for soluble sample material on the one hand, and on the other hand it decreases possible lensing effects which could occur due to transparent coatings on the light absorbing particles: The refractive index of the mixture (1.35) lies in the range of reported refractive indices of typical aerosol constituents (about 1.4) (Hitzenberger and Tohno, 2001; Wonaschuetz et al., 2009 and references therein). The relative refractive index between the liquid and the coating is then ≈1.04 so the coating is nearly “invisible” in the liquid and possible lensing effects are suppressed.

The absorption signal of the sphere is recorded at three different wavelengths (450, 550 and 650 nm). As absorption cannot be measured directly because of possible multiple reflections at the coating of the sphere, the absorption signal has to be compared to calibration curves obtained with standards for BC (Elftex 124, Cabot Corporation) and BrC (Humic Acid Sodium salt, Acros Organics, no. 68131-04-4 was used as a proxy material). The exact calibration procedure is described by Wonaschuetz et al. (2009). The signals associated with BC and BrC are separated using an iterative algorithm.

In the case that the sample contains no measurable amount of BrC (i.e. when the iterative procedure diverges or yields negative values for BrC, the “green” signal is used to calculate BC from the respective calibration curve. In case the iteration converges, the BC and BrC values are taken from the fourth iteration step.

The detection limits of the Integrating Sphere technique are given by the range and precision of the calibration curves (Wonschuetz et al., 2008) and the precision of the light intensity detection as 1 µg

for BC and 10 µg for BrC. The results of the integrating sphere method have to be understood as "Humic acid sodium salt – equivalent" and "Elftex-equivalent".

4.5 WAXD

An X-ray scattering system (Bruker AXS Nanostar) was used to perform wide-angle X-ray diffraction (WAXD) for a first feasibility study (see section 5.1). In this instrument Cu-K_α radiation with a wavelength of λ = 0.1542 nm is produced in an X-ray tube (Incoatec High Brilliance, 50kV, 1mA). The beam is collimated by a pinhole system and has a diameter of about 0.5 mm. The system was used with an image plate and with an area detector (VÅNTEC 2000, gas detector based on microgap technology) which were mounted at a distance of 10 cm and 5 cm to the sample. The samples were put in vacuum (<1mbar) to minimize scattering by surrounding gas.

The X-ray patterns were calibrated with Al_2O_3 powder and radially averaged in order to obtain diffractograms with scattering intensities depending on the absolute value of the scattering vector $q = \frac{4\pi}{\lambda} sin\theta$, where 2θ is the scattering angle.

5. Preparatory tests

For structural analyses of graphitic-like materials or soot wide angle X-ray diffraction (WAXD) and Raman spectroscopy can be used. Information about the degree of graphitisation or structural ordering can be obtained with both techniques. However, the choice of the technique for this study had to take the conditions of thermal-optical analysis into account, where sampling substrates have to be stable when exposed to temperatures up to at least 850°C. Heat treatment of laboratory generated as well as atmospheric aerosol samples was performed with the thermal-optical EC/OC analyser described in section 4.2, where normally quartz fiber filters are used as sampling substrate (see section 6). Therefore preparatory tests with both measurement techniques were necessary to investigate whether analyses with quartz fiber filters as background, the use of other temperature resistant filter materials or the separation of the sample material from the filter are feasible. After these tests the WAXD technique was not further pursued because of complications with quartz fiber filters as background material. Raman spectroscopy, on the other hand, was found to be easily applicable on these samples. Nevertheless, the test measurements with WAXD are described here for documentation purposes.

5.1 WAXD

The WAXD measurements in this section were performed in the laboratory of the Dynamics of Condensed systems group of the faculty of physics, University of Vienna with generous support by Prof. H. Peterlik.

The most convenient substrates for WAXD measurements (e.g. aluminum foil, glass, PVC/PP) are characterized by low and / or well reproducible X-ray scattering so that the background signal can be clearly distinguished from the signal of the sample. Obviously the temperature resistance of these materials is not high enough to use them as support material during heat treatment in the thermal-optical instrument, so in a first test, a commercially available adhesive tape was used to separate the sample material from the quartz fiber filters. Although this was possible with filters highly loaded with CAST soot, the removal of sample material from the much more lightly loaded atmospheric aerosol filters without pulling off a layer of quartz fibers was impossible.

The quartz fibers, however, were found to cause a strong background signal over the whole range of WAXD compared to the signal from the samples. Moreover, the diffraction curves differed for different filters (even from the same batch) and filter positions (Fig. 9) and varied with filter handling (pretreatment and storage).

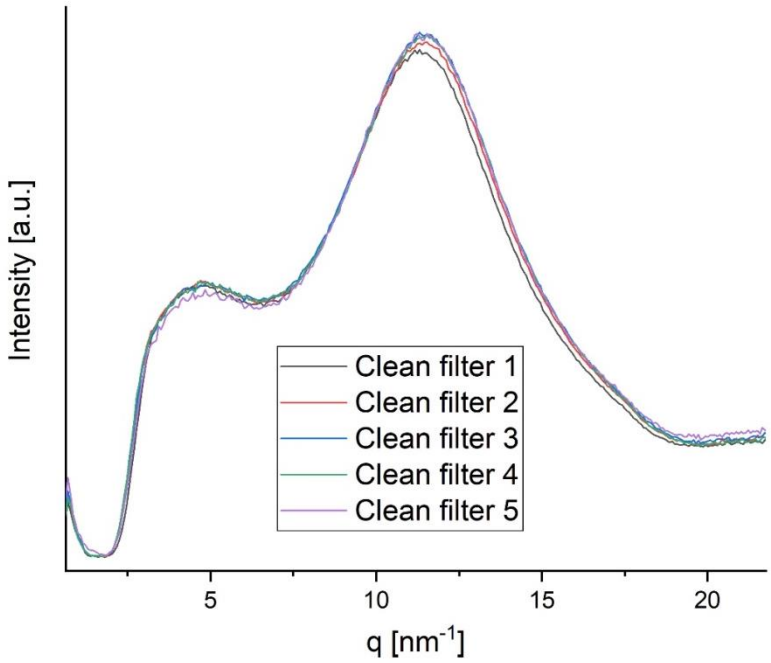

Figure 9: Diffractograms of different clean quartz fiber filters depending on the scattering vector q. The diffractograms can differ for different filters which makes it challenging to use quartz fiber filters as background for WAXD.

First test measurements were performed with a commercially available graphite powder (sold as lubricant for cylinder locks) on a quartz fiber filter. About 1 mg of graphite powder was put on the filter and washed into the substrate with acetone. In the diffractogram in Fig. 10 a sharp peak is visible at 18.5 nm^{-1}. This corresponds to an interlayer distance of 0.335 nm, which is consistent with the 002 layer distance in graphite (Kwiecinska and Petersen, 2004). The high loading of the filter together with the high degree of structural ordering of graphite leads to a peak that is well distinguishable from the filter background (blue line in Fig 10).

However, such high filter loadings are not realistic for aerosol samples and soot is generally less ordered than pure graphite and produces therefore lower and broader diffraction peaks. The atmospheric aerosol samples analyzed in this work have EC loadings of about 3µg/cm^2 on average (Sommer, 2020). Moreover analysis in the thermal-optical instrument requires filter EC loadings less than 15 µg/cm^2 (https://www.sunlab.com/about-us/methodology/).

A more "realistic" filter loading was therefore tested using a quartz fiber filter spiked with about 20 µg of a standard carbon black (Elftex 124, Cabot Corporation). Diffractograms of the loaded filter and of a clean filter are shown in Fig 11. The curves are very similar – they differ in the same range as the curves of different clean filters in Fig. 9 – and no additional peak is visible. The subtraction of the signal of the clean filter as "background" gives an artificial peak that is caused by the variability of the filters rather than by the structure of carbon black (insert in Fig. 11).

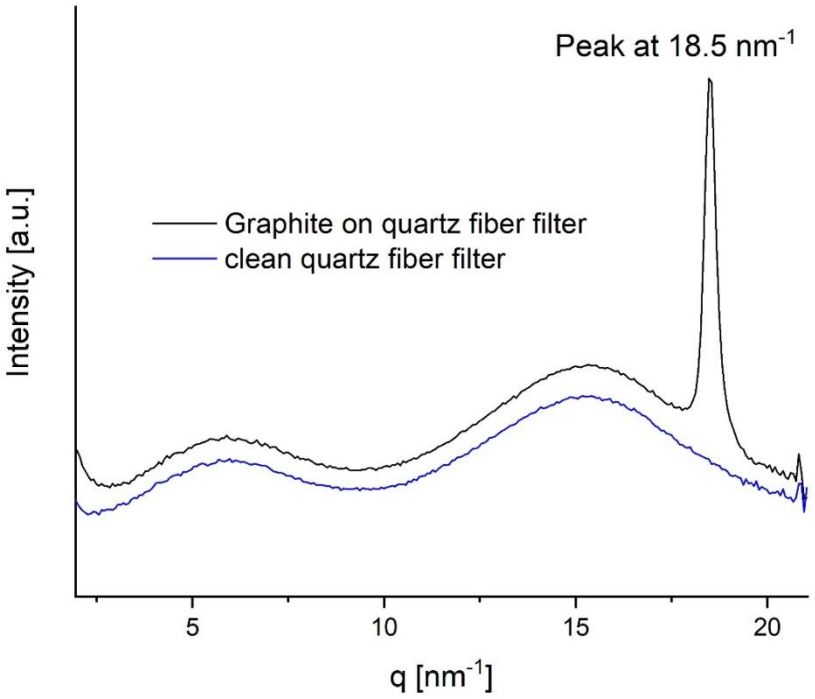

Figure 10: Diffractograms of a preheated clean quartz fiber filter (blue line) and a quartz fiber filter loaded with graphite powder (black line) which was washed into the filter material with acetone. The filter with graphite was heated to 600°C and organic material was removed. Graphite shows a clear peak at 18.5 nm^{-1} that is clearly distinguishable from the quartz fiber background.

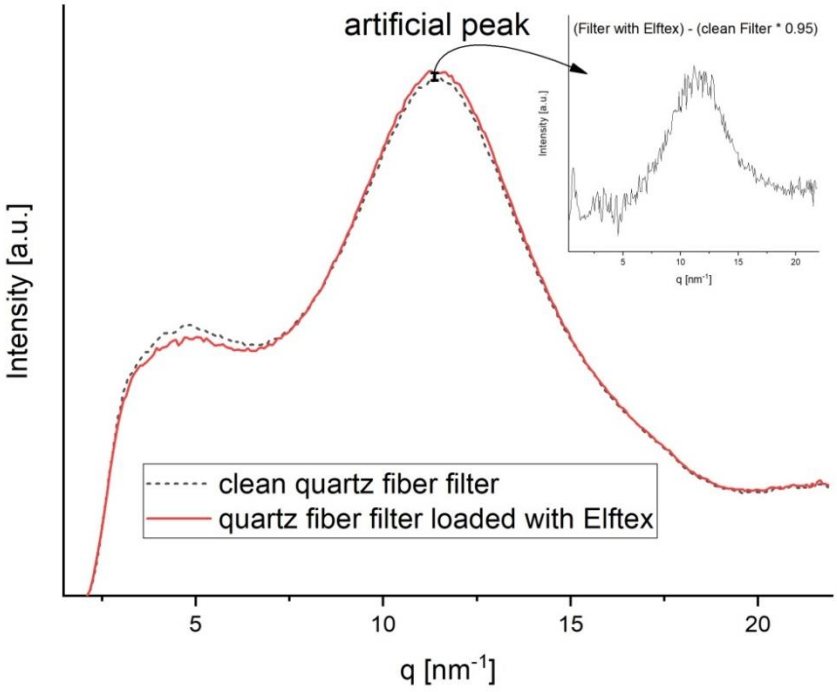

Figure 11: WAXD diffraction patterns of a loaded quartz fiber filter, spiked with 20 µg of Elftex (red solid line) and a clean quartz fiber filter (black dashed line). A possible Elftex-peak is not distinguishable from the signal of the filter material. When the curve of the clean filter is considered as background and subtracted from the curve of the loaded filter an artificial peak arises (insert). For background subtraction the signal of the clean filter is multiplied with 0.95 to avoid negative intensity values and to take into account the absorption of Elftex (choice of factor: H. Peterlik, pers. comm. 2015).

Figure 12 shows a diffractogram of pure Elftex for comparison. For the measurement Elftex powder was placed between two layers of adhesive tape as support material and the tape-background was subtracted. The diffractogram of Elftex has a broad peak with a maximum at about 18nm^{-1} and a second – lower – peak at about 29.8nm^{-1}. The positions of both peaks are in good agreement with data reported for carbon black and soot e.g. by Sahu et al. (2014). They associate the higher peak with graphitic like (sp^2) planes (interlayer distance about 0.35 nm) and the lower peak with diamond like (sp^3) planes (interlayer distance about 0.21 nm) which are both typical for amorphous carbon.

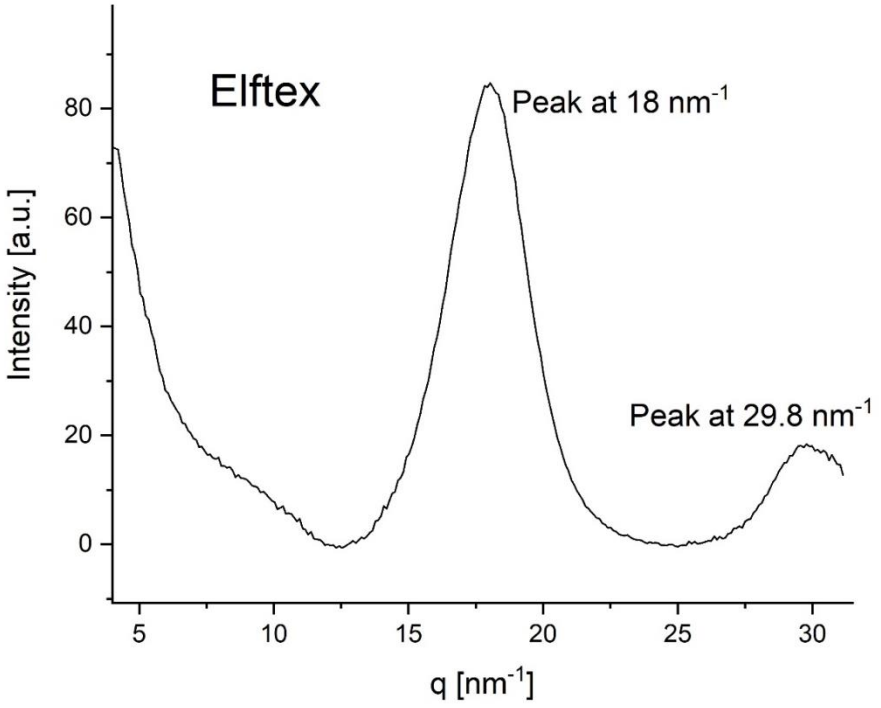

Figure 12: Diffractogram of a carbon black standard (Elftex) measured between two layers of commercially available adhesive tape. The background signal of the weakly scattering double layered tape was subtracted from the raw data. The two peaks at 18 nm^{-1} and 29.8 nm^{-1} can be associated with the sp^2 bonded graphitic like layers as well as with diamond-like sp^3 bonds.

Although a typical soot peak is distinguishable from the background when an adequate support material is used, a reliable background subtraction of a quartz fiber background is challenging. The variability of the filter material results in differences in the diffractograms of different clean filters or at different filter positions. As a possible solution for this problem, a new sample holder was built, that allows measurements at the same filter position when the sample is removed from the instrument and replaced later, so that the filter background can be measured after burning off the sample material. In this sample holder (Fig. 13) the filter piece is clamped between two ceramic plates. A hole in each plate permits the X-ray beam to pass during the WAXD measurements. The two ceramic plates are fastened in the slot of a steel block. The block can be placed in a corresponding aluminum holder which is fixed in the WAXD instrument. In the first step the diffraction pattern of the loaded filter is recorded. After the measurement the block with the ceramic plates and the loaded filter is removed and inserted in a ventilated tube furnace and heated for 10 minutes at 700°C in air. This temperature and duration was found to be sufficient to burn off the sample material so that the clean filter is left.

After cooling, the block is replaced in the aluminum holder in the WAXD instrument and the heated (clean) filter is measured.

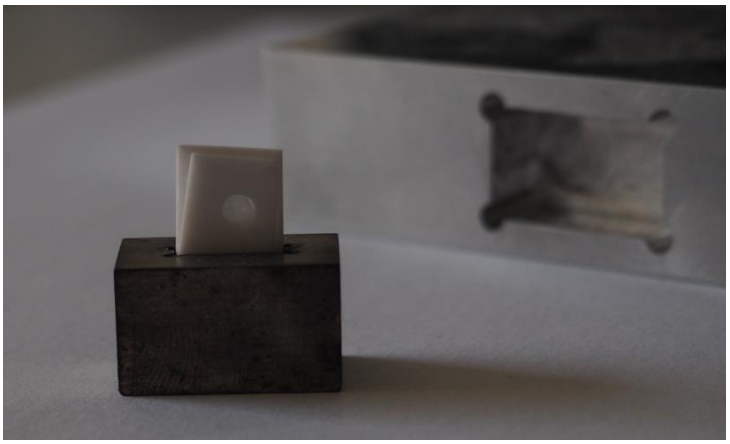

Figure 13: Sample holder consisting of a steel block with two ceramic plates that hold the filter piece. In the background the corresponding aluminum holder is visible, which is fixed in the instrument during measurement. The block with the ceramic plates and the filter can be removed and replaced easily. The sample holder was machined by the workshop of the Faculty of Physics according to the design of the Dynamics of Condensed Systems group.

This procedure was tested with CAST soot and atmospheric aerosol samples, but first measurements indicated that the background signal changed after heating. Figure 14 shows diffractograms of a temperature series of a clean filter obtained by using the new filter holder. Diffractograms were taken for the same (clean) filter unheated and heated to 725, 750, 775 and 800°C. After each measurement the filter was heated to the next temperature level for ten minutes and then reinserted in the WAXD instrument. The diffraction curves change visibly during the whole heating procedure and differ appreciably for the unheated filter and the filter heated to 800°C. The shoulder between 3 and 10 nm^{-1} decreases while the peak at about 15 nm^{-1} increases. The increase and the slight narrowing of this peak could possibly be explained by a rearrangement of the SiO_2 tetrahedrons in the amorphous structure of the quartz fibers and / or the formation of more densely packed structures at elevated temperatures.

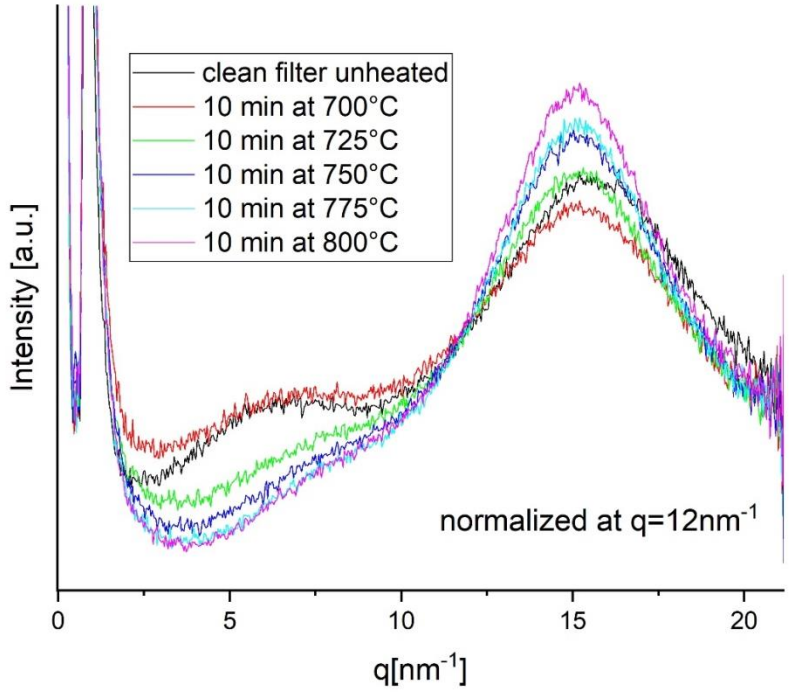

Figure 14: Diffractograms of a clean filter heated to 700, 725, 750, 775 and 800°C for ten minutes. The diffactograms are taken at the same filter position using the sample holder described in the text. The broad peak at 15 nm^{-1} increases during heating while the shoulder at lower q decreases.

Because of these problems with the filter background, WAXD was not further pursued as a technique to investigate structural changes of soot both in atmospheric aerosol samples and in standard soots produced in the CAST burner.

5.2 Raman

5.2.1 Quartz fiber background

In contrast to the problems we faced with WAXD measurements, the quartz fiber filter background was relatively unproblematic for Raman measurements. Figure 15 shows Raman spectra of a clean filter and of two aliquots of an atmospheric aerosol filter (sampled on quartz fiber filter on 01.07.2015), one heated and one unheated. The intensities of the Raman signals of the loaded filters are much higher than the intensity of the (background) signal of a clean quartz fiber filter. Especially for the unheated sample the high fluorescence background caused by the sample (see section 6.2.2) seems to mask the background signal of the quartz fibers. Generally, the Raman signals of the unheated samples and of the samples heated to the lower temperature levels of the thermal-optical measurement protocols (up to about 600°C in He) were strong enough that the influence of the quartz fiber background is negligible. Only when little material was present on a filter, which e.g. occurred when some samples had been heated to higher temperatures or in the presence of oxygen, the signal of the quartz fibers influenced the Raman spectrum. However, the peaks in the spectrum of the clean filter are well defined and reproducible (insert Fig. 15) so they can be subtracted from the raw spectrum in these cases. Moreover, the quartz peaks with the highest intensities lie in the region between 1600 and 1900 cm^{-1}, so they do not influence the peak heights of the soot spectrum.

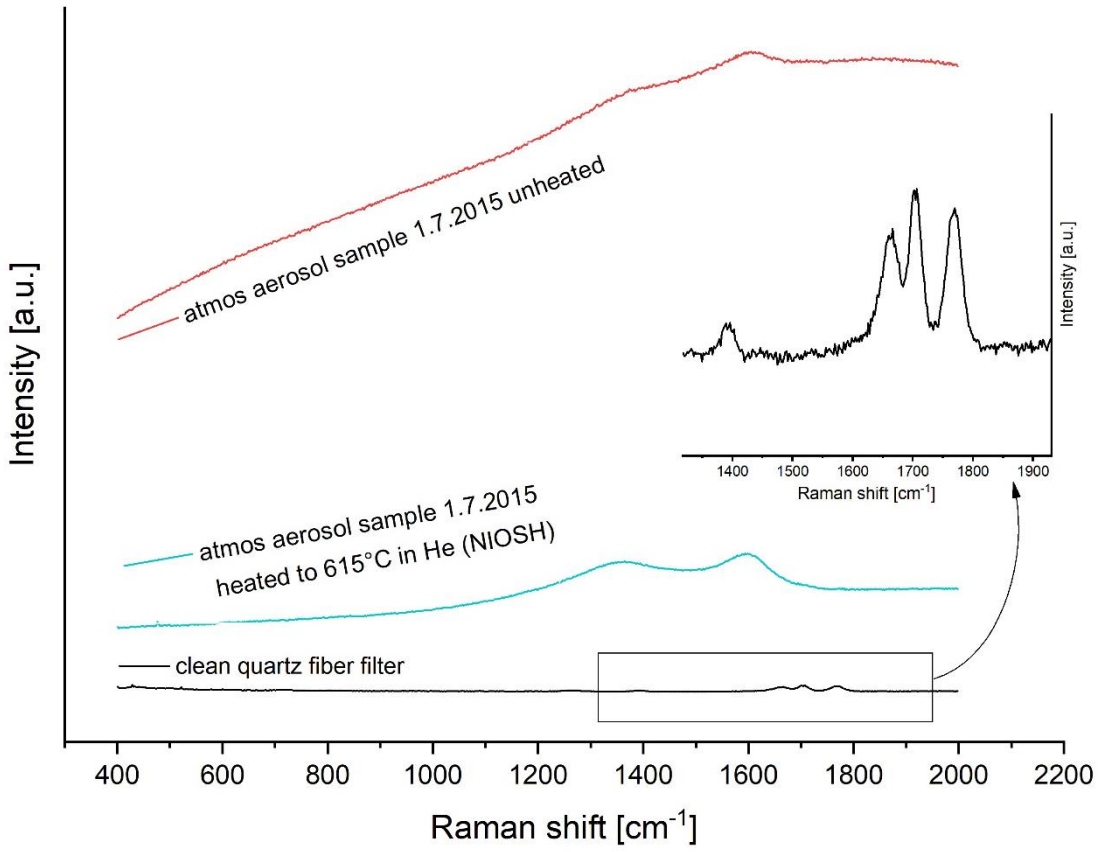

Figure 15: Raman spectra of a clean quartz fiber filter (black line), an unheated atmospheric aerosol sample (red line) and a heated atmospheric aerosol sample (blue line). The spectrum of the quartz fiber background does not interfere visibly with the spectra of the (heated and unheated) aerosol material. The peaks in the quartz fiber spectrum (insert) are well defined and reproducible and can be easily subtracted for samples with low soot loadings.

5.2.2 Comparability of two parallel filter samples

CAST soot was sampled using two parallel filter holders (see section 6.1.2) because the deposit on a single filter was not sufficient for all measurements performed in Publication 1 (Raman spectroscopy, Integrating Sphere, UV-Vis, TEM). Therefore prior to the analyses the general comparability of two parallel loaded filters was tested. For these tests the soot generator was set to C/O = 0.353 giving EC/TC = 0.13 and BC/LAC=0.09. The aerosol exiting the CAST generator was split up and sampled by two filters mounted in identical filter holders (a and b; see section 6.1.2 and Publication 1). The Raman spectra were recorded at three randomly selected positions of each filter and are shown in Fig. 16. The spectra are comparable for both filter samples to the same extent as for different measurement positions on one single filter, particularly in the peak positions, heights and widths.

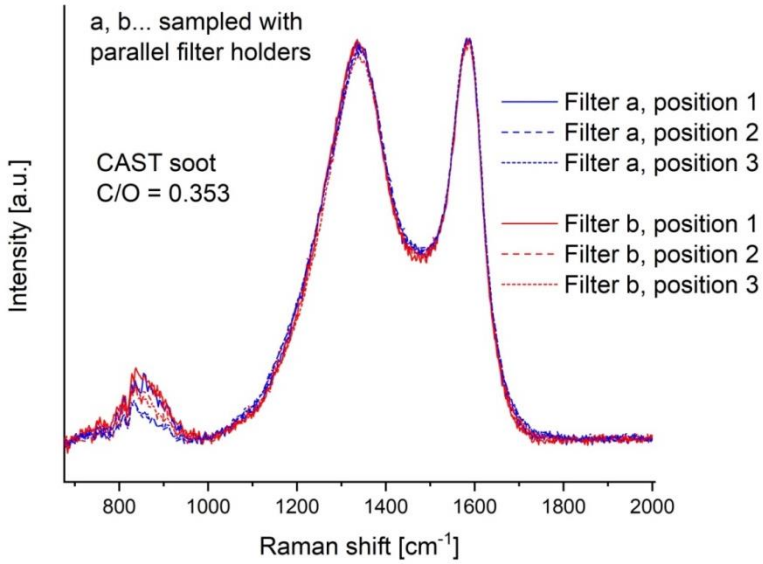

Figure 16: Raman spectra of CAST soot sampled with two parallel filter holders (blue lines for filter holder a, red lines for filter holder b). The spectra were measured at three different positions on each sample (position 1, 2, 3) and are comparable among each other. The spectra are normalized to the maximum of the G-peak.

The peak between 800 and 900 cm^{-1} might be caused by aliphatic compounds and was not taken into account for analyses because in most cases separation from the fluorescent background signal was difficult (see below 6.2.2).

5.2.3. Influence of different Baselines

Raman spectra of soot and atmospheric aerosol samples often are affected by a fluorescence background caused e.g. by organic material. This background must be subtracted prior to further analyses using a baseline curve that represents the fluorescence signal adequately; in this work a B-spline based on selected anchor points was used (see section 6.2.2). The intensity of the fluorescence background was found to be high compared to the intensity of the Raman signal of soot especially for (unheated) atmospheric aerosol samples or CAST soot samples with a large amount of OC. In these cases it is often not unambiguously clear which curve should be chosen (i.e. where the anchor points should be set) for background subtraction. Therefore the influence of varying baseline curves on the

corrected Raman signal of soot was estimated by calculating and subtracting ten different baseline curves for one single raw spectrum. Figure 17 shows two examples for different baselines both calculated using a B-spline fit but based on different positions of the 12 anchor points.

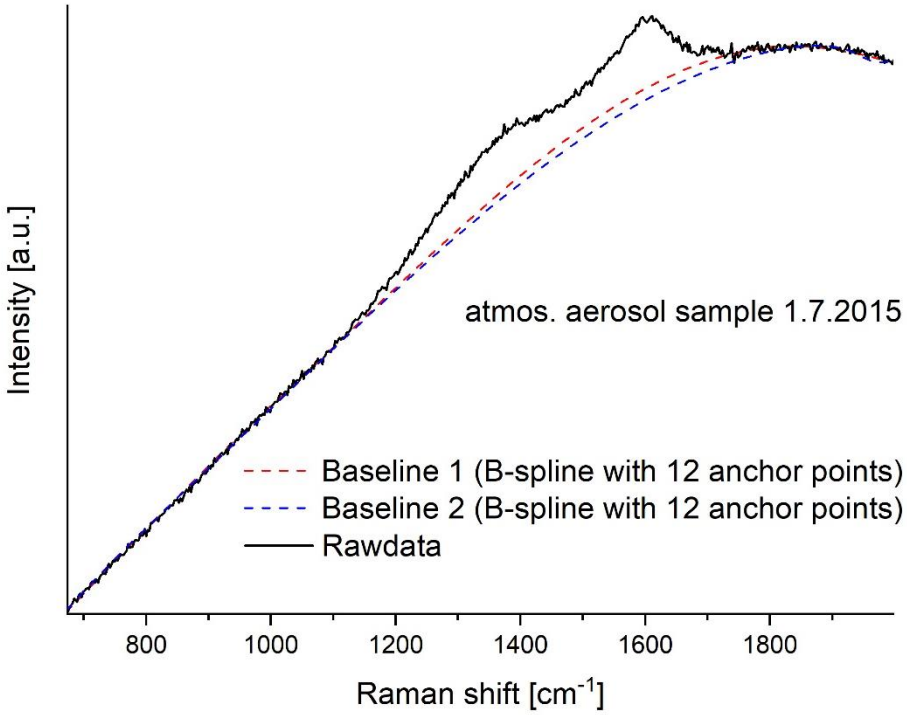

Figure 17: Raw Raman spectrum of an atmospheric aerosol sample (1.7.2015), with a high fluorescent background and a relatively low soot signal (black solid line). Two examples of different baselines are shown (dashed red and blue lines).

The ten corrected spectra obtained using different baseline corrections of the raw spectrum of the atmospheric aerosol sample (01.07.2015) were averaged. The mean spectrum is shown in Fig. 18 (red line). The blue line in Fig. 18 shows the mean spectrum of the spectra measured at ten different positions of the same sample and corrected using similar baselines. It can be seen, that the use of slightly different baselines leads to approximately the same variations as the measurement at different filter positions.

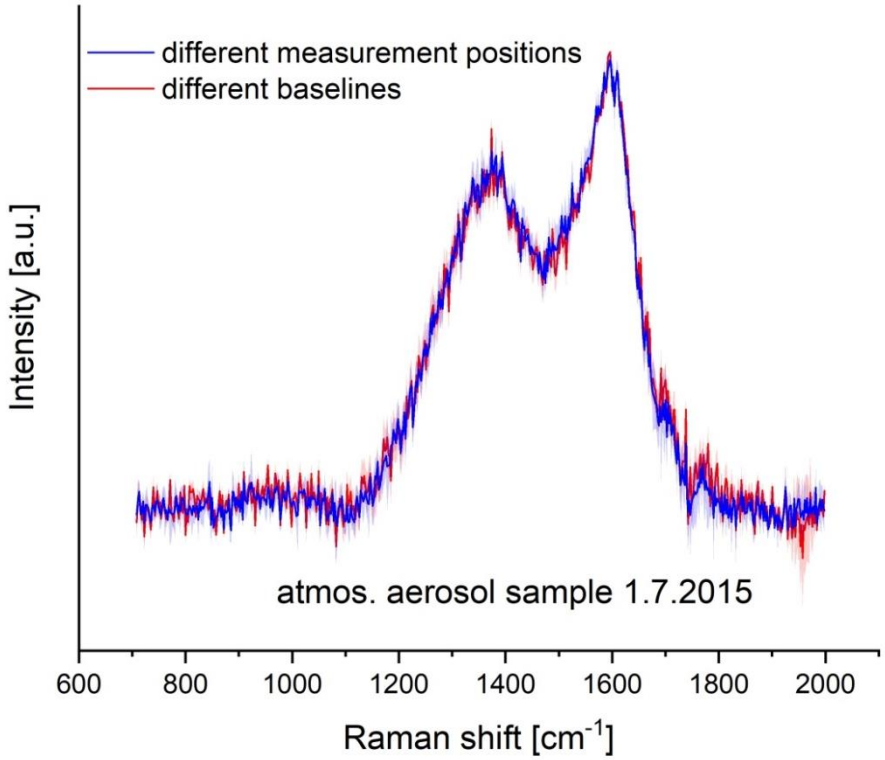

Figure 18: Blue line: Mean of spectra measured at 10 different filter positions and baseline corrected. Red line: Mean of 10 baseline corrected spectra derived from a single measured spectrum but corrected with slightly differing baselines. Standard deviations of the mean spectra are shown as shaded areas in both cases.

6. Experimental

6.1 Sampling

6.1.1. Pretreatment and storage of filters

In this study CAST soot and atmospheric aerosol were sampled on quartz fiber filters (Pall Tissuquartz 2500 QAT-UP, 47 mm). All filters had been prebaked for one hour at 450°C and stored in a water-vapor-saturated atmosphere for at least 24 hours before sampling. As described by Jankowski et al. (2008), this pretreatment of the filters ensures low OC (<0.2 µg/cm^2) values of the blank filters. The storage in the watervapor-atmosphere prevents the re-adsorption of volatile organic species after heating. All loaded filters were stored in petri dishes at -22°C except during sample preparation and analysis.

6.1.2. Sampling of CAST soot

A miniCAST soot generator (type 5201C Jing-CAST Technologies, section 4.1) was used to produce soot samples with varying EC/TC or BC/LAC ratios. The burning conditions for Publication 1 (section 7 and 11) were chosen in order to obtain soot samples with markedly different properties especially in their compositions of BrC and BC. So prior to the measurements for the publication, soots produced under different combustion conditions with C/O ratios between 0.275 and 0.5 ("Black", "Brown", A, B, C, D, in Table 3) were sampled for test measurements. The soots "black" (BC/LAC=0.99) and "brown" (BC/LAC=0.11) were chosen for the measurements in Publication 1 and are described in section 7 and 11. The test measurements with soot produced under the burning conditions A-D are summarized in section 9.1.

CAST burning conditions	**"Black"**	**"Brown"**	**A**	**B**	**C**	**D***
Propane	40 ml/min	50 ml/min	40 ml/min	40 ml/min	70 ml/min	
Oxidation Air	1.04 l/min	0.9 l/min	0.95 l/min	0.9 l/min	1 l/min	
Nitrogen	0	0	0	0	0	
Dilution Air	20 l/min	10 l/min	20 l/min	10 l/min	10 l/min	
Quench gas (N_2)	7 l/min	7 l/min	7 l/min	7 l/min	7 l/min	
C/O	0.275	0.397	0.301	0.353	0.5	0.441

*Table 3: Settings of the gas flows and resulting C/O ratios in the miniCAST soot generator for the production of soot with varying properties. The combustion conditions "black" and "brown" are used in publication 1. The other settings were used for test measurements summarized in section 9.1. *Filter D and the corresponding C/O value was provided by L. Witek (pers. comm.).*

For sampling, part of the exhaust aerosol stream was diverted through an 8 mm tube mounted at right angle to the exhaust tube (d≈35 mm) about 20 cm after the outlet of the CAST generator. The aerosol stream was then diluted with 5-6 l/min filtered air that was filtered using a HEPA (high-efficiency particulate air) filter, regulated with a needle valve and measured with a rotameter. The diluted aerosol flow was then split up and drawn through quartz fiber filters placed in two identical filter holders. The total flow through the sampling line was regulated by a critical orifice to 12.5 L/min. Before sampling, the CAST generator was operated with the chosen gas flow settings for about 15 minutes to reach stable burning conditions.

6.1.3. Sampling of atmospheric aerosol

Atmospheric aerosol was sampled with an automatic filter sampler (SEQ47/50, Sven Leckel) at the rooftop lab of the physics building of the University of Vienna. The building is located at about 1.5 km from the city center in a densely built-up area, impacted by inner-city traffic. However, the lab lies about 35 m above ground and faces the enclosed source-free courtyard of the building, so the sampled aerosol is not affected by direct traffic emissions and can be considered as urban background aerosol (Reisinger et al., 2008; Hitzenberger et al., 2006).

The filter sampler was set to a nominal flow of 2.3m^3/h and daily 23h samples were obtained. The filters were changed automatically at 11:00 (UTC+1) each day. The sampling was then paused for one hour and started again at 12:00 (UTC+1). Filter samples were loaded for nearly every day in the years 2014 to 2016 and samples for Publication 2 were chosen from this set of filters.

6.2. Measurement scheme

Overviews of the measurement schemes of Publications 1 and 2 are given in Fig. 19. In order to analyze structural changes of CAST soot and atmospheric aerosol during the heating of a thermal-optical measurement procedure (EUSAAR2 and NIOSH870), heated samples were prepared in the thermal-optical instrument. Unheated and heated samples were then analyzed with Raman spectroscopy to gain information about the structural ordering in the sample.

In Publication 1 (section 7 and 11) unheated and heated samples were also analyzed with UV-Vis spectroscopy, the integrating sphere method and transmission electron microscopy (TEM). In Publication 2 (section 8 and 12) measurements additional to the Raman spectroscopy were performed only for the unheated samples (TEM, integrating sphere method ion chromatography).

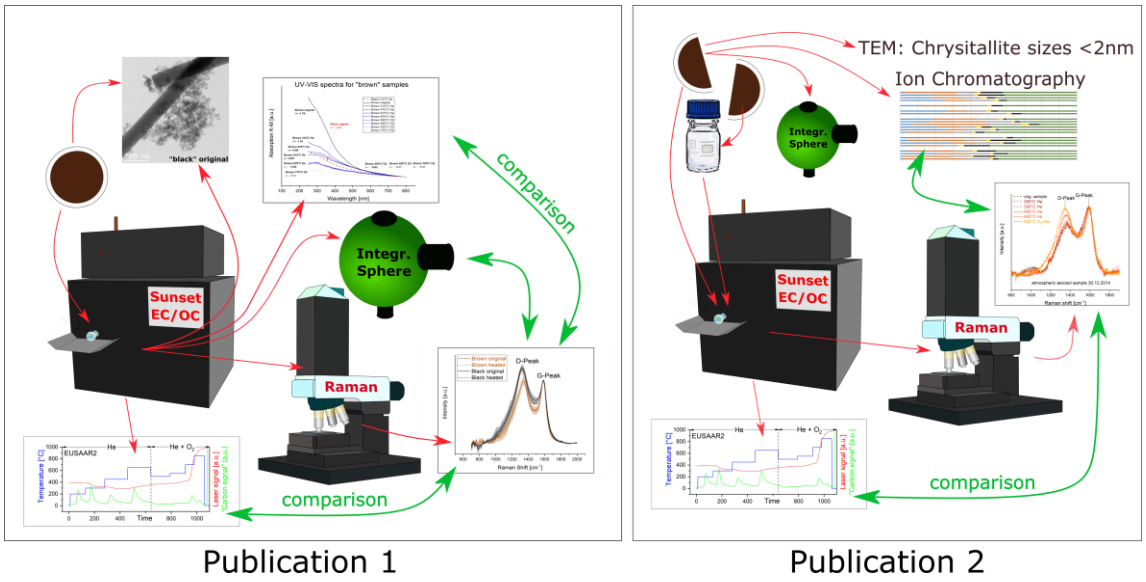

Figure 19: Measurement scheme for Publication 1 and 2. In Publication 1, aliquots of the CAST soot filters were heated. The unheated and heated samples were measured with Raman spectroscopy, UV-Vis spectroscopy, Integrating sphere method and transmission electron microscopy (TEM). In Publication 2 aliquots of washed and unwashed atmospheric aerosol filter samples were analyzed and heated in the EC/OC analyzer and Raman spectra were recorded for washed and unwashed, unheated and heated samples. The unwashed and unheated samples were analyzed with transmission electron microscopy (TEM), Integrating sphere method and ion chromatography. In both publications the Raman spectra were compared to the results of all other measurements.

6.2.1. Sample preparation (heating and washing of the samples)

The thermal-optical instrument was used for the preparation of the heated samples to expose them to the same gas atmospheres and heating rates as during thermal-optical measurement of the NIOSH870 (Birch and Cary, 1996) and EUSAAR2 (Cavalli et al., 2010) protocols (temperatures, gas atmospheres and residence times are listed in Table 2 in section 4.2.).

New parameter files (i.e. files containing settings of the gas atmospheres, power of the heating coils, temperature levels and durations etc.) were created for each temperature level of the NIOSH870 and EUSAAR2 protocol. An example of a parameter file corresponding to the 615°C level in He (following NIOSH870) is given in Table 4. The thermogram obtained when a filter sample is heated following this shortened parameter file is shown in Fig. 20. Using these adapted parameter files, aliquots of the filter samples were heated according to NIOSH870 or EUSAAR2 protocol up to the chosen temperature level. Then the samples were cooled down rapidly in a helium atmosphere and extracted from the oven as soon as the temperature dropped below 75°C.

```
'NIOSH_heating_to_615.par
' <mode, time, temperature, power
constant, time constant, blower
mode, T-offset>
'n.b. regimen must end 'Offline'
mode.
Minimum Step Time,45
Maximum Step Time,300
Helium, 10, 1, .001, 100, 16, -4
' start ramping the temperature
Helium, 80, 310, .05, 95, 0, 3
Helium, 60, 475, .08, 70, 0, 1
Helium, 60, 615, .16, 45, 0, -4
' All done!
Offline, 1, 0, .001, 100, 16
' end.
```

← First temperature level: 310°C, 80 sec
← Second temperature level: 475°C, 60 sec
← Third temperature level: 615°C, 60 sec
← Cooling (blower max)

Table 4: Example of a parameter file for the heat treatment of a sample corresponding to the third temperature level in He (615°C) following the NIOSH870 protocol. Parameters in each line: mode, time, temperature, power constant, time constant, blower mode (0 =min, 16=max), T-offset (power constant and time constant control the temperature ramps between the constant temperature levels and are instrument specific as well as the temperature-offsets). The heated sample was extracted when the temperature in the offline mode had dropped below 75°C.

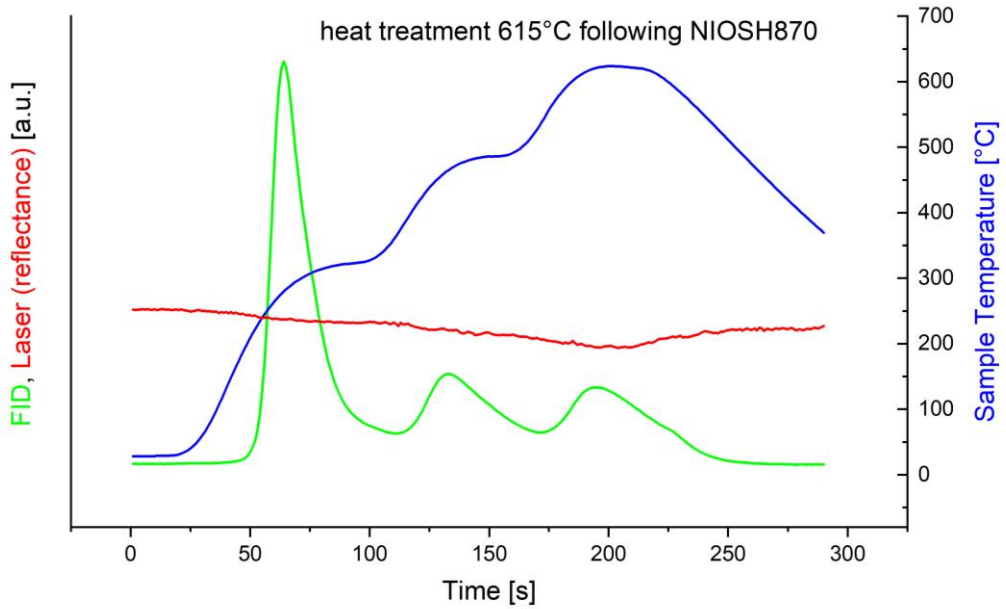

Figure 20: Thermogram of an atmospheric aerosol sample heated following the protocol in Table 1. The temperature (blue line) in the main oven increases stepwise in a He atmosphere and follows the curve of the NIOSH870 protocol until the third temperature level (615°C). The FID signal (green) and the laser signal (red) have therefore similar values as during a normal run of the full NIOSH870 protocol. At the end of this shortened heating procedure, the blower is turned on, the oven is cooled down and the heated sample is extracted when the temperature drops below 75°C (not shown in the figure).

Prior to the thermal-optical analyses and preparation of the heated samples, temperature calibrations were conducted following the recommendations in the instrument manual to avoid systematic errors due to offsets in the temperature curves, which otherwise could lead to biases of up to 12% for OC and 7% for EC (Pavlovic et al., 2014).

A subset of the atmospheric aerosol samples (Publication 2, section 8 and 12) was washed to remove most of WSOC and other soluble aerosol material (e.g. Gao et al., 2003; Kirchstetter et al., 2004). Eight of the 21 atmospheric aerosol filter samples were cut in half and aliquots of one half each were directly heat treated and analyzed with Raman microscopy. The other half of each filter was put into 100 ml glass bottles with 80 ml of Milli-Q water (18 MΩcm, Millipore). The bottles were then shaken in a shaking water bath (GFL Technology, 180 type GFL 1086) at room temperature for 20 minutes with 100 rpm. Directly after shaking the filters were taken out of the bottles, put into petri dishes and dried in a desiccator at room temperature for 2-3 days. The dry filters where then stored at -22°C until aliquots were heat treated and analyzed with Raman spectroscopy.

6.2.2. Measurement of Raman spectra and data processing

All Raman spectra were recorded using the Horiba Jobin Yvon LabRAM 800HR confocal Raman microscope, described in section 4.3, equipped with two lasers, a HeNe laser (wavelength 632.8 nm and a frequency-doubled NdYAG laser (wavelength 532 nm). For Publication 1 (section 7) only the 632.8 nm HeNe-laser was used, while measurements for Publication 2 (section 8) were performed using both lasers.

Generally, the laser beam was focused on the sample with the 20x magnification objective (CF Plan, NA=0.35, WD 20.5 mm, Nikon). Only for samples with low loadings (i.e. samples heated to higher temperatures) the long wide distance (LWD) 100x magnification objective (MPlanN, NA= 0.75, WD 0.21 mm, Olympus) was used to focus on single particles. Raman spectra were recorded in the range from 200 to 2000 cm^{-1} and calibrated with the silicon peak at 520.07 cm^{-1}.

For the CAST soot samples analyzed for Publication 1 (section 7 and 11) Raman spectra were obtained at 12 measurement spots of each (unheated and heated) filter sample, such that three positions were focused manually and four points were measured automatically around each position. For the test measurements shown in section 9.1, Raman spectra were recorded only for one to five different filter positions, which all were focused separately.

For most of the atmospheric aerosol samples studied in Publication 2 (section 8 and 12) ten spots were selected within a roughly focused area of (1x2) mm and all spots were measured automatically. For the samples heated to high temperatures (e.g. 500°C in $He+O_2$ (EUSAAR2), 870°C in He (NIOSH870)) single particles were focused with the LWD 100x objective. In these cases spectra were obtained only at five different spots.

Light absorption in the visible wavelength range and the stimulation of fluorescence light were the two most restricting confounders during the measurements of our CAST soot and atmospheric aerosol samples. The first was most problematic for samples with a high content of BC and led to thermal destruction of the material so that soot burned off completely in the illuminated spot. To avoid this, the laser power was reduced to below 25%.

The fluorescence signal, caused mainly by some organic substances, was high for samples with a high OC content and could lead to high signal to noise ratios. To improve this, the stimulation of

fluorescence was reduced by reducing the laser power (down to 1% for some cases) and part of the fluorescence signal was blocked by closing the confocal hole (down to 3 µm).

However, the potential for a reduction of fluorescence and therefore the optimization of the signal to noise ratio are limited. Both, reduced laser power and smaller aperture of the confocal hole lead to a reduction of the Raman signal, so longer integration times are necessary for the recording of a single spectrum. A balance between signal to noise ratio, integration time, and number of single spectra accumulated during one measurement run was therefore necessary. The exact values – adapted for different samples – are given in the publications.

Data analysis was performed using the software OriginPro© 2018 (9.5) by OriginLab Corporation. A baseline corresponding to the fluorescence background (as shown in Fig. 17, section 5.2.2) was fitted using the built-in tool of the software: up to 20 anchor points were set manually alongside the raw spectrum in the regions before and after the actual soot spectrum (ca. 200-1100 cm^{-1} and 1800-2000 cm^{-1}). The anchor points were connected with cubic B-splines, i.e. third grade polynomials which are differentiable twice at the connection positions. The anchor points were adjusted minimally for each spectrum until a smooth fit of the background was obtained.

After subtraction of the baseline the spectra were normalized to the maximum of the G-peak. Means and standard deviations were calculated collecting all spectra of one sample. Based on these mean spectra further analyses were performed using the built-in fitting tool of OriginPro©. The Raman spectra in Publication 1 (section 7 and 11) were fitted with five curves as described by Sadezky et al. (2005). The initial positions of all curves first were fixed at the values given in Table 1 (section 3.1.2) and released one after the other during the fitting process. Standard deviations were used as weighting of the fit since accuracy was mainly needed around the peaks (where standard deviations were small) and not in the periphery (where standard deviations were larger).

7. Overview Publication 1

Structural changes of CAST soot during a thermal–optical measurement protocol (T. Haller, C. Rentenberger, J. C. Meyer, L. Felgitsch, H. Grothe, and R. Hitzenberger, 2019)

The aim of the first publication was to investigate structural changes of two different CAST soots which occur during the thermal-optical measurement procedure using the NIOSH870 protocol. This measurement protocol was chosen because of its high maximum temperature in the inert phase of 870°C and the resulting tendency to form pyrolyzed carbon (PC). Since the EUSAAR2 protocol was developed to reduce charring (Cavalli et al., 2010), it seemed not suitable to use EUSAAR2 for the first structural investigations of PC.

A "brown" and a "black" CAST soot each were sampled on quartz fiber filters using two parallel filter holders as described in section 6.1.2. The settings of the miniCAST generator and the EC/TC and BC/LAC ratios of the samples are summarized in Table 5. The "black" sample was produced under oxygen-rich burning conditions (C/O = 0.275) and consists of 99% EC and 85% BC, resp. The "brown" sample was produced under fuel-rich conditions (C/O = 0.397) and has a high BrC content of 91%.

CAST burning conditions	"Black" sample	"Brown" sample
Propane	40 ml/min	50 ml/min
Oxidation Air	1.04 l/min	0.9 l/min
Nitrogen	0	0
Dilution Air	20 l/min	10 l/min
Quench gas (N_2)	7 l/min	7 l/min
C/O	0.275	0.397
EC/TC	0.99	0.11
BC/LAC	0.85	0.09

Table 5: Settings of the CAST soot generator used for the production of the two soots used in Publication 1.

The values for EC, OC and TC were obtained with the NIOSH870 thermal-optical measurement method using the thermal-optical instrument (Sunset Instruments Inc.) described in section 4.2. BC and BrC values were measured with the integrating sphere method (see section 4.5).

Heated aliquots of the filter samples were prepared corresponding to each temperature level of NIOSH870 as described in section 6.2.1: Aliquots of the filters were heated in the thermal-optical instrument following the temperature curves and gas atmospheres of NIOSH870 up to the desired temperature level. The temperature protocol was then interrupted; the sample cooled down in the oven to below 75°C and was then extracted. For both samples a whole set of heated filter punches (i.e. one heated filter punch for each temperature level) was prepared.

The unheated and heated filter samples were analyzed with Raman spectroscopy, UV-Vis spectroscopy and the integrating sphere method. TEM images were recorded by C. Rentenberger for the unheated samples and for the samples heated to 615°C, 870°C in He and 700°C in He+O_2, and crystallite sizes were calculated using the full width at half maximum (FWHM) of the electron diffraction peak at 2.8 nm^{-1}.

A clear difference between the “black” and the “brown” sample is visible in the TEM images of the unheated samples: The “black” sample consists of agglomerates of spherical primary particles with onion-like graphitic structures arranged around the center of the particle as described e.g. by Sadezky et al. (2005) and Kim et al. (2015). For the “brown” sample no ordered internal structure is visible and the particles adhere to the filter fibers like an oily substance described by Moore et al. (2014) as “condensed organic species”.

The Raman spectra of both (unheated) samples show two broad overlapping peaks with maxima at about 1580 cm^{-1} (G-peak) and about 1350 cm^{-1} (D-peak) as reported e.g. by Sadezky et al. (2005) and Ferrari and Robertson (2000). However, the D/G ratio of the Raman spectrum of the “brown” sample is lower than for the “black” sample indicating a lower degree of structural ordering of the “brown” sample.

The Raman spectra of the “black” sample do not change visibly (Fig. 21), when the sample is heated following the temperature curve of the NIOSH870 protocol indicating that the structural ordering in the sample does not change during heating. This is confirmed by the results of the electron diffraction measurements: The coherently scattering domain size lies around 1.2 nm for the “black” unheated and heated sample (Note: In Publication 1 all crystallite sizes had been erroneously multiplied by a factor of 2, personal communication C. Rentenberger; this however has no effect on the data interpretation). For the “brown” sample the D/G peak ratio increases when the sample is heated to the highest temperature level in He (870°C) and remains stable during further heating in the oxidizing phase which indicates an increase of structural ordering at 870°C in He. The coherently scattering domain size obtained from electron diffraction increases from 0.8 nm for the unheated “brown” sample to about 1 nm for the sample heated to 870°C in He. In contrast to the changes in the Raman spectra, which occur only at 870°C in He, the FWHM of the electron diffraction peak at 2.8 cm^{-1} changes also at lower temperature levels in He.

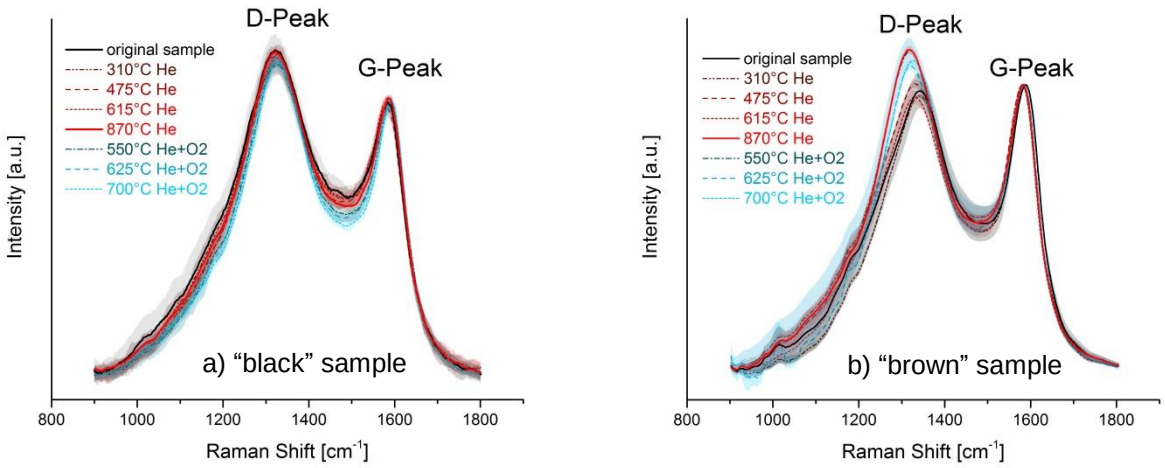

Figure 21: Raman spectra of unheated and heated aliquots of the black sample (a) and the brown sample (b). The spectra of the black sample do not change prominently during heating while the spectra of the brown sample change visibly at 870°C in He. The spectra are smoothed and normalized to the maximum of the G-peak. The standard deviations are shown as shaded areas. This figure is taken from Publication 1 (Haller et al., 2019).

The amount of BC – measured with the integrating sphere – remains relatively stable when the black sample is heated in the inert phase (up to 870°C in He) and decreases during heating in the oxidizing phase. For the brown sample, the amount of BC increases steadily during heating in the inert phase and decreases when oxygen is added. The Ångström exponent – obtained from the UV-Vis spectra – is -0.92 for the "black" unheated sample and remains relatively stable, when the sample is heated. The Ångström exponent of the "brown" sample is -1.79 for the unheated sample and increases continuously to -0.62 when the sample is heated up to 870°C in He. The reflectance laser signal in the thermal-optical instrument remains stable in the inert phase, when the "black" sample is heated. For the "brown" sample, the laser signal decreases continuously during the inert phase and starts to increase during the 870°C temperature level in He.

All measurement techniques used for Publication 1 show clearly that the structure of the "black" sample does not change when the sample is heated following the NIOSH870 protocol. On the other hand, the "brown" sample undergoes structural changes during heating in the inert phase. All applied analyses indicate that the structure of the heated (870°in He) "brown" sample resembles more or less the structure of the "black" sample. The Raman spectra change suddenly at 870°C in He and do not change during the preceding temperature levels (200°C – 615°C). However, the change of the Ångström exponent, the darkening of the sample (traced by the laser signal in the thermal-optical instrument), the change of the coherently scattering domain sizes obtained from electron diffraction and the formation of BC occur continuously during the whole inert phase. The interpretation of these somewhat contradictory findings is not unambiguously clear: The Raman spectra of the (unheated and heated) "brown" sample indicate, that no new graphene-layers are built during the first three temperature levels in He (up to 615°C) but the change of the Ångström exponent indicate a decreasing optical band gap in the material. A possible explanation could be that free bonds which emerge when oxygen and hydrogen leave the sample at temperatures above 250°C, could be incorporated in the remaining molecule and form conjugated double bonds and increase aromaticity. Also the loss of oxygenated groups can lead to a darkening of the substance. Both changes would lead to the observed optical changes (i.e. UV-Vis spectra, BC from integrating sphere measurement and laser signal in the thermal-optical instrument) but would not influence the peak heights of the Raman spectra.

8. Overview Publication 2

Investigation of structural changes of atmospheric aerosol samples during two thermal–optical measurement procedures (EUSAAR2, NIOSH870)
(T. Haller, E. Sommer, T. Steinkogler, C. Rentenberger, A. Wonaschuetz, A. Kasper-Giebl, H. Grothe, and R. Hitzenberger, 2021)

In the second publication the measurement scheme developed during the work for the first publication and tested for the relative simple case of two laboratory-generated combustion aerosols was applied to atmospheric aerosol samples. Compared to CAST soot, atmospheric aerosol can be a much more complex mixture because of the influence of various aerosol sources and the contribution of inorganic compounds such as nitrates, sulfates, chlorides, ammonium-salts, etc. From a two year set (2014-2015) of atmospheric aerosol filter samples, 21 atmospheric aerosol samples were chosen on the basis of their LAC loadings and BrC/LAC ratios (BC and BrC values were measured by E. Sommer for the whole period (Sommer, 2020) and were kindly made available for this work). From the winter period, 14 samples with high LAC loadings (between about 8 and 27 μg/cm^2) and high BrC loadings were selected (BrC/ LAC from about 0.3 to 0.7). From the summer period, seven samples with BrC below detection limit were selected. TC values varied between 7 and 34 μg/cm^2 for summer samples and from 13 to 71 μg/cm^2 for winter samples.

The analysis of the samples for EC, OC and TC was performed with the thermal-optical instrument (section 4.2) using the EUSAAR2 protocol as this protocol is used as a European standard method (Brown et al., 2017). Major ions (Na^+, NH_4^+, Mg^{2+}, Ca^{2+}, K^+, Cl^-, NO_2^-, NO_3^-, SO_4^-) were determined by ion chromatography (analyses performed by Thomas Steinkogler in the group of Anne Kasper-Giebl). For all samples aliquots were heated in the thermal-optical instrument as described in section 6.2.1. For six samples out of the chosen 21 filters, heated aliquots were prepared corresponding to all inert temperature levels of the NIOSH870 protocol (i.e. 310, 475, 615 and 870°C in He) and corresponding to the first five temperature levels of the EUSAAR2 protocol (i.e. 200, 300, 450, 650°C in He and 500°C in He+O_2). For the other eight samples out of 21 one half of each filter was washed with Milli-Q water (18 MΩcm, Mlillipore) to remove most of the water soluble organic carbon (WSOC) and other water soluble components, to investigate the influence of water soluble substances on charring. For these eight samples heated aliquots were prepared for the washed and unwashed part only for the first five temperature levels of the EUSAAR2 protocol.

Raman spectra were obtained for all washed and unwashed, heated and unheated samples. All Raman spectra show two broad overlapping peaks around 1580 cm^{-1} (G-peak) and around 1350 cm^{-1} (D-peak). For the washed samples the D/G peak ratio of the Raman spectra does not change significantly (according to a t-test with a significance level α= 5%) during heating with the EUSAAR2 protocol. This holds also for samples where D/G increases when the unwashed counterpart is heated. The transmission and reflectance laser signals stay nearly constant during the inert phase of EUSAAR2 for the washed samples but decrease for their unwashed counterparts. Both findings indicate that in the absence of WSOC the sample does not undergo significant structural changes during heating in the inert phase. This is in good agreement with Yu et al. (2002) who found that WSOC contributed most to charring.

For six unwashed samples the changes of the Raman spectra were compared for samples heated following NIOSH870 and EUSAAR2: For some samples the D/G peak ratio was higher when the sample was heated to the maximum inert temperature of NIOSH870 (870°C in He) compared to the highest inert temperature of EUSAAR2 (650°C in He). This indicates that pyrolyzed carbon (PC) that is formed during heating with NIOSH870 might have a higher degree of structural ordering at least for some cases.

For all 21 samples Raman spectra were obtained for samples heated following EUSAAR2. Significant changes in the D/G peak ratios (t-test with α=5%) of the Raman spectra were observed at different temperature levels between 450°C and 500°C in He. Five categories (plus one category "undefined") were identified, depending on the temperature levels, where significant changes in the Raman spectra (and therefore changes in the structural ordering) occur:

For samples in the category *"early change"* D/G increases at 450°C and 650°C in He, for *"early and fast change"* D/G increases only at 450°C in He. For samples in the category *"late change"* D/G increases at 650°C in He and 500°C in He+O_2, for the category *"late and fast change"* the increase of D/G occurs only at 650°C in He. For samples in the category *"no change"* D/G peak ratios of the Raman spectra do not change significantly. (The definition of the categories is described in more detail in the publication).

The chemical compositions of the samples (BC, BrC, major ions) were analyzed in order to find similarities for samples where structural changes occur at the same temperature levels, but no relationship was visible.

Additionally, the progress of the (transmission and reflectance) laser signals during the thermal-optical measurement with EUSAAR2 was compared to the assignment of the samples to the Raman categories. For all samples the (transmission and reflectance) laser signal decreases during heating in the inert phase until it starts to increase at 870°C in He. No relation was found with the progress of changes of the Raman spectra. This is most noticeable for the samples in the category *"no structural change"*: Although the Raman spectra indicate that structural ordering does not increase when these samples are heated following EUSAAR2, the laser signal shows a darkening of the sample. This indicates that – similar to the findings in Publication 1 – the processes that lead to a darkening of the sample do not necessarily include an increase of structural ordering. These processes could be for instance the separation of oxygen or hydrogen at temperatures above 250°C, a decomposition of oxygen containing surface groups, the loss of C-H "out-of-plane" bonds around 350-400°C or a decrease of cross-linkages between polyaromatic units or carbon-chains (e.g. Le et al., 2019). These findings indicate that care must be taken in the interpretation of a decreasing (transmission / reflectance) laser signal during thermal-optical analysis: The darkening of a sample is not necessarily caused by an increase of structural ordering or the building of graphitic-like structures. On the other hand, a relatively constant transmission / reflectance laser signal seems to indicate that structural ordering does not increase at least for the washed samples.

9. Additional results

9.1 Raman spectra of additional CAST-samples

For Publication 1 two CAST soots with C/O= 0.275 (“black”) and 0.397 (“brown”) were selected for the analysis of structural changes during the heating procedure of NIOSH870. Moreover, Raman measurements of heated and unheated CAST soot samples were performed for four additional settings of the CAST generator during a first testing phase. All samples together cover a range of C/O ratios between 0.275 and 0.5. In contrast to the samples analyzed for the publication, Raman spectra were recorded only for one to three filter positions for most of the additional samples (five positions for some of the unheated samples). Nevertheless, these measurements were found to agree with the general trend of structural changes during heat treatment of CAST soot samples as shown in Publication 1. The C/O ratios used for the production of these samples are listed in Table 6 together with the corresponding BC/LAC and EC/TC values. The stoichiometric C/O ratio for a – theoretical – total combustion is 0.3 (see section 2.3) which corresponds approximately to the combustion setting nr 2. The settings 1 and 2 can therefore be designated as oxygen rich, the settings 3-6 as fuel rich. Consequently the samples produced with the first two settings have clearly higher BC/LAC and EC/TC ratios than those produced with the settings 3-6.

Setting nr	C/O	BC/LAC	EC/TC
1 (“black”)	0.275	0.99	0.85
2	0.301	0.56	0.64
3	0.353	0.09	0.13
4 (“brown”)	0.397	0.11	0.09
5	0.441	0.09	0.04
6	0.5	0.06	0.10

Table 6: Carbon to oxygen (C/O) ratios and BC/LAC and EC/TC ratios for the CAST soot samples described in Publication 1 and in this section. The corresponding settings of the CAST generator are listed in Table 4 (section 6.1.1). Setting nr 1 and nr 2 correspond to the samples “black” and “brown” analyzed in Publication 1.

Figure 22 shows Raman spectra of soot obtained with the CAST settings listed in Table 6. The Raman spectra for the oxygen rich and fuel rich settings can be clearly distinguished: The relative D peak is higher for lower C/O ratios (0.2275 and 0.301) with D/G peak ratios around 1.16. The samples with higher C/O ratios (between 0.353 and 0.5) have lower D/G peak ratios around 1.09. These differences indicate a higher degree of structural ordering for the first two samples that might be caused by the large amount of EC. Ess et al. (2021) report comparable features of their Raman spectra measured on soot produced by a miniCAST generator. General differences between oxygen rich and oxygen poor burning conditions in particle size, BC / EC content and composition of particle coatings were also reported by Moore et al. (2014). Witek (2017) found for soot produced with our miniCAST generator and the same setup a clear difference between settings 1-2 and 3-6 not only in the BC/LAC and EC/TC ratios but also in the particle size distributions. The maximum of the number size distribution is around 87 nm for settings 1-2 and around 54 nm for settings 3-6.

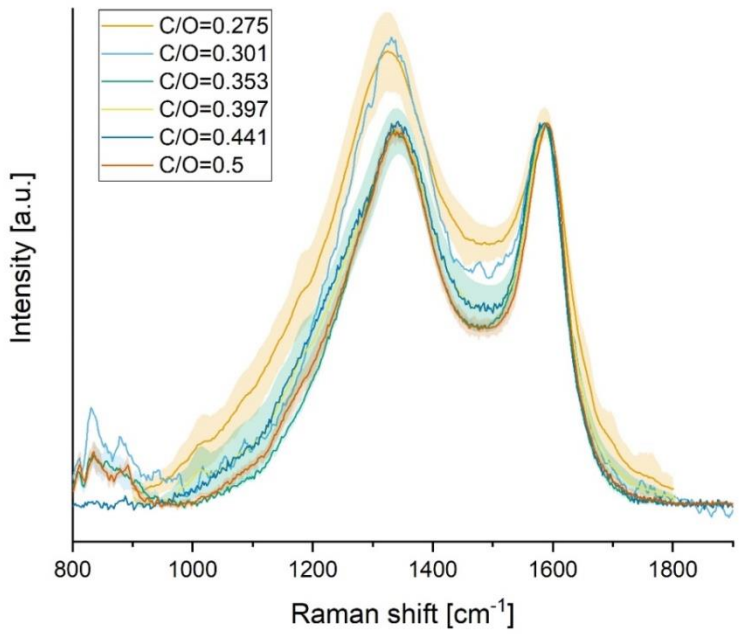

Figure 22: Raman spectra of unheated CAST soot samples with different burning conditions (C/O ratios). The spectra are normalized to the maximum G-peak. The two curves with the higher D-peaks correspond to samples obtained under oxygen rich conditions whereas the other curves correspond to samples obtained under oxygen poor burning conditions. For samples where measurements were performed at different filter positions, mean spectra and their standard deviations were calculated. The standard deviations are plotted as shaded areas.

Fig 23 shows Raman spectra of the CAST soot samples (except for the two samples shown in Publication 1) for the whole heating series of the NIOSH870 protocol. The changes in structural ordering during heating are comparable to the observations in Publication 1: Visible changes in the Raman spectra occur at the highest temperature level in helium (870°C) for all samples with fuel rich burning conditions and a low amount of BC and EC. The Raman spectra of the sample with C/O=0.301 (EC/TC=0.64, Fig 23a) do not change visibly during heating as it was also observed for the oxygen rich ("black") sample in the publication.

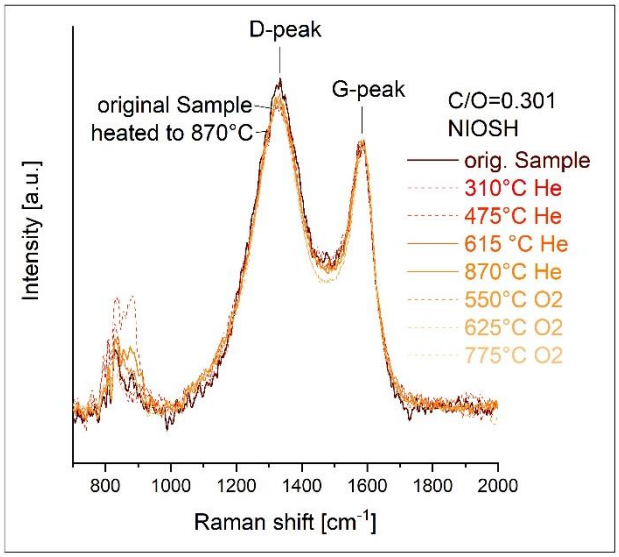

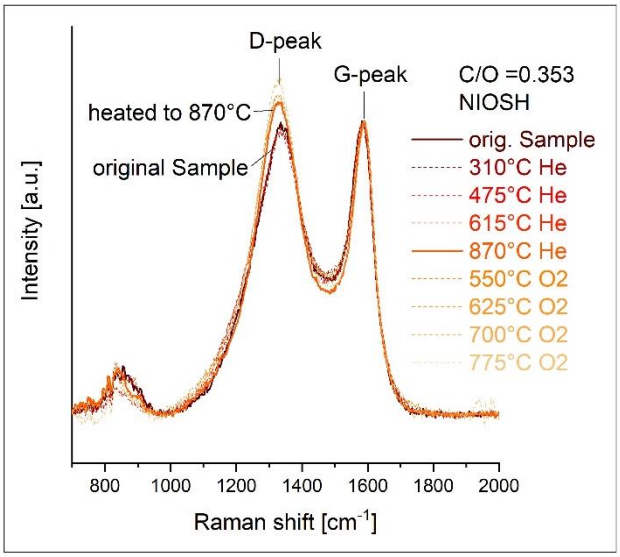

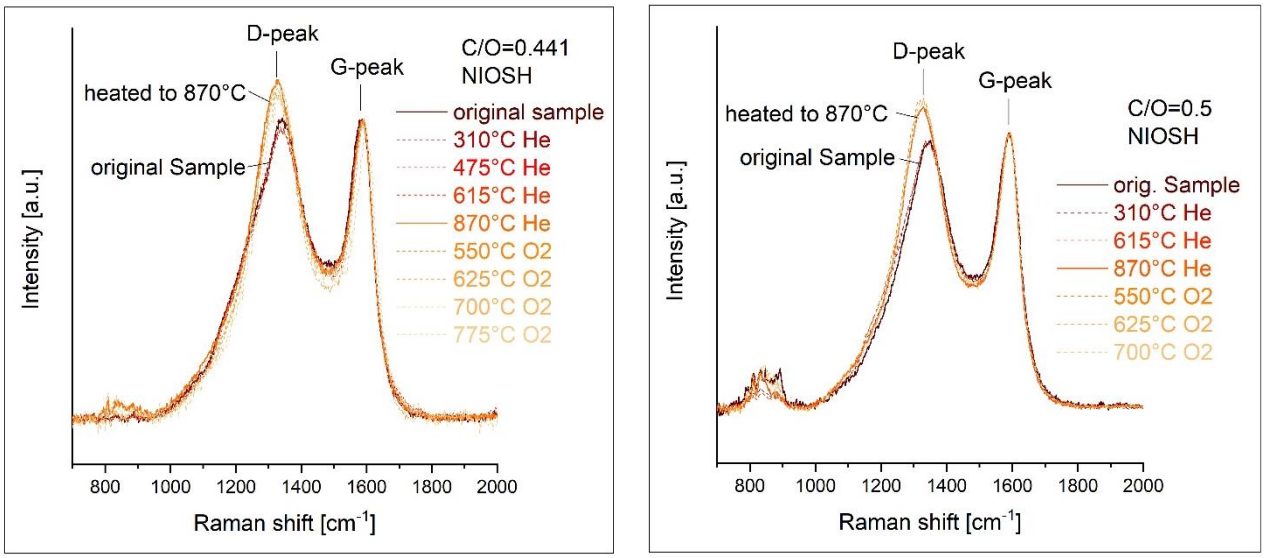

Figure 23: Raman spectra of heated and unheated CAST soot samples produced under different burning conditions, heated following the NIOSH870 protocol. The spectra are normalized to the maximum of the G-peak. D/G peak ratios do not change for the sample produced with C/O=0.301 but change for samples with C/O ratios clearly higher than the stoichiometric C/O ratio.

Fig 24 shows a comparison of the spectra of all samples heated to 870°C in He. The D/G ratio increases for samples with oxygen-poor burning conditions during heating and reach nearly the same height D/G of the spectra corresponding to oxygen-rich conditions. However, slight differences are visible between the samples with the highest and lowest C/O ratios.

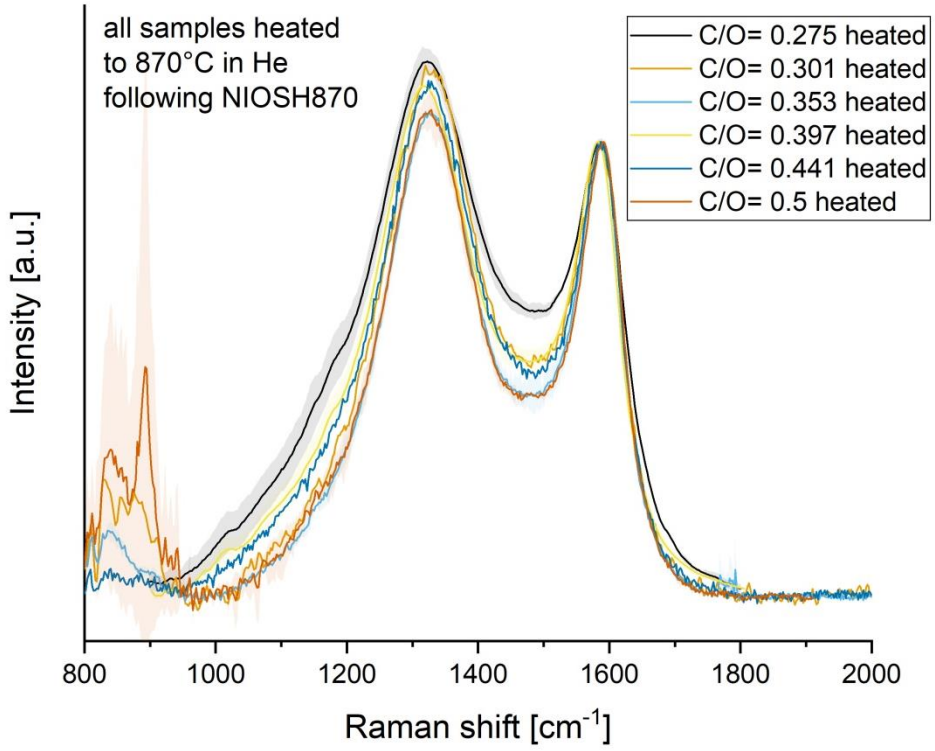

Figure 24: Raman spectra of all analyzed CAST soot samples heated to the highest temperature level (870°C) of the inert phase of NIOSH870. The spectra are normalized to the G-peak maximum. For samples measured at more than one filter position, standard deviatons are shown as shaded areas.

For setting nr 6 (C/O=0.5) Raman spectra were also recorded for samples heated following the EUSAAR2 protocol (Fig. 25). The most pronounced change of the spectra occurs at the highest temperature level in the inert phase (650°C), which is also the case when the sample is heated following NIOSH870 (Fig. 23, d). The relative increase of the D-peak at the end of the inert phase seems to be slightly larger when the sample is heated following NIOSH870 (D/G=1.06) than when it is heated following EUSAAR2 (D/G=1.02). This difference, however, may not be distinguishable from the signal noises. In comparison, for some atmospheric aerosol samples a larger increase of structural ordering was found in Publication 2, when the samples were heated following NIOSH870.

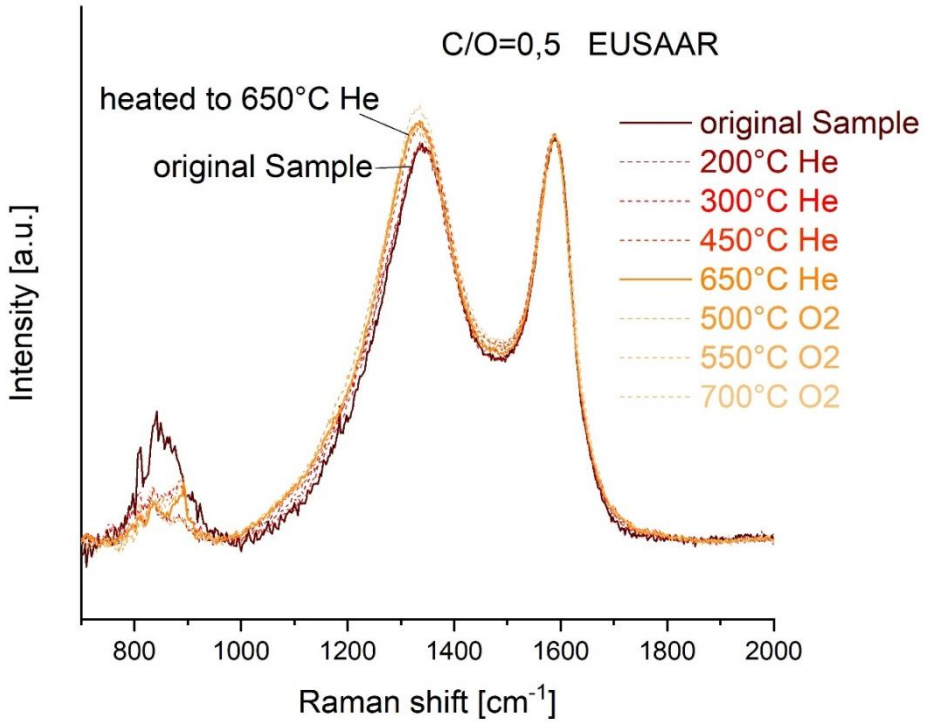

Figure 25: Raman spectra of a unheated and heated CAST soot sample produced under burning condition nr 6 (C/O=0.5) and heated following the EUSAAR2 protocol. The spectra are normalized to the maximum of the G-peak. Although the most pronounced change in the relative D peak height occurs at the highest temperature level in He, the increase of the peak is slightly lower than when the same sample is heated following NIOSH870 (Fig 23,d).

9.2 Additional analyses of atmospheric aerosol samples

In Publication 2 atmospheric aerosol samples were categorized according to the changes of their Raman spectra during heating (see sections 8 and 12). In the publication the categorizations were compared to the composition (major ions, BC/BrC) of the samples and to the progress of the transmission and reflection laser signal during the thermal-optical analyses. No relations were found. Additionally EC/TC ratios as well as air mass origin of the samples were set in relation to the assignment of the samples to the Raman categories. Also here no relations were found. These additional analyses are summarized here for the sake of completeness.

9.2.1 Comparison of EC/OC ratios and structural changes

Generally, at least some fraction of OC is often thought to char (interpreted from the darkening of the sample) during heating in He while EC should not undergo appreciable restructuring processes. On the basis of the Raman measurements on (unheated and heated) CAST soot samples (section 9.1, 7 and 11) samples with a lower EC/TC ratio were expected to be more likely to change their structure during heating than samples with a higher EC/TC ratio. Figure 26 shows EC/TC ratios of samples assigned to the Raman categories defined in Publication 2 (section 8 and 12): No relation between EC/TC and the Raman categories is visible. In particular samples in the category “no structural change” (i.e. the Raman spectra do not change over the whole heating process) do not have higher EC/TC ratios than samples in the other categories as it was the case for the CAST soot samples described above.

However, the EC/TC ratios of the samples in this category lie approximately in the range between the EC/TC ratios of the CAST soot samples with and without a change in structural ordering during the heating procedure of the NIOSH870 protocol (setting 2 and 3 in section 9.1). Moreover, differences in the compositions between the CAST soot samples and atmospheric aerosol samples could lead to different behaviors of both sample types and to more complex changes in structural ordering during the heating of atmospheric aerosol samples.

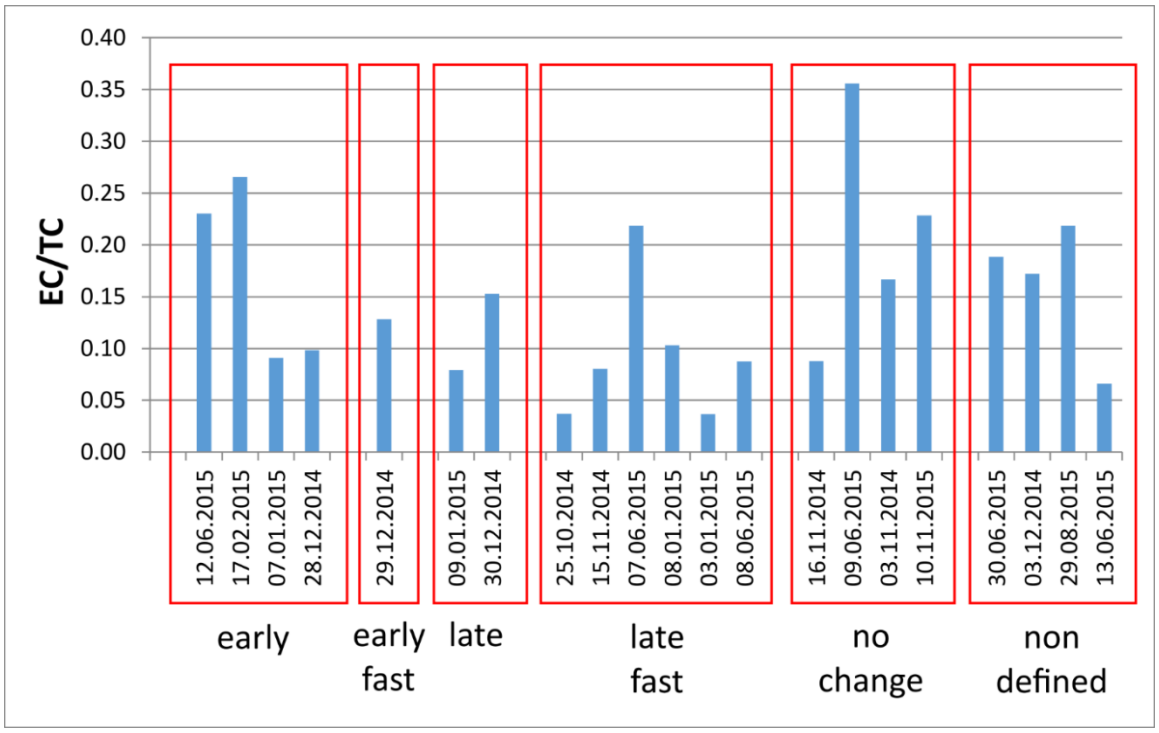

Figure 26: EC/TC ratios of samples assigned to the Raman categories representing the behavior of the Raman spectra during the heating procedure of the thermal-optical analysis using EUSAAR2. The categories are defined in Publication 2 and described in section 8. No relation between EC/TC and the changes in structural ordering is visible.

9.2.2. Possible influence of sources and source regions on structural changes

Different compositions and structures of the organic material in a specific sample could be caused by different sources and transformation of the combustion aerosol during atmospheric transport. Air mass back trajectories (72h, starting at 48.00°N, 16.00°E (Vienna), at altitudes of 100, 300 and 500 m above ground level) were calculated for each sampling day of the analyzed atmospheric aerosol samples using the HYSPLIT model (Draxler and Hess, 1997, 1998; Draxler, 1999). Two main sectors of air mass origin were defined depending on the contributions of different energy sources in the related regions: The western sector includes mainly back trajectories passing France and Southern Germany. The eastern sector ranges from the North (Northern Germany, Poland and the Czech Republic) over the East (Slovakia, Hungary, Romania) to the South (Croatia, Slovenia). The gross inland consumption of different energy sources differs in both sectors: In the eastern sector brown coal combustion is a major source of combustion aerosol. Germany, Poland, the Czech Republic, Greece, Bulgaria, Romania and Hungary contribute most to the gross inland consumption of brown coal in Europe (Eurostat, online). Although Germany has a high overall brown coal consumption (between 150 and 200 million

tons per year; Eurostat, online), most of the German lignite-fired power plants lie in the North of Germany (Saxony-Anhalt, North Rhine-Westphalia, Saxony, Lower Saxony, Brandenburg, Hessen; Umweltbundesamt, online) so most of German brown coal combustion occurs in the sector defined here as eastern sector. On the other hand, most of biomass combustion in Europe occurs in France and Germany (Eurostat, online), so as the aerosol from the sector defined here as western sector may be influenced by biomass burning products.

Both soot from brown coal combustion and soot from biomass burning were found to have higher BrC/LAC ratios than soot from fossil fuel combustion (Sun et al., 2017; Liu et al., 2013; Kirchstetter et al., 2004, Hoffer et al., 2006, Schmidl et al., 2008). Based on the fuel consumption data, appreciable amounts of BrC could have been transported to Vienna from all directions. However, Fan et al. (2016) found that at least part of BrC, namely the water soluble fraction of humic like substances (HULIS), has different molecular structures in biomass burning aerosols and brown coal combustion aerosols: The water soluble HULIS contain more aromatic compounds when they derive from brown coal combustion compared to biomass burning (Fan et al., 2016), so at least part of BrC could consist of molecules with higher aromaticity for air mass back trajectories in the Eastern sector. Moreover, also mixing states and fractions of soluble material per particle depend on the air mass origins (Okada and Hitzenberger, 2001). In order to investigate an effect of these possible differences in aerosol composition and aromaticity of at least part of BrC on the results of the Raman analyses, air mass back trajectories are plotted in Fig 27. The trajectories are sorted according to the assignment of the samples to the Raman categories. No relationship between air mass back trajectory and the assignment to the Raman categories is visible. This could be due to a too similar composition of the aerosols despite differences in combustion fuels since BrC species arrive from all directions to Vienna, or to a predominance of carbonaceous aerosol emitted directly in Vienna (mostly diesel soot from traffic – 80% of fuel sale in Austria in 2015 was diesel: WKO, Mineralölindustrie (2020)) and its immediate surroundings, which would mask the effects of particles originating from trans-boundary transport.

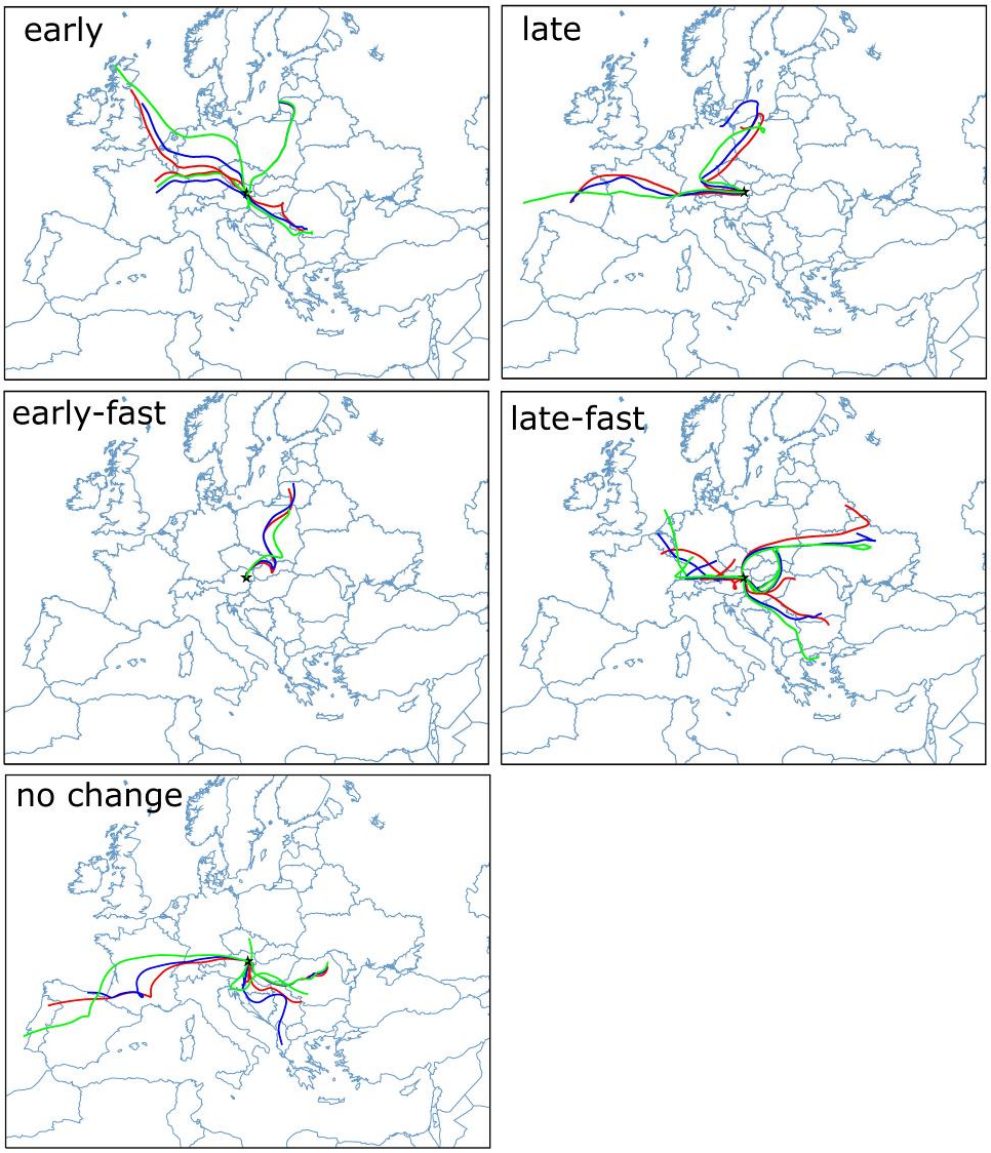

Figure 27: Back trajectories sorted by the categories representing the different behavior of the Raman signal during the thermal-optical heating procedure (early structural change, late structural change, early and fast structural change, late and fast structural change and no change). The different colors represent the altitudes AGL (green=500 m, blue=300 m, red=100 m). All trajectories start at 13:00 UTC.

10. Summary and overall conclusion

The aim of this work was to shed light on the processes that can lead to biases of EC and OC results obtained with different thermal-optical measurement protocols by investigating structural changes of carbonaceous aerosols during the heating procedure in a thermal-optical instrument. Although several authors (e.g. Yu et al., 2002; Wang et al., 2010; Bladt et al., 2014; Cavalli et al., 2010; Cheng et al., 2012 addressed the charring of a sample during heating in the inert phase, by the start of this work no literature was available that focused on the actual structural changes of carbonaceous species in terms of graphitization. In this work these changes of structural ordering during heating according to the NIOSH870 and EUSAAR2 protocols were analyzed with Raman spectroscopy for CAST soot samples as well as for atmospheric aerosol samples.

For the CAST soot samples (Publication 1 and section 9.1) a relatively simple scheme of structural changes during heating with NIOSH870 was found: For the two samples produced under oxygen-rich burning conditions (C/O ≤ 0.301) with high amounts of EC and BC no changes of the Raman spectra and therefore no changes of structural ordering were visible. For the samples produced under oxygen-poor burning conditions (C/O ≥ 0.353) containing large amounts of OC and BrC the D/G peak ratio of the Raman spectra increased suddenly when the samples were heated to 870°C in He indicating an increase of structural ordering at this temperature level. It is noteworthy that the D/G ratios of the Raman spectra of the (unheated) samples produced under oxygen-rich burning conditions are higher than D/G ratios for the (unheated) samples produced under oxygen-poor burning conditions (section 9.1). During heating to 870°C the D/G peak ratio of the latter resembles more or less the D/G peak ratiot of the first. For the CAST soot sample produced with C/O=0.397 (“brown” sample in Publication 1) additionally to Raman spectroscopy, electron diffraction and UV-Vis spectroscopy were performed. The results of all three techniques (D/G ratio, crystallite sizes, Ångström exponent) show that the structure of this “brown” sample resembles more or less the structure of the (unheated) sample produced with C/O=0.275 (“black” sample in Publication 1) when it is heated to 870°C in He. Although the Raman spectra of the CAST soot samples changed only during the highest inert temperature level of the NIOSH870 protocol or did not change at all, no such simple behavior was visible for 21 atmospheric aerosol samples heated following the EUSAAR2 protocol (Publication 2): Changes of the D/G peak ratio of the Raman spectra occurred between 300°C in He and 500°C in He+O_2. Moreover, for some samples the changes occurred only during one temperature level, for other samples at two consecutive levels and for some samples the Raman spectra did not change significantly. However, no relation was found between the progress of structural changes during heating (i.e. the temperature levels, where significant changes of the Raman spectra were visible) and several properties of the respective sample (BC/LAC, EC/TC, composition of major ions, air mass back trajectories). This lack of relations might be caused by the complex compositions of atmospheric aerosol samples and resulting counteracting influences of different compounds. This would be in agreement to the findings of Yu et al. (2002) who report that one and the same compound can favor or hinder charring depending on the chemical composition of the carbonaceous species in the sample.

For a subset of six atmospheric aerosol samples changes of the Raman spectra were compared for samples heated following NIOSH870 and following EUSAAR2: The D/G ratios were higher for some samples when they were heated to the highest inert temperature level of NIOSH870 (870°C in He)

compared to the highest inert temperature level of EUSAAR2 (650°C in He). This gives evidence that in some cases PC that is produced during NIOSH870 might have a higher degree of structural ordering than PC formed during EUSAAR2.

Another subset of eight atmospheric aerosol samples was washed with water to remove WSOC and other water soluble substances. For all of these washed samples, the Raman spectra did not change during heating following the EUSAAR2 protocol also when the Raman spectra of their unwashed counterparts changed. The transmission / reflectance laser signals remained constant during the inert phase for the washed samples but decreased for their unwashed counterparts. Both findings are in good agreement with Yu et al. (2002) who found that WSOC contributed most to charring.

In both publications changes of the optical properties of the samples during heating in the thermal-optical instrument were examined. In Publication 1 the unheated and heated samples were analyzed with UV-Vis spectroscopy and the integrating sphere method. Additionally the progress of the transmission / reflection laser signals during thermal-optical analyses was observed. In Publication 2 information about optical properties was obtained only from the patterns of the transmission / reflection laser signals during the thermal-optical measurement. The changes of the optical properties of the CAST soot sample produced under oxygen-poor burning conditions (heated with NIOSH870) as well as for the (unwashed) atmospheric aerosol samples (heated with EUSAAR2) did not coincide with the changes of the Raman spectra (i.e. D/G ratio) during heating: The Ångström exponent, BC content (both Publication 1) and laser signals (Publication 1 and 2) changed continuously also during lower temperature levels, where Raman spectra did not change. This is most striking especially for four (unwashed) atmospheric aerosol samples (Publication 2) where the D/G peak ratio of the Raman spectra did not change significantly but the laser signal decreased during heating following the EUSAAR2 protocol.

These findings indicate that some processes that occur during thermal-optical analyses of the “brown” CAST soot sample (C/O=0.397) and several atmospheric aerosol samples lead to a darkening of the samples but do not influence the D/G peak ratio of the Raman spectra. This is in agreement with findings of Yu et al. (2002) who describe a possible formation of light-absorbing but non-graphitic intermediate OC products during thermal-optical analyses. These processes could be e.g. the separation of oxygen and hydrogen at temperatures above 250°C in He (Petzold et al., 2013; Chow et al., 2004, Le et al., 2019). The resulting free bonds might be incorporated in the remaining molecule and form conjugated double bonds. Also a decomposition of oxygen containing surface groups (C-O; C=O), a decrease of cross-linkages between polyaromatic units and carbon chains or the loss of C-H “out-of-plane” bonds around 350-400°C might be possible (Le et al., 2019). All of these processes might lead to a darkening of the sample but would not influence the relative peak heights of the Raman spectra.

The major conclusion of the studies on CAST soot and atmospheric samples is the finding that a darkening of a sample during thermal-optical analysis (monitored by the decreasing laser signal and often described as “charring” or “pyrolysis”) is not necessarily caused by an increase of structural ordering or the building of graphitic-like structures during heating in the inert phase. For the washed samples (Publication 2) and the “black” CAST soot sample (Publication 1) the (transmission / reflectance) laser signals did not decrease during heating and also the Raman spectra did not change. At least for these cases it seems possible to conclude from a stable laser signal to a lack of graphitization of the sample.

Literature

Adachi, Kouji; Buseck, Peter R. (2013): Changes of ns-soot mixing states and shapes in an urban area during CalNex. In: Journal of Geophysical Research: Atmospheres 118 (9), P. 3723–3730. DOI: 10.1002/jgrd.50321.

Adachi, Kouji; Chung, Serena H.; Buseck, Peter R. (2010): Shapes of soot aerosol particles and implications for their effects on climate. In: Journal of Geophysical Research: Atmospheres 115 (D15), P. 6469. DOI: 10.1029/2009JD012868.

Andreae, M. O.; Gelencsér, A. (2006): Black carbon or brown carbon? The nature of light-absorbing carbonaceous aerosols. In: Atmos. Chem. Phys. 6 (10), p. 3131–3148. DOI: 10.5194/acp-6-3131-2006.

Bautista, Angel T.; Pabroa, Preciosa Corazon B.; Santos, Flora L.; Quirit, Leni L.; Asis, Joannes Luke B.; Dy, Marie Alexandra K.; Martinez, Jason Patrick G. (2015): Intercomparison between NIOSH, IMPROVE_A, and EUSAAR_2 protocols: Finding an optimal thermal–optical protocol for Philippines OC/EC samples. In: *Atmospheric Pollution Research* 6 (2), p. 334–342. DOI: 10.5094/APR.2015.037.

Birch, M. E.; Cary, R. A. (1996): Elemental Carbon-Based Method for Monitoring Occupational Exposures to Particulate Diesel Exhaust. In: Aerosol Science and Technology 25 (3), p. 221–241. DOI: 10.1080/02786829608965393.

Bladt, Henrike; Ivleva, Natalia P.; Niessner, Reinhard (2014): Internally mixed multicomponent soot: Impact of different salts on soot structure and thermo-chemical properties. In: *Journal of Aerosol Science* 70, p. 26–35. DOI: 10.1016/j.jaerosci.2013.11.007.

Bladt, Henrike; Ivleva, Natalia P.; Niessner, Reinhard (2014): Internally mixed multicomponent soot: Impact of different salts on soot structure and thermo-chemical properties. In: Journal of Aerosol Science 70, p. 26–35. DOI: 10.1016/j.jaerosci.2013.11.007.

Bond, T. C.; Doherty, S. J.; Fahey, D. W.; Forster, P. M.; Berntsen, T.; DeAngelo, B. J. et al. (2013): Bounding the role of black carbon in the climate system: A scientific assessment. In: *J. Geophys. Res. Atmos.* 118 (11), p. 5380–5552. DOI: 10.1002/jgrd.50171.

Bond, Tami C.; Bergstrom, Robert W. (2006): Light Absorption by Carbonaceous Particles: An Investigative Review. In: Aerosol Science and Technology 40 (1), p. 27–67. DOI: 10.1080/02786820500421521.

Bondy, Amy L.; Bonanno, Daniel; Moffet, Ryan C.; Wang, Bingbing; Laskin, Alexander; Ault, Andrew P. (2018): The diverse chemical mixing state of aerosol particles in the southeastern United States. In: Atmospheric Chemistry and Physics 18 (16), p. 12595–12612. DOI: 10.5194/acp-18-12595-2018.

Brown, Richard J. C.; Beccaceci, Sonya; Butterfield, David M.; Quincey, Paul G.; Harris, Peter M.; Maggos, Thomas et al. (2017): Standardisation of a European measurement method for organic carbon and elemental carbon in ambient air: results of the field trial campaign and the determination of a measurement uncertainty and working range. In: Environ. Sci.: Processes Impacts 19 (10), p. 1249–1259. DOI: 10.1039/C7EM00261K.

Cappa, Christopher D.; Onasch, Timothy B.; Massoli, Paola; Worsnop, Douglas R.; Bates, Timothy S.; Cross, Eben S. et al. (2012): Radiative absorption enhancements due to the mixing state of atmospheric black carbon. In: Science (New York, N.Y.) 337 (6098), p. 1078–1081. DOI: 10.1126/science.1223447.

Cavalli, F.; Viana, M.; Yttri, K. E.; Genberg, J.; Putaud, J.-P. (2010): Toward a standardised thermal-optical protocol for measuring atmospheric organic and elemental carbon: the EUSAAR protocol. In: Atmos. Meas. Tech. 3 (1), p. 79–89. DOI: 10.5194/amt-3-79-2010.

Cheng, Yuan; Duan, Feng-kui; He, Ke-bin; Du, Zhen-yu; Zheng, Mei; Ma, Yong-liang (2012): Intercomparison of thermal-optical method with different temperature protocols: Implications from source samples and solvent extraction. In: Atmospheric Environment 61, p. 453–462. DOI: 10.1016/j.atmosenv.2012.07.066.

China, Swarup; Mazzoleni, Claudio; Gorkowski, Kyle; Aiken, Allison C.; Dubey, Manvendra K. (2013): Morphology and mixing state of individual freshly emitted wildfire carbonaceous particles. In: Nature communications 4, p. 2122. DOI: 10.1038/ncomms3122.

Chow, Judith C.; Watson, John G.; Chen, L.-W. Antony; Arnott, W. Patrick; Moosmüller, Hans; Fung, Kochy (2004): Equivalence of Elemental Carbon by Thermal/Optical Reflectance and Transmittance with Different Temperature Protocols. In: Environ. Sci. Technol. 38 (16), p. 4414–4422. DOI: 10.1021/es034936u.

Chung, Seung-Hyun; Violi, Angela (2011): Peri-condensed aromatics with aliphatic chains as key intermediates for the nucleation of aromatic hydrocarbons. In: *Proceedings of the Combustion Institute* 33 (1), p. 693–700. DOI: 10.1016/j.proci.2010.06.038.

Chung, Seung-Hyun; Violi, Angela (2011): Peri-condensed aromatics with aliphatic chains as key intermediates for the nucleation of aromatic hydrocarbons. In: Proceedings of the Combustion Institute 33 (1), p. 693–700. DOI: 10.1016/j.proci.2010.06.038.

Commodo, Mario; Falco, Gianluigi de; Larciprete, Rosanna; D'Anna, Andrea; Minutolo, Patrizia (2016): On the hydrophilic/hydrophobic character of carbonaceous nanoparticles formed in laminar premixed flames. In:

Cuesta, A.; Dhamelincourt, P.; Laureyns, J.; Martínez-Alonso, A.; Tascón, J.M.D. (1994): Raman microprobe studies on carbon materials. In: *Carbon* 32 (8), p. 1523–1532. DOI: 10.1016/0008-6223(94)90148-1.

De Gouw, Joost; Jimenez, Jose L. (2009): Organic aerosols in the Earth's atmosphere. In: *Environmental science & technology* 43 (20), p. 7614–7618. DOI: 10.1021/es9006004.

Deboudt, Karine; Flament, Pascal; Choël, Marie; Gloter, Alexandre; Sobanska, Sophie; Colliex, Christian (2010): Mixing state of aerosols and direct observation of carbonaceous and marine coatings on African dust by individual particle analysis. In: Journal of Geophysical Research: Atmospheres 115 (D24), p. 833. DOI: 10.1029/2010JD013921.

Demtröder, Wolfgang (2010): Experimentalphysik 3. 4., überarb. Aufl. Berlin: SPRINGER (Springer-Lehrbuch).

Dieing, Thomas; Hollricher, Olaf; Toporski, Jan (2011): Confocal Raman Microscopy. Berlin, Heidelberg: Springer-Verlag Berlin Heidelberg (Springer Series in Optical Sciences, 158).

Dieing, Thomas; Hollricher, Olaf; Toporski, Jan (2011): Confocal Raman Microscopy. Berlin, Heidelberg: Springer-Verlag Berlin Heidelberg (Springer Series in Optical Sciences, 158).

Dippel, B.; Jander, H.; Heintzenberg, J. (1999): NIR FT Raman spectroscopic study of flame soot. In: *Physical Chemistry Chemical Physics* 1 (20), p. 4707–4712. DOI: 10.1039/a904529e.

Draxler, R. R., Hess, G. D.: Description of the HYSPLIT4 modeling system: NOAA Tech. Memo. ERL ARL-224, NOAA Air Resources Laboratory, Silver Spring, Md [Online], 1997.

Draxler, R. R.: HYSPLIT4 User's Guide. NOAA Tech. Memo. ERL ARL-230, NOAA Air Resources Laboratory, Silver Spring, Md [Online], 1999.

Ess, M. N.; Ferry, D.; Kireeva, E. D.; Niessner, R.; Ouf, F.-X.; Ivleva, N. P. (2016): In situ Raman microspectroscopic analysis of soot samples with different organic carbon content: Structural changes during heating. In: *Carbon* 105 (5), p. 572–585. DOI: 10.1016/j.carbon.2016.04.056.

Ess, Michaela N.; Bertò, Michele; Irwin, Martin; Modini, Robin L.; Gysel-Beer, Martin; Vasilatou, Konstantina (2021): Optical and morphological properties of soot particles generated by the miniCAST 5201 BC generator. In: *Aerosol Science and Technology*, p. 1–25. DOI: 10.1080/02786826.2021.1901847.

Eurostat, online: https://ec.europa.eu/eurostat/statistics-explained/index.php?title=Coal_production_and_consumption_statistics, last access 09.06.2021.

Fan, Xingjun; Wei, Siye; Zhu, Mengbo; Song, Jianzhong; an Peng, Ping (2016): Comprehensive characterization of humic-like substances in smoke PM 2.5 emitted from the combustion of biomass materials and fossil fuels. Atmospheric Chemistry and Physics, 16(20), 13321-13340. DOI: 10.5194/ACP-16-13321-2016.

Ferrari, A. C.; Robertson, J. (2000): Interpretation of Raman spectra of disordered and amorphous carbon. In: Physical Review B 61 (20), p. 14095–14107. DOI: 10.1103/PhysRevB.61.14095.

Frenklach, Michael (2002): Reaction mechanism of soot formation in flames. In: Physical Chemistry Chemical Physics 4 (11), p. 2028–2037. DOI: 10.1039/b110045a.

Fushimi, Akihiro; Nakajima, Daisuke; Furuyama, Akiko; Suzuki, Go; Ito, Tomohiro; Sato, Kei et al. (2021): Source contributions to multiple toxic potentials of atmospheric organic aerosols. In: The Science of the total environment 773, p. 145614. DOI: 10.1016/j.scitotenv.2021.145614.

Gao, Song; Hegg, Dean A.; Hobbs, Peter V.; Kirchstetter, Thomas W.; Magi, Brian I.; Sadilek, Martin (2003): Water-soluble organic components in aerosols associated with savanna fires in southern Africa: Identification, evolution, and distribution. In: J. Geophys. Res. 108 (D13), n/a-n/a. DOI: 10.1029/2002JD002324.

Gelencsér, A.; Hoffer, A.; Kiss, G.; Tombáz, E.; Kurdi, R.; Bencze, L. (2003): In-situ Formation of Light-Absorbing Organic Matter in Cloud Water. In: Journal of Atmospheric Chemistry 45 (1), p. 25–33. DOI: 10.1023/A:1024060428172.

Giannoni, Martina; Calzolai, Giulia; Chiari, Massimo; Cincinelli, Alessandra; Lucarelli, Franco; Martellini, Tania; Nava, Silvia (2016): A comparison between thermal-optical transmittance elemental carbon measured by different protocols in PM2.5 samples. In: The Science of the total environment 571, p. 195–205. DOI: 10.1016/j.scitotenv.2016.07.128.

Giannoni, Martina; Calzolai, Giulia; Chiari, Massimo; Cincinelli, Alessandra; Lucarelli, Franco; Martellini, Tania; Nava, Silvia (2016): A comparison between thermal-optical transmittance elemental carbon measured by different protocols in PM2.5 samples. In: The Science of the total environment 571, p. 195–205. DOI: 10.1016/j.scitotenv.2016.07.128.

Graber, E. R.; Rudich, Y. (2006): Atmospheric HULIS: How humic-like are they? A comprehensive and critical review. In: Atmos. Chem. Phys. 6 (3), p. 729–753. DOI: 10.5194/acp-6-729-2006.

Haarer, Dietrich; Spiess, Hans Wolfgang (1995): Spektroskopie amorpher und kristalliner Festkörper. Heidelberg: Steinkopff. ISBN: 10.1007/978-3-642-57871-7.

Haller, Theresa; Rentenberger, Christian; Meyer, Jannik C.; Felgitsch, Laura; Grothe, Hinrich; Hitzenberger, Regina (2019): Structural changes of CAST soot during a thermal–optical measurement protocol. In: Atmospheric Measurement Techniques 12 (7), p. 3503–3519. DOI: 10.5194/amt-12-3503-2019.

Haller, Theresa; Sommer, Eva; Steinkogler, Thomas; Rentenberger, Christian; Wonaschuetz, Anna; Kasper-Giebl, Anne et al. (2021): Investigation of structural changes of atmospheric aerosol samples during two thermal–optical measurement procedures (EUSAAR2, NIOSH870). In: Atmos. Meas. Tech. 14 (5), p. 3721–3735. DOI: 10.5194/amt-14-3721-2021.

Han, Yongming; Cao, Junji; Chow, Judith C.; Watson, John G.; An, Zhisheng; Jin, Zhangdong et al. (2007): Evaluation of the thermal/optical reflectance method for discrimination between char- and soot-EC. In: Chemosphere 69 (4), p. 569–574. DOI: 10.1016/j.chemosphere.2007.03.024.

Hand, Victoria L.; Capes, Gerard; Vaughan, David J.; Formenti, Paola; Haywood, Jim M.; Coe, Hugh (2010): Evidence of internal mixing of African dust and biomass burning particles by individual particle analysis using electron beam techniques. In: J. Geophys. Res. 115 (D13), p. 8484. DOI: 10.1029/2009JD012938.

Heidenreich, R. D.; Hess, W. M.; Ban, L. L. (1968): A test object and criteria for high resolution electron microscopy. In: J Appl Crystallogr 1 (1), p. 1–19. DOI: 10.1107/S0021889868004930.

Heintzenberg, Jost (1982): Size-segregated measurements of particulate elemental carbon and aerosol light absorption at remote arctic locations. In: Atmospheric Environment (1967) 16 (10), p. 2461–2469. DOI: 10.1016/0004-6981(82)90136-6.

Highwood, Eleanor J.; Kinnersley, Robert P. (2006): When smoke gets in our eyes: The multiple impacts of atmospheric black carbon on climate, air quality and health. In: Environment International 32 (4), p. 560–566. DOI: 10.1016/j.envint.2005.12.003.

Hitzenberger, R.; Dusek, U.; Berner, A. (1996): Black carbon measurements using an integrating sphere. In: Journal of Geophysical Research: Atmospheres 101 (D14), p. 19601–19606. DOI: 10.1029/95JD02412.

Hitzenberger, R.; Petzold, A.; Bauer, H.; Ctyroky, P.; Pouresmaeil, P.; Laskus, L.; Puxbaum, H. (2006): Intercomparison of Thermal and Optical Measurement Methods for Elemental Carbon and Black Carbon at an Urban Location. In: Environ. Sci. Technol. 40 (20), p. 6377–6383. DOI: 10.1021/es051228v.

Hitzenberger, R.; Tohno, p. (2001): Comparison of black carbon (BC) aerosols in two urban areas – concentrations and size distributions. In: Atmospheric Environment 35 (12), p. 2153–2167. DOI: 10.1016/S1352-2310(00)00480-5.

Hoffer, A.; Gelencsér, A.; Blazsó, M.; Guyon, P.; Artaxo, P.; Andreae, M. O. (2006): Diel and seasonal variations in the chemical composition of biomass burning aerosol. In: Atmos. Chem. Phys. 6 (11), p. 3505–3515. DOI: 10.5194/acp-6-3505-2006.

Hoffer, A.; Gelencsér, A.; Blazsó, M.; Guyon, P.; Artaxo, P.; Andreae, M. O. (2006): Diel and seasonal variations in the chemical composition of biomass burning aerosol. In: Atmos. Chem. Phys. 6 (11), p. 3505–3515. DOI: 10.5194/acp-6-3505-2006.

Houska, C. R.; Warren, B. E. (1954): X-Ray Study of the Graphitization of Carbon Black. In: Journal of Applied Physics 25 (12), p. 1503–1509. DOI: 10.1063/1.1702373.

IPCC: Clouds and Aerosols. Climate Change 2013: The Physical Science Basis. Contribution of Working Group I to the Fifth Assessment Report of the Intergovernmental Panel on Climate Change, edited by: Stocker, T. F., Qin, D., Plattner, G.-K., Tignor, M., Allen, S. K., Boschung, J., Nauels, A., Xia, Y., Bex, V., and Midgley, P. M., Cambridge University Press, Cambridge, United Kingdom and New York, NY, USA, 2013.

Ivleva, Natalia P.; Messerer, Armin; Yang, Xin; Niessner, Reinhard; Pöschl, Ulrich (2007): Raman microspectroscopic analysis of changes in the chemical structure and reactivity of soot in a diesel exhaust aftertreatment model system. In: Environmental science & technology 41 (10), p. 3702–3707. DOI: 10.1021/es0612448.

Jankowski, Nicole; Schmidl, Christoph; Marr, Iain L.; Bauer, Heidi; Puxbaum, Hans (2008): Comparison of methods for the quantification of carbonate carbon in atmospheric PM10 aerosol samples. In: Atmospheric Environment 42 (34), p. 8055–8064. DOI: 10.1016/j.atmosenv.2008.06.012.

Jawhari, T.; Roid, A.; Casado, J. (1995): Raman spectroscopic characterization of some commercially available carbon black materials. In: Carbon 33 (11), p. 1561–1565. DOI: 10.1016/0008-6223(95)00117-V.

Kang, Shichang; Zhang, Yulan; Qian, Yun; Wang, Hailong (2020): A review of black carbon in snow and ice and its impact on the cryosphere. In: Earth-Science Reviews 210 (11), p. 103346. DOI: 10.1016/j.earscirev.2020.103346.

Kholghy, Mohammad Reza; Veshkini, Armin; Thomson, Murray John (2016): The core–shell internal nanostructure of soot – A criterion to model soot maturity. In: Carbon 100, p. 508–536. DOI: 10.1016/j.carbon.2016.01.022.

Kim, J.; Bauer, H.; Dobovicnik, T.; Hitzenberger, R.; Lottin, D.; Ferry, D.; Petzold, A. (2015): Assessing Optical Properties and Refractive Index of Combustion Aerosol Particles Through Combined Experimental and Modeling Studies. In: Aerosol Science and Technology 49 (5), p. 340–350. DOI: 10.1080/02786826.2015.1020996.

Kirchstetter, Thomas W.; Novakov, T.; Hobbs, Peter V. (2004): Evidence that the spectral dependence of light absorption by aerosols is affected by organic carbon. In: J. Geophys. Res. 109 (D21), n/a-n/a. DOI: 10.1029/2004JD004999.

Kwiecińska, B.; Petersen, H.I (2004): Graphite, semi-graphite, natural coke, and natural char classification—ICCP system. In: International Journal of Coal Geology 57 (2), p. 99–116. DOI: 10.1016/j.coal.2003.09.003.

Laskin, Alexander; Laskin, Julia; Nizkorodov, Sergey A. (2015): Chemistry of atmospheric brown carbon. In: Chemical reviews 115 (10), p. 4335–4382. DOI: 10.1021/cr5006167.

Le, K. C., Pino, T., van Pham, T., Henriksson, J., Török, S., and Bengtsson, P.-E.: Raman spectroscopy of mini-CAST soot with various fractions of organic compounds: Structural characterization during heating treatment from 25 _C to 1000 _C, Combust. Flame, 209, 291–302, https://doi.org/10.1016/j.combustflame.2019.07.037, 2019.

Liu, J.; Bergin, M.; Guo, H.; King, L.; Kotra, N.; Edgerton, E.; Weber, R. J. (2013): Size-resolved measurements of brown carbon in water and methanol extracts and estimates of their contribution to ambient fine-particle light absorption. In: Atmos. Chem. Phys. 13 (24), p. 12389–12404. DOI: 10.5194/acp-13-12389-2013.

Liu, Jiu-Meng; Du, Zhen-yu; Liang, Lin-Lin; Yu, Qin-Qin; Shen, Guo-Feng; Ma, Yong-liang et al. (2019): Uncertainties in thermal-optical measurements of black carbon: Insights from source and ambient samples. In: The Science of the total environment 656, p. 239–249. DOI: 10.1016/j.scitotenv.2018.11.353.

Liu, Mingxu; Matsui, Hitoshi (2021): Aerosol radiative forcings induced by substantial changes in anthropogenic emissions in China from 2008 to 2016. In: Atmos. Chem. Phys. 21 (8), p. 5965–5982. DOI: 10.5194/acp-21-5965-2021.

Mamakos, Athanasios; Khalek, Imad; Giannelli, Robert; Spears, Matthew (2013): Characterization of Combustion Aerosol Produced by a Mini-CAST and Treated in a Catalytic Stripper. In: Aerosol Science and Technology 47 (8), p. 927–936. DOI: 10.1080/02786826.2013.802762.

Mesquita, Sofia R.; van Drooge, Barend L.; Dall'Osto, Manuel; Grimalt, Joan O.; Barata, Carlos; Vieira, Natividade et al. (2017): Toxic potential of organic constituents of submicron particulate matter (PM1) in an urban road site (Barcelona). In: Environmental science and pollution research international 24 (18), p. 15406–15415. DOI: 10.1007/s11356-017-9201-4.

Michelsen, Hope A.; Colket, Meredith B.; Bengtsson, Per-Erik; D'Anna, Andrea; Desgroux, Pascale; Haynes, Brian S. et al. (2020): A Review of Terminology Used to Describe Soot Formation and Evolution under Combustion and Pyrolytic Conditions. In: ACS nano 14 (10), p. 12470–12490. DOI: 10.1021/acsnano.0c06226.

Moore, Richard H.; Ziemba, Luke D.; Dutcher, Dabrina; Beyersdorf, Andreas J.; Chan, Kevin; Crumeyrolle, Suzanne et al. (2014): Mapping the Operation of the Miniature Combustion Aerosol Standard (Mini-CAST) Soot Generator. In: Aerosol Science and Technology 48 (5), p. 467–479. DOI: 10.1080/02786826.2014.890694.

Nakayama, Tomoki; Matsumi, Yutaka; Sato, Kei; Imamura, Takashi; Yamazaki, Akihiro; Uchiyama, Akihiro (2010): Laboratory studies on optical properties of secondary organic aerosols generated during the photooxidation of toluene and the ozonolysis of α -pinene. In: J. Geophys. Res. 115 (D24). DOI: 10.1029/2010JD014387.

Naumer, Hans; Heller, Wolfgang (Hg.) (1997): Untersuchungsmethoden in der Chemie. Einführung in die moderne Analytik. 3., erw. und neubearb. Aufl. Weinheim: Wiley-VCH.

Online: http://onlinelibrary.wiley.com/book/10.1002/9783527630929.

Oeser, Thomas (2019): Kristallstrukturanalyse durch Röntgenbeugung. Spektroskopiekurs kompakt. Wiesbaden: Springer.

Ofner, J.; Krüger, H.-U.; Zetzsch, C. (2010): Time Resolved Infrared Spectroscopy of Formation and Processing of Secondary Organic Aerosol. In: Zeitschrift für Physikalische Chemie 224 (7-8), p. 1171–1183. DOI: 10.1524/zpch.2010.6146.

Okada, Kikuo; Hitzenberger, Regina M. (2001): Mixing properties of individual submicrometer aerosol particles in Vienna. In: Atmospheric Environment 35 (32), p. 5617–5628. DOI: 10.1016/S1352-2310(01)00126-1.

Panteliadis, P.; Hafkenscheid, T.; Cary, B.; Diapouli, E.; Fischer, A.; Favez, O. et al. (2015): ECOC comparison exercise with identical thermal protocols after temperature offset correction – instrument diagnostics by in-depth evaluation of operational parameters. In: Atmos. Meas. Tech. 8 (2), p. 779–792. DOI: 10.5194/amt-8-779-2015.

Park, Jae Sung; Choi, Chang Kyoung; D. Kihm, Kenneth (2004): Optically sliced micro-PIV using confocal laser scanning microscopy (CLSM). In: Exp Fluids 37 (1), p. 105–119. DOI: 10.1007/s00348-004-0790-6.

Pavlovic, J.; Kinsey, J. S.; Hays, M. D. (2014): The influence of temperature calibration on the OC–EC results from a dual-optics thermal carbon analyzer. In: *Atmospheric Measurement Techniques* 7 (9), p. 2829–2838. DOI: 10.5194/amt-7-2829-2014.

Pawlyta, Mirosława; Hercman, Helena (2016): Transmission electron microscopy (TEM) as a tool for identification of combustion products: application to black layers in speleothems. In: ASGP. DOI: 10.14241/asgp.2016.004.

Petzold, A.; Ogren, J. A.; Fiebig, M.; Laj, P.; Li, S.-M.; Baltensperger, U. et al. (2013): Recommendations for reporting "black carbon" measurements. In: Atmos. Chem. Phys. 13 (16), p. 8365–8379. DOI: 10.5194/acp-13-8365-2013.

Piazzalunga, A.; Bernardoni, V.; Fermo, P.; Valli, G.; Vecchi, R. (2011): Technical Note: On the effect of water-soluble compounds removal on EC quantification by TOT analysis in urban aerosol samples. In: Atmos. Chem. Phys. 11 (19), p. 10193–10203. DOI: 10.5194/acp-11-10193-2011.

Pierce, J. R.; Chen, K.; Adams, P. J. (2007): Contribution of primary carbonaceous aerosol to cloud condensation nuclei: processes and uncertainties evaluated with a global aerosol microphysics model. In: Atmos. Chem. Phys. 7 (20), p. 5447–5466. DOI: 10.5194/acp-7-5447-2007.

Pöschl, Ulrich (2005): Atmospheric aerosols: Composition, transformation, climate and health effects. In: Angewandte Chemie (International ed. in English) 44 (46), p. 7520–7540. DOI: 10.1002/anie.200501122.

Pratt, Kerri A.; Prather, Kimberly A. (2010): Aircraft measurements of vertical profiles of aerosol mixing states. In: Journal of Geophysical Research 115 (D11), p. 3131. DOI: 10.1029/2009JD013150.

Putaud, Jean-P; Raes, Frank; van Dingenen, Rita; Brüggemann, Erika; Facchini, M.-Cristina; Decesari, Stefano et al. (2004): A European aerosol phenomenology—2: chemical characteristics of particulate matter at kerbside, urban, rural and background sites in Europe. In: *Atmospheric Environment* 38 (16), p. 2579–2595. DOI: 10.1016/j.atmosenv.2004.01.041.

Reisinger, P.; Wonaschütz, A.; Hitzenberger, R.; Petzold, A.; Bauer, H.; Jankowski, N. et al. (2008): Intercomparison of Measurement Techniques for Black or Elemental Carbon Under Urban Background Conditions in Wintertime: Influence of Biomass Combustion. In: Environ. Sci. Technol. 42 (3), p. 884–889. DOI: 10.1021/es0715041.

Sadezky, A.; Muckenhuber, H.; Grothe, H.; Niessner, R.; Pöschl, U. (2005): Raman microspectroscopy of soot and related carbonaceous materials: Spectral analysis and structural information. In: Carbon 43 (8), p. 1731–1742. DOI: 10.1016/j.carbon.2005.02.018.

Sahu, V.; Shekhar. S.; Ahuja, P.; Gupta, G.; Singh, S. K.; Sharma, R. K.; Singh, G. (2013): Synthesis of hydrophilic carbon black; role of hydrophilicity in maintaining the hydration level and protonic conduction. In: RSC Adv. 3 (12), p. 3917–3924. DOI: 10.1039/C3RA23136D.

Saleh, R.; Hennigan, C. J.; McMeeking, G. R.; Chuang, W. K.; Robinson, E. S.; Coe, H. et al. (2013): Absorptivity of brown carbon in fresh and photo-chemically aged biomass-burning emissions. In: Atmos. Chem. Phys. 13 (15), p. 7683–7693. DOI: 10.5194/acp-13-7683-2013.

Schmidl, Christoph; Bauer, Heidi; Dattler, Astrid; Hitzenberger, Regina; Weissenboeck, Gerlinde; Marr, Iain L.; Puxbaum, Hans (2008): Chemical characterisation of particle emissions from burning leaves. In: Atmospheric Environment 42 (40), p. 9070–9079. DOI: 10.1016/j.atmosenv.2008.09.010.

Schnaiter, M.; Gimmler, M.; Llamas, I.; Linke, C.; Jäger, C.; Mutschke, H. (2006): Strong spectral dependence of light absorption by organic carbon particles formed by propane combustion. In: *Atmospheric Chemistry and Physics* 6 (10), p. 2981–2990. DOI: 10.5194/acp-6-2981-2006

Sommer, Eva (2020): Current and historical soot particle concentrations in the Vienna urban aerosol. Master Thesis. University of Vienna, Vienna.

Spracklen, D. V.; Carslaw, K. S.; Pöschl, U.; Rap, A.; Forster, P. M. (2011): Global cloud condensation nuclei influenced by carbonaceous combustion aerosol. In: *Atmos. Chem. Phys.* 11 (17), p. 9067–9087. DOI: 10.5194/acp-11-9067-2011.

Subramanian, Ramachandran; Khlystov, Andrey Y.; Robinson, Allen L. (2006): Effect of Peak Inert-Mode Temperature on Elemental Carbon Measured Using Thermal-Optical Analysis. In: Aerosol Science and Technology 40 (10), p. 763–780. DOI: 10.1080/02786820600714403.

Sullivan, A. P.; Weber, R. J.; Clements, A. L.; Turner, J. R.; Bae, M. S.; Schauer, J. J. (2004): A method for on-line measurement of water-soluble organic carbon in ambient aerosol particles: Results from an urban site. In: Geophys. Res. Lett. 31 (13). DOI: 10.1029/2004GL019681.

Sun, Haolin; Biedermann, Laura; Bond, Tami C. (2007): Color of brown carbon: A model for ultraviolet and visible light absorption by organic carbon aerosol. In: *Geophysical Research Letters* 34 (17), p. 3131. DOI: 10.1029/2007GL029797.

Sun, Jianzhong; Zhi, Guorui; Hitzenberger, Regina; Chen, Yingjun; Tian, Chongguo; Zhang, Yayun et al. (2017): Emission factors and light absorption properties of brown carbon from household coal combustion in China. In: Atmos. Chem. Phys.

Sze, S. K.; Siddique, N.; Sloan, J. J.; Escribano, R. (2001): Raman spectroscopic characterization of carbonaceous aerosols. In: *Atmospheric Environment* 35 (3), p. 561–568. DOI: 10.1016/S1352-2310(00)00325-3.

Török, Sandra; Malmborg, Vilhelm B.; Simonsson, Johan; Eriksson, Axel; Martinsson, Johan; Mannazhi, Manu et al. (2018): Investigation of the absorption Ångström exponent and its relation to physicochemical properties for mini-CAST soot. In: *Aerosol Science and Technology* 52 (7), p. 757–767. DOI: 10.1080/02786826.2018.1457767.

Tuccella, Paolo; Pitari, Giovanni; Colaiuda, Valentina; Raparelli, Edoardo; Curci, Gabriele (2021): Present-day radiative effect from radiation-absorbing aerosols in snow. In: *Atmos. Chem. Phys.* 21 (9), p. 6875–6893. DOI: 10.5194/acp-21-6875-2021.

Tuinstra, F.; Koenig, J. L. (1970): Raman Spectrum of Graphite. In: The Journal of Chemical Physics 53 (3), p. 1126–1130. DOI: 10.1063/1.1674108.

Umweltbundesamt online, https://www.umweltbundesamt.de/dokument/datenbank-kraftwerke-in-deutschland, last access 20.05.2021

Uy, Dairene; Ford, Monica A.; Jayne, Douglas T.; O'Neill, Ann E.; Haack, Larry P.; Hangas, Jon et al. (2014): Characterization of gasoline soot and comparison to diesel soot: Morphology, chemistry, and wear. In: Tribology International 80, p. 198–209. DOI: 10.1016/j.triboint.2014.06.009.

Valencia, Sebastian; Ruiz, Sebastián; Manrique, Javier; Celis, Cesar; Figueira da Silva, Luís Fernando (2021): Soot modeling in turbulent diffusion flames: review and prospects. In: *J Braz. Soc. Mech. Sci. Eng.* 43 (4). DOI: 10.1007/s40430-021-02876-y.

Volkamer, Rainer; Jimenez, Jose L.; San Martini, Federico; Dzepina, Katja; Zhang, Qi; Salcedo, Dara et al. (2006): Secondary organic aerosol formation from anthropogenic air pollution: Rapid and higher than expected. In: *Geophys. Res. Lett.* 33 (17), p. 4407. DOI: 10.1029/2006GL026899.

Wang, Hai (2011): Formation of nascent soot and other condensed-phase materials in flames. In: Proceedings of the Combustion Institute 33 (1), p. 41–67. DOI: 10.1016/j.proci.2010.09.009.

Wang, Y.; Chung, A.; Paulson, S. E. (2010): The effect of metal salts on quantification of elemental and organic carbon in diesel exhaust particles using thermal-optical evolved gas analysis. In: *Atmospheric Chemistry and Physics* 10 (23), p. 11447–11457. DOI: 10.5194/acp-10-11447-2010.

Witek, Lorenz (2017): Charakterisierung von CAST Ruß bezüglich seiner optischen und hygroskopischen Eigenschaften. Master thesis, University of Vienna, Vienna.

WKO, Mineralölindustrie: https://www.wko.at/branchen/industrie/mineraloelindustrie/statistik.html, last access: 17 June 2021.

Wonaschuetz, Anna; Hitzenberger, Regina; Bauer, Heidi; Pouresmaeil, Parissa; Klatzer, Barbara; Caseiro, Alexandre; Puxbaum, Hans (2009): Application of the Integrating Sphere Method to Separate the Contributions of Brown and Black Carbon in Atmospheric Aerosols. In: Environ. Sci. Technol. 43 (4), p. 1141–1146. DOI: 10.1021/es8008503.

Wonaschuetz, Anna; Haller, Theresa; Sommer, Eva; Witek, Lorenz; Grothe, Hinrich; Hitzenberger, Regina (2019): Collection of soot particles into aqueous suspension using a particle-into-liquid sampler. In: Aerosol Science and Technology 53 (1), p. 21–28. DOI: 10.1080/02786826.2018.1540859.

Yang, Hong; Yu, Jian Zhen (2002): Uncertainties in charring correction in the analysis of elemental and organic carbon in atmospheric particles by thermal/optical methods. In: *Environmental science & technology* 36 (23), p. 5199–5204. DOI: 10.1021/es025672z.

Yang, Hong; Yu, Jian Zhen (2002): Uncertainties in charring correction in the analysis of elemental and organic carbon in atmospheric particles by thermal/optical methods. In: *Environmental science & technology* 36 (23), p. 5199–5204. DOI: 10.1021/es025672z.

Ye, Qing; Gu, Peishi; Li, Hugh Z.; Robinson, Ellis S.; Lipsky, Eric; Kaltsonoudis, Christos et al. (2018): Spatial Variability of Sources and Mixing State of Atmospheric Particles in a Metropolitan Area. In: Environmental Science & Technology 52 (12), p. 6807–6815. DOI: 10.1021/acs.est.8b01011.

Yttri, K. E.; Aas, W.; Bjerke, A.; Cape, J. N.; Cavalli, F.; Ceburnis, D. et al. (2007): Elemental and organic carbon in PM10: a one year measurement campaign within the European Monitoring and Evaluation Programme EMEP. In: Atmos. Chem. Phys. 7 (22), p. 5711–5725. DOI: 10.5194/acp-7-5711-2007.

Yu, Jian Zhen; Xu, Jinhui; Yang, Hong (2002): Charring characteristics of atmospheric organic particulate matter in thermal analysis. In: *Environmental science & technology* 36 (4), p. 754–761. DOI: 10.1021/es015540q.

Yu, Jian Zhen; Xu, Jinhui; Yang, Hong (2002): Charring Characteristics of Atmospheric Organic Particulate Matter in Thermal Analysis. In: Environ. Sci. Technol. 36 (4), p. 754–761. DOI: 10.1021/es015540q.

Zhang, Guohua; Bi, Xinhui; He, Junjie; Chen, Duohong; Lo Chan, Yin; Xie, Guangwu et al. (2014): Variation of secondary coatings associated with elemental carbon by single particle analysis. In: Atmospheric Environment 92, p. 162–170. DOI: 10.1016/j.atmosenv.2014.04.018.

Zhang, Q.; Worsnop, D. R.; Canagaratna, M. R.; Jimenez, J. L. (2005): Hydrocarbon-like and oxygenated organic aerosols in Pittsburgh: insights into sources and processes of organic aerosols. In: *Atmos. Chem. Phys.* 5 (12), p. 3289–3311. DOI: 10.5194/acp-5-3289-2005.

Zhang, Xiao; Wang, Hong; Che, Hui-Zheng; Tan, Sai-Chun; Yao, Xiu-Ping; Peng, Yue; Shi, Guang-Yu (2021): Radiative forcing of the aerosol-cloud interaction in seriously polluted East China and East China Sea. In: *Atmospheric Research* 252, p. 105405. DOI: 10.1016/j.atmosres.2020.105405.

Zhang, Xiaolu; Trzepla, Krystyna; White, Warren; Raffuse, Sean; Hyslop, Nicole Pauly (2021): Intercomparison of thermal–optical carbon measurements by Sunset and Desert Research Institute (DRI) analyzers using the IMPROVE_A protocol. In: *Atmos. Meas. Tech.* 14 (5), p. 3217–3231. DOI: 10.5194/amt-14-3217-2021.

Zhao, Dandan; Xin, Jinyuan; Gong, Chongshui; Quan, Jiannong; Wang, Yuesi; Tang, Guiqian et al. (2021): The impact threshold of the aerosol radiative forcing on the boundary layer structure in the pollution region. In: *Atmos. Chem. Phys.* 21 (7), p. 5739–5753. DOI: 10.5194/acp-21-5739-2021.

Zhao, Gang; Li, Fei; Zhao, Chunsheng (2020): Determination of the refractive index of ambient aerosols. In: *Atmospheric Environment* 240, p. 117800. DOI: 10.1016/j.atmosenv.2020.117800.

Zickler, Gerald A.; Smarsly, Bernd; Gierlinger, Notburga; Peterlik, Herwig; Paris, Oskar (2006): A reconsideration of the relationship between the crystallite size La of carbons determined by X-ray diffraction and Raman spectroscopy. In: Carbon 44 (15), p. 3239–3246. DOI: 10.1016/j.carbon.2006.06.029.

11. Publication 1

This chapter was published on 2 July 2019 in the Journal Atmospheric Measurement Techniques.

Atmos. Meas. Tech., 12, 3503–3519, 2019
https://doi.org/10.5194/amt-12-3503-2019

Structural changes of CAST soot during a thermal–optical measurement protocol

Theresa Haller[1], Christian Rentenberger[1], Jannik C. Meyer[1], Laura Felgitsch[2], Hinrich Grothe[2], and Regina Hitzenberger[1]

[1]Faculty of Physics, University of Vienna, Vienna, 1090, Austria

[2]Institute of Materials Chemistry, TU Wien, Vienna, 1060, Austria

Correspondence: Regina Hitzenberger (regina.hitzenberger@univie.ac.at)

Received: 8 January 2019 – Discussion started: 11 February 2019

Revised: 7 May 2019 – Accepted: 9 May 2019 – Published: 2 July 2019

Abstract. Thermal–optical measurement techniques are widely used to classify carbonaceous material. The results of different methods for total carbon are comparable but can vary by > 44% for elemental carbon. One major cause of variation is the formation of pyrolyzed carbon during the heating process which occurs mainly in samples with a high amount of brown carbon (BrC). In this study the structural changes of two different CAST (combustion aerosol standard) aerosol samples caused by the heating procedure in a thermal–optical instrument were investigated with UV–VIS and Raman spectroscopy, the integrating-sphere technique (IS) and transmission electron microscopy. All analysis techniques showed significant structural changes for BrC-rich samples at the highest temperature level (870°C) in helium. The structure of the heated BrC-rich sample resembles the structure of an unheated BrC-poor sample. Heating the BrCrich sample to 870°C increases the graphitic domain size within the material from 1.6 to 2nm. Although the Raman spectra unambiguously show this increase in ordering only at the highest temperature step, UV–VIS and IS analyses show a continuous change in the optical properties also at lower temperatures. The sample with a negligible amount of BrC, however, did not show any significant structural changes during the whole heating procedure.

1 Introduction

Carbonaceous material contributes a large amount to atmospheric aerosols from 20% of alpine $PM_{2.5}$ up to 40% of urban $PM_{2.5}$ (Pöschl, 2005) and up to 50% in PM_{10} (Yttri et al., 2007). Major sources include incomplete combustion of fossil and biogenic fuels, emission of primary particles by the biosphere, and gas-to-particle conversion of precursor gases emitted by the biosphere or anthropogenic activities (IPCC, 2013; Després et al., 2012; Zhu et al., 2018; McNeill, 2017). Carbon-containing aerosols influence the global radiation balance due to their optical properties and their capability to act as cloud condensation nuclei and ice-nucleating particles. In particular, black carbon (BC) has an important effect on radiative forcing as it has the strongest light absorption of all aerosol components (Bond and Bergstrom, 2006; IPCC, 2013). Carbonaceous material has also been found to cause various deleterious health effects (Highwood and Kinnersley, 2006; Anderson et al., 2012; Mesquita et al., 2017; EEA, 2017; Partanen et al., 2018; Rohr and McDonald, 2015).

Depending on its origin carbonaceous material ranges from agglomerations of primary spherical particles with a graphitic-like internal structure to non-ordered organic material. While primary carbonaceous particles produced under well-defined combustion conditions are rather homogeneous, real-atmosphere carbonaceous particles are internal mixtures of different carbonaceous and non-carbonaceous materials of various origins (e.g., Okada and Hitzenberger, 2001; Zhang et al., 2014; Ye et al., 2018; IPCC, 2013; Deboudt et al.,2010; Pratt and Prather, 2010; Bondy et al., 2018; Adachi et al., 2010; Adachi and Buseck, 2013; China et al., 2013; Cappa et al., 2012). As carbonaceous aerosol material plays such an important role and is so diverse, the correct determination of carbonaceous fractions in the aerosol is essential. However, this endeavor is not trivial because measurement techniques are influenced not only by the properties of the material itself, but also by the non-carbonaceous materials associated with the particles and their mixing state.

During the past decades, numerous methods were developed, and intercomparison studies of different methods applied to both laboratory-generated and ambient aerosol were performed, which showed similarities and discrepancies of the results of different methods depending on sources and aerosol constituents (see, e.g., the overviews given by Watson et al., 2005; Venkatachari et al., 2006; Müller et al., 2004).

Analysis techniques can be grouped broadly into optical techniques, which utilize light absorption and its wavelength dependence, and thermal techniques, which separate the material based on its thermal properties. Another distinction can be made between filter-based techniques and techniques that analyze airborne particles in situ, such as photoacoustic spectrometry (e.g., Arnott et al., 1999; Moosmüller et al., 1998) and the SP2 instrument (e.g., Stephens et al., 2003; Schwartz et al., 2006). Usually, the term black carbon (BC) is used for the carbonaceous fraction with high light absorption in the whole visible wavelength range, and brown carbon (BrC) is used for the carbonaceous fraction with a pronounced wavelength-dependent absorption with high absorption in the blue and weak absorption in the red part of the spectrum (Petzold et al., 2013). Thermal techniques separate carbonaceous material into organic carbon (OC, thermally unstable) and elemental carbon (EC, thermally refractory). The latter oxidizes in air at temperatures above 600°C (Andreae and Gelencsér, 2006) and does not evaporate in the absence of oxygen below fairly high temperatures (the definitions range from 550°C, Bond and Bergstrom, 2006; to 700°C, Chow et al., 2004). EC and BC are often loosely used as synonymous, as both are strongly light absorbing, although the terms are not the same since EC is defined by thermal and BC by optical properties of the material (Buseck et al., 2014; Petzold et al.,

2013). The comparability of BC and/or EC values measured with different techniques depends on the composition of the aerosol and the measurement method (Cheng et al., 2012; Cavalli et al., 2010). Optically determined BrC is a subfraction of thermally determined OC and originates mainly from combustion of biomass or biofuels (Mayol-Bracero, 2002; Hoffer et al., 2006; Schmidl et al., 2008; Park et al., 2018; Fan et al., 2016; Park and Yu, 2016; Sun et al., 2017). The thermal and optical behavior of carbonaceous material is caused by its internal structure (i.e., chemical composition, ordering and bonding types). As outlined by Pöschl (2005) there is no sharp boundary between the thermally unstable OC and EC but a continuous transition from organic carbon to elemental carbon in terms of structure as well as of thermal and optical properties: the higher the degree of graphitization, the higher the thermal stability and the broader the wavelength range of light absorption are.

In order to account for pyrolyzation of OC during the heating process used in the thermal techniques, thermal–optical techniques were developed. In these techniques the sample is heated stepwise first in an inert He atmosphere to a maximum temperature, which depends on the measurement protocol (see below), and then oxygen is added to the carrier gas and the sample is further heated. The amount of carbon leaving the filter at each temperature step is detected. The darkening of the sample due to pyrolysis is traced by monitoring a transmission/reflection laser signal. After the addition of oxygen both the originally present EC and the pyrolyzed carbon (PC) are oxidized during the successive heating steps. All carbon leaving the filter until the laser signal has reached its original value is assumed to originate from PC and is attributed to the OC fraction in the subsequent evaluation.

The crucial assumption for this laser correction is that either PC has the same molecular structure as the original EC or that PC burns off completely before EC is oxidized. None of these conditions is fulfilled, as was shown by Yu and Yang (2002), who found that in many cases the light absorption coefficient (σ) of the two fractions is not the same at least at the wavelength used in their thermal–optical instrument (680nm). Moreover, the value of σ of PC is not constant even during a single thermal analysis. This uncertainty in accounting for PC leads to uncertainties in the OC/EC split, which is the subject of numerous instrument intercomparison studies (see, e.g., the overview given by Cavalli et al., 2010).

Different thermal–optical measurement protocols vary in height and duration of the individual temperature steps, particularly in the maximum temperature of the inert (He) mode – maximum temperatures between 580°C (IMPROVE A, Chow et al., 2004) and 870°C (NIOSH870, Panteliadis et al., 2015; Birch and Cary, 1996). This leads to different charring behaviors of OC. As a consequence the OC/EC split varies with the temperature protocol, while the total carbon (TC, i.e., the sum of OC; EC; and, if present, carbonate carbon) values usually are quite comparable. Different thermal methods agree within 5%–15% in the amount of TC but vary up to 44% for EC (Reisinger et al., 2008; Cavalli et al., 2010; Yu and Yang, 2002; Cheng et al., 2012; Hitzenberger et al., 2006; Panteliadis et al., 2015).

The largest discrepancies between thermal–optical methods applied to atmospheric samples occur in the presence of appreciable amounts of BrC (e.g., Wonaschütz et al., 2009; Reisinger et al., 2008). Kim et al. (2015) compared OC and EC values obtained with two different thermal–optical protocols (NIOSH and EUSAAR) for laboratory-generated soot from propane combustion (produced by a miniCAST burner). For EC/TC ratios > 0.5, the differences of EC/TC between both methods were below 15%. For lower EC/TC ratios when significant amounts of BrC (measured with an optical method) were present, larger differences (30%) are noticeable.

Besides the presence of BrC, metal salts were also found to affect the OC/EC split in thermal–optical methods by enhancing the charring of OC and/or by reducing the oxidation temperature of EC (Wang et al., 2010; Bladt et al., 2014).

The aim of the present study was to shed more light on the processes which lead to the discrepancies between measurement methods using different thermal–optical protocols. The formation of PC during thermal–optical measurements is not yet fully understood. The purpose was to investigate the structural changes of carbonaceous aerosol samples occurring during pyrolysis. In order to exclude the effects of other, non-carbonaceous material on the charring process, the structure of two different types of laboratory-generated soot – one with a high tendency to form PC and one with a negligible tendency to form PC – was analyzed in different stages of pyrolyzation in order to obtain more information about the internal structure of PC and its differences or analogies to the structure of EC. A thermal–optical EC–OC analyzer (Sunset Instruments Inc.; see description below) was used not only for the analysis of these soot samples but also as a means for sample preparation in order to obtain pyrolyzed samples from each heating step that had been exposed to the same atmospheres, heating rates and temperature plateaus as during the thermal–optical analysis. This approach permits an investigation of the structural changes of the material as they occur during the thermal–optical heating procedure. Although charring of organic material has also been observed in SP2 measurements (Sedlacek et al., 2018), the present study is focussed on the processes occurring in filter samples.

2 Properties of soot

2.1 Structure of soot

The general term soot is usually used for particulate products of incomplete combustion or pyrolysis of fossil fuels or organic materials (Andreae and Gelencsér, 2006; Pöschl, 2005; Bond and Bergstrom, 2006).

The structure of soot depends on the fuel and on the combustion conditions. Soot produced under oxygen-rich combustion conditions and high temperatures consists of agglomerated primary particles with sizes between 10 and 30nm (Sadezky et al., 2005). The primary particles consist of onion-like turbostratically ordered graphitic layers. The graphitic domains typically include 3–4 graphene layers and have an extent of about 3nm with interlayer distances of about 3.5Å (Sadezky et al., 2005), which is larger than the interlayer distance of an ideal graphitic lattice (3.35Å) because of the turbostratic arrangement. The atoms in graphitic-like material are bound with π bonds, which form conjugated systems and hence long-range orbitals. As the optical gap is small (≈ 0.5eV for disordered graphitic layers; Robertson and O'Reilly, 1987), light from a broad spectral range is absorbed (Bond and Bergstrom, 2006; Chhowalla et al., 1997).

In contrast to this highly ordered type of soot, the molecular structure of BrC, which is formed under oxygen-poor and low-temperature combustion conditions, is similar to that of polycyclic hydrocarbons (PAH) or humic-like substances (HULIS) (Graber and Rudich, 2006; Sun et al., 2007). Due to the smaller expansion of the molecular orbitals there is a larger optical gap between the filled valence band and the unfilled conduction band, which leads to a decreasing absorption efficiency towards the long-wave part of the visible spectrum (Bond, 2001; Kim et al., 2015; Andreae and Gelencsér, 2006).

2.2 CAST soot

For the present study, a combustion aerosol standard burner (type miniCAST) was used to produce differently structured soot by varying the combustion conditions. A detailed description of the miniCAST burner is given below. Different fuel-to-air ratios in the flame lead to different compositions and structures of the produced particles. According to Kim et al. (2015) and Mamakos et al. (2013) the particles obtained under oxygen-rich settings are comparable to diesel exhaust aerosols. They show a high EC fraction and form relatively large fractal agglomerates with mobility diameters between 70 and 130nm, which are composed of small (25–30nm) spherical primary particles (Kim et al., 2015). Under oxygenpoor combustion conditions, spherical particles with sizes in the range 10–60nm and a low EC fraction (Kim et al., 2015) are formed. While soot from biomass burning contains also ionic components such as Na^+, NH_4^+, Ca^{2+}, Mg^{2+}, K^+, Cl^-, NO_3^- and SO_4^{2-} which could lead to catalysis effects in the thermal–optical analysis (Ichikawa and Naito, 2017; Wang et al., 2010), these compounds are negligible in soot produced by the CAST burner since only pure propane and air contribute to the combustion.

2.3 Basics of Raman spectroscopy of soot

Raman scattering has been used for the structural investigation of soot for several years (Rosen and Novakov, 1978; Sadezky et al., 2005; Ferrari and Robertson, 2000; Schmid et al., 2011; Knauer et al., 2009; Ivleva et al., 2007a, b). It is sensitive to different C–C bonding types (e.g., graphitic structures) in a material (Sadezky et al., 2005) and depends on the ordering of sp^2 sites (Ferrari and Robertson, 2000).

Ideal graphite shows a single peak at a Raman shift of ≈ 1580cm^{-1} (G peak or graphitic peak), which is related to the ideal hexagonal environment in the extended graphene layers (E_{2g} symmetry). For nonideal graphite, an additional peak at ≈ 1350cm^{-1} (D peak or defect peak) appears, which is due to impurities and/or smaller graphene layers and the thus increased number of layer edges. Due to the missing neighbor atoms at these edges, the symmetry of the C–C vibration is reduced to A_{1g}. When the ordering in the material decreases – which is the case in soot – the two formerly sharp peaks broaden and overlap (see also Figs. 5 and 6) as a consequence of more than two overlapping Raman bands. To separate the contributions of the bands, different authors suggest different curve-fitting methods with up to five signals with either Gaussian or Lorentzian shape (Dippel et al., 1999; Jawhari et al., 1995; Sze et al., 2001; Cuesta et al., 1994). A comparison study performed by Sadezky et al. (2005) found that a five-curve fit with four Lorentzian and one Gaussian curves represents most of their spectra best. The curve shapes, band positions and related vibration modes are listed in Table 1.

Table 1. Band positions and line shapes for the five fitting curves of soot Raman spectra (Sadezky et al., 2005).

Band	Shape	Position (cm^{-1})	Vibration mode
D1fit	Lorentzian	≈ 1360	Disordered graphitic lattice (A_{1g} symmetry), graphene layer edges
D2fit	Lorentzian	≈ 1620	Disordered graphitic lattice (E_{2g} symmetry), surface graphene layers
D3fit	Gaussian	≈ 1500	Amorphous carbon
D4fit	Lorentzian	≈ 1180	Disordered graphitic lattice (A_{1g} symmetry), polyenes, ionic impurities
*G*fit	Lorentzian	≈ 1580	Ideal graphitic lattice (E_{2g} symmetry)

The ratio of the intensities of the D and G peak (I_D/I_G) can be linked to the crystallite size (L_a) within the investigated material (Ferrari and Robertson, 2000; Tuinstra and Koenig, 1970). Ferrari and Robertson (2000) propose an increase in L_a with increasing I_D/I_G below $L_a \approx 2$nm. In this regime I_D/I_G is proportional to the probability to find 6-fold aromatic rings in the cluster (Ferrari and Robertson, 2000). For larger crystallite sizes I_D/I_G decreases with increase in L_a (Tuinstra and Koenig, 1970). I_D/I_G shows a maximum at $L_a \approx 2$nm but has a broad transition regime between the increasing and decreasing branch. Zickler et al. (2006) compare the I_D/I_G ratio of Raman spectra of charcoal obtained from spruce wood with the crystallite sizes obtained from X-ray diffraction and confirm the proposal of Ferrari and Robertson experimentally. Based on these findings, several authors (Commodo et al., 2016; Ess et al., 2016; Ivleva et al., 2007a, b) use increasing I_D/I_G ratios as criteria to detect an increasing degree of ordering in soot.

3 Experimental setup

For the production of well-defined combustion soot, a combustion aerosol standard soot generator (type miniCAST 5201C Jing-CAST Technologies, http://www.sootgenerator. com, last access: 7 June 2019) was used. In this burner, soot is produced in a propane and air co-flow diffusion flame which was quenched with nitrogen directly after the combustion zone in order to prevent further combustion processes. The particle flow is subsequently diluted with air. The burning conditions were varied by setting different air-to-fuel ratios to produce differently structured soot.

Prior to this study, samples were obtained for a variety of air-to-fuel ratios and analyzed for BC and BrC with the integrating-sphere technique (IS; see below). Based on these experiments, two different combustion conditions were chosen here to produce two types of soot: one representing a BrC-rich sample (“brown”) and the other a BrC-poor sample (“black”) (Table 2). The samples have a completely different morphology, as is shown below in Figs. 9 and 10.

For sampling, quartz fiber filters (Pall Tissuquartz 2500 QAT-UP, 47mm) were used. The filters had been prebaked at 450°C for an hour and stored for at least 24h in a water-vapor-saturated atmosphere before sampling to prevent adsorption of volatile organic substances during handling (Jankowski et al., 2008). The loaded filters were stored at −22°C except during analysis and further sample preparation (see below). The setup of the sampling system is shown in Fig. 1.

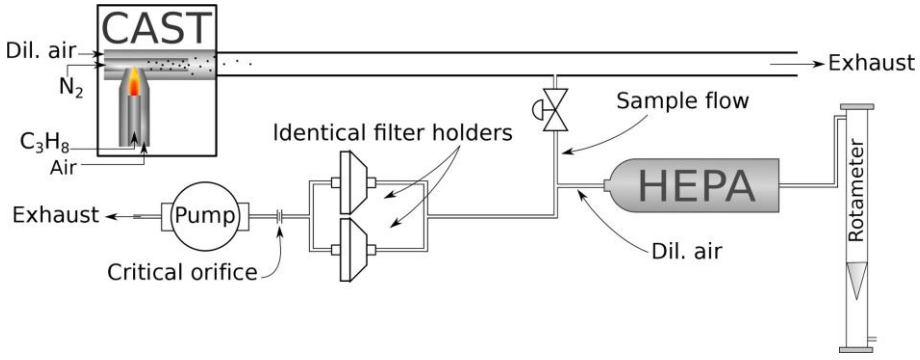

Figure 1. Setup of the sampling. Soot produced by the CAST generator is first diluted within the generator. The sample flow is drawn from the exit line of the CAST generator and further diluted with filtered air (dilution flow regulated with a needle valve and measured with a rotameter). Aerosol is sampled in parallel on filters placed in two identical filter holders. Total flow in the sampling line is regulated by a critical orifice (12.5Lmin−1).

Part of the exhaust stream of the miniCAST was diverted and drawn through two parallel filters placed in identical holders. The total flow in this sampling line was controlled by a critical orifice (12.5Lmin^{-1}). The aerosol flow was diluted with 5Lmin^{-1} air filtered with a HEPA (high-efficiency particulate air) filter,

except for samples to be analyzed with UV–VIS spectroscopy, where the flow had to be diluted with 6Lmin^{-1} air to prevent too-dark filter deposits. The dilution air was regulated with a needle valve and measured with a rotameter. For each of the following measurement techniques (UV–VIS, Raman spectroscopy, IS, TEM) a set of eight 1.5cm^2 filter punches was taken from the filters. For the preparation of the heated samples, the EC–OC analyzer (see description below) was programmed according to the NIOSH870 protocol and used as an oven. Each filter punch was inserted into the analyzer and underwent part of the NIOSH870 heating procedure, from the beginning to one of the first eight prescribed temperature levels (see Table 2).

Table 2. CAST burning conditions used for the black and the brown sample. The dilution air refers to the CAST internal dilution.

CAST burning conditions	Black	Brown
Propane	40mLmin^{-1}	50mLmin^{-1}
Oxidation air	1.04Lmin^{-1}	0.9Lmin^{-1}
Nitrogen	0	0
Dilution air	20Lmin^{-1}	10Lmin^{-1}
Quench gas (N_2)	7Lmin^{-1}	7Lmin^{-1}
C/O	0.275	0.397

At that point the automated heating procedure was interrupted and the oven cooled down to below 75°C in Helium. Then the punches where removed from the instrument and transferred directly into Petri dishes. The dishes were closed with Parafilm strips and stored at −22°C until the further measurements. This procedure was performed for four sets of filter punches to be analyzed with the different techniques.

4 Analysis techniques

4.1 Thermal–optical measurements

For the analysis of the filter samples and the heating of the samples a dual-optics EC–OC analyzer (Sunset Instruments Inc.) was used. In the first heating steps, the samples are heated in helium. In the second part of the analysis the samples are exposed to an oxidizing atmosphere consisting of 2% oxygen and 98% helium. Reflectance and transmittance signals of laser light (635nm) are used to monitor the darkening of the sample caused by pyrolysis during heating in the inert atmosphere. In this study, the NIOSH870 protocol was used. Temperature steps and residence times are listed in Table 3.

Table 3. Temperature steps and residence times for the NIOSH870 protocol (Panteliadis et al., 2015; Birch and Cary, 1996).

Carrier gas	Temperature (°C)	Residence time (s)
He	310	80
He	475	60
He	615	60
He	870	90
$He+O_2$	550	45
$He+O_2$	625	45
$He+O_2$	700	45
$He+O_2$	775	45
$He+O_2$	850	45
$He+O_2$	870	120

The NIOSH870 protocol was chosen here to investigate the structural changes of soot during pyrolysis, because of the strong charring occurring in the He mode at the high temperatures. The EUSAAR2 protocol (Cavalli et al., 2010), which is now used widely in the EU (Brown et al., 2017), minimizes charring and is therefore less suitable for the investigation of PC.

4.2 Integrating sphere (IS)

BC and BrC (often taken together as light-absorbing carbon,LAC) of the original and the heated samples were analyzed with an extension of the original integrating-sphere technique (described, e.g., by Hitzenberger and Tohno, 2001). In this technique, a sample (e.g., a filter punch) is immersed in a liquid and introduced into the center of an integrating sphere illuminated with diffuse light. In our study, a 15.24cm (6in.) integrating sphere (Labsphere, Inc.) coated internally with a nearly ideally diffusely reflective (> 99%) material (Spectraflect™) was used. Samples were immersed in a mixture of 10% isopropanol, 40% H_2O and 50% acetone in PE vials. Enhanced absorption caused by a possible coating effect is reduced: soluble coatings are removed from the particles and the effect of insoluble coatings is reduced because of the low relative refractive index of these coatings compared to the liquid (Hitzenberger and Tohno, 2001). In the extended technique (Wonaschütz et al., 2009) the sphere is illuminated with a halogen light source equipped with three interference filters (450, 550 and 650nm) and the wavelength-dependent light signal is recorded with a photodiode. The contributions of BC and BrC to the absorption signal are separated in an iterative procedure using calibration curves obtained with a proxy for BC (Elftex 124, Cabot Corp.) and a proxy for BrC (humic acid sodium salt, Acros Organics, no. 68131044).

4.3 Raman spectroscopy

In this study a confocal Raman microscope (Horiba Jobin Yvon LabRAM 800HR) was used. The Raman microscope was equipped with a 632.8nm HeNe laser (maximum output < 20mW) and a charge-coupled device (CCD) camera (Peltier cooled at −60°C). The laser beam was focused on the sample with a 20× magnification objective (CF Plan, 20×/0.35, WD 20.5mm, Nikon). The spectra were calibrated with the Rayleigh line at 0cm^{-1} and the silicon peak at 521cm^{-1}. The laser power was reduced to 10% for analyzing black samples and 25% for brown samples to prevent thermal destruction of the material. All instrument settings (grating 300 lines per mm, 3–4cm^{-1} resolution; confocal hole 1000µm; acquisition time 5s with 30 accumulations) were chosen after a set of test measurements to provide the best signal-to-noise ratio for the analysis. As the samples burned off partially at the 775°C temperature step in the EC– OC analyzer, the Raman spectra were recorded only for the first seven temperature steps.

The spectra were recorded in the range from 200 to 2000cm^{-1} at four measurement points at three positions for each sample to account for possible variations within a filter sample. The averaged spectra for each filter were analyzed using OriginPro2016, which has built-in functions for baseline correction. Baselines were fitted with a B-spline function based on approximately 20 anchor points. After subtraction of the baseline, the spectra were fitted with five curves (four Lorentzian, one Gaussian; see Table 1). As initial values for the fit, the band positions obtained by Sadezky et al. (2005) and listed above (Table 1) were used. The standard deviations of the mean spectra were used in the fitting software as weighting of the fit.

4.4 TEM – transmission electron microscopy

A 200kV transmission electron microscope (TEM) Philips CM200 equipped with a Gatan™ Orius CCD camera was used to analyze the nanostructure of the original and the heated samples. Single filter fibers were separated from the samples and placed onto holey carbon films or between copper grids to facilitate studying freestanding soot particles. High-resolution microscopic images and diffraction patterns of particles deposited at the lateral edges of the fibers were taken. Intensity profiles of the diffraction patterns were obtained by both azimuthal integration along rings and background correction using PASAD-tools (Gammer et al., 2010). For comparison a simulated profile of graphite was calculated with JEMS software (Stadelmann, 2004).

4.5 UV–VIS spectroscopy

A LAMBDA 750 UV–VIS spectrometer (PerkinElmer, Waltham, Massachusetts, US), equipped with a tungsten and a deuterium lamp, was used to measure the diffuse reflectance of the samples. Reflectance measurements were carried out from 800 to 200nm with an interval of 1nm. At 319.2nm the instrument switches from the tungsten (visible) to the deuterium (UV) lamp. For the measurement the original and heated samples were put into quartz vials without any liquid. The diffusely reflected light from the filter punches was collected with a 60mm integrating sphere and detected with a photomultiplier. Absorbance spectra where calculated with the Kubelka–Munk equation (Kubelka and Munk, 1931) from the measured reflectance spectra. Although the Kubelka–Munk theory was developed originally for powder samples, its applicability to aerosol filter samples was shown by Aryal et al. (2014).

Absorbance spectra were calculated from the measured reflection signals $R_\infty(\lambda)$ using the Kubelka–Munk function:

$$\text{K-M}(\lambda) = \frac{(1-R_\infty(\lambda))^2}{2R_\infty(\lambda)} \qquad (1)$$

where K-M(λ) is proportional to the absorbance, assuming infinite sample thickness. The spectra were corrected for background signals obtained from three filter blanks.

5 Results and discussion

5.1 Thermal–optical analysis

In the thermal–optical analysis most of the carbon of the black sample evolves in the He+O_2 phase. Throughout the successive heating steps, the laser reflectance signal remains relatively constant until EC oxidizes (Fig. 2). On the other hand, most of the carbon of the brown sample evolves in the He phase (Fig. 3). The laser reflectance signal decreases during the first three temperature steps, indicating a pyrolysis of the organic material. The signal starts to increase slightly at the last temperature step (870°C) in He and increases rapidly at 625°C after O_2 is added, indicating the combustion of initial EC and/or pyrolyzed OC (PC). The laser signal reaches its initial value at the end of the 700°C temperature step; therefore approximately half of the carbon signal in the oxidizing atmosphere is assigned to OC following the normal procedure of the thermal–optical analysis method. Results from EC and OC measurements are summarized in Table 3. Figures 2 and 3 show full thermograms of a black and a brown sample.

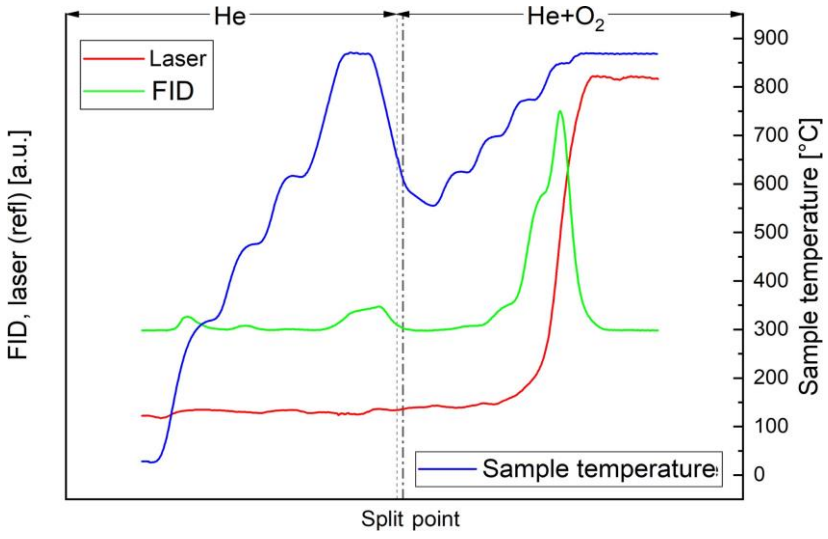

Figure 2. Thermogram of the black sample. The blue line is the temperature measured at the position of the sample, the red line the laser reflectance signal and the green line the signal of the flame ionization detector (FID), which is proportional to the amount of carbon leaving the filter. The split point was set at the point where the laser signal reached its initial value. The FID signal before the split point (broken line) is assigned to OC and after the split point to EC. The dotted line separates the inert and oxidizing phases.

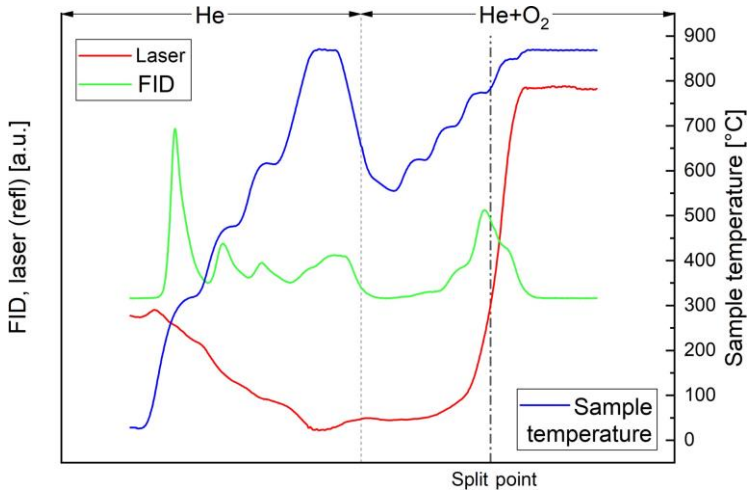

Figure 3. Thermogram of the brown sample. The blue line is the temperature measured at the position of the sample, the red line the laser reflectance signal and the green line the signal of the flame ionization detector (FID), which is proportional to the amount of carbon leaving the filter. The split point was set at the point where the laser signal reached its initial value. The FID signal before the split point (broken line) is assigned to OC and after the split point to EC. The dotted line separates the inert and oxidizing phases.

5.2 Black and brown carbon

Figure 4 shows the change in BC and BrC during the thermal–optical analysis. The changing BC content of the sample is qualitatively consistent with the interpretation of the laser signal in the thermal–optical analysis: BC in the black sample decreases somewhat during the whole analysis cycle, while BrC is below the detection limit for each temperature step.

For the brown sample, BrC decreases continuously during the whole He mode, while BC increases over the He mode up until 870°C (He) and decreases in the He+O_2 mode. These findings confirm that BC is built during the thermal–optical analysis of an organic-carbon-containing sample.

Table 4 summarizes the composition of the original brown and black samples regarding their EC, OC, BC and BrC content: the black sample consists mainly of EC or BC with a negligible amount of BrC. On the contrary, the brown sample contains only about 10% EC or BC and approximately 90% BrC.

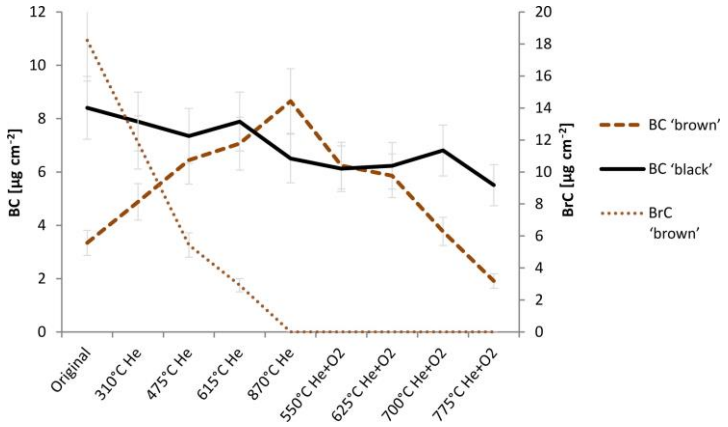

Figure 4. Change in BC and BrC measured with the IS method during heating according to the NOSH870 protocol measurement for the black and the brown sample. BC brown and BrC brown refer to the amount of BC and BrC of the brown sample; BC black refers to the amount of BC of the black sample. BrC of the black sample is below detection limit for the original and the heated samples, respectively. The error bars indicate deviations of ±14%. Laboratory intern test measurements gave variations in this range for filter samples measured in the integrating sphere.

Table 4. Results of thermal–optical and integrating-sphere measurements.

	Thermal–optical measurement	Integrating sphere method
	EC/TC	BC/LAC
Black	0.85	0.99
Brown	0.09	0.11

5.3 Raman spectra

The change in the Raman spectra due to the heating process in the thermal–optical instrument is shown in Figs. 5 and 6. For a better comparison the spectra are normalized to the maximum of the G peak. While the maxima of the D and G peak do not change for the black sample, the spectra of the brown sample show a relative increase in the D peak for samples heated at 870°C in He. The peak does not increase continuously over the whole heating process, which indicates a significant structural change especially at this temperature step. Following the interpretation of Ferrari and Robertson (2000) and its application to soot samples by Commodo et al. (2016), Ess et al. (2016) and Ivleva et al. (2007a, b), this increase in the D peak indicates an increased amount of polyaromatic rings in the sample which can be associated with a higher degree of ordering.

For a better comparison, the spectra of the black and brown original samples and samples heated to 870°C in He are shown in Fig. 7. The D peak of the brown heated sample reaches nearly the height of the D peak of the black original and heated samples.

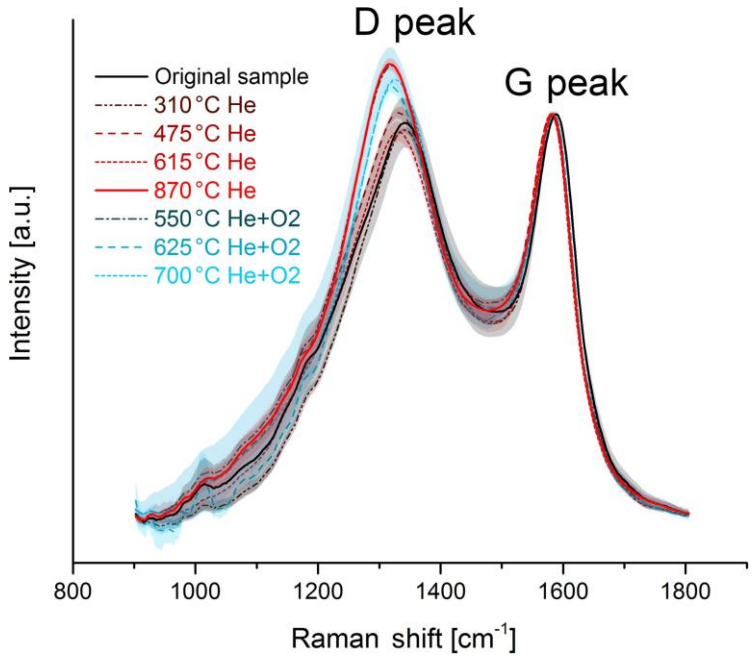

Figure 5. Raman spectra of the original and the heated brown sample. The black and red solid lines represent the original sample and the sample heated to 870°C in He, where a significant structural change occurs. The mean spectra are smoothed and normalized to the maximum of the G peak. The shaded areas represent the standard deviations of the mean spectra.

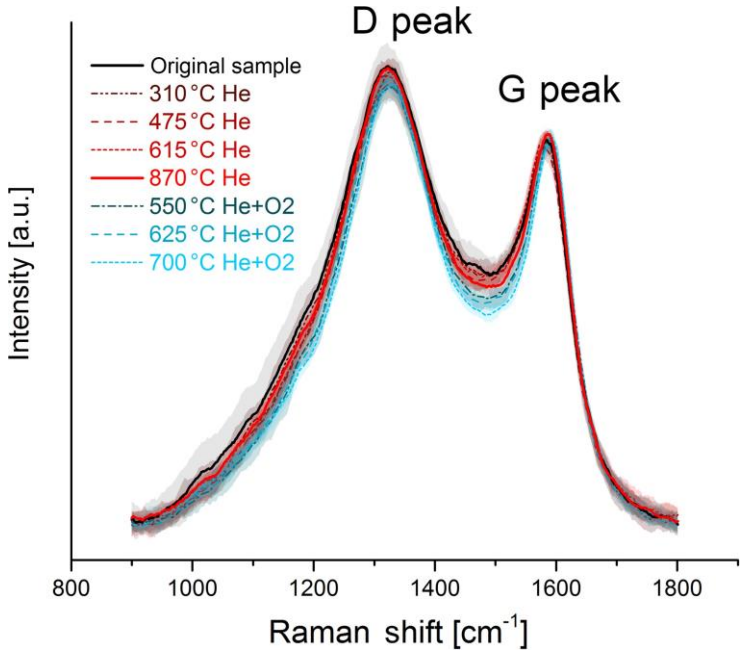

Figure 6. Raman spectra of the original and the heated black sample. The black and red solid lines represent the original sample and the sample heated to 870°C in He. In contrast to the spectra of the brown sample, no significant change in the D-peak height due to heating is visible here. The mean spectra are smoothed and normalized to the maximum of the G peak. The shaded areas represent the standard deviations of the mean spectra.

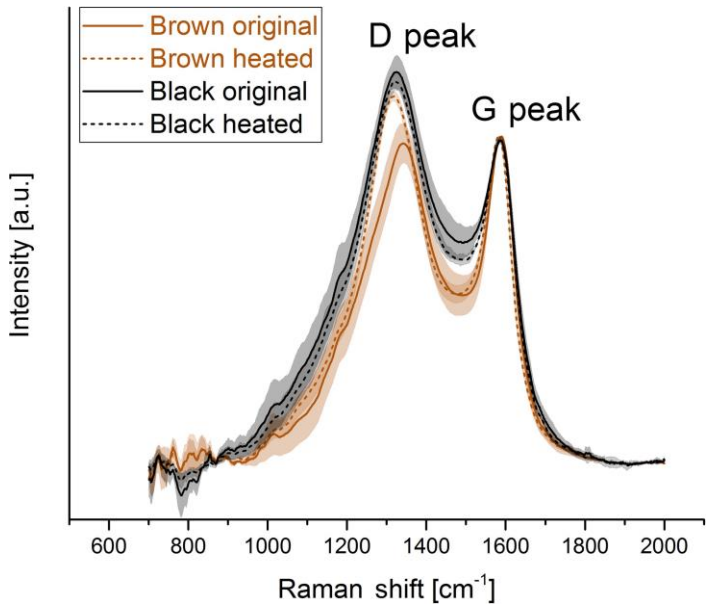

Figure 7. Comparison of the Raman spectra of the original and heated (870°C He) samples for the brown and the black sample. The D peak of the spectrum of the brown sample reaches the height of the D peak of the black sample when the sample is heated to 870°C in He.

Figure 8 shows the five-curve fits of these four spectra. All fits were performed on the smoothed and averaged versions of the spectra. It is obvious that there is no significant change in the five peaks between the original and heated black sample. However, the spectra of the brown sample show a significant change at the $D4_{fit}$ peak (≈ 1200cm^{-1}) and the $D1_{fit}$ peak (≈ 1350cm^{-1}), when the sample is heated to 870°C in He: while the $D4_{fit}$ peak (which is related to C=C double bonds, Sadezky et al., 2005) decreases, the $D1_{fit}$ peak (related to graphene layer edges, Sadezky et al., 2005) increases. This implies that the material in the heated sample contains fewer C=C double bonds and more graphene layer edges compared to the original brown sample.
Possible explanations could be a decomposition and evolution of molecules with C=C bonds (e.g., polyenes) and a coincident fragmentation of preexisting graphene layers or a transformation of molecules with C=C bonds into new small graphene layers. Both scenarios would lead to a higher amount of graphene layer edges (and an increased $D1_{fit}$ peak) and a lower amount of C=C bonds (and a decreased $D4_{fit}$ peak).

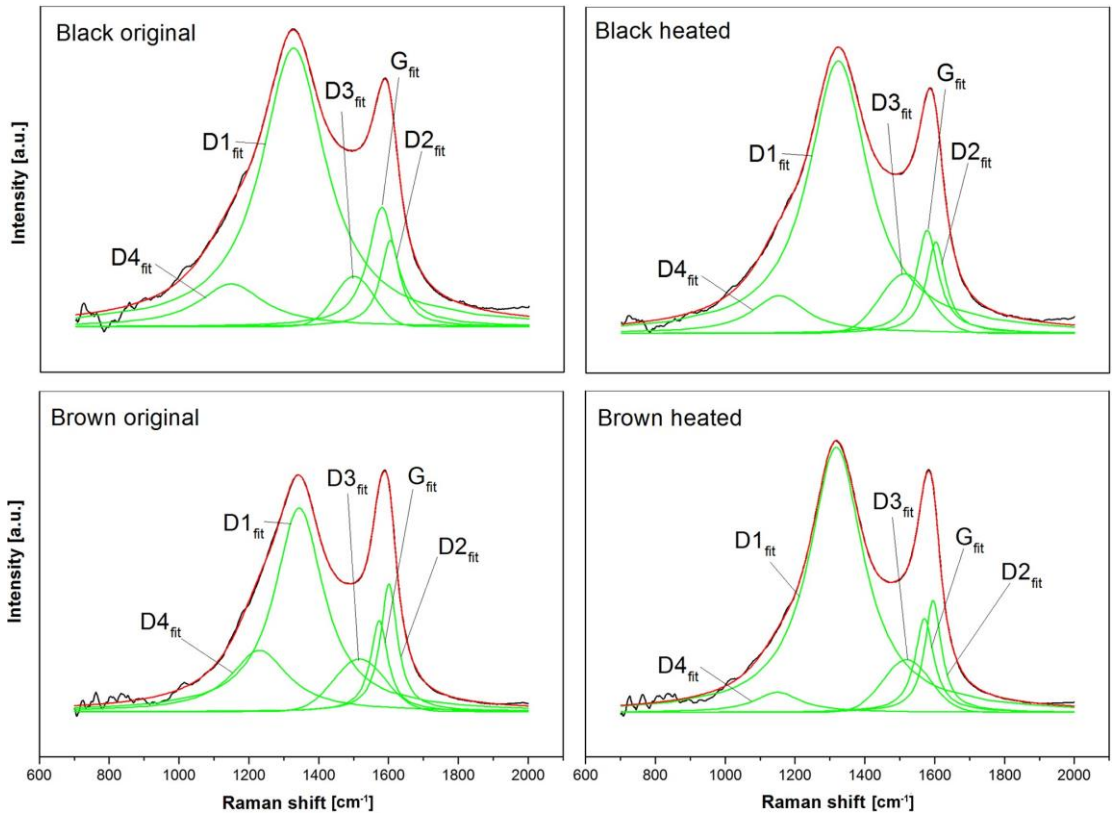

Figure 8. Five-curve fits of the original and heated (870°C He) spectra using the band positions and curve shapes of Sadezky et al. (2005). The black lines are the measured intensities, the green lines the five fitting curves (D1fit–D4fit and Gfit) and the red lines the fitted spectra. The fitted curves of the black sample are similar before and after heating, while the D1fit and D4fit of the brown sample change.

TEM images (see below) show that the ordering in the brown sample increases when it is heated to 870°C in He. The UV–VIS spectra (see below) show a decreasing absorption coefficient which requires a growth instead of a fragmentation of the conjugated orbitals in the material. Both findings are more consistent with the second process.

5.4 TEM – transmission electron microscopy

The TEM images of the black and brown samples show entirely different morphologies. The soot in the black sample consists of agglomerates of spherical primary particles with diameters of about 20nm (Fig. 9). The primary particles show an onion-like graphitic structure as it is also reported by Sadezky et al. (2005) and Kim et al. (2015). From the TEM images of the brown sample an ordered internal structure is not visible. The particles seem to consist of an oily substance (described as "condensed organic species" by Moore et al., 2014) which adheres well to the filter fibers (Fig. 10). However, analysis of the electron diffraction patterns indicates a small degree of ordering (see below).

After heating to 870°C under helium atmosphere, the black sample shows the same graphitic-like structure as the original black sample. However, the brown heated (870°C He) sample seems to have a more ordered internal structure in the form of layers than its original version as indicated by stronger noticeable local fringe-like contrast (Fig. 11).

The electron diffraction patterns (Fig. 12) of both heated and original samples show rings with maxima at 2.8nm^{-1} (A), 4.9nm^{-1} (B) and 8.4nm^{-1} (C). The positions of the rings are very similar to those of simulated graphite with randomly oriented small graphitic domains (cf. inset in Fig. 13).

Therefore we conclude that the ring A at 2.8nm^{-1} can be related to the layer distance of graphite and the ring B at 4.9nm^{-1} to the (100) or (101) planes of graphite. All rings appear in the diffraction patterns of both the black and the brown samples in Fig. 12, but they are broader for the brown original sample. The latter result is demonstrated more clearly in the intensity profiles calculated by azimuthal integration along rings (Fig. 13) and indicates that the brown original sample is less ordered than the black sample. This finding is also consistent with the Raman spectra and the realspace TEM images. Based on the comparison of the positions and profiles of the experimental peaks to the simulated ones, it is concluded that all samples contain small graphitic-like atomic arrangements. The tendency of the maximum A to larger diffraction vectors by thermal treatment of the brown sample refers to a slight reduction of the distance of graphitic layers by heating resembling that of the black one.

The quantitative evaluation of the peak width by the full width at half maximum (FWHM) is displayed for the different samples in Fig. 14. In the case of the brown sample the FWHM of ring B decreases by 30% as a consequence of heating. This result can be interpreted as an increase in the coherently scattering domain size (Fultz and Howe, 2001) and an increased degree of structural order during heating.

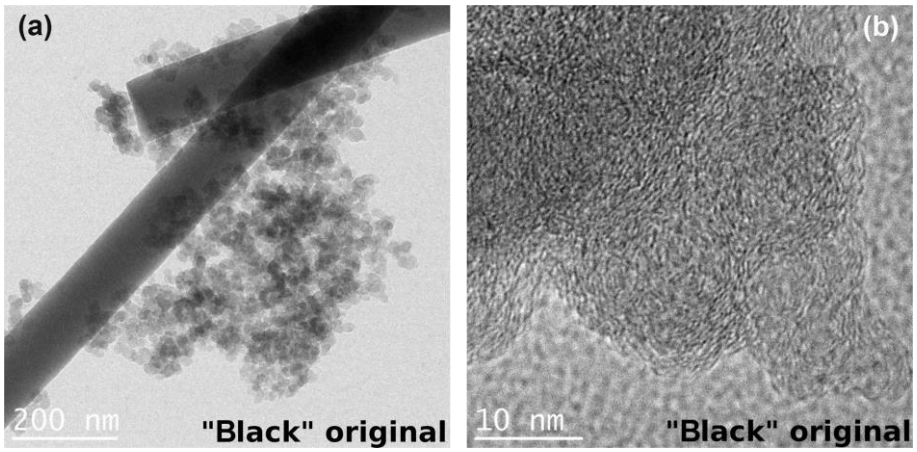

Figure 9. TEM images of the black original sample with two different magnifications. The black sample consists of agglomerates of spherical primary particles. The higher magnification shows an onion-like structure of the single spheres as reported by Sadezky et al. (2005) and Kim et al. (2015).

This interpretation holds also for the other peaks; for example, the FWHM value of peak A at 2.8nm^{-1} changes from 0.54±0.05 to 0.45±0.04nm^{-1} by heating up to 870°C (Figs. 13 and 14).

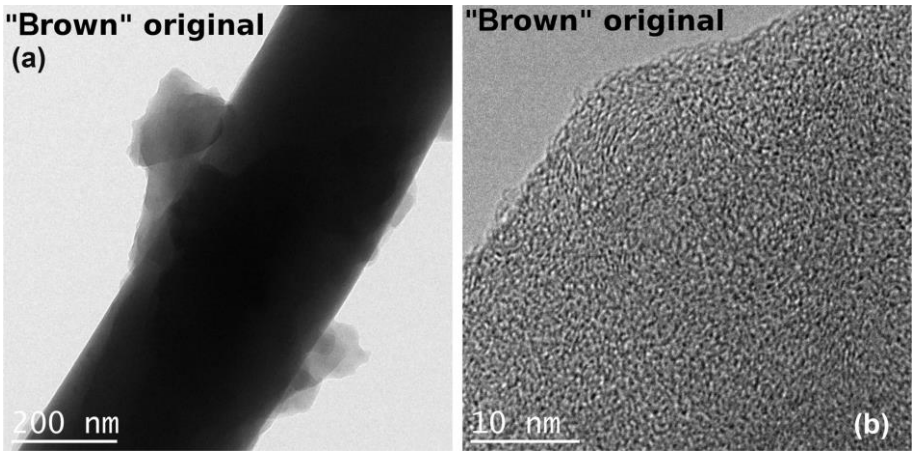

Figure 10. TEM images of the brown original sample taken at two different magnifications. The brown sample consists of unstructured droplets. The disordered structure is visible in the right image.

Based on these FWHM values and using the Scherrer equation (Fultz et al., 2001) the size of the coherently scattering domains (in the direction perpendicular to the (002) layers) changes from about 1.6 to 2nm as a consequence of heating. On the other hand, the FWHM of the black sample does not change and neither does the internal structure of the material (Figs. 13 and 14). Black original and heated samples were found to have coherently scattering domains with sizes of about 2.2nm from which we conclude a slight difference in the structural ordering between the black and the brown heated sample. The changes in the graphitic domain size of the brown sample during heating confirm the findings of the Raman measurements but the temperature dependence is still different. As shown in Fig. 14 the FWHM of the brown sample decreases already at temperatures below 870°C. This is in contrast to the Raman spectra, where a sudden change in the shape of the curves occurs at 870°C in He. The cause for this difference is not completely clear. A possible explanation might be a reorientation and alignment of existing clusters and layers and therefore an increase in the size of

coherently scattering domains at temperatures below 870°C. This would not necessarily change the Raman signal since the structure within the clusters can be kept unchanged and the existing clusters would only rotate, rearrange and align.

5.5 UV–VIS spectroscopy

Figure 15 shows the wavelength dependence of light absorption by the brown and black original and heated samples. The wavelength dependence of the brown sample changes during the heating process. The absorption spectra for the black heated and original samples, however, do not change significantly, particularly not in one distinct direction. The spectrum of the brown original sample has a strong wavelength dependence, but during the heating process this spectrum changes and becomes more and more similar to the spectra of the black samples.

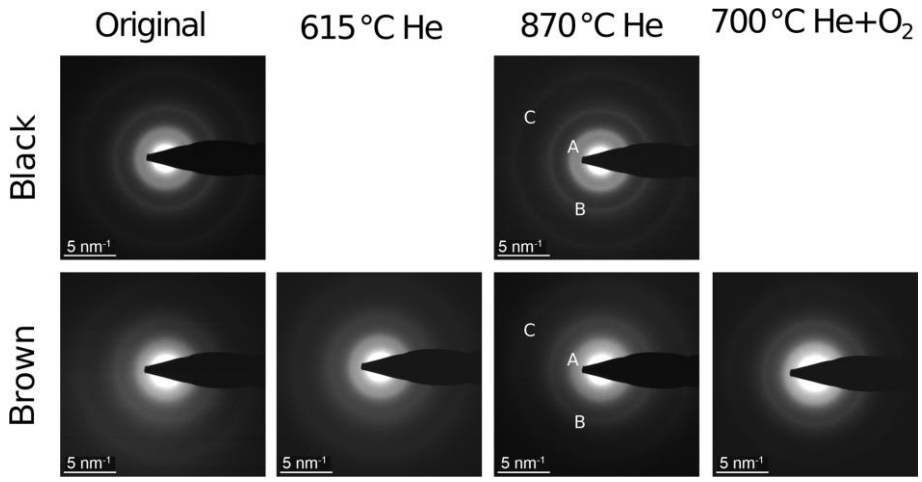

Figure 12. Electron diffraction patterns of black and brown samples; original and heated. A, B and C indicate the ring maxima at 2.8, 4.9 and 8.4nm^{-1}, respectively.

The wavelength dependence of the absorption was fitted using the Ångström power law:

$$\ln(I/I_0) = K \cdot \lambda^{\alpha}, \qquad (2)$$

where I_0 is the incident intensity, I the reflected intensity, α the Ångström exponent, λ the wavelength and K a constant. Figure 16 shows the absorption spectra for the brown original and heated samples with the spectrum for the black original sample for comparison. The Ångström exponents of the respective curves are given in the figure.

The spectrum of the original brown sample starts with an Ångström exponent of $\alpha = -1.79$. During the heating process the wavelength dependence decreases and reaches values of $\alpha \approx -0.63$ after the heating step of 870°C in He, which is even lower than the Ångström exponent for the black original sample ($\alpha = -0.92$).

The low Ångström exponent (−0.35) of the sample heated to 775°C in O_2 might suffer from measurement uncertainties. At this heating stage, most of the absorbing material has already been burned off the filter and the K–M absorption signals are already very small.

This decrease in the Ångström exponent for the brown sample indicates an increase in BC, which is consistent with the findings of the IS measurements. At the heating stage of 870°C in He and after this stage, the Ångström exponent is even lower than for the black original sample.

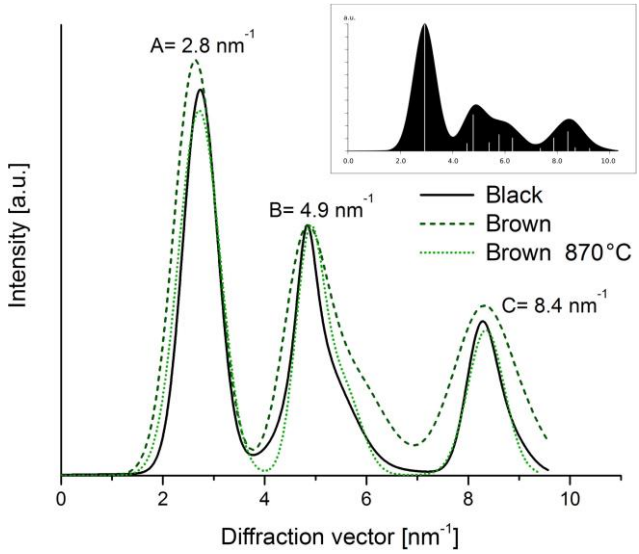

Figure 13. Intensity profiles of diffraction patterns taken from the black and brown original sample and the brown heated (870°C He) sample. The intensities of all three samples were normalized to the peak intensity at 4.9nm^{-1}. The image in the right corner shows the simulation for a graphitic material with small and randomly oriented graphitic clusters.

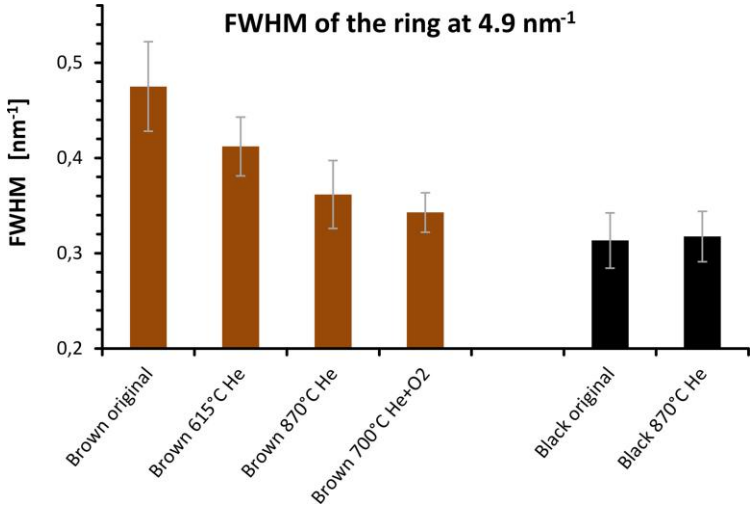

Figure 14. FWHM of the 4.9nm^{-1} maximum of electron diffraction of the original and heated samples for selected temperatures. The FWHM of the brown sample decreases during the heating process and reaches values near the FWHM of the black sample after heating at 870°C in He.

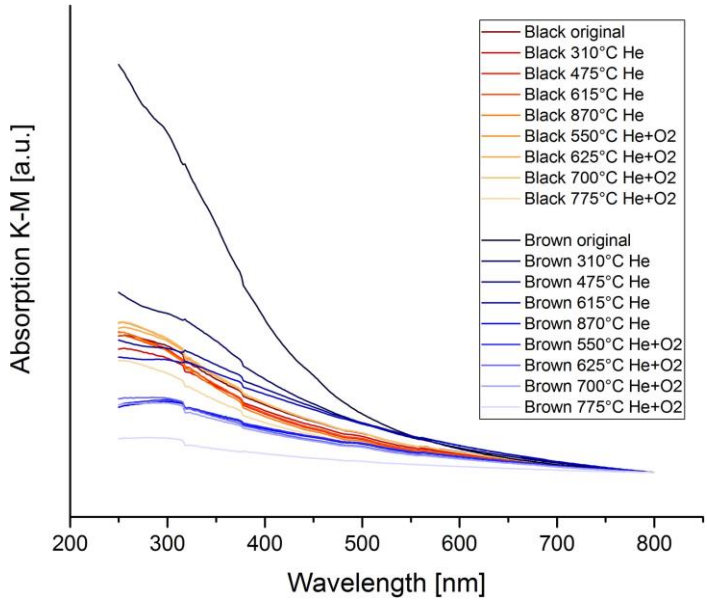

Figure 15. UV–VIS spectra for the black and brown heated and original samples. The spectra are normalized at 800nm for better comparison. The wavelength dependence does not change significantly during the thermal–optical heating process for the black sample, while the wavelength dependence decreases continuously for the brown sample.

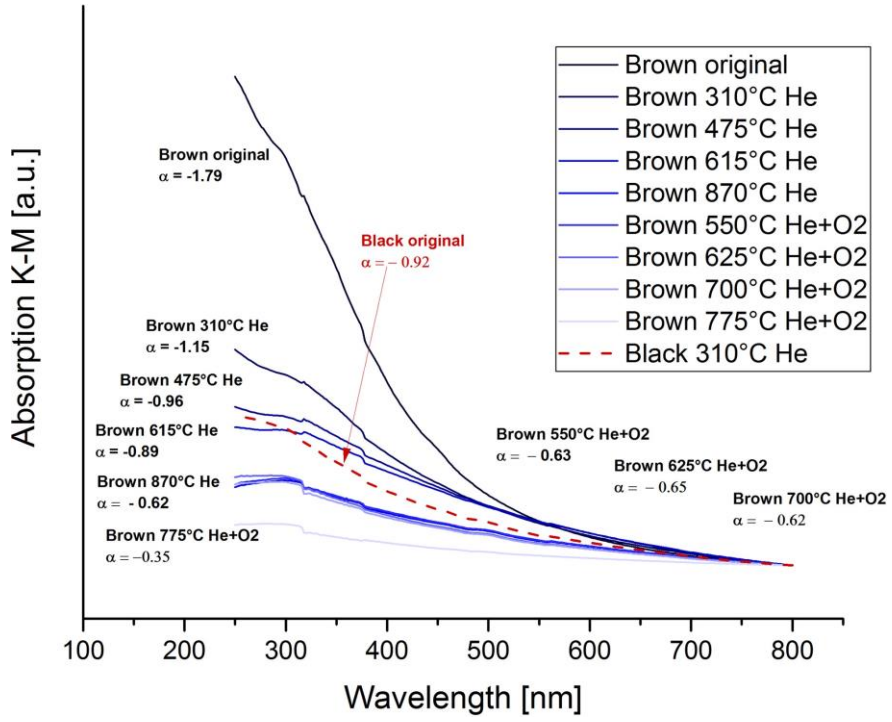

Figure 16. UV–VIS spectra for the brown original and heated samples and corresponding Ångström exponents. The dashed red line shows the spectrum of the black original sample for comparison.

Absorption Ångström exponents depend on both the refractive index and on the size of the absorbing particles (Bohren and Huffman, 1998). Absorption by small particles (in the Rayleigh regime) has a stronger wavelength dependence than that by larger particles in the Mie scattering size range. The observed behavior of the Ångström exponents could be caused by the different sizes and shapes of the particles of the black sample compared to particles in the brown sample. As we saw from the TEM

images, the particles of the black sample consist of agglomerates of spherical primary particles with diameters of about 20nm, whereas the particles in the brown sample are larger than these primary particles. This large size difference is not substantially changed due to heating.

6 Conclusion

From the various analyses a change in structure of the brown sample during thermal analysis can be clearly seen. For the black sample which consists of agglomerates of spherules with graphitic-like structure no such change occurs. These findings are supported by all analysis techniques employed here (UV–VIS measurements, Raman spectroscopy, TEM and IS). The interpretation of the data of the brown sample, however, is quite complex and in some cases more than one interpretation might be possible. The Raman spectra show that the structure of the brown sample changes significantly at 870°C in the He atmosphere. According to Ferrari and Robertson (2000) the relative increase in the D peak in the spectra indicates an increase in clustered aromatic rings in the material. Also the five-curve fits of the spectra suggest that new small graphitic layers could be formed during the 870°C heating step. The TEM measurements confirm the increase in ordering in the brown sample since the FWHM of the electron diffraction maxima, e.g., at 4.9nm^{-1}, decreases when the sample is heated. Consequently, an increase in domain size from 1.6 to 2nm can be estimated for the original and heated brown sample, respectively. The FWHM, i.e., the level of ordering and the domain size, stays nearly constant over the subsequent cooling and reheating process in the He+O_2 atmosphere. Although the FWHM value, the coherently scattering domain size and the layer distance at 870°C reach nearly the same values as those of the black sample, slight structural differences of the brown and black sample are still present and can be, for example, related to the more perfect stacking of graphene-like layers in the black sample.

Likewise, the wavelength dependence of the UV–VIS spectra of the brown sample resembles the wavelength dependence of the black sample when the sample is heated to 870°C in He. The Ångström exponent stays constant during the subsequent heating steps in He+O_2.

So all of the applied analysis techniques agree that the structure of the brown sample resembles more or less the structure of the black sample when the sample is heated to 870°C in He. All techniques also show that the structure does not change further during the subsequent heating steps.

For the last temperature step in the Helium phase (870°C) the results of the different measurement techniques applied in this study are consistent among themselves. However, the findings for samples heated at lower temperatures are somewhat contradictory: while the Raman spectra change suddenly at 870°C in He and do not change significantly during the preceding temperature steps (highest temperature 615°C in He), the decrease in the wavelength dependence and the darkening (i.e., the laser signal in the EC–OC analyzer) occur during the whole heating process. The change in the FWHM of the 4.9nm^{-1} of the electron diffraction maximum and the formation of BC also occur continuously.

It is not unambiguously clear how the structural change proceeds during the first three heating steps. The optical measurement techniques suggest a continuous change, as the optical signals change continuously. The electron diffraction patterns also imply a continuous change. On the other hand, the Raman spectra clearly show that Raman sensitive structures do not change significantly during the first three heating steps, which indicates that no new graphene layers (i.e., a clustering of aromatics) are built. But the weakening of the wavelength dependence indicates a decrease in the optical band gap in

the material, which might be due to an increasing size of polyaromatic and graphene-like structures, i.e., larger conjugated π molecular orbitals.

Oxygen and hydrogen can leave the sample at temperatures above 250°C in He (Petzold et al., 2013; Chow et al., 2004). The free bonds could be incorporated in the remaining molecule and form conjugated double bonds and increase aromaticity, which would lead to the observed change in the UV–VIS spectra. Also oxygenated groups at the edges of the molecules have effects on the optical behavior: a decrease in oxygen leads to a darkening of the substance, i.e., weaker wavelength dependence. Both of these changes would explain the optical behavior of the sample but would not significantly affect the Raman spectra of soot.

Even though it is not unambiguously clear which differences in the structures lead to the conflicting results, our findings indicate that different physical–chemical processes occur at the lower temperatures in comparison to the 870°C (He) step. This is consistent with the findings of Yu and Yang (2002), who showed that the value of σ of PC in some cases is not constant during a single thermal analysis.

Overall we conclude that the most significant and at the same time irreversible structural change of the pyrolyzed organic material in our samples happens at 870°C in He in the measurement protocol used here and that new graphenelike layers are built. We can only speculate, however, on the causes of the continuous darkening of the sample during the lower-temperature steps.

Data availability. Data can be accessed by contacting the corresponding author.

Author contributions. TH performed the conceptualization of the experimental setup, all measurements except TEM, the evaluation and interpretation of data and the preparation of the manuscript. CR performed the TEM measurements and wrote the TEM section. JCM contributed to discussions and provided input for TEM measurements. LF provided cooperation regarding UV–VIS measurements and wrote part of the UV–VIS methods section. HG contributed to discussions, provided input for the Raman and UV–VIS measurements, and acquired funding. RH performed the conceptualization, supervised, contributed to discussions, and provided extensive input to the text.
Competing interests. The authors declare that they have no conflict of interest.

Acknowledgements. This work was supported by the Austrian Science Fund (FWF), grant P26040. The integrating-sphere technique was developed within the grant H-85/92 Hochschuljubiläumstiftung der Stadt Wien. We thank Karin Wieland for the valuable advice for the Raman measurements.

Financial support. This research has been supported by the Austrian Science Fund (FWF) (grant no. P26040).

Review statement. This paper was edited by Pierre Herckes and reviewed by Darrel Baumgardner and one anonymous referee.

References

Adachi, K. and Buseck, P. R.: Changes of ns-soot mixing states and shapes in an urban area during CalNex, J. Geophys. Res., 9, 3723–3730, https://doi.org/10.1002/jgrd.50321, 2013.

Adachi, K., Chung, S. H., and Buseck, P. R.: Shapes of soot aerosol particles and implications for their effects on climate, J. Geophys. Res., D15, 6469, https://doi.org/10.1029/2009JD012868, 2010.

Anderson, J. O., Thundiyil, J. G., and Stolbach, A.: Clearing the air. A review of the effects of particulate matter air pollution on human health, J. Med. Toxicol., 2, 166–175, https://doi.org/10.1007/s13181-011-0203-1, 2012.

Andreae, M. O. and Gelencsér, A.: Black carbon or brown carbon? The nature of light-absorbing carbonaceous aerosols, Atmos. Chem. Phys., 6, 3131–3148, https://doi.org/10.5194/acp-63131-2006, 2006.

Arnott, W. P., Moosmüller, H., Fred Rogers, C., Jin, T., and Bruch, R.: Photoacoustic spectrometer for measuring light absorption by aerosol. Instrument description, Atmos. Environ., 17, 2845– 2852, https://doi.org/10.1016/S1352-2310(98)00361-6, 1999.

Aryal, R., Terman, P., and Voss, K. J.: Comparison of Two FilterBased Reflectance Methods to Measure the Light Absorption by Atmospheric Aerosols, J. Atmos. Ocean. Tech., 4, 923–929, https://doi.org/10.1175/JTECH-D-13-00131.1, 2014.

Birch, M. E. and Cary, R. A.: Elemental Carbon-Based Method for Monitoring Occupational Exposures to Particulate Diesel Exhaust, Aerosol Sci. Technol., 3, 221–241, https://doi.org/10.1080/02786829608965393, 1996.

Bladt, H., Ivleva, N. P., and Niessner, R.: Internally mixed multicomponent soot. Impact of different salts on soot structure and thermo-chemical properties, J. Aerosol Sci., 70, 26–35, https://doi.org/10.1016/j.jaerosci.2013.11.007, 2014. Bohren, C. F. and Huffman, D. R.: Absorption and Scattering of Light by Small Particles, Wiley, New York, 1998.

Bond, T. C.: Spectral dependence of visible light absorption by carbonaceous particles emitted from coal combustion, Geophys. Res. Lett., 21, 4075–4078, https://doi.org/10.1029/2001GL013652, 2001.

Bond, T. C. and Bergstrom, R. W.: Light Absorption by Carbonaceous Particles. An Investigative Review, Aerosol Sci. Technol., 1, 27–67, https://doi.org/10.1080/02786820500421521, 2006.

Bondy, A. L., Bonanno, D., Moffet, R. C., Wang, B., Laskin, A., and Ault, A. P.: The diverse chemical mixing state of aerosol particles in the southeastern United States, Atmos. Chem. Phys., 18, 12595–12612, https://doi.org/10.5194/acp-18-125952018, 2018.

Brown, R. J. C., Beccaceci, S., Butterfield, D. M., Quincey, P. G., Harris, P. M., Maggos, T., Panteliadis, P., John, A., Jedynska, A., Kuhlbusch, T. A. J., Putaud, J.-P., and Karanasiou, A.: Standardisation of a European measurement method for organic carbon and elemental carbon in ambient air. Results of the field trial campaign and the determination of a measurement uncertainty and working range, Environ. Sci.-Pro. Imp., 10, 1249– 1259, https://doi.org/10.1039/C7EM00261K, 2017.

Buseck, P. R., Adachi, K., Gelencsér, A., Tompa, É., and Pósfai, M.: Ns-Soot. A Material-Based Term for Strongly LightAbsorbing Carbonaceous Particles, Aerosol Sci. Technol., 7, 777–788, https://doi.org/10.1080/02786826.2014.919374, 2014.

Cappa, C. D., Onasch, T. B., Massoli, P., Worsnop, D. R., Bates, T. S., Cross, E. S., Davidovits, P., Hakala, J., Hayden, K. L., Jobson, B. T., Kolesar, K. R., Lack, D. A., Lerner, B. M., Li,S.-M., Mellon, D., Nuaaman, I., Olfert, J. S., Petäjä, T., Quinn, P. K., Song, C., Subramanian, R., Williams, E. J., and Zaveri, R. A.: Radiative absorption enhancements due to the mixing state of atmospheric black carbon, Science, 6098, 1078–1081, https://doi.org/10.1126/science.1223447, 2012.

Cavalli, F., Viana, M., Yttri, K. E., Genberg, J., and Putaud, J.-P.: Toward a standardised thermal-optical protocol for measuring atmospheric organic and elemental carbon: the EUSAAR protocol, Atmos. Meas. Tech., 3, 79–89, https://doi.org/10.5194/amt-3-792010, 2010.

Cheng, Y., Duan, F.-K., He, K.-B., Du, Z.-Y., Zheng, M., and Ma, Y.-L.: Intercomparison of thermal-optical method with different temperature protocols. Implications from source samples and solvent extraction, Atmos. Environ., 453–462, https://doi.org/10.1016/j.atmosenv.2012.07.066, 2012.

Chhowalla, M., Robertson, J., Chen, C. W., Silva, S. R. P., Davis, C. A., Amaratunga, G. A. J., and Milne, W. I.: Influence of ion energy and substrate temperature on the optical and electronic properties of tetrahedral amorphous carbon (ta-C) films, J. Appl. Phys., 1, 139–145, https://doi.org/10.1063/1.364000, 1997.

China, S., Mazzoleni, C., Gorkowski, K., Aiken, A. C., and Dubey, M. K.: Morphology and mixing state of individual freshly emitted wildfire carbonaceous particles, Nat. Commun., 4, 2122, https://doi.org/10.1038/ncomms3122, 2013.

Chow, J. C., Watson, J. G., Chen, L.-W. A., Arnott, W. P., Moosmüller, H., and Fung, K.: Equivalence of Elemental Carbon by Thermal/Optical Reflectance and Transmittance with Different Temperature Protocols, Environ. Sci. Technol., 16, 4414–4422, https://doi.org/10.1021/es034936u, 2004.

Commodo, M., de Falco, G., Larciprete, R., D'Anna, A., and Minutolo, P.: On the hydrophilic/hydrophobic character of carbonaceous nanoparticles formed in laminar premixed flames, Exp. Therm. Fl. Sci., 73, 56–63, https://doi.org/10.1016/j.expthermflusci.2015.09.005, 2016.

Cuesta, A., Dhamelincourt, P., Laureyns, J., Martínez-Alonso, A., and Tascón, J. M. D.: Raman microprobe studies on carbon materials, Carbon, 8, 1523–1532, https://doi.org/10.1016/00086223(94)90148-1, 1994.

Deboudt, K., Flament, P., Choël, M., Gloter, A., Sobanska, S., and Colliex, C.: Mixing state of aerosols and direct observation of carbonaceous and marine coatings on African dust by individual particle analysis, J. Geophys. Res., D24, 833, https://doi.org/10.1029/2010JD013921, 2010.

Després, V., Huffman, J. A., Burrows, S. M., Hoose, C., Safatov, A., Buryak, G., Fröhlich-Nowoisky, J., Elbert, W., Andreae, M., Pöschl, U., and Jaenicke, R.: Primary biological aerosol particles in the atmosphere. A review, Tellus B, 1, 15598, https://doi.org/10.3402/tellusb.v64i0.15598, 2012.

Dippel, B., Jander, H., and Heintzenberg, J.: NIR FT Raman spectroscopic study of flame soot, Phys. Chem. Chem. Phys., 20, 4707–4712, https://doi.org/10.1039/a904529e, 1999.

EEA: Air Quality in Europe – 2017 Report, EAA report, Copenhagen, 2017.

Ess, M. N., Ferry, D., Kireeva, E. D., Niessner, R., Ouf, F.X., and Ivleva, N. P.: In situ Raman microspectroscopic analysis of soot samples with different organic carbon content. Structural changes during heating, Carbon, 105, 572–585, https://doi.org/10.1016/j.carbon.2016.04.056, 2016.

Fan, X., Wei, S., Zhu, M., Song, J., and Peng, P.: Comprehensive characterization of humic-like substances in smoke PM2.5 emitted from the combustion of biomass materials and fossil fuels, Atmos. Chem. Phys., 16, 13321–13340, https://doi.org/10.5194/acp-16-13321-2016, 2016.

Ferrari, A. C. and Robertson, J.: Interpretation of Raman spectra of disordered and amorphous carbon, Phys. Rev. B, 20, 14095– 14107, https://doi.org/10.1103/PhysRevB.61.14095, 2000.

Fultz, B. and Howe, J. M.: Transmission electron microscopy and diffractometry of materials, Physics and astronomy online library, Springer, Berlin, 2001.

Gammer, C., Mangler, C., Rentenberger, C., and Karnthaler, H. P.: Quantitative local profile analysis of nanomaterials by electron diffraction, Scripta Materialia, 3, 312–315, https://doi.org/10.1016/j.scriptamat.2010.04.019, 2010.

Graber, E. R. and Rudich, Y.: Atmospheric HULIS: How humiclike are they? A comprehensive and critical review, Atmos. Chem. Phys., 6, 729–753, https://doi.org/10.5194/acp-6-7292006, 2006.

Highwood, E. J. and Kinnersley, R. P.: When smoke gets in our eyes. The multiple impacts of atmospheric black carbon on climate, air quality and health, Environ. Int., 4, 560–566, https://doi.org/10.1016/j.envint.2005.12.003, 2006.

Hitzenberger, R. and Tohno, S.: Comparison of black carbon (BC) aerosols in two urban areas – concentrations and size distributions, Atmos. Environ., 12, 2153–2167, https://doi.org/10.1016/S1352-2310(00)00480-5, 2001.

Hitzenberger, R., Petzold, A., Bauer, H., Ctyroky, P., Pouresmaeil, P., Laskus, L., and Puxbaum, H.: Intercomparison of Thermal and Optical Measurement Methods for Elemental Carbon and Black Carbon at an Urban Location, Environ. Sci. Technol., 20, 6377–6383, https://doi.org/10.1021/es051228v, 2006.

Hoffer, A., Gelencsér, A., Blazsó, M., Guyon, P., Artaxo, P., and Andreae, M. O.: Diel and seasonal variations in the chemical composition of biomass burning aerosol, Atmos. Chem. Phys., 6, 3505–3515, https://doi.org/10.5194/acp-6-3505-2006, 2006.

Ichikawa, Y. and Naito, S.: Chemical Compositions of Primary $PM_{2.5}$ Derived from Biomass Burning Emissions, Ajae, 11, 79– 95, https://doi.org/10.5572/ajae.2017.11.2.079, 2017.

IPCC: Clouds and Aerosols. Climate Change 2013: The Physical Science Basis. Contribution of Working Group I to the Fifth Assessment Report of the Intergovernmental Panel on Climate Change, edited by: Stocker, T. F., Qin, D., Plattner, G.-K., Tignor, M., Allen, S. K., Boschung, J., Nauels, A., Xia, Y., Bex, V., and Midgley, P. M., Cambridge University Press, Cambridge, United Kingdom and New York, NY, USA, 2013.

Ivleva, N. P., McKeon, U., Niessner, R., and Pöschl, U.: Raman Microspectroscopic Analysis of Size-Resolved Atmospheric Aerosol Particle Samples Collected with an ELPI. Soot, HumicLike Substances, and Inorganic Compounds, Aerosol Sci. Technol., 7, 655–671, https://doi.org/10.1080/02786820701376391, 2007a.

Ivleva, N. P., Messerer, A., Yang, X., Niessner, R., and Pöschl, U.: Raman Microspectroscopic Analysis of Changes in the Chemical Structure and Reactivity of Soot in a Diesel Exhaust Aftertreatment Model System, Environ. Sci. Technol., 10, 3702– 3707, https://doi.org/10.1021/es0612448, 2007b.

Jankowski, N., Schmidl, C., Marr, I. L., Bauer, H., and Puxbaum, H.: Comparison of methods for the quantification of carbonate carbon in atmospheric PM_{10} aerosol samples, Atmos. Environ., 34, 8055–8064, https://doi.org/10.1016/j.atmosenv.2008.06.012, 2008.

Jawhari, T., Roid, A., and Casado, J.: Raman spectroscopic characterization of some commercially available carbon black materials, Carbon, 11, 1561–1565, https://doi.org/10.1016/00086223(95)00117-V, 1995.

Kim, J., Bauer, H., Dobovicnik, T., Hitzenberger, R., Lot-ˇ tin, D., Ferry, D., and Petzold, A.: Assessing Optical Properties and Refractive Index of Combustion Aerosol Particles Through Combined Experimental and Modeling Studies, Aerosol Sci. Technol., 5, 340–350, https://doi.org/10.1080/02786826.2015.1020996, 2015.

Knauer, M., Schuster, M. E., Su, D., Schlögl, R., Niessner, R., and Ivleva, N. P.: Soot Structure and Reactivity Analysis by Raman Microspectroscopy, Temperature-Programmed Oxidation, and High-Resolution Transmission Electron Microscopy, J. Phys. Chem. A, 50, 13871–13880, https://doi.org/10.1021/jp905639d, 2009.

Kubelka, P. and Munk, F.: Ein Beitrag zur Optik der Farbanstriche, Zeitschrift für Technische Physik, 12, 593–601, 1931.

Mamakos, A., Khalek, I., Giannelli, R., and Spears, M.: Characterization of Combustion Aerosol Produced by a Mini-CAST and Treated in a Catalytic Stripper, Aerosol Sci. Technol., 8, 927– 936, https://doi.org/10.1080/02786826.2013.802762, 2013.

Mayol-Bracero, O.L.: Water-soluble organic compounds in biomass burning aerosols over Amazonia. Apportionment of the chemical composition and importance of the polyacidic fraction, J. Geophys. Res., D20, 995, https://doi.org/10.1029/2001JD000522, 2002.

McNeil, V. F.: Atmospheric Aerosols. Clouds Chemistry and Climate, Annu.Rev.Chem.Biomol. Eng., 1, 427-444. https://doi.org/10.1146/annurev-chembioeng-060816-101539, 2017.

Mesquita, S. R., van Drooge, B. L., Dall'Osto, M., Grimalt, J.
O., Barata, C., Vieira, N., Guimarães, L., and Piña, B.: Toxic potential of organic constituents of submicron particulate matter (PM1) in an urban road site (Barcelona), Environ. Sci. Pollut. Res., 18, 15406–15415, https://doi.org/10.1007/s11356-0179201-4, 2017.

Moore, R. H., Ziemba, L. D., Dutcher, D., Beyersdorf, A. J., Chan, K., Crumeyrolle, S., Raymond, T. M., Thornhill, K. L., Winstead, E. L., and Anderson, B. E.: Mapping the Operation of the Miniature Combustion Aerosol Standard (MiniCAST) Soot Generator, Aerosol Sci. Technol., 5, 467–479, https://doi.org/10.1080/02786826.2014.890694, 2014.

Moosmüller, H., Arnott, W. P., Rogers, C. F., Chow, J. C., Frazier, C. A., Sherman, L. E., and Dietrich, D. L.: Photoacoustic and filter measurements related to aerosol light absorption during the Northern Front Range Air Quality Study (Colorado 1996/1997), J. Geophys. Res., D21, 28149–28157, https://doi.org/10.1029/98JD02618, 1998. Müller, K., Spindler, G., Maenhaut, W., Hitzenberger, R., Wieprecht, W., Baltensperger, U., and ten Brink, H.: INTERCOMP2000, a campaign to assess the comparability of methods in use in Europe for measuring aerosol composition, Atmos. Environ., 38, 6459–6466, https://doi.org/10.1016/j.atmosenv.2004.08.031, 2004.

Okada, K. and Hitzenberger, R. M.: Mixing properties of individual submicrometer aerosol particles in Vienna, Atmos. Environ., 32, 5617–5628, https://doi.org/10.1016/S1352-2310(01)001261, 2001.

Panteliadis, P., Hafkenscheid, T., Cary, B., Diapouli, E., Fischer, A., Favez, O., Quincey, P., Viana, M., Hitzenberger, R., Vecchi, R., Saraga, D., Sciare, J., Jaffrezo, J. L., John, A., Schwarz, J., Giannoni, M., Novak, J., Karanasiou, A., Fermo, P., and Maenhaut, W.: ECOC comparison exercise with identical thermal protocols after temperature offset correction – instrument diagnostics by in-depth evaluation of operational parameters, Atmos. Meas. Tech., 8, 779–792, https://doi.org/10.5194/amt-8779-2015, 2015.

Park, S. S. and Yu, J.: Chemical and light absorption properties of humic-like substances from biomass burning emissions under controlled combustion experiments, Atmos. Environ., 136, 114– 122, https://doi.org/10.1016/j.atmosenv.2016.04.022, 2016.

Park, S., Son, S.-C., and Lee, S.: Characterization, sources, and light absorption of fine organic aerosols during summer and winter at an urban site, Atmos. Res., 213, 370–380, https://doi.org/10.1016/j.atmosres.2018.06.017, 2018.

Partanen, A.-I., Landry, J.-S., and Matthews, H. D.: Climate and health implications of future aerosol emission scenarios, Environ. Res. Lett., 13, 024028, https://doi.org/10.1088/17489326/aaa511, 2018.

Petzold, A., Ogren, J. A., Fiebig, M., Laj, P., Li, S.-M., Baltensperger, U., Holzer-Popp, T., Kinne, S., Pappalardo, G., Sugimoto, N., Wehrli, C., Wiedensohler, A., and Zhang, X.-Y.: Recommendations for reporting "black carbon" measurements, Atmos. Chem. Phys., 13, 8365–8379, https://doi.org/10.5194/acp13-8365-2013, 2013.

Pöschl, U.: Atmospheric Aerosols. Composition, Transformation, Climate and Health Effects, Angew. Chem. Int. Ed., 46, 7520–7540, https://doi.org/10.1002/anie.200501122, 2005.

Pratt, K. A. and Prather, K. A.: Aircraft measurements of vertical profiles of aerosol mixing states, J. Geophys. Res., D11, 3131, https://doi.org/10.1029/2009JD013150, 2010.

Reisinger, P., Wonaschütz, A., Hitzenberger, R., Petzold, A., Bauer, H., Jankowski, N., Puxbaum, H., Chi, X., and Maenhaut, W.: Intercomparison of Measurement Techniques for Black or Elemental Carbon Under Urban Background Conditions in Wintertime. Influence of Biomass Combustion, Environ. Sci. Technol., 3, 884–889, https://doi.org/10.1021/es0715041, 2008.

Robertson, J. and O'Reilly, E. P.: Electronic and atomic structure of amorphous carbon, Phys. Rev. B, 6, 2946–2957, https://doi.org/10.1103/PhysRevB.35.2946, 1987.

Rohr, A. and McDonald, J.: Health effects of carboncontaining particulate matter. Focus on sources and recent research program results, Crit. Rev. Toxicol., 2, 97–137, https://doi.org/10.3109/10408444.2015.1107024, 2015.

Rosen, H. and Novakov, T.: Identification of primary particulate carbon and sulfate species by Raman spectroscopy, Atmos. Environ., 12, 923–927, https://doi.org/10.1016/0004-6981(78)900318, 1978.

Sadezky, A., Muckenhuber, H., Grothe, H., Niessner, R., and Pöschl, U.: Raman microspectroscopy of soot and related carbonaceous materials. Spectral analysis and structural information, Carbon, 8, 1731–1742, https://doi.org/10.1016/j.carbon.2005.02.018, 2005.

Schmid, J., Grob, B., Niessner, R., and Ivleva, N. P.: Multiwavelength Raman Microspectroscopy for Rapid Prediction of Soot Oxidation Reactivity, Anal. Chem., 4, 1173–1179, https://doi.org/10.1021/ac102939w, 2011.

Schmidl, C., Bauer, H., Dattler, A., Hitzenberger, R., Weissenboeck, G., Marr, I. L., and Puxbaum, H.: Chemical characterisation of particle emissions from burning leaves, Atmos. Environ., 40, 9070–9079, https://doi.org/10.1016/j.atmosenv.2008.09.010, 2008.

Schwarz, J. P., Gao, R. S., Fahey, D. W., Thomson, D. S., Watts, L. A., Wilson, J. C., Reeves, J. M., Darbeheshti, M., Baumgardner, D. G., Kok, G. L., Chung, S. H., Schulz, M., Hendricks, J., Lauer, A., Kärcher, B., Slowik, J. G., Rosenlof, K. H., Thompson, T. L., Langford, A. O., Loewenstein, M., and Aikin, K. C.: Single-particle measurements of midlatitude black carbon and light-scattering aerosols from the boundary layer to the lower stratosphere, J. Geophys. Res., D16, 2845, https://doi.org/10.1029/2006JD007076, 2006.

Sedlacek, A. J., Onasch, T. B., Nichman, L., Lewis, E. R., Davidovits, P., Freedman, A., and Williams, L.: Formation of refractory black carbon by SP2-induced charring of organic aerosol, Aerosol Sci. Technol., 12, 1345–1350, https://doi.org/10.1080/02786826.2018.1531107, 2018.

Stadelmann, P.: Java Electron Microscopy Software JEMS, available at: https://cime.epfl.ch/ (last access: 7 June 2019), 2004.

Stephens, M., Turner, N., and Sandberg, J.: Particle identification by laser-induced incandescence in a solid-state laser cavity, Appl. Optics, 19, 3726, https://doi.org/10.1364/AO.42.003726, 2003.

Sun, H., Biedermann, L., and Bond, T. C.: Color of brown carbon. A model for ultraviolet and visible light absorption by organic carbon aerosol, Geophys. Res. Lett., 17, 3131, https://doi.org/10.1029/2007GL029797, 2007.

Sun, J., Zhi, G., Hitzenberger, R., Chen, Y., Tian, C., Zhang, Y., Feng, Y., Cheng, M., Zhang, Y., Cai, J., Chen, F., Qiu, Y., Jiang, Z., Li, J., Zhang, G., and Mo, Y.: Emission factors and light absorption properties of brown carbon from household coal combustion in China, Atmos. Chem. Phys., 17, 4769–4780, https://doi.org/10.5194/acp-17-4769-2017, 2017.

Sze, S. K., Siddique, N., Sloan, J. J., and Escribano, R.: Raman spectroscopic characterization of carbonaceous aerosols, Atmos. Environ., 3, 561–568, https://doi.org/10.1016/S13522310(00)00325-3, 2001.

Tuinstra, F. and Koenig, J. L.: Raman Spectrum of Graphite, J. Chem. Phys., 3, 1126–1130, https://doi.org/10.1063/1.1674108, 1970.

Venkatachari, P., Zhou, L., Hopke, P. K., Schwab, J. J., Demerjian, K. L., Weimer, S., Hogrefe, O., Felton, D., and Rattigan, O.: An Intercomparison of Measurement Methods for Carbonaceous Aerosol in the Ambient Air in New York City, Aerosol Sci. Technol., 40, 788–795, https://doi.org/10.1080/02786820500380289, 2006.

Wang, Y., Chung, A., and Paulson, S. E.: The effect of metal salts on quantification of elemental and organic carbon in diesel exhaust particles using thermal-optical evolved gas analysis, Atmos. Chem. Phys., 10, 11447–11457, https://doi.org/10.5194/acp-1011447-2010, 2010.

Watson, J. G., Chow, J. C., and Chen, L. W. A.: Summary of Organic and Elemental Carbon/Black Carbon Analysis Methods and Intercomparisons, Aerosol Air Qual. Res., 5, 65–102, 2005.

Wonaschütz, A., Hitzenberger, R., Bauer, H., Pouresmaeil, P., Klatzer, B., Caseiro, A., and Puxbaum, H.: Application of the Integrating Sphere Method to Separate the Contributions of Brown and Black Carbon in Atmospheric Aerosols, Environ. Sci. Technol., 43, 1141–1146, https://doi.org/10.1021/es8008503, 2009.

Ye, Q., Gu, P., Li, H. Z., Robinson, E. S., Lipsky, E., Kaltsonoudis, C., Lee, A. K. Y., Apte, J. S., Robinson, A. L., Sullivan, R. C., Presto, A. A., and Donahue, N. M.: Spatial Variability of Sources and Mixing State of Atmospheric Particles in a Metropolitan Area, Environ. Sci. Technol., 12, 6807–6815, https://doi.org/10.1021/acs.est.8b01011, 2018.

Yttri, K. E., Aas, W., Bjerke, A., Cape, J. N., Cavalli, F., Ceburnis,D., Dye, C., Emblico, L., Facchini, M. C., Forster, C., Hanssen, J. E., Hansson, H. C., Jennings, S. G., Maenhaut, W., Putaud, J. P., and Tørseth, K.: Elemental and organic carbon in PM10: a one year measurement campaign within the European Monitoring and Evaluation Programme EMEP, Atmos. Chem. Phys., 7, 5711–5725, https://doi.org/10.5194/acp-7-5711-2007, 2007.

Yu, J. Z., Xu, J., and Yang, H.: Charring Characteristics of Atmospheric Organic Particulate Matter in Thermal Analysis, Environ. Sci. Technol., 36, 754–761, https://doi.org/10.1021/es015540q, 2002.

Zhang, G., Bi, X., He, J., Chen, D., Lo Chan, Y., Xie, G., Wang, X., Sheng, G., Fu, J., and Zhou, Z.: Variation of secondary coatings associated with elemental carbon by single particle analysis, Atmos. Environ., 92, 162–170, https://doi.org/10.1016/j.atmosenv.2014.04.018, 2014.

Zhu, Y., Huang, L., Li, J., Ying, Q., Zhang, H., Liu, X., Liao, H., Li, N., Liu, Z., Mao, Y., Fang, H., and Hu, J.: Sources of particulate matter in China. Insights from source apportionment studies published in 1987–2017, Environ. Int., 115, 343–357, https://doi.org/10.1016/j.envint.2018.03.037, 2018.

Zickler, G. A., Smarsly, B., Gierlinger, N., Peterlik, H., and Paris, O.: A reconsideration of the relationship between the crystallite size *L*a of carbons determined by X-ray diffraction and Raman spectroscopy, Carbon, 44, 3239–3246, https://doi.org/10.1016/j.carbon.2006.06.029, 2006.

12. Publication 2

This chapter was published on 21 May 2021 in the Journal Atmospheric Measurement Techniques.

Atmos. Meas. Tech., 14, 3721–3735, 2021
https://doi.org/10.5194/amt-14-3721-2021

Investigation of structural changes of atmospheric aerosol samples during two thermal–optical measurement procedures (EUSAAR2, NIOSH870)

Theresa Haller[1] , Eva Sommer[1], Thomas Steinkogler[2], Christian Rentenberger[1], Anna Wonaschuetz[1], Anne Kasper-Giebl[2], Hinrich Grothe[3], and Regina Hitzenberger[1]

[1]Faculty of Physics, University of Vienna, Vienna, 1090, Austria

[2]Institute of Chemical Technologies and Analytics, TU Wien, Vienna, 1060, Austria

[3]Institute of Materials Chemistry, TU Wien, Vienna, 1060, Austria

Correspondence: Theresa Haller (theresa.haller@univie.ac.at)

Received: 30 September 2020 – Discussion started: 2 November 2020

Revised: 16 March 2021 – Accepted: 14 April 2021 – Published: 21 May 2021

Abstract. Thermal–optical measurement techniques are widely used for the monitoring of carbonaceous aerosols. Although results of different thermal–optical measurement techniques are comparable for total carbon, they can vary widely for values of elemental carbon especially in the presence of brown carbon. Charring of organic material during the inert heating phase of thermal–optical measurements has been found to be a major confounder, but no literature about investigations of structural changes during this process in atmospheric aerosols is available. In a recent study we investigated these structural changes for combustion aerosol standard (CAST) soot. Now we apply this approach to selected atmospheric aerosol filter samples and a subset of eight washed filter samples with low loadings of watersoluble organic carbon (WSOC). To investigate structural changes, Raman spectra were obtained for samples heated to the corresponding temperature levels and gas atmospheres of the EUSAAR2 and NIOSH870 protocols. The temperature levels where changes in the Raman spectra occurred (i.e., changes in structure) varied for different samples. For the washed samples with low WSOC loadings and absence of other water-soluble aerosol components such as inorganic salts, changes in structural ordering and darkening of the samples were not observed. We were able to show for the first time that the darkening of a sample (measured in terms of transmission laser signal) is not necessarily caused by an increase of structural ordering in the sample. Possible transformations at lower temperatures could include a formation of non-graphitic light-absorbing intermediate organic carbon, a release of C−H groups or a decrease of carbonyl groups.

1 Introduction

Carbonaceous matter is an important component of atmospheric aerosols because of its adverse impacts on climate and human health (e.g., Bond and Bergstrom, 2006; Highwood and Kinnersley, 2006). It spans a rather continuous range from highly light-absorbing graphitic-like material to non-absorbing organic molecules (e.g., Pöschl, 2005) and is usually classified optically into light-absorbing carbon (LAC) covering brown carbon (BrC) and black carbon (BC) or thermochemically into organic carbon (OC), elemental carbon (EC), and inorganic or carbonate carbon (CC) (Petzold et al., 2013). However, these definitions are tied to measurement methods rather than to the actual internal structure of the material, which makes reliable measurements challenging. Using thermal measurement techniques, OC is defined as the thermally unstable carbonaceous material which evolves in the absence of oxygen at temperatures below 550– 700°C (Bond and Bergstrom, 2006; Chow et al., 2004). EC is defined as the fraction which does not evolve below 550– 700°C in the absence of oxygen and combusts in the presence of oxygen at temperatures above 600°C (Andreae and Gelencsér, 2006).

Results for EC and OC measured with different thermal– optical techniques suffer from biases by up to 44% for EC, while the values of total carbon (TC=EC+OC) are comparable within 5%–15% (e.g., Reisinger et al., 2008; Cavalli et al., 2010; Yu et al., 2002; Cheng et al., 2012; Hitzenberger et al., 2006; Panteliadis et al., 2015; Müller et al., 2004; Venkatachari et al., 2006; Watson et al., 2005; ten Brink et al., 2004). The largest discrepancies were found for samples obtained under wintry conditions and in the presence of biomass smoke (Reisinger et al., 2008; Wonaschuetz et al., 2009; Cheng et al., 2012), when large amounts of BrC can be found (Lukács et al., 2007). The optical absorptivity of BrC is markedly higher in the shortwave range of the visible spectrum than in the longwave range. BrC is more thermally refractory than other organic matter and can therefore be seen as a substance with properties intermediate between those of elemental and organic carbon (e.g., Pöschl, 2005).

In thermal–optical measurement techniques a filter sample is heated stepwise first in an inert atmosphere and then in an oxidizing atmosphere, and the amount of carbon leaving the filter is measured. Different temperature protocols vary in height and duration of the temperature steps and particularly in the maximum temperature of the inert phase (550–900°C; Cavalli et al., 2010). A potential darkening of the sample during the inert phase, commonly explained by pyrolysis and/or charring of the sample producing “pyrolyzed carbon” (PC), is monitored with a transmission and/or reflection laser signal.

The transmission and/or reflection laser signal is used to correct for PC. The amount of carbon detected before this signal reaches its initial value (i.e., the split point) is assigned to OC and carbon detected after this point is assigned to EC. However, this optical correction is based on two essential assumptions which are not generally fulfilled: firstly, PC does not evolve totally before EC, and secondly the specific light absorption coefficients of PC and EC are not equal (Yu et al., 2002; Chow et al., 2004; Subramanian et al., 2006; Han et al., 2007). Moreover, the specific light absorption coefficient of PC can change during the heating procedure (Yu et al., 2002). Because of these uncertainties, the optical correction can lead to an over- or underestimation of EC or OC (Yu et al., 2002; Cheng et al., 2012).

Extensive efforts were undertaken to refine the original thermal–optical measurement procedure (Birch and Cary, 1996) in order to achieve a more accurate setting of the split point and to reduce the formation of PC (e.g., Cavalli et al., 2010; Chow et al., 2004; Cheng et al., 2012). EUSAAR2 was found to

produce less PC than other protocols during analyses of ambient European aerosols (Cavalli et al., 2010) and was subsequently selected as the European standard method (Brown et al., 2017).

Despite all efforts, pyrolysis is still a problematic factor in thermal–optical analyses depending on sample composition. Water-soluble organic carbon (WSOC) was found to be responsible for a large fraction of charring (13%–66%; Yu et al., 2002). Several inorganic constituents can influence charring in complex and sometimes contradictory ways: ammonium bisulfate enhances the charring of starch and cellulose but reduces the charring of levoglucosan (Yu et al., 2002). Metal salts can generally enhance the charring of OC at least in diesel soot and ambient aerosols (Wang et al., 2010). As a consequence of this interplay of several complex chemical reactions, there is no unequivocal effect of non-carbonaceous aerosol constituents on the charring behavior (Wang et al., 2010; Yu et al., 2002; Bladt et al., 2014), and a simple prediction of the charring behavior of an atmospheric aerosol sample is currently impossible.

Most of the studies of pyrolysis during thermal–optical measurement procedures only analyze the laser signals (e.g., Cavalli et al., 2010; Cheng et al., 2012; Yu et al., 2002) or the thermal properties of PC (Yu et al., 2002). The terms “charring” and “pyrolysis” are often used interchangeably to describe processes leading to sample darkening which is implicitly assumed to be caused by a formation of a more structured phase of carbon. Underlying structural changes are not explained. Le et al. (2019) investigated structural changes of laboratory-generated aerosols (produced in a CAST (combustion aerosol standard) soot generator) during heat treatment in N_2 and give detailed information about evolution and restructuring of carbonaceous species. However, the gas atmospheres as well as the heating rates differ from the conditions during thermal–optical analyses.

To our knowledge, no study to date has addressed the structural changes of an atmospheric aerosol sample during a thermal–optical measurement procedure by analyzing graphitization or structural ordering. In a previous study (Haller et al., 2019), we investigated the increase of structural ordering of two widely different combustion aerosol standard soot types (produced by propane combustion in a CAST burner) during a thermal–optical heating procedure (NIOSH870). Using Raman spectroscopy, we found that structural ordering increased at 870 °C when a BrC-rich (and BC-poor) sample was heated in a He atmosphere, while a BC-rich (and BrC-poor) sample did not further change its already high degree of graphitization. This approach is now applied to the much more complex situation of atmospheric aerosols. For 21 atmospheric aerosol samples selected from a 2-year set of daily filter samples, the changes of structural ordering during the inert phases of the NIOSH870 (Birch and Cary, 1996) and EUSAAR2 (Cavalli et al., 2010) protocols were investigated. From a subset of filters, WSOC and other soluble aerosol material was removed by washing. The protocols were chosen because of the different production of PC reported by Cavalli et al. (2010). A dual-optics thermal– optical analyzer (Sunset Instruments Inc.) was used to produce heated samples and to determine EC and OC. Samples heated to each temperature plateau of the inert phases of both temperature protocols were analyzed with Raman spectroscopy to investigate the degree of intermolecular ordering in the material. Several properties of the samples (e.g., ionic composition, EC/OC, BC/BrC) were compared with the progress of structural changes derived from the Raman spectra.

2 Experimental

2.1 Sampling

Atmospheric aerosol was sampled on quartz fiber filters (Pall Tissuquartz 2500 QAT-UP, 47mm) at the rooftop lab of the physics building of the University of Vienna (35m above ground) located about 1.5km from the city center. Although the building is located in an area highly impacted by traffic, the aerosol at the rooftop lab can be seen as an urban background site, since the sampling inlet faces the enclosed source-free courtyard of the building. The aerosol was sampled with an automatic sequential filter sampler (SEQ47/50, Sven Leckel) equipped with a $PM_{2.5}$ inlet and set to a flow rate of $2.3 m^3 h^{-1}$. Sampling time was set to 23h from 12:00 to 11:00 (UTC+1) of the next day. The loaded filters were stored in the filter sampler for about 1 to 2 weeks in a closed magazine before they were transferred to the lab and stored at −22°C in petri dishes closed with Parafilm®. Before sampling, the filters had been heated at 450°C for an hour to remove volatile organic substances and stored for at least 24h in a water-vapor-saturated atmosphere to prevent readsorption of OCs (Jankowski et al., 2008) and to ensure lowOC blanks (blank values typically around $0.2 \mu g C cm^{-2}$). The samples were collected in 2014 and 2015 for nearly every day. BC and BrC values were obtained from these filters using the integrating sphere method (Sommer, 2020).

2.2 Integrating sphere method

Light-absorbing carbon (LAC) (i.e., BrC and BC) was analyzed for all filter samples with an extension (Wonaschuetz et al., 2009) of the original integrating sphere technique (an extensive description is given by Hitzenberger and Tohno, 2001). Circular filter punches with diameters of 10mm were immersed in a mixture of 10% isopropanol, 40% H_2O and 50% acetone in polyethylene (PE) vials. The immersion in this mixture reduces enhanced absorption caused by possible non-absorbing coatings of the particles: soluble material is removed, and the effect of insoluble coatings is reduced due to the similar refractive indices of the liquid and the coatings (Hitzenberger and Tohno, 2001). The PE vials were placed in the center of a 6 in. integrating sphere coated internally with a highly diffusely reflective material (Spectraflect™). The sample was illuminated with a halogen light source equipped with a diffusor and three interference filters (450, 550 and 650nm), and the wavelength-dependent light signal was recorded with a photodiode.

The BC and BrC content in the sample was then calculated in an iterative procedure described by Wonaschuetz et al. (2009), comparing the wavelength-dependent light signals with calibration curves obtained with a proxy for BC (Elftex 124, Cabot Corp.) and a proxy for BrC (humic acid sodium salt, Acros Organics, no. 68131044). The values for BrC should therefore be understood as “humic acid sodium salt equivalent” and refer to the total mass of BrC including other atoms (humic acid sodium salt contains 47% carbon by mass). Detection limits are 1µg per sample for BC and 10µg per sample for BrC.

2.3 Sample selection and preparation

From the total set of 660 filter samples, 21 samples were chosen for further analysis. As the focus of this study is on the restructuring of carbonaceous material with special emphasis on the presence of BrC, winter samples with highBrC loadings and high BrC/LAC ratios and summer samples with BrC loadings below detection limit were selected. The seven samples from summer 2015 had LAC loadings between about 3 and $5 \mu g cm^{-2}$ with BrC/LAC=0. The 14 samples from winter 2014/2015 had LAC

loadings between about 8 and 27μgcm^{-2} and BrC/LAC ratios from about 0.3 to 0.7, which were the highest BrC/LAC ratios in this period. TC values varied from 7 to 34μgcm^{-2} for summer samples and from 13 to 71μgcm^{-2} for winter samples.

To investigate the effect of WSOC, 8 randomly selected filters (out of the 21 samples) were cut in half and one piece of each filter was immersed in 80mL of Milli-Q water (18MΩcm, Millipore) in 100mL bottles and shaken mechanically in a shaking water bath (GFL Technology, type GFL 1086) for about 20min at room temperature with 100rpm to remove most of the WSOC as well as other soluble aerosol material (e.g., Gao et al., 2003; Kirchstetter and Novakov, 2004). The washed filters were removed from the bottles, transferred into petri dishes and dried in a desiccator for 3–4d. The dry filters were then stored at −22°C in closed petri dishes. In the following discussions, aliquots of the untreated (i.e., unheated and unwashed) filters are referred to as "original" samples.

2.4. Thermal–optical measurements and preparation of heated samples

The EC and OC content of the samples was measured with a dual-optics thermal–optical instrument (Sunset Instruments Inc.). In this instrument the sample is heated stepwise first in He and then in an oxidizing atmosphere (2% O_2 in He). The duration times of the steps and the temperatures and atmospheres for two different heating protocols (EUSAAR2 and NIOSH870) are listed in Table 1. The evolving carbon during each temperature step is tracked by a flame ionization detector (FID). The FID signal is proportional to the evolving carbon content and is calibrated by introducing a known amount of methane at the end of each filter measurement. The darkening of the sample during the heating procedure in the inert phase is monitored with a laser signal (in transmission and reflection with wavelength of 635nm), which is used afterwards to correct the results for pyrolysis: a split point is defined when the laser signal reaches its initial value, and the carbon evolving prior to the split point is assigned to OC and the carbon evolving afterwards to EC. The precision of the instrument is 6% for OC as well as for EC, and the lower detection limit is 0.1μgCcm^{-2} for OC and EC.

Twelve out of the 21 atmospheric aerosol samples were analyzed with both EUSAAR2 and NIOSH870 protocols (Table 1); the other 8 samples were only with EUSAAR2, as parts of these filters were washed to remove water-soluble material including WSOC (see below) and were therefore not available for extra analysis with another protocol. For both protocols, heated samples were prepared corresponding to the temperature levels of the inert phase and the first oxidizing temperature level of EUSAAR2: aliquots of the filters were heated in the instrument following the NIOSH870 and EUSAAR2 temperature steps and atmospheres, respectively, before the procedure was interrupted at the desired temperature level. All samples were cooled down in He to below 75°C, removed from the oven and stored in a closed petri dish at laboratory temperature.

2.5. Raman spectroscopy

For the investigation of the soot structure, a confocal Raman microscope (Horiba Jobin-Yvon LabRAM 800HR) was used. The Raman microscope was equipped with a 632.8nm HeNe laser (maximum output <20mW), a 532nm frequency-doubled Nd:YAG DPSS (diode-pumped solidstate) laser (Oxxius LMX-532, maximum output <52mW) and a CCD camera (Peltier cooled to −60°C). The laser beam was focused onto the sample with a 20× magnification objective lens (CF Plan, 20×/0.35, WD 20.5mm, Nikon) and a 100× long working distance (LWD) objective lens (MPlanN, 100×/0.75, WD 0.21mm, Olympus). The spectra were calibrated with the silicon peak at 520.07cm^{-1}. Generally Raman signals were obtained

for 10 spots for each (unheated and heated) filter sample within an area of (1×2)mm^2. We found that this area was large enough to characterize a whole sample. Only for some samples with too low loadings were five spots focused manually. The acquisition times were chosen between 0.005 and 3s and 30– 3000 single spectra were accumulated for each position (slit of 400µm, confocal hole of 500µm). A laser power between 25% and 100% was used. Generally laser power was lowered for highly absorbing samples to prevent thermal destruction of the material and for samples containing fluorescent material to reduce the interfering fluorescence background. The particular settings (acquisition time, number of accumulations, laser power) were chosen individually to obtain the best signal-to-noise ratio for each sample, since the fluorescence background intensity was different for the samples and for different excitation wavelengths.

Due to instrument availability, all samples were measured using the HeNe (red) laser, except the heated and unheated samples of the washed filters (see below) and their unwashed counterparts, which were measured using the Nd:YAG (green) laser. For samples heated to 500°C in O_2+He (EUSAAR2) and 870°C in He (NIOSH870), which were measured using the red laser, a 100× LWD objective lens and a smaller confocal hole (3µm) were used to focus on single particles since the red laser in combination with the 20× objective lens was not sufficient to obtain spectra for the small amounts of material left on the filters at these heating stages. The laser power was decreased to 1% and accumulations of 400 single spectra and an acquisition time of 0.5s were required. Because of these restrictions, Raman spectra were obtained for only five different spots for these samples. Mean spectra and their standard deviations were calculated for the spectra of all samples using the 5 to 10 spectra obtained from different measurement positions.

Typical Raman spectra of soot and related carbonaceous material show two overlapping peaks at about 1350cm^{-1} (*D*-peak or defect peak) and 1580cm^{-1} (*G*-peak or graphitic peak) (e.g., Fig. 1). Several authors (e.g., Sadezky et al., 2005; Le et al., 2019; Zickler et al., 2006, and references there) suggest that these peaks arise from five or more bands attributed to different vibrational modes in the soot structure. Detailed descriptions are given by, for example, Rosen and Novakov (1978), Sadezky et al. (2005), Ferrari and Robertson (2000), Schmid et al. (2011), Knauer et al. (2009) and Ivleva et al. (2007). The ratio of the *D* and *G* peak intensities (*D/G*) is an indication of the degree of structural ordering in the carbonaceous material (Tuinstra and Koenig, 1970; Ferrari and Robertson, 2000). For small crystallite sizes L_a <2nm, as can be found in combustion soot particles (see e.g., Haller et al., 2019), *D/G* is proportional to the probability to find sixfold aromatic rings in the cluster, which means that an increasing *D/G* ratio indicates increasing crystallite sizes (Ferrari and Robertson, 2000; Zickler et al., 2006) and therefore an increase of structural ordering. Ferrari and Robertson (2000) propose proportionality between D/G and L_a^2 with a wavelength-dependent factor. Because of this wavelength dependence, we discuss here only samples where all spectra (original, washed, heated, unheated) were obtained with the same excitation wavelength. A more detailed description of the interpretation of Raman spectra of soot can be found in the studies by Ferrari and Robertson (2000) or Haller et al. (2019). Several other authors use this interpretation of the *D/G* ratio for Raman spectra of combustion aerosol samples (e.g., Commodo et al., 2016; Ess et al., 2016) and use a higher *D/G* ratio as an indication of a higher degree of structural ordering within the material.

Carrier Gas	NIOSH870				EUSAAR2			
	duration	T [°C]	code	Raman	duration	T [°C]	code	Raman
He	80	310	NI310	✓	120	200	EU200	✓
He	80	475	NI475	✓	150	300	EU300	✓
He	80	615	NI615	✓	180	450	EU450	✓
He	110	870	NI870	✓	180	650	EU650	✓
He	45	550			30	-		
He+O_2	45	550			120	500	EU500	✓
He+O_2	625	45			120	550		
He+O_2	700	45			70	700		
He+O_2	775	45			80	850		
He+O_2	850	45			-	-		

Table 1. Duration times, temperatures and gas atmospheres for the two different thermal–optical measurement protocols (NIOSH870, EUSAAR2). The "Raman" column indicates that heated samples were analyzed with Raman spectroscopy for the respective temperature (see below). The codes are used when we refer to samples heated to a certain temperature – symbolized by the numeric index – following NIOSH870 (NI) or EUSAAR2 (EU).

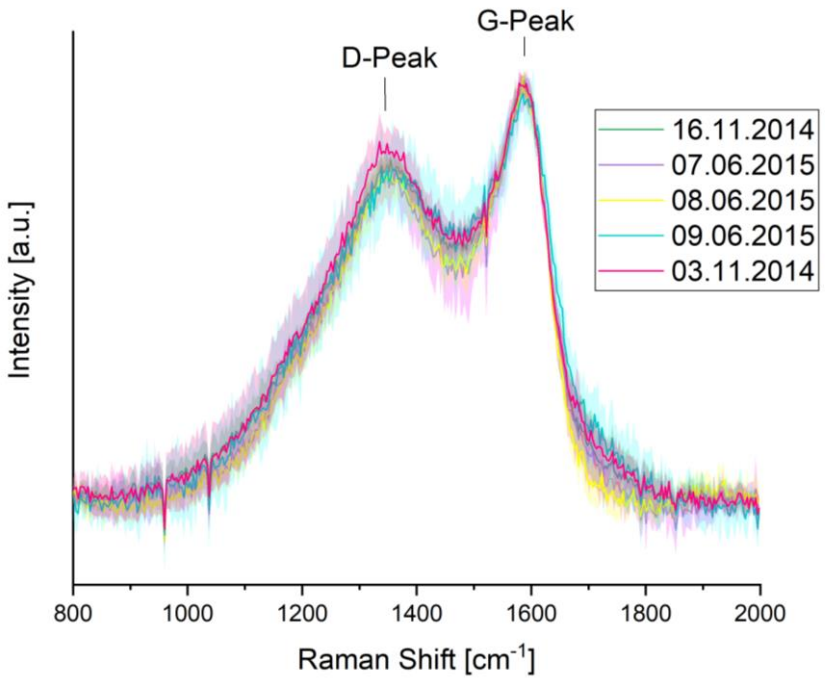

Figure 1. Raman spectra for a representative subset of original (unheated, unwashed) samples. Error bars (standard deviation of the mean spectra) are displayed as shaded areas. The spectra are similar among themselves within their error bars especially in the peak heights. For a better illustration, only five spectra were selected. All other spectra of original samples are comparable within their error bars.

2.6. Electron microscopy

As crystallite sizes are important for the interpretation of the D/G ratio in the Raman spectra, the crystallite sizes of three samples (16.11.2014, 09.06.2015, 10.11.2015) were exemplarily determined from electron diffraction patterns obtained with an electron microscope. A 200 kV transmission electron microscope (TEM) Philips CM200 equipped with a Gatan™ Orius CCD camera was used to obtain electron diffraction patterns. Intensity profiles of the diffraction patterns were obtained by both azimuthal integration along rings and background correction using PASAD-tools (Gammer et al., 2010). By fitting pseudo-Voigt functions to the intensity profiles taken from at least 6 different locations on each sample, the average full width at half maximum of the first intense diffraction peak was determined and used to calculate the mean crystallite size with the Scherrer equation (Fultz et al., 2001).

2.7. Ion chromatography

Aliquots of the filters (areas between 78 and 101 mm^2 depending on filter loadings) were extracted in 2 mL of ultrapure water (MilliQ, 18 MΩcm, Millipore). After ultrasonic agitation for 20 minutes and centrifugation for 5 minutes at 13400 rpm, the extracts were analyzed by suppressed ion chromatography. For the determination of the anions (Cl^-, NO_2^-, NO_3^- and SO_4^{2-}) a Dionex Aquion system (Thermo Fisher) equipped with CS16 and CG16 columns, a CERS 500 self-regenerating suppressor and a DS6 heated conductivity detector was used. The cations (Na^+, NH_4^+, Mg^{2+}, Ca^{2+} and K^+) were determined with a Dionex ICS-1100 system (Thermo Fisher) equipped with AS22 and AG22 columns, an AERS 500 self-regenerating suppressor and a DS6 heated conductivity detector. The calibration was performed with external standards, prepared from Merck stock solutions with 1000 ppm. The limit of detection for Cl^- is 0.005 mg/L, for all other analytes 0.01 mgL^{-1}.

3 Results

3.1 Properties of the original (unwashed and unheated) samples

The Raman spectra of all samples (e.g., Figs. 1, 2, 3) show two distinct peaks around 1350cm^{-1} (*D*-peak or defect peak) and 1580cm^{-1} (*G*-peak or graphitic peak) which is typical for soot. The Raman spectra of the original samples are surprisingly similar (Fig. 1), although the samples differ in composition. This could be explained by an appreciably higher contribution of graphite-like material to the Raman signal in comparison to the contribution of possibly coexisting organic or brown carbon.

Sommer (2020) found for the whole set of our samples that the fraction of BC in $PM_{2.5}$ (measured with the integrating sphere method) was relatively constant over the whole year. Traffic is one of the major sources of BC in Vienna in summer as well as in winter. In winter, space heating contributes only a small amount to BC, because district heating and natural gas are used in most households in Vienna (about 45% each in 2017/18; Statistik Austria, 2021) followed by electricity (about 6% in 2017/18; Statistik Austria, 2021). All of these are relatively clean systems regarding particle production. On the other hand, wood combustion is used by less than 1% of the households in Vienna, and oil or coal combustion are negligible (Statistik Austria, 2021). BrC emission factors of wood combustion can be nearly 10 times the emission factors for BC (e.g., Sun et al., 2021). Our winter samples have less than 70% BrC in LAC; therefore, also for the samples with the highest amount of BrC, nearly 80% of wintertime BC derives from traffic. In 2015 about 57% of all passenger cars and nearly 100% of heavy-duty vehicles in Vienna had diesel engines. Diesel fuel accounted for about 80% to total fuel sales in

2015 in Austria (WKO, Mineralölindustrie, 2020). Traffic is therefore a relatively constant and homogeneous source of carbonaceous aerosol, especially diesel soot. This could explain the similarity of the Raman spectra of all original samples.

Crystallite sizes of the three samples analyzed by TEM are well below 2nm (mean crystallite size of all three samples: 1.13±0.1nm). These sizes match with the crystallite sizes of two CAST soot samples in our recent publication (recalculated: 1.2±0.1nm for a BC-rich sample and 0.8±0.1nm for a BrC-rich sample; Haller et al., 2019). We therefore assume that the crystallite sizes of the other atmospheric aerosol samples in this study also should be below 2nm.

3.2 Structural changes of the washed samples

Washed and unwashed filter samples were analyzed with EUSAAR2, and Raman spectra were obtained for the nonheated and heated washed and unwashed samples. Figure 2 shows two typical thermograms: one of an unwashed and one of a washed part of the same filter. While the transmission laser signal of the unwashed sample decreases during the inert phase, the signal of the washed sample is nearly constant until it starts to increase during the 650°C step in He. The initial laser signal for the washed sample is higher than the one for the original sample indicating that part of the lightabsorbing material was removed during the washing procedure. Since the samples were shaken in this process, also substances which are not soluble in water (e.g., BC) could have been removed mechanically. This was confirmed by integrating sphere measurements: part of BC (about 60%) is absent and BrC is below detection limit also for samples with a high amount of BrC in the unwashed counterpart.

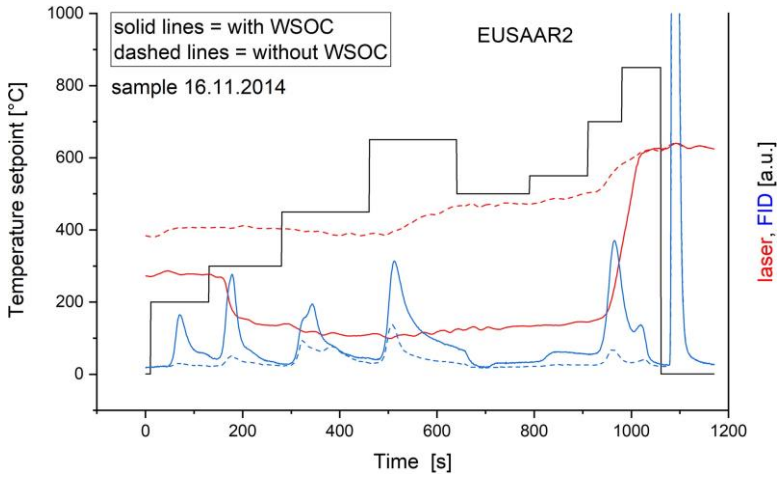

Figure 2. Typical thermogram of a sample with (solid lines) and without (dashed lines) WSOC. The transmission laser signal decreases during the first three temperature levels for the unwashed sample (red solid line) but stays nearly constant for the washed sample (red dashed line). The FID signals are lower for all temperature levels for the washed sample (blue dashed line) than for the unwashed sample (blue solid line). The black solid line represents the ideal progress of the sample temperature.

The differences in the laser signals between original and washed samples hold for all of the eight investigated samples (Fig. S1 in the Supplement). These findings are in good agreement with Yu et al. (2002), who found that WSOC accounted for a large contribution (13%–66%) to the charring during NIOSH-like heating procedures.

The *D/G* ratios of the Raman spectra of most unwashed samples increase during the heating procedure above 450°C (Fig. 3a and Sect. 3.3.2), indicating an increase of structural ordering according to Ferrari and Robertson (2000). On the other hand, the Raman spectra of the washed samples do not change noticeably during the heating process even when their unwashed counterparts have changing Raman signals (Fig. 3), indicating that no increase of structural ordering occurs during heating of the washed samples. This is in good agreement with the findings of Yu et al. (2002), who based their interpretation of charring of WSOC on thermal and optical properties of their heated samples. We can confirm this now by showing that the washed samples indeed do not change their structure (i.e., do not build graphite-like material) during heating. In contrast to cases where the laser signal decreases despite constant *D/G* ratios (as described in Sect. 3.3.1), it seems to be possible to conclude from an unchanged laser signal to a lack of structural ordering of the material.

The laser signals start to increase during the last temperature step in He (650°C) also for the washed samples. The Raman spectra of these samples show that structural ordering does not increase during the heating procedure and the relatively constant (transmission and/or reflectance) laser signals during the first three temperature levels suggest that no noticeable pyrolysis occurs. Therefore, we assume that some of the light-absorbing material which was originally on the filter evolves in the absence of oxygen at 650°C.This could be caused by a premature evolution of EC due to oxygenation with oxygen supplied by mineral oxides or catalysis by metal or other inorganic salts (Chow et al., 2001; Wang et al., 2010).

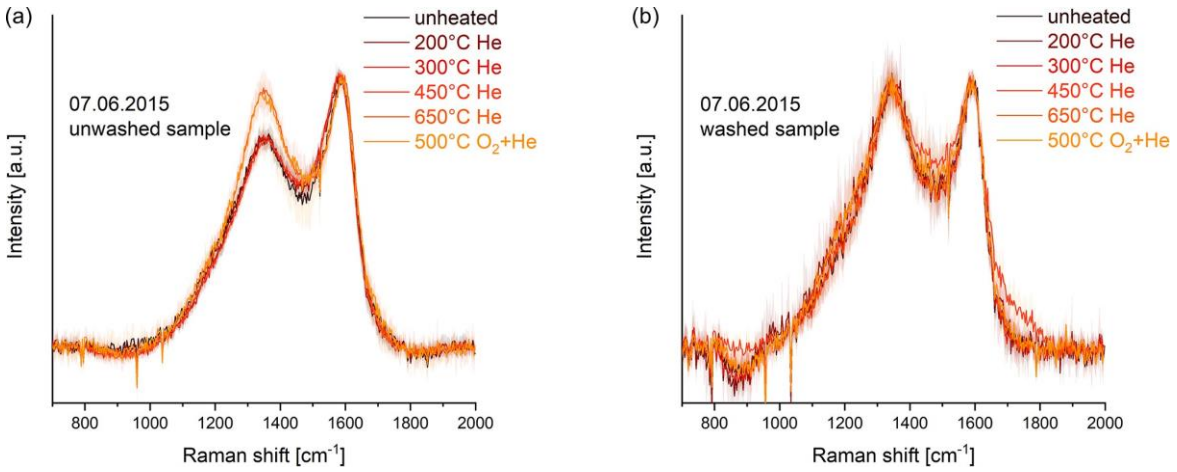

Figure 3. Progress of the Raman spectra during the heating procedure (EUSAAR2) of the washed (a) and unwashed (b) part of a representative atmospheric aerosol sample (7 June 2015). Error bars are shown as shaded areas. The Raman spectra of the unwashed sample change at 650°C in He (late and fast change; see categorization below), while the spectra of the washed sample do not change noticeably during heating following EUSAAR2.

3.3 Analysis of the unwashed (heated and original) samples

3.3.1 Comparison of structural changes EUSAAR2 vs. NIOSH870 after the inert phase

A comparison between NIOSH870 and EUSAAR2 protocols was performed for a subset of six unwashed samples (five winter, one summer). The *D/G* ratio increased during the course of the inert phase for both protocols (EUSAAR2 and NIOSH870). However, for three samples (13 June 2015, 3 December 2014, 25 October 2015) out of six, the *D/G* ratio at the maximum He temperature is significantly larger for NIOSH870 than for EUSAAR2 (Fig. 4). For the sample on 25 October 2015, *D/G* of EU500 (i.e., the

first temperature step in He+O_2) also remains lower than the *D/G* of NI870. For the other three samples (8 January 2015, 17 February 2015, 9 January 2015), relative *D*-peak intensities are similar for NI870 and EU650 as well as for EU500.

The larger increase of *D/G* for NI870 for some samples can be interpreted as a stronger increase of structural ordering, when these samples are heated according to the NIOSH870 protocol compared to EUSAAR2.

These differences could be caused by a stronger graphitization during the NIOSH870 protocol than during EUSAAR2 at least in three cases out of six. This would mean that PC developed during the heating with different protocols might also have different optical properties which would influence the decrease of the transmission and/or reflection laser signal during the thermal–optical measurement procedure. This would be in good agreement with Yu et al. (2002), who found that light absorption coefficients of PC formed during a thermal–optical heating procedure are not identical over the whole heating procedure. It is plausible that this might be true also for two protocols with different maximum temperatures in He. The higher *D/G* ratio for a higher heating temperature is also in accordance with Le et al. (2019), who found increasing *D/G* ratios between 600 and 800°C for their OC-rich samples heated in N_2.

As suggested by Chow et al. (2001), part of EC could leave the filter already during the 870°C temperature level in helium because of oxygenation or catalysis caused by mineral or other oxides at temperatures >700°C. This premature evolution of relatively structured material could also affect the *D/G* ratio during the highest inert temperature step in NIOSH870.

Therefore, we assume that the higher *D/G* ratio of NI870 for some samples could be a combination of stronger graphitization caused by the higher temperature and premature oxidation of EC during the 870°C level in NIOSH870. 3.3.2 Structural changes during EUSAAR2.

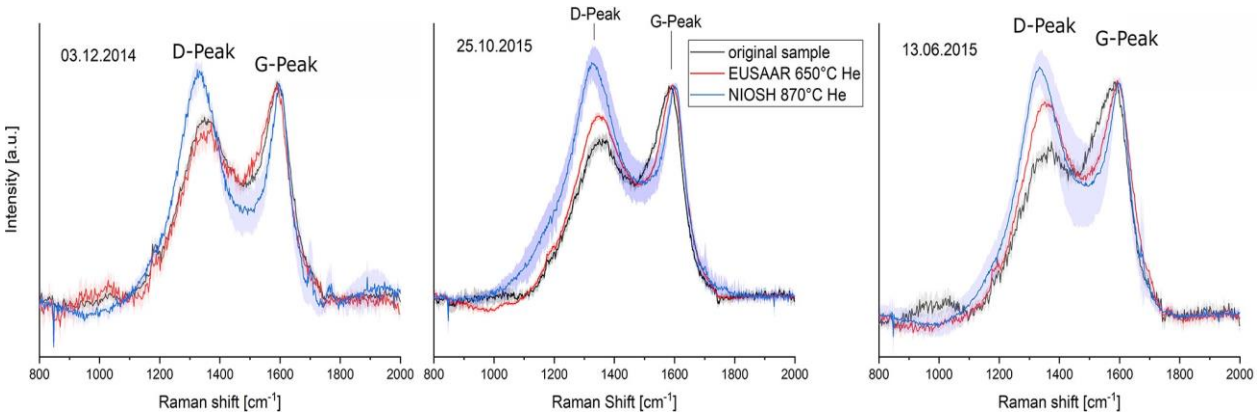

Figure 4. Comparison of Raman spectra of EU650 (red lines) and NI870 (blue lines) for the three samples where D/G of NI870 is larger than D/G of EU650 (from left to right: 3 December 2014, 25 October 2015 and 13 June 2015). Error bars are shown as shaded areas. The D/G ratio increases for NIOSH870 as well as for EUSAAR2 compared to the spectrum of the original sample (black lines), but the relative D-peak of NI870 is visibly higher than the D-peak of EU650 for all three samples

For all of the 21 (unwashed) samples, Raman spectra were taken for unheated samples and for samples heated according to the EUSAAR2 protocol. In most cases (17 out of 21) the *D/G* ratio increases during the heating process, indicating an increase of structural ordering. However, distinct changes of the Raman spectra occur at different temperature levels during the heating procedure in the inert phase (450– 650°C) or the oxidizing phase (500°C). Moreover in some cases the change happens only at one temperature level or extends over two temperature levels. Therefore, the samples were classified into six categories (subsequently referred to as "Raman categories") depending on the temperature levels where significant changes in the Raman signals occur: the significance was investigated by performing unpaired, twosided *t* tests for all spectra compared to the spectra of the next higher and lower temperature level, respectively, using a significance level α of 5%. Some slight decreases in the *D/G* peak ratio between EU200 and EU300 are visible, but they are not significant except for 1 sample out of 21 (13 June 2015, p =0.035). A possible explanation of this decrease is given by Le et al. (2019), who observed a similar behavior during heating in N_2 and gave as a reason for the evaporation of OC volatile components and cyclization of molecular structures. Since this decreasing *D/G* ratio is not significant in most of our samples, we focus here only on increasing *D/G* ratios. The six categories were defined as follows. (Sample codes are explained in Table 1 and examples for the categories are shown in Fig. 5a–e.)

- *Early structural change (four samples). D/G* ratio of the Raman spectrum obtained for EU450 is significantly higher according to a *t* test with α = 5% than *D/G* ratio of the spectrum for EU300. And *D/G* ratio of EU650 is significantly higher than *D/G* of EU450. The *D/G* ratios do not increase significantly between unheated sample, EU200 and EU300 and between EU650 and EU500 (Fig. 5a).

- *Late structural change (two samples). D/G* ratio of the Raman spectrum of EU650 is significantly higher than *D/G* of the Raman spectrum of EU450 and *D/G* of the Raman spectrum of EU500 is significantly higher than *D/G* of EU650. The *D/G* ratio does not increase significantly between the unheated sample, EU200, EU300, EU450 or EU650 (Fig. 5b).

- *No change (four samples).* All mean spectra lie within the error bars of the other spectra, and *D/G* ratios do not change significantly (Fig. 5c).

- *Fast and early structural change (one sample). D/G* ratio of the Raman spectrum of EU450 is significantly higher than *D/G* of EU300, and *D/G* does not decrease significantly between EU200 and EU300 as well as between EU450, EU650 and EU500 (Fig. 5d).

- *Fast and late structural change (six samples). D/G* ratio of the Raman spectrum of EU650 is significantly higher than *D/G* of EU450, and *D/G* does not increase significantly between EU200, EU300 and EU450 as well as between EU650 and EU500 (Fig. 5e).

- *Undefined (four samples).* Changes of the Raman spectra cannot be assigned unambiguously to one of the other five categories as a consequence of too strong noise signals.

The changes of peak ratios as a function of temperature level are shown in Fig. 5 for all samples of each category as well as examples for the changes in the Raman spectra. It is remarkable that the spectra of the heated samples differ and show different progresses over the heating procedure (Fig. 5), although the Raman spectra of the original (unheated) samples are comparable. Therefore, we conclude that the differences in the progress of restructuring might not be caused by the degree of structural ordering of the original samples or at least cannot be simply predicted by their Raman spectra.

3.3.3 Structural changes and laser signals (EUSAAR2)

During the thermal–optical analysis procedure with EUSAAR2 as well as with NIOSH870 decreasing (transmission and reflection), laser signals were observed during the inert phase for all unwashed samples. The signals started to increase again during the last temperature level in He for both protocols. This increase was also described by other authors (e.g., Chow et al., 2004; Yu et al., 2002).

For a more detailed analysis of the progress of the laser signals, we focus on EUSAAR2 here. During the heating following EUSAAR2, the reflection laser signals decrease in more or less pronounced steps at each temperature level in the He phase, and no distinct differences between the samples and therefore no relationship between the changes of the Raman spectra and the reflection laser signals are visible. For the transmission signals, two different types of decrease can be observed. For some samples, the signal decreases with a pronounced step during the 300°C temperature level in He. For other samples, the transmission laser signal shows a relatively steady decrease before it reaches its minimal value. However, no relation between the slope of the decrease and the Raman categories is visible. The diagrams can be found in the Supplement (Figs. S2 and S3).

Figure 6 shows a comparison of the *D/G* ratio and the value of the transmission laser signal at the end of each temperature level in EUSAAR2 sorted by the Raman categories. It is obvious that the decrease of the transmission signal is not related to the increase of the *D/G* ratio. Samples with similar behavior of the Raman signals can have different curves of the transmission laser signals and vice versa. It is also noteworthy that the strongest decreases of the transmission laser signals do not occur at the temperature levels where changes in the Raman spectra are observable (450, 650°C). We found similar effects in our earlier study (Haller et al., 2019) where we compared UV–Vis spectra of heated (NIOSH870 protocol) CAST soot samples with the changes of the respective Raman spectra. The UV–Vis spectra started to change at lower temperatures, while the Raman spectra changed only at the highest temperature in He (870°C).

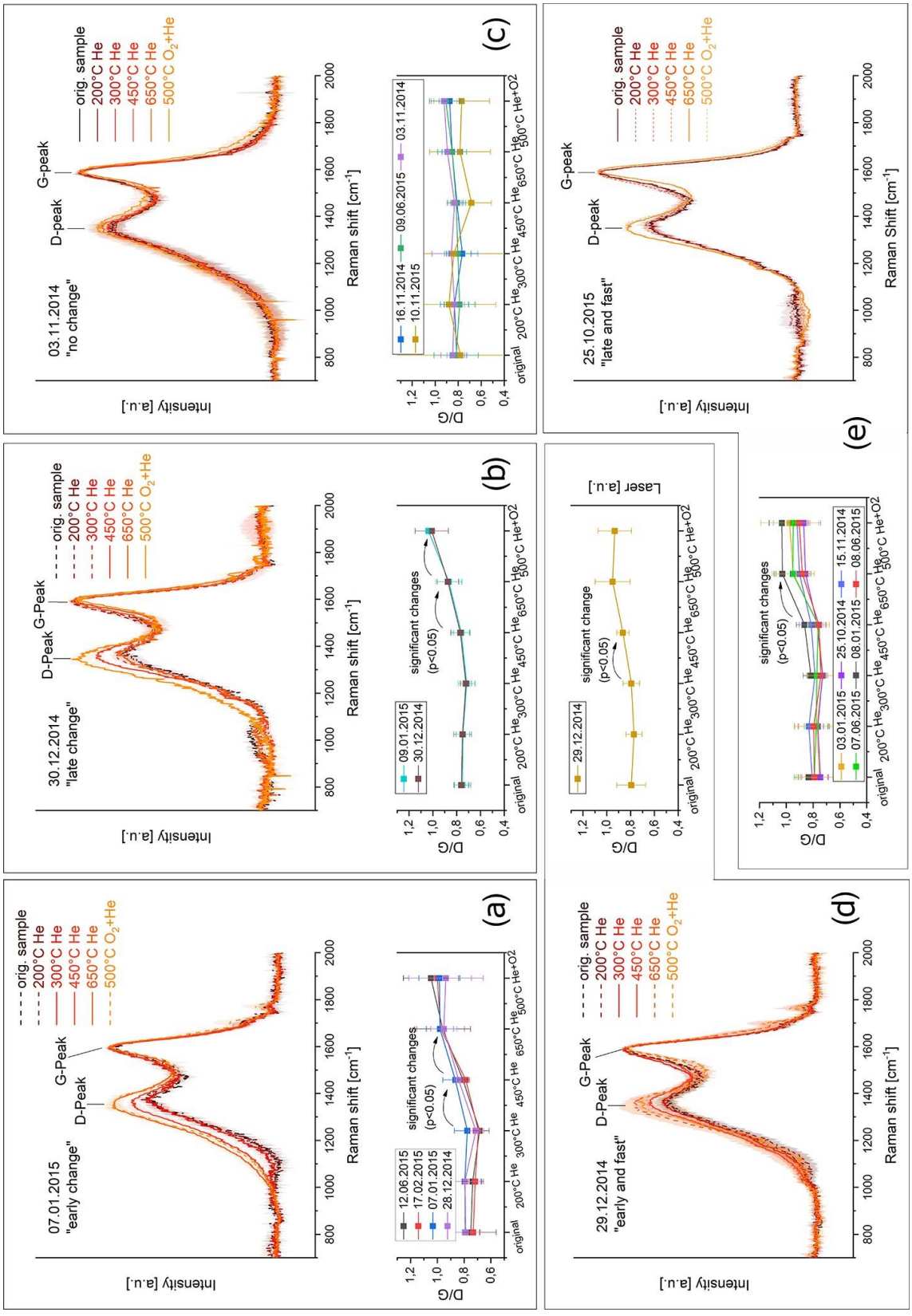

Figure 5. Examples of Raman spectra for of heated and unheated filter samples assigned to the categories "early structural change" (a), "late structural change" (b), "no structural change" (c) "early and fast structural change" (d) and "late and fast structural change" (e). Error bars are shown as shaded areas. The changes of D/G ratio with heating temperature are shown for all samples assigned to the respective category in an additional image. Arrows indicate the temperature levels where significant changes were identified according to a t test (α = 5%).

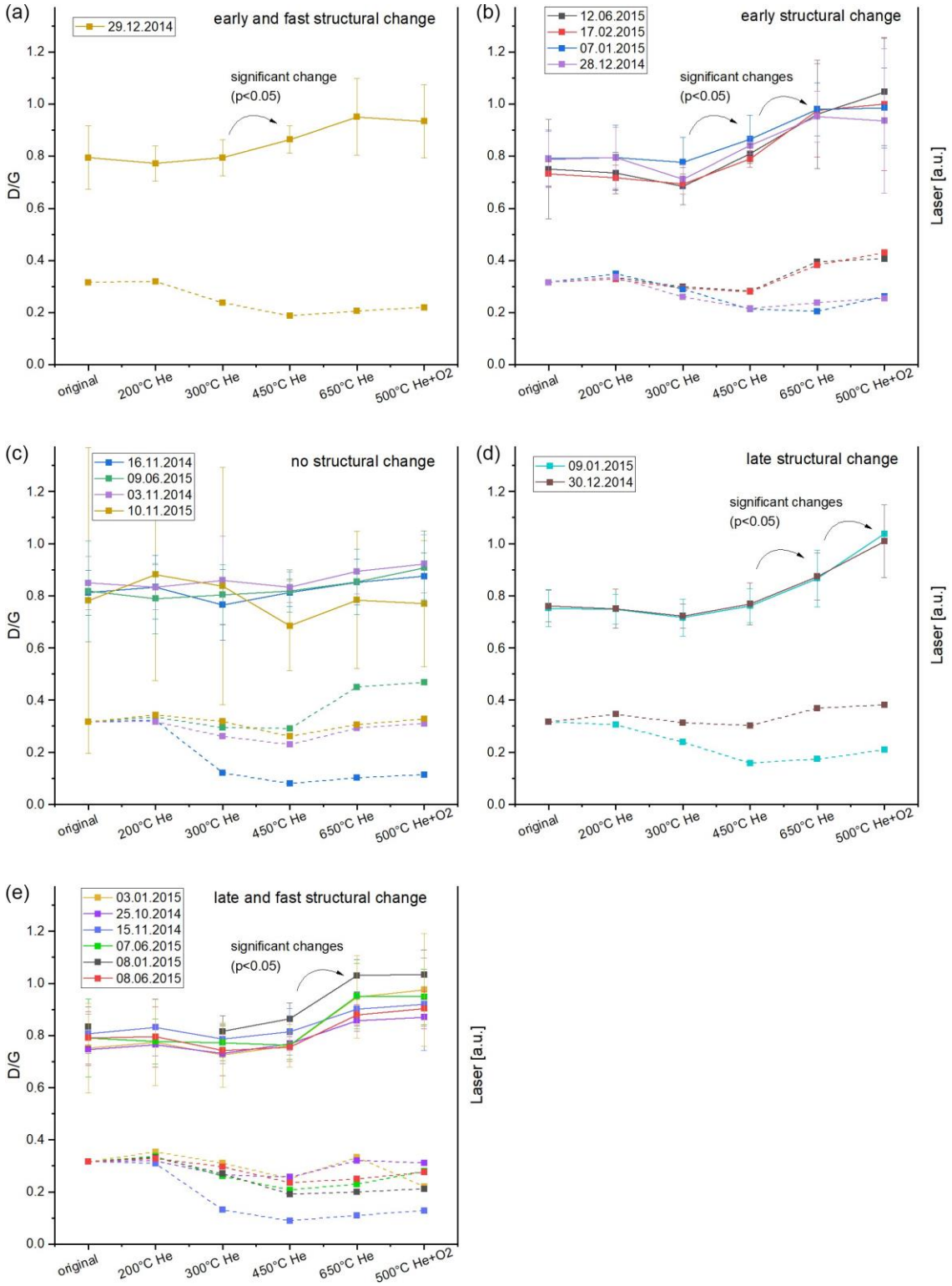

Figure 6. Comparison of the changes of D/G peak ratios (solid lines, left axis) and transmission laser signals (dashed lines, right axis) at the end of each temperature level sorted by Raman categories. Standard deviations of D/G are calculated from the standard deviations of the Raman spectra. All laser signals are normalized to the signal at the end of the measurement procedure (i.e., signal of the clean filter). The curves for the different filters are shifted at the y axis so that all curves start at the same point (original sample). It is visible that changes in D/G and changes in laser signal are not related.

This lack of correlation between laser signal and *D/G* ratio is most striking for the four samples with no change in the Raman spectra of the heated samples (Fig. 6c). Although the Raman spectra do not indicate an increase of structural ordering, the (transmission, reflection) laser signals decrease during the heating procedure in He. Therefore, we conclude that the formation or increase of graphite-like structures cannot be the only reason for the darkening (i.e., stronger absorption of the red laser signal). Our data give evidence that non-graphitic material with smaller optical band gaps and therefore higher absorbance at 635nm than in the unheated material might be formed. This corresponds also to the findings of Yu et al. (2002), who assume that light-absorbing intermediate OC products are formed during the inert phase of the thermal–optical measurement procedures they used (a NIOSH method and other experimental temperature protocols). Le et al. (2019) performed a detailed analysis of several heated CAST soot samples and suggest a removal of C−H "out-of-plane" bonds around 350–400°C, a decomposition of oxygen containing surface groups (C−O,C=O) or a decrease of cross-linkages between polyaromatic units and carbon chains. All of these transformations could influence the optical properties without an increase of graphite-like structures.

3.3.4 Possible relations of structural changes with other parameters

Generally, the charring behavior of aerosol samples or the reliability of thermal–optical measurements is often reported to be influenced by the composition of the aerosol (e.g., Wang et al., 2010; Yu et al., 2002; Reisinger et al., 2008; Wonaschuetz et al., 2009). Since our samples show differing charring behaviors, we investigated possible relations to the aerosol composition using the unwashed samples. We compared the progress of structural changes (expressed by the assignment to the Raman categories) to the chemical composition of the non-carbonaceous matter and to the composition of the carbonaceous matter (LAC/BC, EC/OC). The ionic composition of the samples sorted by their Raman categories is shown in Fig. 7.

No relationship between the ionic components and the progress of restructuring of the material is visible. This could be explained by the study by Yu et al. (2002), who showed that one and the same compound can enhance or reduce charring depending on the chemistry of the organic substances present in the sample. Although they analyzed only three standards for organic carbon, it is possible that similar counteracting influences could be found also for other organic substances which could suppress a possible relationship between charring and the inorganic material within a sample.

The progress of structural changes is also unrelated to the BrC/LAC ratio (Fig. 8). Samples with BrC below detection limit are found in nearly all the Raman categories. Especially the samples in the category "no change" during heating do not have appreciably lower BrC/LAC ratios than others. This is quite interesting, because previous studies in Austrian aerosol (e.g., Reisinger et al., 2008; Wonaschuetz et al., 2009) found larger discrepancies between EC values obtained with different thermal–optical methods for atmospheric aerosol samples with high contributions of BrC to LAC, up to about 0.9 (Wonaschuetz et al., 2009) and 0.75 (Reisinger et al., 2008). These values are comparable to the BrC/LAC of about 0.7 in our study. At the time of the earlier studies, it was not possible to determine whether these discrepancies were due to a higher tendency of BrC to char (and therefore influence the EC/OC split) or from other BrC-related processes. Our findings suggest that the relative amount of BrC has no influence on the increase of structural ordering during the heating procedure at least for the samples analyzed here. The discrepancies between different thermal–optical methods for BrC-rich samples might therefore have other reasons than a restructuring of BrC in terms of increased structural ordering.

4 Conclusion

The aim of this study was to investigate structural changes of carbonaceous matter during thermal–optical analyses. Two different thermal–optical measurement protocols with different maximum temperatures in the He phase (EUSAAR2, NIOSH870) were used to show the progress of restructuring of carbonaceous material during heating. Raman spectra of unheated and heated samples were taken for 21 atmospheric aerosol samples. A subset of these samples was washed with water to remove WSOC and other water-soluble constituents. The transmission laser signal patterns during the EUSAAR2 protocol and the progress of structural changes were compared for the washed samples and their unwashed counterparts.

We found that the laser signals did not decrease during the heating procedure of the washed samples but decreased when the unwashed samples were heated. This is in good agreement with Yu et al. (2002), who observed that water-soluble material contributed most to charring. The *D/G* peak ratios of the Raman spectra of the washed samples did not change appreciably during heating in He following the EUSAAR2 protocol. We therefore infer that the relatively constant transmission laser signal can indeed be interpreted as a lack of graphitization.

A comparison between EUSAAR2 and NIOSH870 was performed for six unwashed samples. EUSAAR2 is used in Europe as a standard method to monitor EC and OC (Brown et al., 2017). One of the arguments for the introduction of EUSAAR2 was that less PC is formed during EUSAAR2 in comparison with other (NIOSH-like) temperature protocols (Cavalli et al., 2010). However, this argument was solely based on the decrease of the transmission laser signal. Structural changes of the material were not investigated. We found now that the *D/G* peak ratios of the Raman spectra can be higher for samples heated to the maximum He temperature of NIOSH870 compared to samples heated to the maximum He temperature of EUSAAR2 at least for some samples, which means that PC formed during NIOSH870 might have a higher degree of structural ordering in these cases.

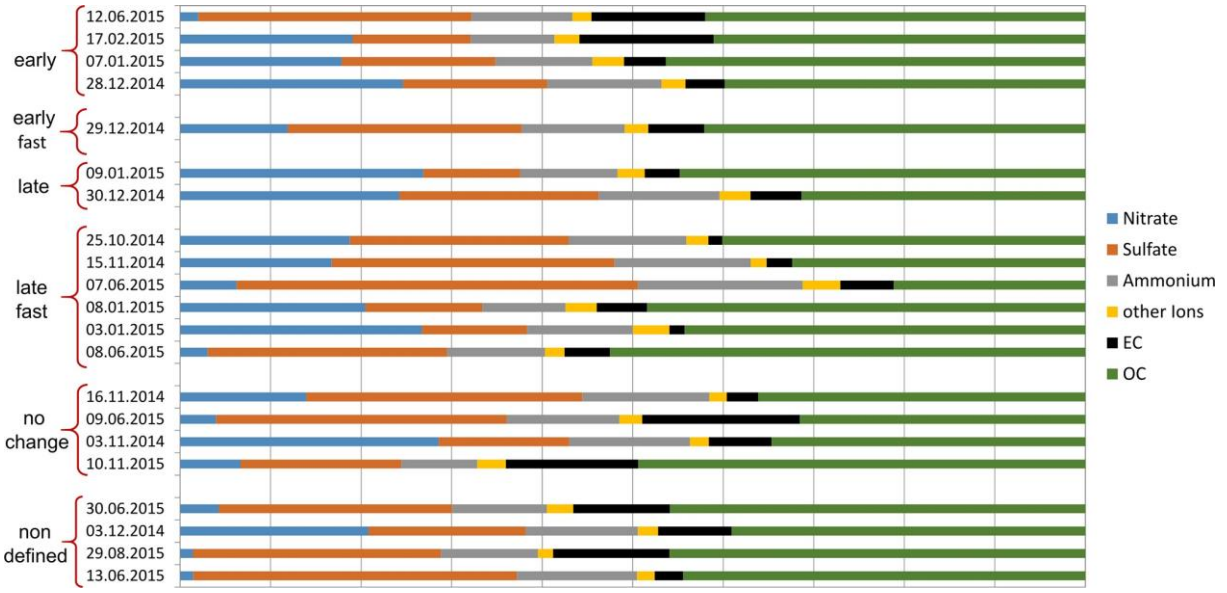

Figure 7. Fractions of analyzed ions, elemental carbon (EC) and organic carbon (OC) sorted by the categories representing the behavior of the Raman spectra during the thermal–optical heating procedure. The contribution of minor ions to the category "other ions" can be found in the Supplement.

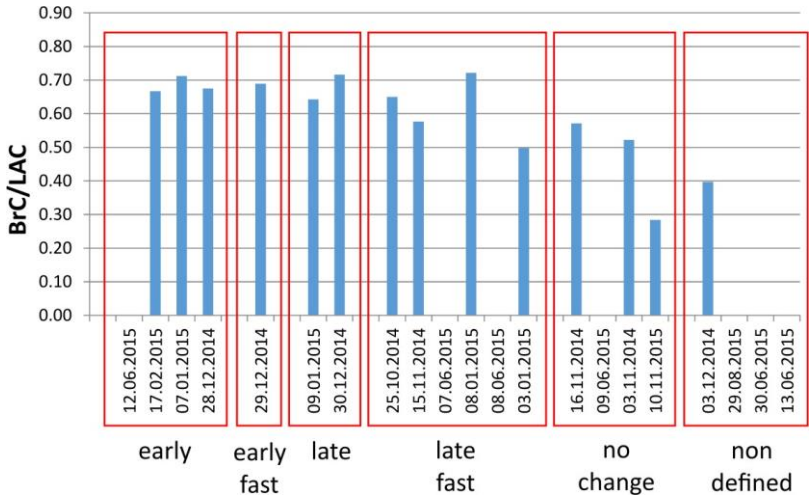

Figure 8. Comparison of BrC/LAC with the categories representing the behavior of the Raman signal during the heating procedure of the thermal–optical analysis. For samples with BrC/LAC=0 (i.e., no bar in the diagram), BrC was below the detection limit (<12.7µgcm^{-2}).

When comparing the Raman spectra for 21 samples heated following the EUSAAR2 protocol, we found a rather complex behavior of structural changes. Since changes in the Raman signals (i.e., the ratio of the peak intensities) occur at different temperature levels, we defined six Raman categories of samples depending on the temperature levels, where significant changes in the Raman spectra occur and how fast they proceed. We tried to find similarities for samples with similar progress of structural changes (i.e., the attribution to one of the six Raman categories) and chemical composition (BC, BrC, major ions), but we did not find any relationship. This is in good agreement with Wang et al. (2010) and Yu et al. (2002), who found that non-carbonaceous components have conflicting influences on the charring behavior during thermal–optical analyses.

We also investigated the progress of the thermal–optical transmission laser signals in relation to the Raman categories corresponding to the temperature levels where visible structural changes occur. It was obvious that the decrease of the transmission signal did not occur at the same temperature levels where structural changes in terms of increased ordering were found. This lack of a relation is most prominent for samples where the *D/G* peak ratios of the Raman spectra do not change during the whole heating procedure in He. Although the Raman spectra do not indicate an increase of structural ordering, the transmission (and reflection) laser signals still decrease during the He phase. Moreover no noticeable differences can be seen between the transmission laser signal patterns of samples where no increase of ordering occurs in comparison with samples where the Raman spectra change during heating.

We therefore conclude that some of the processes that lead to a darkening of the sample (i.e., more absorption at 635nm) do not affect the relative peak heights of the Raman spectra, which means that structural ordering does not increase (similar findings as well as their interpretation were described for CAST soot samples in our previous publication; Haller et al., 2019). Processes suggested by various authors include, for example, the separation of oxygen and hydrogen at temperatures above 250°C in He (Petzold et al., 2013; Chow et al., 2004, Le et al., 2019), the decomposition of oxygen containing surface groups (C−O,C=O) or a decrease of crosslinkages between polyaromatic units and carbon chains (Le et al., 2019). All of these transformations could affect the optical properties of the material

without affecting the *D/G* peak ratio of the Raman spectra. These findings are in good agreement with Yu et al. (2002), who describe a possible formation of light-absorbing intermediate (non-graphitic) OC products during the inert phase of thermal–optical analyses.

In the literature the darkening of a sample during thermal– optical analysis is often explained by "charring" or "pyrolysis", although exact descriptions of the underlying structural changes are not given. Based on our findings, it is important to point out that what is called "charring" or "pyrolysis" is not necessarily an increase of structural ordering. Particularly the group of samples where the *D/G* peak ratio does not change over the whole heating procedure gives evidence that the darkening of the sample cannot be understood as building of graphite-like structures in all cases. We therefore suggest that the widely used terms "charring" and "pyrolysis" should be used carefully when the darkening of a sample during thermal–optical measurement procedures is interpreted.

In summary, we can say that restructuring of carbonaceous matter during thermal–optical analysis is very complex and not easily predictable for atmospheric aerosol samples. At least for the washed samples, the constant transmission and/or reflection signal indicates an absence of graphitization, but for all samples a decrease of the transmission or reflection laser signal during the heating procedures is not a reliable indicator for an increase of structural ordering since other processes can also lead to a darkening of the material.

Data availability. Data can be accessed by contacting the corresponding author.

Supplement. The supplement related to this article is available online at: https://doi.org/10.5194/amt-14-3721-2021-supplement.

Author contributions. TH performed the conceptualization of the experimental setup, most measurements (except TEM, BrC/BC, ion chromatography), the data evaluation and interpretation and prepared the article. ES performed the BrC/BC measurements. TS performed the ion chromatography measurements and wrote the text in the Experimental section. CR performed the TEM measurements and wrote the TEM section. AW supervised the BrC/BC measurements. AKG contributed to discussions and provided input for the ion chromatography and to the article in general. HG contributed to discussions and provided input for the Raman measurements. RH performed the conceptualization and supervision of the study, contributed to discussions and provided extensive input to the text.

Competing interests. The authors declare that they have no conflict of interest.

Acknowledgements. This work was supported by the Austrian Science Fund (FWF), grant P26040. The integrating sphere technique was developed thanks to grant H-85/92, Hochschuljubiläumstiftung der Stadt Wien.

We thank the Analytical Instrumentation Center (AIT) of the Vienna University of Technology and the group of Bernhard Lendl for providing the Raman microscope, and we thank Angelika Geroldinger for the advice regarding the statistical tests.

Financial support. This research has been supported by the Austrian Science Fund (grant no. P26040) and the Hochschuljubiläumstiftung der Stadt Wien (grant no. H-85/92).

Review statement. This paper was edited by Zamin A. Kanji and reviewed by two anonymous referees.

References

Andreae, M. O. and Gelencsér, A.: Black carbon or brown carbon? The nature of light-absorbing carbonaceous aerosols, Atmos. Chem. Phys., 6, 3131–3148, https://doi.org/10.5194/acp-63131-2006, 2006.

Birch, M. E. and Cary, R. A.: Elemental Carbon-Based Method for Monitoring Occupational Exposures to Particulate Diesel Exhaust, Aerosol Sci. Tech., 25, 221–241, https://doi.org/10.1080/02786829608965393, 1996.

Bladt, H., Ivleva, N. P., and Niessner, R.: Internally mixed multicomponent soot: Impact of different salts on soot structure and thermo-chemical properties, J. Aerosol Sci., 70, 26–35, https://doi.org/10.1016/j.jaerosci.2013.11.007, 2014.

Bond, T. C. and Bergstrom, R. W.: Light Absorption by Carbonaceous Particles: An Investigative Review, Aerosol Sci. Tech., 40, 27–67, https://doi.org/10.1080/02786820500421521, 2006.

Brown, R. J. C., Beccaceci, S., Butterfield, D. M., Quincey, P. G., Harris, P. M., Maggos, T., Panteliadis, P., John, A., Jedynska, A., Kuhlbusch, T. A. J., Putaud, J.-P., and Karanasiou, A.: Standardisation of a European measurement method for organic carbon and elemental carbon in ambient air: results of the field trial campaign and the determination of a measurement uncertainty and working range, Environ. Sci.-Proc. Imp., 19, 1249–1259, https://doi.org/10.1039/C7EM00261K, 2017.

Cavalli, F., Viana, M., Yttri, K. E., Genberg, J., and Putaud, J.-P.: Toward a standardised thermal-optical protocol for measuring atmospheric organic and elemental carbon: the EUSAAR protocol, Atmos. Meas. Tech., 3, 79–89, https://doi.org/10.5194/amt-3-792010, 2010.

Cheng, Y., Duan, F.-K., He, K.-B., Du, Z.-Y., Zheng, M., and Ma, Y.-L.: Intercomparison of thermal-optical method with different temperature protocols: Implications from source samples and solvent extraction, Atmos. Environ., 61, 453–462, https://doi.org/10.1016/j.atmosenv.2012.07.066, 2012.

Chow, J. C., Watson, J. G., Crow, D., Lowenthal, D. H., and Merrifield, T.: Comparison of IMPROVE and NIOSH Carbon Measurements, Aerosol Sci. Tech., 34, 23–34, https://doi.org/10.1080/027868201300081923, 2001.

Chow, J. C., Watson, J. G., Chen, L.-W. A., Arnott, W. P., Moosmüller, H., and Fung, K.: Equivalence of Elemental Carbon by Thermal/Optical Reflectance and Transmittance with Different Temperature Protocols, Environ. Sci. Technol., 38, 4414–4422, https://doi.org/10.1021/es034936u, 2004.

Commodo, M., de Falco, G., Larciprete, R., D'Anna, A., and Minutolo, P.: On the hydrophilic/hydrophobic character of carbonaceous nanoparticles formed in laminar premixed flames, Exp. Therm. Fluid Sci., 73, 56–63, https://doi.org/10.1016/j.expthermflusci.2015.09.005, 2016.

Ess, M. N., Ferry, D., Kireeva, E. D., Niessner, R., Ouf, F.X., and Ivleva, N. P.: In situ Raman microspectroscopic analysis of soot samples with different organic carbon content: Structural changes during heating, Carbon, 105, 572–585, https://doi.org/10.1016/j.carbon.2016.04.056, 2016.

Ferrari, A. C. and Robertson, J.: Interpretation of Raman spectra of disordered and amorphous carbon, Phys. Rev. B, 61, 14095– 14107, https://doi.org/10.1103/PhysRevB.61.14095, 2000.

Fultz, B. and Howe, J. M.: Transmission electron microscopy and diffractometry of materials, Physics and astronomy online library, Springer, Berlin, Germany, 2001.

Gammer, C., Mangler, C., Rentenberger, C., and Karnthaler, H. P.: Quantitative local profile analysis of nanomaterials by electron diffraction, Scripta Mater., 63, 312–315, https://doi.org/10.1016/j.scriptamat.2010.04.019, 2010.

Gao, S., Hegg, D. A., Hobbs, P. V., Kirchstetter, T. W., Magi, B. I., and Sadilek, M.: Water-soluble organic components in aerosols associated with savanna fires in southern Africa: Identification, evolution, and distribution, J. Geophys. Res., 108, 8491, https://doi.org/10.1029/2002JD002324, 2003.

Haller, T., Rentenberger, C., Meyer, J. C., Felgitsch, L., Grothe, H., and Hitzenberger, R.: Structural changes of CAST soot during a thermal–optical measurement protocol, Atmos. Meas. Tech., 12, 3503–3519, https://doi.org/10.5194/amt-12-3503-2019, 2019.

Han, Y., Cao, J., Chow, J. C., Watson, J. G., An, Z., Jin, Z., Fung, K., and Liu, S.: Evaluation of the thermal/optical reflectance method for discrimination between char- and soot-EC, Chemosphere, 69, 569–574, https://doi.org/10.1016/j.chemosphere.2007.03.024, 2007.

Highwood, E. J. and Kinnersley, R. P.: When smoke gets in our eyes: The multiple impacts of atmospheric black carbon on climate, air quality and health, Environ. Int., 32, 560–566, https://doi.org/10.1016/j.envint.2005.12.003, 2006.

Hitzenberger, R. and Tohno, S.: Comparison of black carbon (BC) aerosols in two urban areas – concentrations and size distributions, Atmos. Environ., 35, 2153–2167, https://doi.org/10.1016/S1352-2310(00)00480-5, 2001.

Hitzenberger, R., Petzold, A., Bauer, H., Ctyroky, P., Pouresmaeil, P., Laskus, L., and Puxbaum, H.: Intercomparison of Thermal and Optical Measurement Methods for Elemental Carbon and Black Carbon at an Urban Location, Environ. Sci. Technol., 40, 6377–6383, https://doi.org/10.1021/es051228v, 2006.

Ivleva, N. P., Messerer, A., Yang, X., Niessner, R., and Pöschl, U.: Raman Microspectroscopic Analysis of Changes in the Chemical Structure and Reactivity of Soot in a Diesel Exhaust Aftertreatment Model System, Environ. Sci. Technol., 41, 3702– 3707, https://doi.org/10.1021/es0612448, 2007.

Jankowski, N., Schmidl, C., Marr, I. L., Bauer, H., and Puxbaum, H.: Comparison of methods for the quantification of carbonate carbon in atmospheric PM10 aerosol samples, Atmos. Environ., 42, 8055–8064, https://doi.org/10.1016/j.atmosenv.2008.06.012, 2008.

Kirchstetter, T. W., Novakov, T., and Hobbs, P. V.: Evidence that the spectral dependence of light absorption by aerosols is affected by organic carbon, J. Geophys. Res., 109, D21208, https://doi.org/10.1029/2004JD004999, 2004.

Knauer, M., Schuster, M. E., Su, D., Schlögl, R., Niessner, R., and Ivleva, N. P.: Soot structure and reactivity analysis by Raman microspectroscopy, temperature-programmed oxidation, and highresolution transmission electron microscopy, J. Phys. Chem. A, 113, 13871–13880, https://doi.org/10.1021/jp905639d, 2009.

Le, K. C., Pino, T., van Pham, T., Henriksson, J., Török, S., and Bengtsson, P.-E.: Raman spectroscopy of miniCAST soot with various fractions of organic compounds: Structural characterization during heating treatment from 25 °C to 1000 °C, Combust. Flame, 209, 291–302, https://doi.org/10.1016/j.combustflame.2019.07.037, 2019.

Lukács, H., Gelencsér, A., Hammer, S., Puxbaum, H., Pio, C., Legrand, M., Kasper-Giebl, A., Handler, M., Limbeck, A., Simpson, D., and Preunkert, S.: Seasonal trends and possible sources of brown carbon based on 2-year aerosol measurements at six sites in Europe, J. Geophys. Res., 112, 1052, https://doi.org/10.1029/2006JD008151, 2007. Müller, K., Spindler, G., Maenhaut, W., Hitzenberger, R., Wieprecht, W., Baltensperger, U., and ten Brink, H.: INTERCOMP2000, a campaign to assess the comparability of methods in use in Europe for measuring aerosol composition, Atmos. Environ., 38, 6459–6466, https://doi.org/10.1016/j.atmosenv.2004.08.031, 2004.

Panteliadis, P., Hafkenscheid, T., Cary, B., Diapouli, E., Fischer, A., Favez, O., Quincey, P., Viana, M., Hitzenberger, R., Vecchi, R., Saraga, D., Sciare, J., Jaffrezo, J. L., John, A., Schwarz, J., Giannoni, M., Novak, J., Karanasiou, A., Fermo, P., and Maenhaut, W.: ECOC comparison exercise with identical thermal protocols after temperature offset correction – instrument diagnostics by in-depth evaluation of operational parameters, Atmos. Meas. Tech., 8, 779–792, https://doi.org/10.5194/amt-8779-2015, 2015.

Petzold, A., Ogren, J. A., Fiebig, M., Laj, P., Li, S.-M., Baltensperger, U., Holzer-Popp, T., Kinne, S., Pappalardo, G., Sugimoto, N., Wehrli, C., Wiedensohler, A., and Zhang, X.-Y.: Recommendations for reporting "black carbon" measurements, Atmos. Chem. Phys., 13, 8365–8379, https://doi.org/10.5194/acp13-8365-2013, 2013.

Pöschl, U.: Atmospheric Aerosols: Composition, Transformation, Climate and Health Effects, Angew. Chem. Int. Ed., 44, 7520–7540, https://doi.org/10.1002/anie.200501122, 2005.

Reisinger, P., Wonaschütz, A., Hitzenberger, R., Petzold, A., Bauer, H., Jankowski, N., Puxbaum, H., Chi, X., and Maenhaut, W.: Intercomparison of Measurement Techniques for Black or Elemental Carbon Under Urban Background Conditions in Wintertime: Influence of Biomass Combustion, Environ. Sci. Technol., 42, 884–889, https://doi.org/10.1021/es0715041, 2008.

Rosen, H. and Novakov, T.: Identification of primary particulate carbon and sulfate species by Raman spectroscopy, Atmos. Environ., 12, 923–927, https://doi.org/10.1016/0004-6981(78)900318, 1978.

Sadezky, A., Muckenhuber, H., Grothe, H., Niessner, R., and Pöschl, U.: Raman microspectroscopy of soot and related carbonaceous materials: Spectral analysis and structural information, Carbon, 43, 1731–1742, https://doi.org/10.1016/j.carbon.2005.02.018, 2005.

Schmid, J., Grob, B., and Niessner, R., Ivleva, N. P.: Multiwavelength Raman Microspectroscopy for Rapid Prediction of Soot Oxidation Reactivity, Anal. Chem., 83, 1173–1179, https://doi.org/10.1021/ac102939w, 2011.

Sommer, E.: Long Term Trends of Black and Brown Carbon Concentrations in the Urban Aerosol of Vienna, Master Thesis, University of Vienna, Vienna, Austria, 2020.

Statistik Austria: https://www.statistik.at/web_de/statistiken/ energie_umwelt_innovation_mobilitaet/energie_und_umwelt/ energie/energieeinsatz_der_haushalte/index.html, last access 18 February 2021.

Subramanian, R., Khlystov, A. Y., and Robinson, A. L.: Effect of Peak Inert-Mode Temperature on Elemental Carbon Measured Using Thermal-Optical Analysis, Aerosol Sci. Tech., 40, 763– 780, https://doi.org/10.1080/02786820600714403, 2006.

Sun, J., Zhang, Y., Zhi, G., Hitzenberger, R., Jin, W., Chen, Y., Wang, L., Tian, C., Li, Z., Chen, R., Xiao, W., Cheng, Y., Yang, W., Yao, L., Cao, Y., Huang, D., Qiu, Y., Xu, J., Xia, X., Yang, X., Zhang, X., Zong, Z., Song, Y., and Wu, C.: Brown carbon's emission factors and optical characteristics in household biomass burning: developing a novel algorithm for estimating the contribution of brown carbon, Atmos. Chem. Phys., 21, 2329–2341, https://doi.org/10.5194/acp-21-2329-2021, 2021.

ten Brink, H., Maenhaut, W., Hitzenberger, R., Gnauk, T., Spindler, G., Even, A., Chi, X., Bauer, H., Puxbaum, H., Putaud, J.P., Tursic, J., and Berner, A.: INTERCOMP2000: the comparability of methods in use in Europe for measuring the carbon content of aerosol, Atmos. Environ., 38, 6507–6519, https://doi.org/10.1016/j.atmosenv.2004.08.027, 2004.

Tuinstra, F. and Koenig, J. L.: Raman Spectrum of Graphite, J. Chem. Phys., 53, 1126–1130, https://doi.org/10.1063/1.1674108, 1970.

Venkatachari, P., Zhou, L., Hopke, P. K., Schwab, J. J., Demerjian, K. L., Weimer, S., Hogrefe, O., Felton, D., and Rattigan, O.: An Intercomparison of Measurement Methods for Carbonaceous Aerosol in the Ambient Air in New York City, Aerosol Sci. Tech., 40, 788–795, https://doi.org/10.1080/02786820500380289, 2006.

Wang, Y., Chung, A., and Paulson, S. E.: The effect of metal salts on quantification of elemental and organic carbon in diesel exhaust particles using thermal-optical evolved gas analysis, Atmos. Chem. Phys., 10, 11447–11457, https://doi.org/10.5194/acp-1011447-2010, 2010.

Watson, J. G., Chow, J. C., and Chen, L.-W. A.: Summary of Organic and Elemental Carbon/Black Carbon Analysis Methods and Intercomparisons, Aerosol Air Qual. Res., 5, 65–102, https://doi.org/10.4209/aaqr.2005.06.0006, 2005.

WKO, Mineralölindustrie: https://www.wko.at/branchen/industrie/ mineraloelindustrie/statistik.html, last access: 19 February 2020.

Wonaschütz, A., Hitzenberger, R., Bauer, H., Pouresmaeil, P., Klatzer, B., Caseiro, A., and Puxbaum, H.: Application of the Integrating Sphere Method to Separate the Contributions of Brown and Black Carbon in Atmospheric Aerosols, Environ. Sci. Technol., 43, 1141–1146, https://doi.org/10.1021/es8008503, 2009.

Yu, J. Z., Xu, J., and Yang, H.: Charring Characteristics of Atmospheric Organic Particulate Matter in Thermal Analysis, Environ. Sci. Technol., 36, 754–761, https://doi.org/10.1021/es015540q, 2002.

Zickler, G. A., Smarsly, B., Gierlinger, N., Peterlik, H., and Paris, O.: A reconsideration of the relationship between the crystallite size La of carbons determined by X-ray diffraction and Raman spectroscopy, Carbon, 44, 3239–3246, https://doi.org/10.1016/j.carbon.2006.06.029, 2006.

Supplement of Investigation of structural changes of atmospheric aerosol samples during two thermal–optical measurement procedures (EUSAAR2, NIOSH870) Haller et al., 2021.

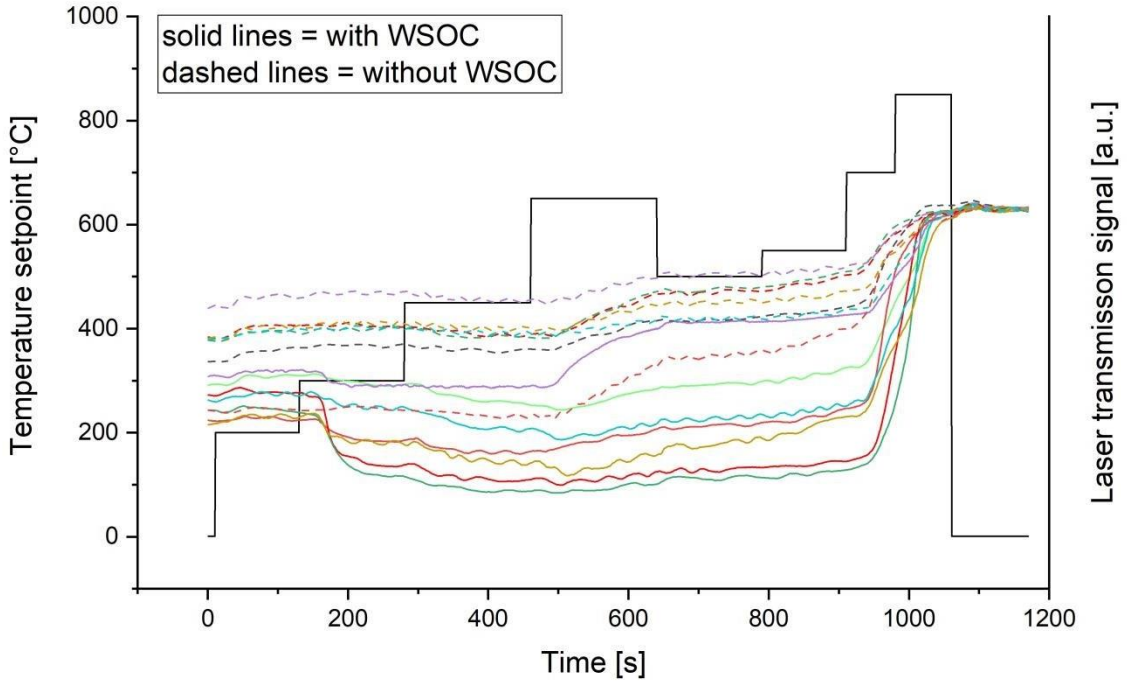

Figure S1: Progress of the laser signals for all samples with and without WSOC measured with the EUSAAR protocol. The lasersignals are normalized to the signal of the clean filter at the end of the procedure.

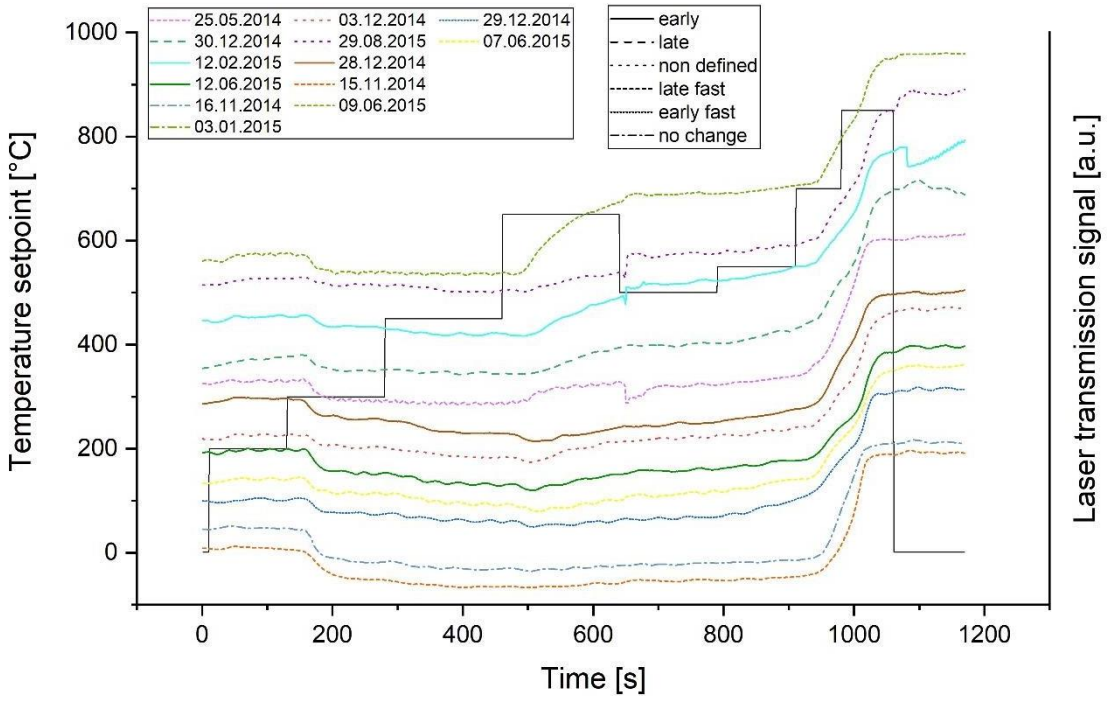

Figure S2: Transmission laser signals during the heating procedure of the EUSAAR2 protocol for all cases with a pronounced step during the 300°C temperature level in He. The different line patterns represent the Raman categories early, late, late and fast, early and fast, no change and non-defined. The black solid line represents the ideal temperature curve in the instrument.

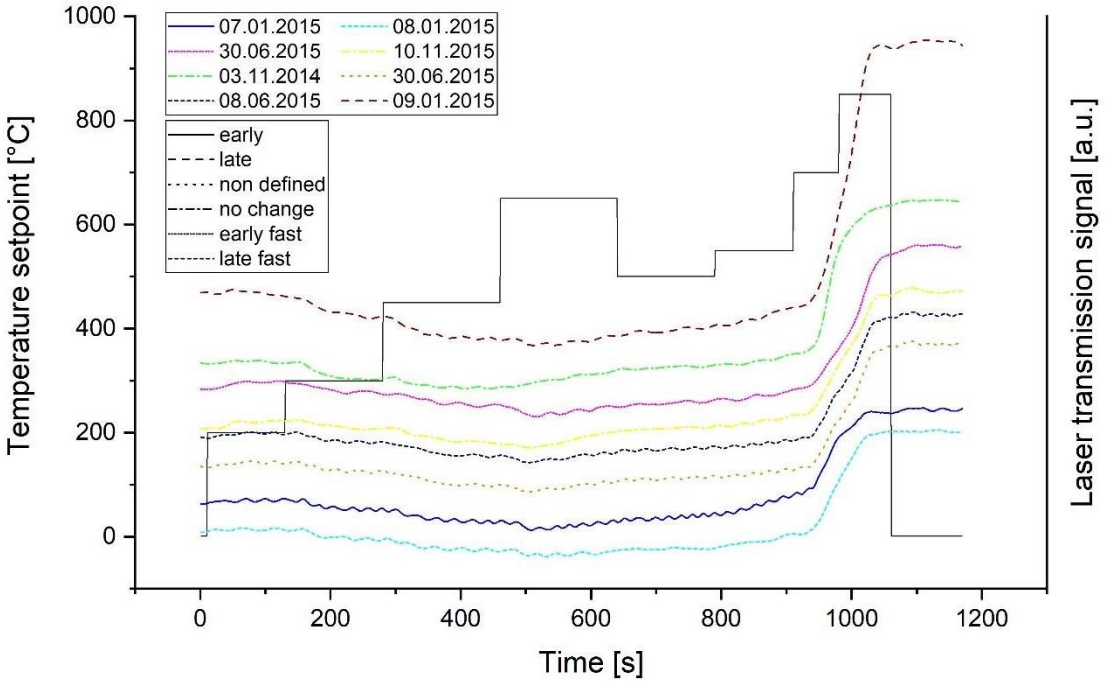

Figure S3: Transmission laser signals during the heating procedure of the EUSAAR2 protocol for all cases with a relatively steady decrease during the first three temperature levels in He. The different line patterns represent the Raman categories early, late, late and fast, early and fast, no change and non-defined. The black solid line represents the ideal temperature curve in the instrument.

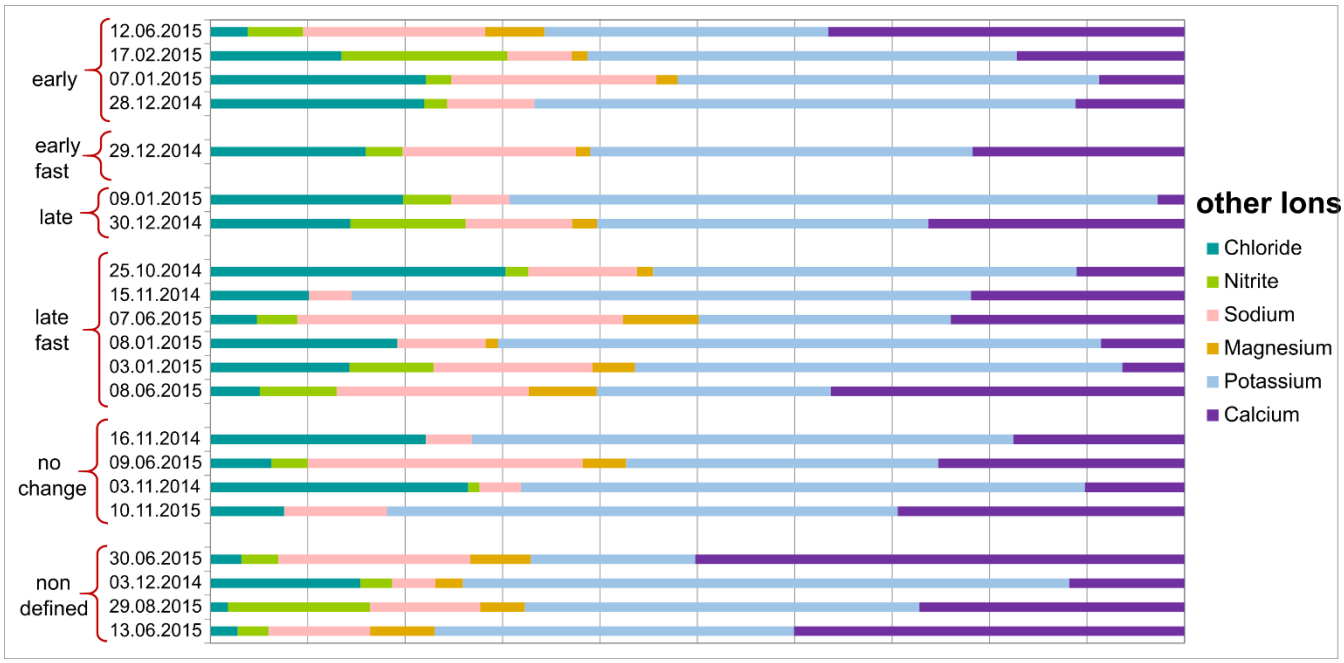

Figure S4: Fractions of analyzed minor ions, which were summarized as "other ions" in Fig. 7 in the main text, sorted by the categories representing the behavior of the Raman spectra during the thermal optical heating procedure.

Appendix: Additional published material

During the work for this thesis, the author participated also in another study (A. Wonaschuetz, T. Haller, E. Sommer, L. Witek; H. Grothe, R. Hitzenberger: Collection of soot particles into aqueous suspension using a particle-into-liquid sampler. 2019 In: Aerosol Science and Technology 53 (1), S. 21–28). Since the topic of this publication is not directly related to the topic of this thesis, and since the investigation was led by A. Wonaschuetz the paper is given here as an appendix.

In the commercial particle-into liquid sampler (PILS, Model 4001, Brechtel, Inc.) aerosol particles are transferred into a liquid (e.g. water) by mixing the aerosol stream with hot steam. In a subsequent cooling step, the aerosol particles act as droplet nuclei, form droplets and increase in size. The droplets are then impacted on a quartz plate which is rinsed continuously with water so that the material included in the droplets is washed into the liquid sample. Particles that do not grow (large enough) should not impact on the plate but follow the gas stream to the exhaust. The general assumption is that only water-soluble and / or hygroscopic particles enter the liquid. Sullivan et al. (2004), e. g. used a PILS to determine the water-soluble organic carbon (WSOC) fraction of atmospheric aerosols using a total organic carbon analyzer, combine these data with results for EC and OC obtained by thermal-optical measurements and report time series of WSOC/OC ratios (Sullivan et al., 2004).

As the behavior of WSOC during thermal optical analyses is of interest for the major focus of the thesis and as the PILS might have been used to separate WSOC from other carbonaceous fractions in CAST soot, the author of the thesis participated also in the PILS study.

In this study, the collection efficiency of a PILS was analyzed for different CAST soots in order to determine the collection efficiency especially for BC – a substance that is generally reported to be hydrophobic (unless it is coated with a hygroscopic film) and water insoluble (e.g. Bond et al., 2013).

CAST soot was produced with the miniCAST (type 5201C Jing-CAST Technologies, section 4.1) using six different C/O ratios between 0.230 and 0.353, where for four settings EC contributed more than 70% to TC. BC and BrC concentrations were determined with the integrating sphere method (see section 4.5) for the aerosol flow entering the PILS (using filter samples) and for the liquid samples leaving the PILS (by analyzing the liquid samples directly). An appreciable collection of insoluble and hydrophobic material by the PILS was found: The overall collection efficiency for BC (averaged over all CAST-settings) was about 20% so care must be taken, when liquid PILS samples are interpreted as liquid containing only soluble and hygroscopic material. This might not be the case under all circumstances.

The publication is reprinted on the following pages as published in the journal Aerosol Science and Technology.

Collection of soot particles into aqueous suspension using a Particle-Into-Liquid Sampler

Anna Wonaschuetz[1], Theresa Haller[1], Eva Sommer[1], Lorenz Witek[1], Hinrich Grothe[2], Regina Hitzenberger[1]

[1] University of Vienna, Faculty of Physics, Vienna, Austria;
[2] TU Wien, Institute of Materials Chemistry, Vienna, Austria

Abstract

Steam collection devices collecting aerosol particles into liquid samples are frequently used to analyze water-soluble particulate material. The fate of water-insoluble components is often neglected. In this work, we show that fresh soot particles can be suspended into pure water using a steam collection device, the Particle-Into-Liquid Sampler (PILS, Weber et al., 2007). The overall collection efficiency of freshly generated soot particles was found to be on the order of 20%. This shows that, depending on the analytic technique employed, the presence of insoluble and/or hydrophobic particles in liquid samples from steam collection cannot be neglected.

Introduction

Steam collection devices are used for collecting aerosol particles into a liquid sample. While details vary from instrument to instrument, the basic principle of operation is the mixing of the aerosol with hot steam, followed by cooling and droplet formation (with the aerosol particles serving as condensation nuclei) and transfer of the droplets into a liquid sample for analysis. A number of analysis methods of the liquid sample are described in the literature: on-line bulk chemical composition measurements using ion chromatography (IC) (Weber et al., 2001; Khlystov, Wyers and Slanina, 1995; Poruthoor and Dasgupta, 1995; Loeflund et al., 2001; Timonen et al., 2010), determination of water-soluble organic carbon (WSOC) by TOC analysis (Sullivan et al., 2004), atomic absorption spectrometry (Kidwll and Ondov, 2004), measurement of aerosol acidity (Ito et al., 1998), fluorometric measurements (Poruthoor and Dasgupta, 1998), and other liquid-phase chemical analysis methods (Sierau et al., 2003; Parshintev et al., 2010; Saarnio et al., 2013; Clark et al., 2013; Violaki et al., 2016; Zhang et al., 2016).

The collection of particles in steam collection devices is based on their ability to act as condensation nuclei at the supersaturation achieved in the cooling section of the instrument. If insoluble particles are hygroscopic (this includes hydrophobic matter that has acquired a hygroscopic surface film, e.g. soot particles with a sulfate coating), at sufficient supersaturation, water will condense on them, and the particles will enter the liquid sample. Supersaturations in steam collecting devices tend to be very high: Khlystov, Wyers and Slanina (1995) report over 200% for their steam jet aerosol collector (SJAC); Kidwell and Ondov (2004) report a maximum theoretical saturation ratio of 1.8 in their instrument. They also state that a saturation ratio of 1.25 is needed to grow hydrophobic particles as small as 0.010 µm to 5 µm within 0.03 s (residence time in device is 0.5 s). For the Particle-Into-Liquid-Sampler (PILS), Sullivan et al. (2004) report that water vapor condenses on all atmospheric particles larger than

10 – 30 nm. Assuming that this includes insoluble, completely wettable particles, this would place a lower boundary on the PILS supersaturation in the range of 7 to 23% (Kelvin diameter between 10 and 30 nm). Given these conditions, the collection of insoluble, even hydrophobic, material into a liquid sample is possible. Also, the generation of samples of insoluble particles in aqueous suspension without the use of any other solvent has practical applications, e.g., in ice nucleation experiments (Zolles et al., 2015; Augustin et al., 2013; Häusler et al., 2017).

The capability of steam collection devices to collect insoluble and/or hydrophobic material is described in the literature, although usually not in much detail: For the Steam Jet Aerosol Collector (SJAC), Slanina et al. (2001) state a sampling efficiency for carbon black particles (d_p >10 nm) of 99.9%, but do not describe how this was determined. Ito et al. (1998) explicitly state that "solid material remains suspended", but do not comment on its fate in the analytical system. Kidwell and Ondov (2004) describe their liquid sample as a slurry containing both soluble and hydrophobic components, both of which were analyzed without physical separation. For the Particle-into-liquid sampler (PILS, a version of which is used in this study), Weber et al. (2001) describe the sample as a "liquid containing particles". For a later version of the PILS, Orsini et al. (2003) state that the "final exiting flow is a solution containing the soluble ions of the collected aerosol particles". The solubility of particles is discussed as a potential source for artefacts, but insolubles are not discussed specifically. In a more detailed investigation, Zhang et al. (2016) report the sampling of slightly water-soluble compounds in a PILS system: Using organic standards of variable solubility, and employing a mixture of isopropanol and water as wash flow (which may increase solubility of some substances), they find a solubility threshold of 1 g L^{-1}, above which a mass collection efficiency of >0.6 is achieved. In some works, insolubles are stated to be removed by an in-line liquid filter placed into the liquid sample flow line (Timonen et al., 2010; Rastogi et al., 2015; Satish et al. 2017), and often, a pore size is given: 0.45 µm (Rastogi et al., 2015; Satish et al. 2017), or 0.5 µm (Sullivan et al., 2004). However, this technique may not be sufficient to remove insolubles for every type of aerosol sample. For example, fresh combustion particles, consisting mostly of insoluble material, are on the order of tens of nanometers in diameter, much smaller than the reported pore size. The actual percentage of particles retained by an inline filter is usually not reported in the PILS literature. In many other studies, the possible presence of insoluble material is not mentioned at all.

An experiment determining explicitly the sampling efficiency of insoluble and hydrophobic material in steam collection devices is missing from the literature to the best of our knowledge. In this work, we examine the possible transfer of insoluble and partially hydrophobic aerosol particles into a PILS liquid sample. We determine the collection efficiency of CAST generated soot by comparing BC concentrations entering and exiting the PILS, using the Integrating Sphere method (Hitzenberger et al., 1996, Wonaschütz et al., 2009) to analyze both the ingoing aerosol and the liquid PILS sample.

Methods

Soot particles were generated with a Combustion Aerosol STandard (CAST) Generator (MiniCAST 5201, Jing (1999); full characterization by Moore et al., 2014). In the CAST, particles are produced in a diffusion flame, with propane (C_3H_8) as combustion gas (combustion gas flow rate Q_{C3H8}), and filtered pressurized air as oxidation gas (oxidation gas flow rate Q_{ox}). Nitrogen can be added (Q_{N2}) to the mix of propane and oxidation gas. The aerosol exiting the combustion chamber is quenched by adding N_2 (7.5 lpm) into the flow, stabilizing the particle size distribution, and diluted by filtered pressurized air (air flow rate Q_p), which compensates for the variations in the amount of soot produced by the CAST at the different combustion conditions. By varying the gas flow rates Q_{C3H8} and Q_{ox}, the carbon/oxygen (C/O) ratio of the combustion process is changed, which in turn influences the physical and chemical properties of the soot particles produced (Moore et al., 2014; Kim et al., 2015). This will be termed "C/O setting" for the remainder of this paper.

The detailed design of the particle-into-liquid sampler (PILS Model 4001, Brechtel, Inc.) is described in the literature (Weber et al., 2001; Orsini et al., 2003; Sorooshian et al., 2006). The aerosol enters the instrument via an impactor with a lower cut diameter of 2.5 µm aerodynamic equivalent diameter. In the instrument, the aerosol is mixed with steam at a temperature of about 97.5 – 100 °C. In the condensation chamber, the particles grow into droplets. The droplets are then transported to, and impacted on a quartz plate. The air flow passes through an internal critical orifice (13.4 lpm), and leaves through the pump exhaust. The impacted droplets are transferred into a wash flow along a mesh wick at the perimeter of the quartz plate. The liquid sample is then collected into flexible tubing attached at the bottom of the mesh wick/quartz plate and transported by a peristaltic pump (flow rate: 0.5 ml/min). The sample passes through a debubbler, which removes any remaining air, and is finally collected in a vial. The reported lower collection limit of particle size is d_p = 30 nm for sulfate particles (Orsini et al., 2003), or between 10 and 30 nm for atmospheric particles (Sullivan et al., 2004).

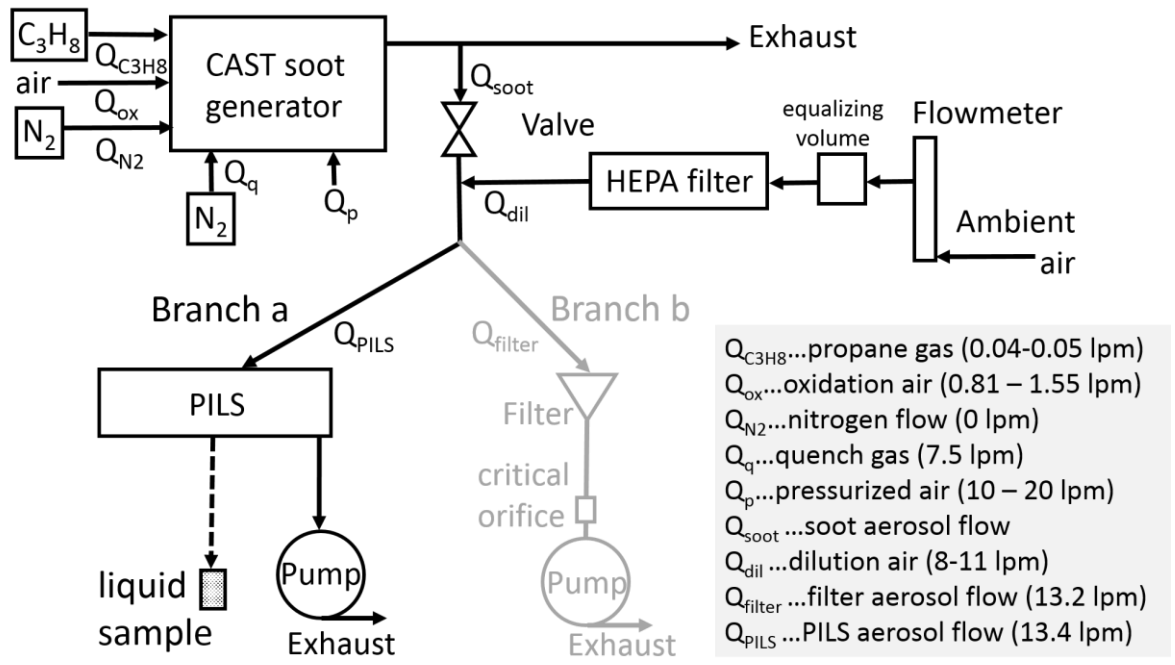

Figure 1: Experimental setup. Branch a: Sampling of soot aerosol by the Particle-Into-Liquid Sampler, Branch b: Filter sampling of the soot aerosol.

Figure 1 shows the experimental setup. Soot aerosol generated by the CAST passes through a valve and is diluted with filtered pressurized air (dilution flow rate Q_{dil}; HEPA filter, Pall Corporation). The aerosol then passes to one of two branches, which are operated alternatingly, by physical attachment/removal: in Branch a (black in Figure 1), the aerosol flow (Q_{PILS}) is controlled by the PILS internal critical orifice. The aerosol enters the PILS, where it is collected into the liquid sample as described above. In Branch b, the particles are collected on a quartz fiber filter (Pallflex Tissuquartz, Pall Corporation, 47 mm diameter, sample area: 40 mm diameter). The filters had been prebaked for 1h at 450°C and equilibrated for 24 h at room temperature in a water-saturated atmosphere to remove adsorbed OC (Jankowski et al., 2008). The aerosol flow rate in the filtration branch (Q_{filter}) is controlled by a separate critical orifice. Filter samples were stored in a freezer after loading and brought to room temperature immediately before analysis. The measured flow rates (flowmeter, Fig. 1) Q_{PILS} and Q_{filter} were (13.4 +/- 0.2) lpm and (13.2 +/- 0.3) lpm, respectively. The possible Q_{dil} and C/O settings were bracketed by the necessity to obtain BC and/or BrC concentrations above the detection limits of the integrating sphere (IS) method (1 - 10 µg BC/sample) and, on the other hand, minimizing PILS cleaning efforts (see also below). Optimum working conditions were found in test measurements and comprised (i) two alternative amounts of sampled liquid (12 ml and 2 ml), (ii) Q_{dil} ranging from 7.5 – 12 lpm, (iii) the C/O settings shown in Table 1. Nitrogen was not added to the mix of propane and oxidation gas (Q_{N2}=0). At these settings, no decrease of Q_{PILS} was observed within the sampling time.

Two experiments were conducted to determine the collection efficiency CE for the soot particles: 1. determination of CE at different C/O settings with constant dilution for each setting; 2. determination of CE at different dilutions (i.e., different soot concentrations) for C/O setting 2.

For Experiment 1, the following measurement procedure was employed for each C/O setting: The flow rate in Branch b was measured by closing the valve and reading the total flow rate from the flowmeter. After this, an appropriate Q_{dil} was set by opening the valve. The aerosol was sampled on a filter for two to five minutes (depending on the dilution). Meanwhile, the PILS was sampling filtered air. The setup was then switched to Branch a, and the total flow rate was measured (valve closed). The valve was opened and adjusted to the desired dilution flow; then, one (for settings 1 and 6) or two (for all other settings) PILS samples were taken with sampling times of 24 min (12 ml of sample) or 4 min (2 ml of sample), respectively. This procedure was repeated five times (three times for setting 6), followed by a last filter sample. The PILS was then rinsed by sampling filtered air for a minimum of one hour. Previous test measurements showed that after 45 minutes no more soot was detectable by the IS method in the PILS sample. As soot deposits accumulated within the PILS components over time, in spite of the rinsing, a rigorous cleaning schedule (impactor surface, mesh wick, debubbler membrane, air flow critical orifice) was kept, which depended on the CAST settings. For example, for settings 2, 3, and 4, around fifteen samples were taken between each cleaning; for setting 5, cleaning was necessary after only 1-2 samples. The components were cleaned in an ultrasonic bath, using isopropanol and/or ultrapure water as solvents.

In Experiment 2, C/O setting 2 was chosen to evaluate the collection efficiency CE. The measurement procedure was analogous; a series of 70 measurements was conducted by varying the dilution air flow rate (Q_{dil}), effecting different incoming soot concentrations. Q_{dil} was varied between 8 and 11 lpm in steps of 0.5 lpm (10 measurements for each Q_{dil} setting).

The analysis of liquid samples with the IS method (Heintzenberg, 1982; Hitzenberger et al., 1996) allows for the detection of black and brown carbon (Wonaschütz et al., 2009; Reisinger et al., 2008). A detailed description of the method can be found in the study by Wonaschütz et al., 2009. Briefly, a

sample vial containing a filter piece immersed in a liquid, or containing a liquid suspension (see below for sample preparation), is placed into the illuminated integrating sphere. The change in the light signal caused by the sample (relative to light signal with an empty vial) is measured and evaluated against calibration standards (suspensions of carbon black and humic acid sodium salt) to obtain the masses of black (BC) and brown (BrC) carbon in the sample. The signals caused by BrC and BC are separated with an iterative procedure using the difference in wavelength dependence of light absorption by the two materials. Concentrations of BC and BrC aerosol are calculated from the area of the analyzed filter piece, the area of the filter deposit, and the flow rates in the experimental setup.

The filter samples were prepared for IS analysis as follows: a circular filter punch (diameter: 10 - 12 mm, depending on the loading of the filter) was inserted into a 5 ml PE vial (50 ml vial for setting 1 and 6), and immersed in 5 ml (18 ml for setting 1 and 6) of a mixture of 50% acetone, 40% water, and 10% isopropanol. For the liquid samples from the PILS, the organic solvents were added in the appropriate ratios, e.g. 0.5 ml of isopropanol and 2.5 ml of acetone to 2 ml of liquid sample (setting 2, 3 and 4) and 3 ml of isopropanol and 15 ml of acetone to 12 ml of liquid sample (setting 1 and 6).

The concentration of BC in Q_{PILS} at the time of the PILS sampling (BC_{in}), is calculated on the basis of the filter measurements. We assume that the CAST generator produces a constant aerosol concentration for each C/O setting, and that the filter sampling efficiency is 1. We also assume that the light absorption properties of the CAST soot particles collected on the filter remain unchanged after passing through the PILS into the liquid sample. BC_{in} concentrations are expressed with respect to the PILS-in flow rate, i.e.

$$[BC_{in}] = [BC_{CAST\text{-}out}]*(Q_{PILS}\text{-}Q_{dil})/Q_{PILS}, \qquad (1)$$

where $BC_{CAST\text{-}out}$ is the BC concentration in the undiluted CAST output flow determined by filter sampling:

$$[BC_{CAST\text{-}out}] = BC_{filter}/(t_{filter}*(Q_{filter} - Q_{dil})). \qquad (2)$$

Here, BC_{filter} is the total amount of BC collected on the filter during the filter sampling time t_{filter}. The BC concentration in Q_{PILS} as detected by PILS sampling (BC_{out}) is also expressed with respect to the PILS-in flow, i.e.:

$$[BC_{out}] = BC_{PILS}/(Q_{PILS}*t), \qquad (3)$$

where BC_{PILS} is the total BC amount in the liquid sample.

In order to determine the collection efficiency CE of the PILS, the BC concentration as determined by PILS sampling ($[BC_{out}]$), was compared with that determined by filter sampling ($[BC_{in}]$):

$$CE = [BC_{out}]/[BC_{in}]. \qquad (4)$$

Over the course of the measurements for Experiment 2 (different dilution for the same C/O setting), it was found that the measurement error incurred by the setting of the flow rates was negligible in comparison to that incurred by uneven filter loading (i.e., variability in the BC loading of different filter punches of the same filter was comparable to the BC loading of punches of different filters). A mean value of $BC_{CAST-out}$ = 3.05 +/- 0.6 mg/m^3 was therefore calculated and used in equation 3.

Auxiliary measurements were conducted to characterize the ingoing soot aerosol and help with the interpretation of the results: Number size distributions of the particles produced at the six different C/O settings were measured: The CAST output was diluted by a factor of 32.5 and passed to a custom-built DMPS System: a Vienna-type DMA (configuration described by Burkart et al., 2011), equipped with a soft x-ray charger (TSI, Inc.) and coupled to a CPC (Model 3776, TSI, Inc.). The number size distributions were recorded for a size range of 10 nm – 926 nm and converted into mass size distribution assuming a nominal density of 0.8 g/cm^3, an estimate based on the effective densities of mini-CAST soot reported by Moore et al.(2014). For each C/O setting, two loaded filters were also randomly chosen for determination of OC-EC: two or three punches (1.5 cm^2) of each filter were analyzed in an OC-EC aerosol analyzer (Sunset Laboratory Inc.), set to the EUSAAR protocol (Cavalli et al., 2010).

Results and Discussion

In this section, we discuss the properties of the ingoing soot aerosol, followed by the results and discussion of the PILS collection efficiency for these particles. Figure 2 shows the contributions of OC and EC in the aerosol generated at the different settings. Evidently, the carbonaceous particulate matter of setting 6 consists mostly (94%) of OC; for setting 1, 52% OC were found. For all other settings, EC is the dominant component, varying between 71 and 94%. Mass size distributions (Figure 3) of the soot particles at the different settings clearly show that settings 1 and 6 have smaller modal diameters (99 and 139 nm, respectively), and the distribution is generally shifted to smaller diameters. The other settings, in turn, have larger modal diameters (184, 238, 248, 262 nm for settings 2, 3, 4, and 5, respectively). The particle size range is consistent with the findings by Moore et al. (2014), who operated their miniCAST at slightly different settings (Q_{C3H8} = 0.06 lpm, Q_{dil} = 20 lpm, Q_{oxi} = 0.6 - 1.8 lpm), but also found modal sizes > 90 nm for the range of C/O ratios used here (0.23 – 0.35). They also report an increasing OC/TC ratio as a function of particle size: in their experiments, OC/TC varies from less than 0.3 for soot modal sizes > 100 nm to over 0.8 for modal sizes < 50 nm (Moore et al., 2014).

Qualitatively, this trend is reproduced here, in that it is the settings with smaller overall size ranges (1 and 6), that show the larger OC/TC ratios (0.94 and 0.52).

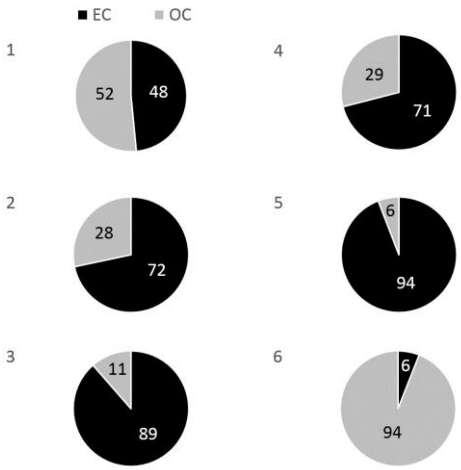

Figure 2. Fraction of OC and EC for the six C/O settings.

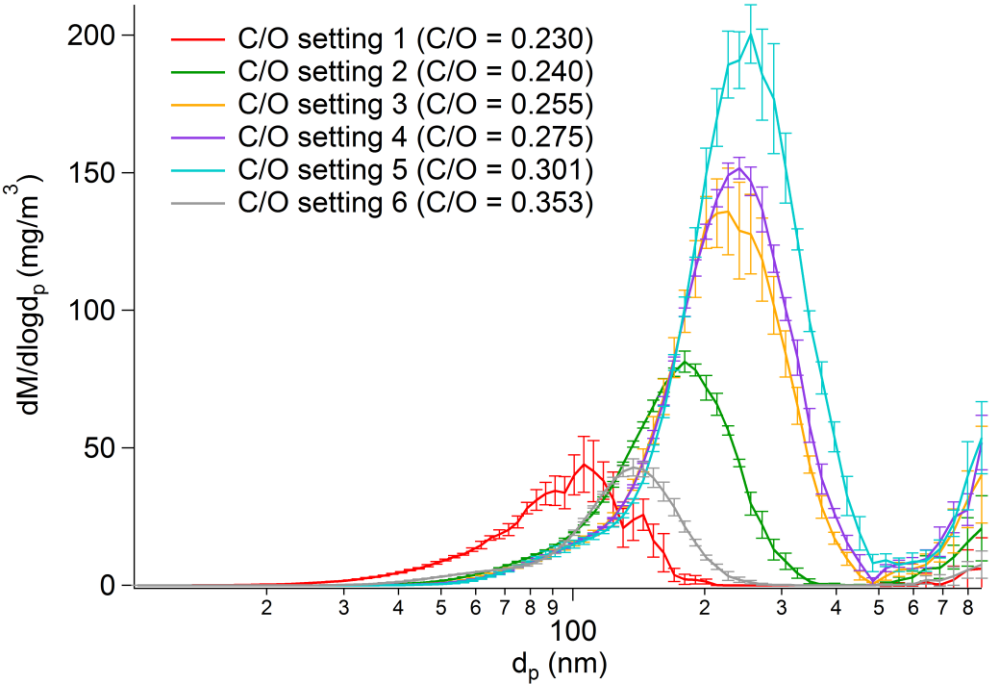

Figure 3. Mass size distributions of CAST soot for the six C/O settings as measured by a DMPS (number size distribution converted assuming a density of 0.8 g/cm^3).

The result of Experiment 1 is shown in Figure 4: The determined overall collection efficiency CE for the CAST soot is 0.20. There is variability in the CE for the different C/O settings: Settings 1 and 6 clearly have a much lower CE than the other four settings. Looking at the size distribution in Figure 3, it is evident that these are the settings with the smallest modal diameter and overall size range. Figure 5 shows [BC_{out}] vs. [BC_{in}] for different BC_{in} concentrations at C/O setting 2. A collection efficiency of 0.26 was determined for a [BC_{in}] concentration range of 469 to 1200 µg/m^3 (R^2 of 0.94), largely consistent with the result shown in Figure 4.

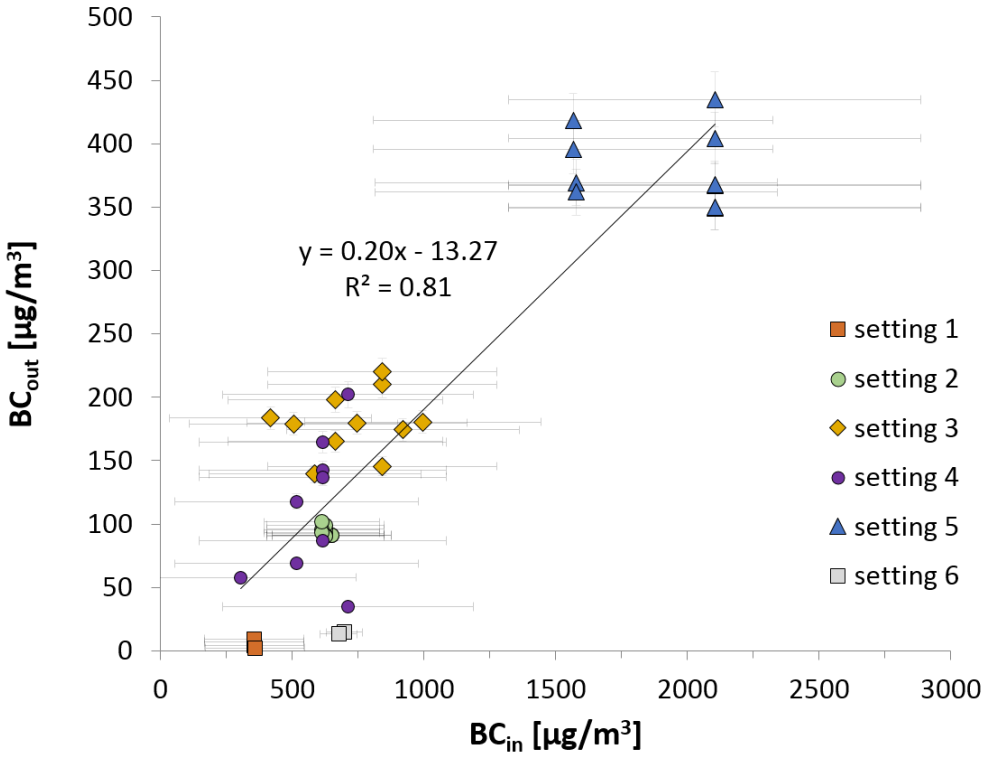

Figure 4. BC_{out} concentrations detected by the PILS vs. calculated BCin concentrations based on filter measurement for the six different CAST C/O settings.

The low collection efficiency is entirely expected, given the insoluble and/or hydrophobic nature of fresh soot. It compares well to the PILS collection efficiencies of <0.2 for the least soluble organic standards presented by Zhang et al. (2016), and it is lower than the PILS CE of 50-94% (particle sizes of 25 – 300 nm) for water-soluble ions reported by Weber et al. (2001). The majority of the soot did not enter the PILS liquid sample. Possible mechanisms are the following: (i) particles do not activate at all, (ii) activated particles may fail to grow large enough to impact on the quartz plate, as suggested by Zhang et al. (2016), (iii) wall losses of collected particles in the liquid sampling line. In cases (i) and (ii), soot particles end up in the exhaust air instead of the liquid sample. After our experiments, accumulated dark deposits were clearly visible in bends of the exhaust air line, showing that mechanisms (i) and/or (ii) are effective. Given the high supersaturation in the PILS, mechanism (i) would effectively require the particles to have an entirely hydrophobic surface. This is not implausible: Henning et al. (2012) find neither CCN activation nor hygroscopic growth of miniCAST soot, regardless of OC content. For fresh aircraft combustion soot, Hitzenberger et al. (2003) find activation ratios

smaller by a factor 10^3 than those of insoluble, but wettable particles of the same size. Popvicheva et al. (2008), however, observe increasing water adsorption with increasing organic content of CAST soot, along with more oxygen-containing groups on the particle surface. Moore et al. (2014) report a hygroscopicity (κ) of miniCAST soot between 0 and 10^{-3} (C/O ratios between 0.21 and 0.29), indicating that soluble compounds are present, depending on the exact combustion settings. In combination with the high supersaturations in the PILS, this indicates that some particles may still activate. Subsequently, mechanism (ii) can take effect and may explain the smaller CE of settings 1 and 6: Zhang et al. (2016) show that hydrophobic components in the particles slow down droplet growth, with negative effects on CE: droplets may not reach the critical size for impaction within the residence time (1 s) in the supersaturated environment in the PILS. In our experiment, this effect may be particularly limiting to the collection of the smaller particles in settings 1 and 6. Finally, black deposits were also observed in the liquid sample path, in particular the impactor surface and the debubbler membrane. This indicates that a fraction of soot particles that were successfully transferred into the liquid sample have been lost during transport in the liquid lines (mechanism (iii)).

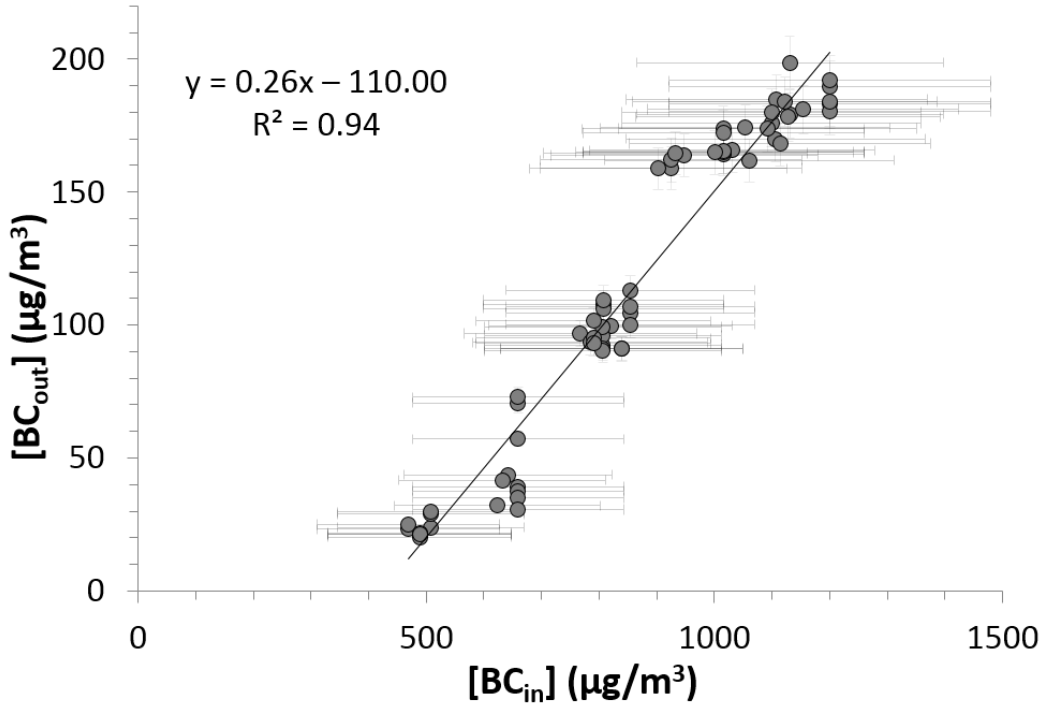

Figure 5. BC_{out} concentrations detected by the PILS vs. calculated BCin concentrations based on filter measurement for C/O setting 2.

Conclusions

We find an appreciable collection of insoluble and hydrophobic material by the PILS. With an overall BC collection efficiency of about 20%, the presence of insoluble and hydrophobic particles in PILS samples should not be assumed to be negligible under all circumstances, especially when sampling at high concentrations. Care must be taken when relying on PILS sampling for definitions of water-soluble components of aerosols. For example, in the original method description (Sullivan et al., 2004) for WSOC analysis of PILS samples (PILS-TOC), WSOC is operationally defined as "the fraction of particulate organic carbon that has been collected in water by the PILS, and at a given liquid concentration, penetrates a 0.5 µm filter and liquid transport tubing, and is detected". As mentioned above, and as shown in Figure 3, insoluble, fresh combustion particles can be much smaller than 0.5 µm and may pass such a filter. In the TOC analyzer, total organic carbon is determined by oxidation using UV irradiation and ammonium persulfate ((NH4)2S2O8), followed by conductivity detection of dissolved CO2. It remains unclear whether a physical separation of soluble and insoluble material is achieved.

In atmospheric samples, the PILS sample should be expected to contain hydrophobic and insoluble material, as mixed particles (soluble and insoluble components) are a common occurrence (e,g, Okada and Hitzenberger, 2001). In general, the relevance of insolubles depends on the analysis method used on the PILS sample, but care must be taken not to view the PILS sample as a liquid containing exclusively soluble material.

Acknowledgements

We gratefully acknowledge financial support from the Austrian Science Foundation (FWF), project number P26040.

References

Augustin, S., Wex, H., Niedermeier, D., Pummer, B., Grothe, H., Hartmann, S., Tomsche, L., Clauss, T., Voigtländer, J., Ignatius, K., Stratmann, F. (2013). Immersion freezing of birch pollen washing water. Atmos. Chem. Phys., 13, 10989–11003. doi:10.5194/acp-13-10989-2013.

Burkart, J., Steiner, G., Reischl, G., Hitzenberger, R. (2011). Long-term study of cloud condensation nuclei (CCN) activation of the atmospheric aerosol in Vienna. Atmos. Environ. 45: 5751-5759, 2011, doi: 10.1016/j.atmosenv.2011.07.022.

Cavalli, F., Viana, M., Yttri, K. E., Genberg, J., Putaud, J.-P (2010). Toward a standardized thermal-optical protocol for measuring atmospheric organic and elemental carbon: the EUSAAR protocol. Atmos. Meas. Tech. 3, 79-89, doi: 10.5194/amt-3-79-2010.

Clark, C.H., Nakao, S., Asa-Awuku, A., Sato, K., Cocker, D.R. (2013). Real-Time Study of Particle-Phase Products from α-Pinene Ozonolysis and Isoprene Photooxidation Using Particle into Liquid Sampling Directly Coupled to a Time-of-Flight Mass Spectrometer (PILS-ToF). Aerosol Sci Technol 47 (12), 1374-1382, doi: 10.1080/02786826.2013.844333.

Häusler, T., Witek, L., Felgitsch, L., Hitzenberger, R., Grothe, H. (2017). Freezing on a Chip—A New Approach to Determine Heterogeneous Ice Nucleation of Micrometer-Sized Water Droplets. Atmosphere, 2018, 9(4), 140, doi:10.3390/atmos9040140.

Heintzenberg, J. (1982). Size-segregated measurements of particulate elemental carbon and aerosol light absorption at remote Arctic locations. Atmos. Environ. 16: 2461 – 2469.

Henning, S., Ziese, M., Kiselev, A., Saathoff, H., Moehler, O., Mentel, T. F., Buchholz, A., Spindler, C., Michaud, V., Monier, M., Sellegri, K., Stratmann, F. (2012), Hygroscopic growth and droplet activation of soot particles: uncoated, succinic or sulfuric acid coated, Atmos. Chem. Phys. 12, 1680-7324, doi: 10.5194/acp-12-4525-2012

Hitzenberger, R., Dusek, U., Berner, A. (1996). Black carbon measurements using an integrating sphere technique. J. Geophys. Res. 101:19601 – 19606.

Hitzenberger, R., Giebl, H., Petzold, A., Gysel, M., Nyeki, S., Weingartner, E., Baltensperger, U., Wilson, C. W. (2003, Properties of jet engine combustor particles during the PartEmis experiment. Hygroscopic properties at supersaturated conditions, Geophys. Res. Lett. 30, 14, 1779, doi:10.1029/2003GL017294

Ito, K., Chasteen, C.C., Chung, H.-K., Poruthoor, S.K., Genfa, Z., Dasgupta, P.K. (1998). A continuous monitoring system for strong acidity in aerosols. Anal. Chem., 70, 2839-2847.

Jankowski, N., Schmidl, C., Marr, I.L., Bauer, H., Puxbaum, H (2008). Comparison of methods for the quantification of carbonate carbon in atmospheric PM10 aerosol samples. Atmos. Environ. 42: 8055-8064

Jing, L. (1999). Standard Combustion Aerosol Generator (SCAG) for Calibration Purposes, in 3rd ETH Workshop on Nanoparticle Measurement, CD-ROM.

Khlystov, A., Wyers, G.P., Slanina J. (1995). The steam-jet aerosol collector. Atmos. Environ. 29:17, 2229-2234.

Kidwell, C.B., Ondov, J.M. (2004). Elemental analysis of sub-hourly ambient aerosol collections. Aerosol Sci. Technol. 38:3, 205-218, doi: 10.1080/02786820490261726.

Kim, J., Bauer, H., Dobovičnik, T., Hitzenberger, R., Lottin, D., Ferry, D., Petzold, A. (2015). Assessing Optical Properties and Refractive Index of Combustion Aerosol Particles Through Combined Experimental and Modeling Studies, Aerosol Sci. Technol., 49:5, 340-350, doi: 10.1080/02786826.2015.1020996.

Loeflund, M., Kasper-Giebl, A., Tscherwenka, W., Schmid, M., Giebl, H., Hitzenberger, R., Reischl, G., Puxbaum, H. (2001). The performance of a gas and aerosol monitoring system (GAMS) for the determination of acidic water soluble organic and inorganic gases and ammonia as well as related particles from the atmosphere. Atmos. Environ. 35: 2861-2869.

Moore, R.H., Ziemba, L.D., Dutcher, D., Beyersdorf, A.J., Chan, K., Crumeyrolle, S., Raymond, T.M., Thornhill, K.L., Winstead, E.L., Anderson, B.E. (2014). Mapping the Operation of the Miniature Combustion Aerosol Standard (Mini-CAST) Soot Generator. Aerosol Sci. Technol. 48:467–479. doi: 10.1080/02786826.2014.890694

Okada, K., Hitzenberger, R (2001). Mixing properties of individual submicrometer aerosol particles in Vienna. Atmos. Environ. 35, 5617 – 5628.

Orsini, D., Ma, Y., Sullivan, A., Sierau, B., Baumann, K., Weber, R.J. (2003). Refinements to the particle-into-liquid sampler (PILS) for ground and airborne measurements of water soluble aerosol composition, Atmos. Environ. 37, 1243–1259. doi: 10.1016/S1352-2310(02)01015-4.

Parshintsev J., Kivilompolo, M., Ruiz-Jimenez, J., Hartonen, K., Kulmala, M., Riekkola, M.-L. (2010). Particle-into-liquid sampler on-line coupled with solid-phase extraction –liquid chromatography-mass spectrometry for the determination of organic acids in atmospheric aerosols. J. Chromatography A, 1217, 5427 – 5433, doi:10.1016/j.chroma.2010.06.026.

Popovicheva, O. B., Persintseva, N. M., Tishkova, V., Shonija, N.K., Zubareva, N.A. (2008). Qhantification of water uptake by soot particles, Environ. Res. Lett. 3, 025009, doi: 10.1088/1748-9326/3/2/025009

Poruthoor, S.K., Dasgupta, P.K. (1995). Continuous Automated Measurement of the Soluble Fraction of Atmospheric Particulate Matter. Anal. Chem. 67, 71-78.

Poruthoor, S.K., Dasgupta, P.K. (1998). Automated particle collection and analysis. Near-real time measurement of aerosol cerium (III). Analytica Chimica Acta 361, 151-159.

Rastogi, N., Patel, A., Singh, A., Singh, D. (2015). Diurnal Variability in Secondary Organic Aerosol Formation over the Indo-Gangetic Plain during Winter Using Online Measurement of Water-Soluble Organic Carbon. Aerosol Air Qual. Res., 15, 2225–2231, doi: 10.4209/aaqr.2015.02.0097.

Reisinger, P., Wonaschütz, A., Hitzenberger, R., Petzold, A., Bauer, H., Jankowski, N., Puxbaum, H., Chi, X., Maenhaut, W. (2008) Intercomparison of Measurement Techniques for Black or Elemental Carbon Under Urban Background Conditions in Wintertime: Influence of Biomass Combustion. Environ. Sci. Technol. 42 (3), 884-889, doi: 10.1021/es0715041

Saarnio, K., Teinilä1, K., Saarikoski, S., Carbone, S., Gilardoni, S., Timonen, H., Aurela, M., Hillamo, R. (2013). Online determination of levoglucosan in ambient aerosols with a particle-into-liquid sampler – high-performance anion-exchange chromatography – mass spectrometry (PILS–HPAEC–MS). Atmos. Meas. Tech., 6, 2839–2849, doi: 10.5194/amt-6-2839-2013.

Satish, R., Shamjad, P., Thamban, N., Tripathi, S., Rastogi, N. (2017). Temporal Characteristics of Brown Carbon over the Central Indo-Gangetic Plain. Environ. Sci. Technol. 2017, 51, 6765−6772, doi: 10.1021/acs.est.7b00734.

Sierau B., Stratmann, F., Pelzing, M., Neusüß, C., Hofman, D., Wilck, M. (2003). A condensation-growth and impaction method for rapid off-line chemical characterization of organic submicrometer atmospheric aerosol particles. J. Aerosol Sci. 34, 225 – 242, doi: 10.1016/S0021-8502(02)00159-3.

Slanina, J., ten Brink, H.M., Otjes, R.P., Even, A., Jongejan, P., Khlystov, A., Waijers-Ijpelaan, A., Hu, M., Lu, Y. (2001). The continuous analysis of nitrate and ammonium in aerosols by the steam jet aerosol collector (SJAC): extension and validation of the methodology. Atmos. Environ 35, 2319-2330.

Sorooshian, A., Brechtel, F. J., Ma, Y. L., Weber, R. J., Corless, A., Flagan, R. C., Seinfeld, J. H. (2006). Modeling and characterization of a particle-into-liquid sampler (PILS). Aerosol Sci. Technol., 40, 396-409, doi: 10.1080/02786820600632282.

Sullivan, A. P., Weber, R. J., Clements, A. L., Turner, J. R., Bae, M. S., Schauer, J. J. (2004). A method for on-line measurement of water-soluble organic carbon in ambient aerosol particles: Results from an urban site. Geophys. Res. Lett., 31:L13105, doi: 10.1029/2004gl019681.

Timonen, H., Aurela, M., Carbone, S., Saarnio, K., Saarikoski, S., Makela, T., Kulmala, M., Kerminen, V. M., Worsnop, D. R., Hillamo, R. (2010). High time-resolution chemical characterization of the water-soluble fraction of ambient aerosols with PILS-TOC-IC and AMS. Atmos. Meas. Tech. 3:1063-1074, doi 10.5194/amt-3-1063-2010.

Violaki, K., Fang, T., Mihalopoulos, N., Weber, R., Nenes, A. (2016). Real-Time, Online Automated System for Measurement of Water-Soluble Reactive Phosphate Ions in Atmospheric. Particles. Anal. Chem. 2016, 88, 7163−7170. doi: 10.1021/acs.analchem.6b01264.

Weber, R. J., Sullivan, A. P., Peltier, R. E., Russell, A., Yan, B., Zheng, M., de Gouw, J., Warneke, C., Brock, C., Holloway, J. S., Atlas, E. L., Edgerton, E. (2001). A study of secondary organic aerosol formation in the anthropogenic-influenced southeastern United States. J. Geophys. Res. 112, D13, doi:10.1029/2007jd00840.

Wonaschütz, A., Hitzenberger, R., Bauer, H., Pouresmaeil, P., Klatzer, B., Caseiro, A., Puxbaum, H. (2009). Application of the Integrating Sphere Method to Separate the Contributions of Black and Brown Carbon in Atmospheric Aerosols. Environ. Sci. Technol. 43:1141 – 1146.

Zhang, X., Dalleska, N. F., Huang, D. D., Bates, K. H., Sorooshian, A., Flagan R. C., Seinfeld, J. H. (2015). Time-resolved molecular characterization of organic aerosols by PILS + UPLC/ESI-Q-TOFMS, Atmos. Environ. 130, 180 – 189, http://dx.doi.org/10.1016/j.atmosenv.2015.08.049.

Zolles, T., Burkart, J., Häusler, T., Pummer, B., Hitzenberger, R., Grothe, H. (2015). Identification of Ice Nucleation Active Sites on Feldspar Dust Particles. J. Phys. Chem. A, 2015, 119 (11), pp 2692–2700. doi: 10.1021/jp509839x.

Acknowledgements

An African proverb says it takes a village to raise a child. The same is true for a PhD student: it takes the support and advice of many people to accomplish a proper scientific work and to bring a thesis to a satisfying end. I yield all of them my thanks and want to name some of them personally.

First of all I want to express my very sincere thanks and respect to my supervisor Prof. Regina Hitzenberger. Without her encouragement I wouldn't have embarked on this whole venture in the first place, and I'm not sure if I would have finished it in the end. I am grateful for her patience and her time for many long, and sometimes certainly nerve-racking, discussions. Despite (or maybe: because of) some disagreements I have learned a lot from her over the last years, not only scientifically but also on a personal level. The latter will hopefully accompany me for a long time regardless of the decisions I make for my future career path.

I want to thank Prof. Hinrich Grothe for giving me the opportunity to use the facilities of the TU Wien. He was always willing to discuss my data interpretation and the chemistry behind it. Without his support, this work wouldn't have been possible.

Many thanks go to Prof. Anne Kasper-Giebl not only for contributing to one of the publications, but also for many discussions about – and help with – the EC/OC Sunset analyzer, which made my frustrations with the instrument more tolerable.

I am grateful to Prof. Herwig Peterlik for his help at the very beginning of this project. He gave me his time to conduct the WAXD measurements with me and to do a first evaluation of the data. I especially thank him for answering my questions in detail in the last months.

Special thanks also to Prof. Christian Rentenberger for performing the TEM measurements and for the discussions on the data.

I also want to thank the Analytical Instrumentation Center (AIT) of the Vienna University of Technology and the group of Bernhard Lendl for providing the Raman microscope. I warmly thank Dr. Karin Wieland who maintained the instrument and dropped by in the lab from time to time and revealed some technical clues and hints.

Warm thanks also to the Aerosol group of the University of Vienna, especially to multiple people who shared with me the "Dissertantenzimmer"; we had numerous inspiring discussions and a lot of fun. In particular I want to thank Dr. Carmen Dameto de España. We started our PhD at the same time and she always encouraged me with her kind personality. Anna Wonaschütz, PhD and Dr. Julia Burkart deserve my gratitude for a series of valuable advice and for the insights they gave me into the work (and life) of a post-doc. I am glad that Anna gave me the opportunity to contribute in her PILS project and I am very thankful for Julia's support while I was writing this thesis.

I owe my thanks also to Prof. Bernadett Weinzierl for the employment during two additional months to cope with a delay caused by the pandemic and for her general support.

I want to thank my friends Dr. Angelika Geroldinger for giving me a quick insight in mathematical statistics, and Mag. Verena Horsky for helping me with a last check of the reference list.

Clearly the whole thesis wouldn't have been possible without financial support. So I want to thank the School- and University Assistance office of the Autonomous Province of Bolzano/Bozen (South Tyrol) for the financial support during the first years of my PhD.
I thank the Austrian Science Fund (FWF) that supported part of this work financially within grant P26040. The integrating sphere technique was developed in 1992 thanks to grant H-85/92, Hochschuljubiläumsstiftung der Stadt Wien.

Curriculum Vitae

Education

PhD student **since 2012**
within the group Aerosol Physics and Environmental Physics,
University of Vienna

Diploma in Physics **November 2011**
Diploma thesis: „Didaktische Rekonstruktion eines Physikpraktikums für Meteorologie“, University of Vienna

Graduation from High School **June 2014**
(Realgymnasium Sterzing – South Tyrol)

Work Experience

Research assistant University of Vienna **2018-2020**
within the group Aerosol and Environmental Physics

Organisation of the group u:queer (voluntary) **since 2019**
Formation and organization of a LGBT+ group for
employees of the University of Vienna

Research assistant University of Vienna **01 – 12 2017**
within the FWF project “The ice nucleation activity of carbonaceous particles”

Physics lessons in a Rudolf-Steiner School **2017 / 2018**
Rudolf-Steiner-Schule Mauer, 1230 Wien

Administrative assistant University of Vienna **01 – 04 2017**
Support oft the lecture „Physik für Biolog*innen“
Organisation of written exams

Several talks and workshops for children **2013 – 2017**
e.g. Children’s University, talks in librabries and schools

Teaching at the University of Vienna **2012 – 2020**

Writing of a nonfiction book for children **2013**
„Alles über Flugzeuge“, G&G-Verlag, Vienna 2013.

Physics teacher in a High Scool **2011 – 2013**
Bundesgymnasium 18, 1180 Wien

Circus teacher **2010 – 2016**

Publications (peer reviewed)

Investigation of structural changes of atmospheric aerosol samples during two thermal-optical measurement procedures (EUSAAR2, NIOSH870); Haller, T., Sommer, E., Steinkogler, T., Rentenberger, C., Wonaschuetz, A., Kasper-Giebl, A., Grothe, H., Hitzenberger, R.; Atmos. Meas. Tech. 14 (5), 3721–3735, 2021.

Structural changes of CAST soot during a thermal–optical measurement protocol; Haller, T., Rentenberger, C., Meyer, J. C., Felgitsch, L., Grothe, H., Hitzenberger, R.; Atmos. Meas. Tech., 7, 3503–3519, 2019.

Collection of soot particles into aqueous suspension using a particle-into-liquid sampler; Wonaschuetz, A., Haller, T., Sommer, E., Witek, L., Grothe, H., Hitzenberger, R.; Aerosol Science and Technology, 1, 21–28, 2019.

Presentations at Conferences

Collection of CAST particles with a particle into liquid sampler (PILS); Witek, L., Haller, T., Wonaschütz, A., Steiner, G., Schuh, H., Häusler, T., Grothe, H. & Hitzenberger, R.; 6 Sep 2016 (Conference poster)

Structural changes of combustion aerosol samples during a thermal-optical measurement protocol; Haller, T., Häusler, T., Witek, L., Grothe, H. & Hitzenberger, R.; 5 Sep 2016 (Conference poster)

Structural changes of a combustion aerosol standard (CAST) soot during a thermal-optical measurement procedure; Haller T., Rentenberger C., Meyer J.C., Felgitsch L., Grothe H., Hitzenberger R.; 2018 (Conference poster)

The ice nucleation activity of black and brown soot aged by exposure to N02 and S02

Grothe, H., Häusler, T., Haselmann, G., Haller, T., Eder, D. & Hitzenberger, R., 6 Apr 2019 (Conference poster)

Comprehensive Assessment of Carbonaceous PM2.5 in Malaysia during Haze Events Influenced by Indonesia Peatland Fire and Non-Haze Period; Kurita H., Fujii Y., Tohno S., Saito N., Kamiya Y., Kameda T., Hitzenberger R., Haller T., Ikeda K., Sakai N., Sulong N.A., Latif M.T., Ohura T.; 2018 (Conference poster)

Long Term Trends of Black and Brown Carbon concentrations in the Urban Aerosol of Vienna; Eva Sommer, Anna Wonaschütz, Theresa Haller, Judith Kasper, Regina Hitzenberger; 2019 (Conference poster)

Structural changes of CAST soot and atmospheric aerosol samples during two thermal-optical analysis protocols (EUSAAR2, NIOSH870); Theresa Haller, Eva Sommer, Hinrich Grothe, Regina Hitzenberger; 2019 (Conference poster)

Differences and analogies of structural changes of CAST-soot and atmospheric aerosol samples during thermal-optical analyses; Theresa Haller, Eva Sommer, Hinrich Grothe, Regina Hitzenberger; (Conference poster)

Collection of black carbon in a Particle-Into-Liquid Sampler; Anna Wonaschuetz, Theresa Haller, Eva Sommer, Lorenz Witek, Hinrich Grothe, Regina Hitzenberger (Conference poster)

Analysis of Structural Changes of Two Different CAST Soots During a Thermal-Optical Measurement Procedure; Theresa Haller, Christian Rentenberger, Jannik C. Meyer, Laura Felgitsch, Hinrich Grothe, Regina Hitzenberger; 2019 (Conference talk, EAC 2019).